The Formation and Age of Leucogranitic Melt in the Garhwal Himalaya

Charlie James Oldman

MSci (Hons) Geology

This thesis is submitted for the degree of Doctor of Philosophy

School of Environment, Earth, and Ecosystem Sciences,

The Open University, United Kingdom

January 2023

Abstract

Metamorphism during orogenic evolution results in the melting of high-grade metamorphic rocks which dramatically decreases mechanical strength, activates shear zones, and may consequently initiate exhumation. The timescales of anatexis, melt amalgamation, migration, and emplacement are the focus of active research and have critical implications for orogenic tectonic development. It is, therefore, important to recognise and distinguish between the geochemical signatures that these processes create and to delineate more precisely the relevant mechanisms and timescales leading to magma genesis. Granitic bodies and source migmatites are exposed across the Himalaya in the Greater Himalayan Sequence (GHS). Many of these granites formed as high-grade metamorphic rocks and were decompressed during the Miocene. However, exact timings of melt formation and melt mechanisms appear to vary laterally across the orogen. This thesis presents constraints on the melt reactions, sources, and timescales of melting episodes that formed the migmatites and leucogranites of the upper GHS using samples from the Alaknanda valley in the Garhwal Himalaya. Detailed petrography and geochemical characterisation of feldspars, micas, and garnet reveal melt reaction systematics through peritectic crystallisation textures and large-ion lithophile element concentrations. Samples are identified with predominately fluid-present, muscovite-dehydration, and biotite-dehydration melting contributions. Combined zircon and monazite geochronology suggests partial melting occurred over an extended period, from 35 to 14 Ma, with melt production sharply increasing around 25 Ma and reaching its peak at 21 Ma, primarily attributed to muscovite-dehydration. Zircon εHf values show little systematic variation with age, suggesting a geochemically-common source of melt. Successive episodes of melt generation around peak metamorphic conditions likely weakened the mid-crustal GHS, priming it for exhumation and subsequent decompression melting.

Acknowledgements

I would like to thank my supervisors, Clare Warren, Tom Argles, Nigel Harris, Sam Hammond, and Chris Spencer. Thank you for all of your enthusiasm in our meetings, both for my research and my personal achievements. Our meetings were often the highlight of my fortnight, not only while we were all stuck at home! A special thank you to Chris for going with me to the Himalaya, it was a defining event in my life, and your guidance was invaluable.

Thank you to all the dedicated technical staff at the Open University, without whom I'd just have a pile of rocks. I'm especially thankful to Barbara Kunz and Giulia Degli Alessandrini for their thoughts, help, and guidance in collecting my geochemical data while dealing with the challenges of operating the labs in the wake of a global pandemic. Thank you to Nick Roberts at NEIF for all of his help collecting monazite dates and in understanding my U-Th-Pb data. I'd also like to thank Zoe Whittaker, at the University of Portsmouth, for letting me use their mineral separation lab and to Catherine, Glen, and Clarence for giving me a welcoming place to stay.

Thank you to all the incredible staff and students in EEES that have filled my tea and lunch breaks with laughter and memorable conversations. A special thank you to Sophie, Emmeline, Stacy, Andrew, Kate, Emily, Ben, and Devyani for being part of our supportive PhD student network and for putting up with all my ranting about rocks and partial melting. Thank you to all the members of the Dynamic Earth research group for all the feedback on my ideas and presentations and for brightening my Monday afternoons.

I'd also like to thank my family who have been so supportive, especially over the last few years. Mum and Dad, thank you for all the trips to museums and to the coast, and for nurturing my curiosity. Thank you, Tom, Alfie, Amelia, Kelda, Fiona, and Jim. And thanks also to my friends back home for reminding me of the real world outside of academia from time to time.

Finally, a thank you to Sophie, Jack, and Baloo. You kept me together through some of the toughest moments of my PhD and the pandemic. I couldn't have got this far without you, and I can't wait to see where we go next.

Contents

Abstract iii

Acknowledgements v

List of Figures ix

List of Tables xvii

List of Abbreviations xviii

1 Introduction 1

1.1 Thesis objectives 3

1.2 Major geological units of the Himalaya 4

1.3 The GHS of the Garhwal Himalaya 6

1.4 Partial melting in the GHS 7

1.5 Tectonic models and exhumation 8

1.5.1 Critical taper and channel flow models 8

1.5.2 The timing and rate of GHS exhumation 8

1.6 Thesis structure 10

2 Fieldwork and sample descriptions: implications for determining melt reaction and percentage 11

2.1 Introduction 11

2.2 Fieldwork and sampling 12

2.3 Methods 18

2.4 Key sample descriptions and field relations by location 19

2.4.1 Hanuman Chatti 19

2.4.2 Badrinath – Hanuman Chatti 26

2.4.3 Rishi Ganga 29

2.4.4 Mana – Alaknanda 45

2.4.5 Joshimath 58

2.5 Collation of textural observations 60

2.5.1 Textures in migmatites 60

2.5.2 Textures in leucogranites 60

2.5.3 Textures in orthogneisses 61

2.6 Discussion 62

2.6.1 Evidence for different melt reactions 62

2.6.2 Evidence for melt proportions in migmatites 64

2.6.3 Deuteric textures 65

2.7 Summary 66

3 Major phase geochemistry and indicators of melt processes 67

3.1 Introduction 67

3.2 Methods 68
3.2.1 EDS guide maps 69
3.2.2 Major element analysis 69
3.2.3 Trace element analysis 69
3.2.4 Thermometry 70
3.3 Results 71
3.3.1 K-feldspar 71
3.3.2 Plagioclase 72
3.3.3 Muscovite 77
3.3.4 Biotite 78
3.3.5 Garnet 82
3.4 Discussion 87
3.4.1. EDS vs LA-ICP-MS datasets 87
3.4.2 What do Ti-in-biotite temperatures record? 88
3.4.3 Geochemical fingerprints of melt reactions 90
3.4.4 Volumes and spatial relationships of melting 93
3.5 Summary 95
4 The timing, conditions, and sources of melt generation 97
4.1 Introduction 97
4.1.1 Zircon 97
4.1.2 Monazite 99
4.2 Methods 100
4.2.1 Zircon and monazite separation 101
4.2.2 Imaging 101
4.2.3 SIMS zircon oxygen isotope analysis 101
4.2.4 Zircon laser ablation U-(Th)-Pb analysis 102
4.2.5 Zircon laser ablation split-stream Lu-Hf isotopes and trace element analysis 103
4.2.6 Monazite laser ablation U-Th-Pb analysis 104
4.3 Results 106
4.3.1 Zircon zoning 106
4.3.2 Zircon chemistry 107
4.3.3 Monazite zoning 121
4.3.4 Monazite U-Th-Pb analysis 123
4.4 Discussion 129
4.4.1 Growth of zircon and monazite 129
4.4.2 The timing of anatexis and implications for Himalayan tectonics 131
4.4.3 Isotopic signatures transferred from source to melt 134
4.5 Summary 137

5 Synthesis 139
5.1 Petrographic and chemical distinctions of fluid-present and fluid-absent melting 141
5.2 Implications for tectonics 143
5.2.1 Constraining P-T-t pathways 143
5.2.2 Evolution of Garhwal crustal architecture 147
5.3 Future work 149
5.3.1 Identification of peritectic products and melt volumes 149
5.3.2 What temperatures do migmatites recorded? 149
5.3.3 Determining melt chemistry 149
5.3.4 Sensitivity of melt reactions and of melting conditions to source lithology 150
6 References 151
7 Appendices 165
7.1 Appendix A 165
7.1.1 EDS data collection and reduction methods 165
7.1.2 EDS standard evaluation and error 166
7.1.3 Major element concentration results 166
7.1.4 Garnet profile endmember compositions 166
7.2 Appendix B 167
7.2.1 LA-ICP-MS standard analyses 167
7.2.2 Trace element concentration results 167
7.3 Appendix C 168
7.3.1 Ti-in-biotite thermometry calculation and results 168
7.4 Appendix D 169
7.4.1 Zircon U-Th-Pb, O, and Hf isotope and trace element standard measurements 169
7.4.2 Zircon spot analysis locations 169
7.4.3 Compiled zircon isotope and trace element results 183
7.4.4 Zircon REE profiles 183
7.5 Appendix E 189
7.5.1 Monazite U-Th-Pb isotope standard measurements 189
7.5.2 Monazite spot analysis locations 189
7.5.3 Monazite U-Th-Pb results 202

List of Figures

Figure 1.1 – P-T diagram of the main melt-forming reactions in pelitic systems. The grey arrow represents the P-T path of the Greater Himalayan Sequence (GHS). After Searle et al. (2009) and Nabelek (2019). 1

Figure 1.2 – Major lithotectonic units and structural features of the Himalayan orogen. a) Geological map of the Himalayan orogenic belt, after Weinberg (2016), used with permission from John Wiley & Sons. b) Schematic cross-section through the Himalaya, after Jessup (2013), edited with permission, Copyright © 2013 by the Geological Society of America. 5

Figure 1.3 – Simplified geological map of the GHS in the eastern Garhwal, showing the Alaknanda and Dhauliganga valleys, after Spencer et al., 2012 and references therein, used with permission from John Wiley & Sons. Inset after Prince et al., 2001. 6

Figure 1.4 – Numerical modelling of GHS wedge-extrusion dynamics. Convergence velocities were 6-5.5 cm/yr at 27 Ma and 5 cm/yr at 22 and 17 Ma. From Figure 8 of Maiti and Mandal (2021). **CC BY 4.0**.................9

Figure 2.1 – Map of sampling localities along the Alaknanda and Rishi Ganga valleys, around Badrinath in the Garhwal Himalaya. Sample localities are marked in blue and labelled by number. Coordinates use the World Geodetic System (WGS84). Note that locality 11 is 15.5 km south-southeast of Hanuman Chatti, near Joshimath. 17

Figure 2.2 – Locality 08 (30.69918°N, 79.50424°E). Sampled metapelitic unit of variable thickness (30-50 cm), with fabric-parallel lenticular leucosomes. On either side of this unit are interbedded metaquartzite and metapsammite units typical of the Pandukeshwar-Badrinath transition. 20

Figure 2.3 – Thin section image of migmatite sample 08, displaying the schistose texture present in the sample and vein-like leucosomes of Qz + Pl + Ms + Kfs. 21

Figure 2.4 – Photomicrographs of feldspar textures in sample 08 (XPL). a) K-feldspar with complex sericitized boundary along contact with muscovite. b) Myrmekitic plagioclase adjacent to K-feldspar....................21

Figure 2.5 – Photomicrographs of garnet grains in sample 09a (PPL). a) Subhedral garnet in phyllosilicate domain with fractures perpendicular to fabric. b) Tabular relict garnet in quartzofeldspathic domain, in-line with fabric. 22

Figure 2.6 – Thin section image of migmatite sample 09b, displaying the schistose texture present in the sample and vein-like leucosomes of Qz + Pl + Ms. 23

Figure 2.7 – Photomicrographs of a garnet in sample 09b. Garnet is in the phyllosilicate domain, elongated with the fabric and rich in quartz inclusions. Imaged in a) PPL and b) XPL. 23

Figure 2.8 – Thin section image of orthogneiss sample 10, displaying feldspar augen and anastomosing biotite. Grey-coloured central regions of augen are antiperthitic K-feldspar intergrowths. 24

Figure 2.9 – Photomicrographs of feldspar textures in sample 10. a) Fine, tabular K-feldspar grain and myrmekitic plagioclase (XPL). b) Coarse plagioclase grain with antiperthitic K-feldspar intergrowths. 25

Figure 2.10 – Photomicrographs of kyanite, sillimanite, and garnet in sample 10. Sillimanite is present as fibrolite clots, while kyanite forms rare tabular grains. Imaged in a) PPL, and b) XPL. 25

Figure 2.11 – Locality 01 (30.71693°N, 79.49751°E). a) Sampled leucogranite body within migmatite complex. b) Detail of melanocratic schlieren in migmatite surrounding the leucogranite. 26

Figure 2.12 – Thin section image of leucogranite sample 01d, displaying fabric of aligned biotite schlieren and elongated garnet. 27

Figure 2.13 – Photomicrographs of various mineral textures in sample 01d. a) Coarse K-feldspar grain with perthitic albite exsolution lamellae. b) Partially chloritized biotite grain with sagenitic rutile growth. c) Muscovite-sericite schliere and clot. d) Highly elongated garnet grain with fractures perpendicular to its length. 28

Figure 2.14 – Locality 02 (30.74428°N, 79.47037°E). a) Leucosome pod with tourmaline schliere, within gneissose migmatite. b) Lenticular leucosome within gneissose migmatite. 29

Figure 2.15 – Thin section image of migmatite sample 02a, displaying elongate fibrolite clot (centre, top to bottom) and uncommon K-feldspar porphyroblasts >5mm (bottom left). 30

Figure 2.16 – Photomicrographs of feldspar and sillimanite textures in sample 02a. a) Medium-grain myrmekitic plagioclase and coarse-grains K-feldspar (XPL). b) Fibrolitic sillimanite with K-feldspar and quartz (PPL). 30

Figure 2.17 – Photomicrographs of feldspar textures in sample 02b. Medium-grained myrmekitic plagioclase adjacent to coarse perthitic K-feldspar. Plagioclase is strongly sericitized, while K-feldspar is preferentially sericitized along albite exsolution lamellae. Imaged in a) PPL, and b) XPL. 31

Figure 2.18 – Locality 03 (30.74440°N, 79.46177°E). Sampled lenticular leucogranite body, >3 m long, with sharp contact with host migmatite visible along its top edge. 32

Figure 2.19 – Photomicrographs of various mineral textures in sample 03. a) Biotite laths with sagenitic rutile (PPL). b) Chlorite with sagenitic rutile (PPL). c) Rare allanite grain, 0.8 mm long (PPL). d) Rare allanite grain (XPL). 33

Figure 2.20 – Thin section image of migmatite sample 04a, displaying biotite schlieren and divide between fine-medium-grained mesosome (left) and coarse-grained leucosome (right). 34

Figure 2.21 – Photomicrographs and BSE image of various mineral textures in sample 04a. a) Quartz films and sericite along muscovite boundaries with K-feldspar (XPL). b) Plagioclase with K-feldspar overgrowth/replacement in the mesosome (XPL). c) Acicular rutile inclusions in quartz (PPL). d) Acicular rutile inclusions in quartz (XPL). e) BSE image of perthitic K-feldspar porphyroblasts in the leucosome. .35

Figure 2.22 – Thin section image of migmatite sample 04b, displaying leucosome (left) and mesosome schollen (right). Biotite marks the primary fabric of the mesosome and leucosome schliere (where disaggregated). 36

Figure 2.23 – Photomicrographs and BSE image of various mineral textures in sample 04b. a) Perthitic K-feldspar porphyroblast and sillimanite-sericite clot (PPL). b) Perthitic K-feldspar porphyroblast and sillimanite-sericite clot (XPL). c) Cluster of K-feldspar grains with muscovite and quartz (PPL). d) Cluster of K-feldspar grains with muscovite and quartz (XPL). e) BSE image of K-feldspar clusters (light grey) in the mesosome. 37

Figure 2.24 – Thin section image of migmatite sample f02, displaying medium-grained mesosome (left) and coarse-grained leucosome with pleochroic tourmaline (right). 38

Figure 2.25 – Photomicrographs of feldspar and mica textures in sample f02. a) Plagioclase with K-feldspar overgrowth/replacement in the mesosome (XPL). b) Irregular biotite laths optically continuous with muscovite in phyllosilicate-rich domains (XPL). 39

Figure 2.26 – Photomicrographs of feldspar and mica textures in sample f03. Myrmekitic plagioclase in contact with K-feldspar grain and pockmarked muscovite with irregular grain boundaries. Imaged in a) PPL, and b) XPL. 40

Figure 2.27 – Photomicrographs and BSE image of various mineral textures in sample f04. a) Myrmekitic plagioclase between perthitic K-feldspar (PPL). b) Myrmekitic plagioclase between perthitic K-feldspar (XPL). c) Muscovite with sericite and irregular grain boundaries with K-feldspar (PPL). d) Muscovite with sericite and irregular grain boundaries with K-feldspar (XPL). e) BSE image of K-feldspar porphyroblasts (light grey) and irregular plagioclase inclusions. 41

Figure 2.28 – Thin section image of migmatite sample f13, displaying medium-grained mesosome with biotite (left) and coarse-grained leucosome with pleochroic tourmaline (right). 42

Figure 2.29 – Photomicrographs of feldspar and sericite textures in sample f13. a) Poikiloblastic K-feldspar, with inclusions of quartz, plagioclase, and muscovite with quartz films (PPL). b) Poikiloblastic K-feldspar, with inclusions of quartz, plagioclase, and muscovite with quartz films (XPL). c) Sericite clot between feldspar grains in the leucosome (PPL). d) Sericite clot between feldspar grains in the leucosome (XPL). 44

Figure 2.30 – Locality 05 (30.77444°N, 79.48951°E). Sampled strongly layered migmatite with alternative leucosomes and melanosomes. Surface mineralisation obscures most of the underlying migmatite. 45

Figure 2.31 – Photomicrographs of various mineral textures in sample 05b. a) K-feldspar grain with extensive sericite alteration and replacement by muscovite (PPL). b) K-feldspar grain with extensive sericite alteration and replacement by muscovite (XPL). c) Sillimanite clot with sericite alteration (PPL). d) Sillimanite clot with sericite alteration (XPL). 46

Figure 2.32 – Locality 06 (30.77517°N, 79.48624°E). Sampled boulder of garnet-tourmaline leucogranite, with sub-parallel tourmaline horizons and surface alteration halos around larger garnet grains. 47

Figure 2.33 – Thin section image of leucogranite sample 06, displaying zoned pleochroic tourmaline (left) and euhedral garnet grain (centre-top). 48

Figure 2.34 – Photomicrographs and BSE image of various mineral textures in sample 06. a) Coarse-grained euhedral K-feldspar with perthitic albite (PPL). b) Coarse-grained euhedral K-feldspar with perthitic albite (XPL). c) Coarse-grained tourmaline with core-rim zoning (PPL). d) Coarse-grained tourmaline with core-rim zoning (XPL). e) Euhedral garnet with distinct core (orange) and rim (PPL). f) Crystallographically oriented rutile needles at garnet core-rim boundary (PPL). 49

Figure 2.34 cont. – g) BSE image of a separated garnet grain in resin, from sample 06, with a core rich in randomly oriented micro-inclusions and irregular oblate quartz in the rim. 50

Figure 2.35 – Locality 07 (30.78055°N, 79.47762°E). Sampled outcrop with central leucocratic dyke (inset – yellow) and disseminated dykelets (inset – blue), cross-cutting the host migmatite. 51

Figure 2.36 – Thin section image of migmatite sample 07a, displaying undulating sillimanite and phyllosilicate-rich layers between leucosomes. 52

Figure 2.37 – Photomicrographs and BSE image of feldspar and sillimanite textures in sample 07a. a) Clusters of perthitic K-feldspar grains and irregular Pl + Qz + Ms (PPL). b) Clusters of perthitic K-feldspar grains and irregular Pl + Qz + Ms (XPL). c) Fibrolitic sillimanite and biotite selvedge along the edge of a K-feldspar cluster (PPL). d) Fibrolitic sillimanite and biotite selvedge along the edge of a K-feldspar cluster (XPL). e) BSE image of a lenticular K-feldspar cluster, >2 cm across, with sillimanite-biotite selvedge along its lower boundary. 53

Figure 2.38 – Photomicrographs and BSE image of various mineral textures in sample 07b. a) Coarse-grain perthitic K-feldspar with inclusions of Pl + Qz + Ms (PPL). b) Coarse-grain perthitic K-feldspar with inclusions of Pl + Qz + Ms (XPL). c) Replacement of K-feldspar with muscovite (PPL). d) Replacement of K-feldspar with muscovite (XPL). e) BSE image of sillimanite schliere with sericite alteration. 55

Figure 2.39 – Thin section images of migmatite sample 07c, displaying irregular leucosomes lined with sillimanite and biotite selvedges. 56

Figure 2.40 – Photomicrographs and BSE image of various mineral textures in sample 07c. a) Inclusion-poor perthitic K-feldspar in the leucosome (PPL). b) Inclusion-poor perthitic K-feldspar in the leucosome (XPL). c) Rare partially-resorbed garnet grain (PPL). d) Rare partially-resorbed garnet grain (XPL). e) Plagioclase phenocryst in a leucosome lined with a sillimanite and biotite selvedge. 57

Figure 2.41 – Photomicrographs of plagioclase and muscovite textures in sample 11a. a) Coarse-grained plagioclase in the leucosome, with inclusions of Qz + Ms + Bt (PPL). b) Coarse-grained plagioclase in the leucosome, with inclusions of Qz + Ms + Bt (XPL). c) Muscovite-sericite clot between plagioclase grains in the leucosome (PPL). d) Muscovite-sericite clot between plagioclase grains in the leucosome (XPL). 59

Figure 2.42 – BSE images of the textural evolution of peritectic K-feldspar during Ms-dehydration melting. a) Topotactic replacement of plagioclase with K-feldspar. b) Continued replacement of plagioclase, forming clusters of K-feldspar in the mesosome. c) K-feldspar grains in clusters anneal, forming poikiloblasts. d) Enhanced melt connectivity coarsens K-feldspar grains, forming porphyroblasts in the leucosome. 63

Figure 3.1 – Feldspar group ternary composition diagrams for individual EDS point analyses of K-feldspar grains in (a) leucogranites (including sample 10 orthogneiss), and (b) migmatites (including sample 09a meta-arkose). Endmember minerals are albite (Ab), anorthite (An), and orthoclase (Or). 71

Figure 3.2 – K-feldspar grain Rb/Sr values plotted against (a) Ba and (b) Eu (ppm). Rb/Sr values are negatively correlated with both Ba and Eu concentrations. Leucogranite 06 is a high-Rb/Sr, low-Ba and Eu outlier, while samples 07c and 10 are low-Rb/Sr, high-Ba and Eu outliers. 72

Figure 3.3 – Feldspar group ternary composition diagrams for individual EDS point analyses of plagioclase grains in (a) leucogranites (including sample 10 orthogneiss), and (b) migmatites (including sample 09a meta-arkose). Endmember minerals are albite (Ab), anorthite (An), and orthoclase (Or). 73

Figure 3.4 – Plagioclase grain Rb/Sr values against (a) Ba and (b) Eu (ppm). Rb/Sr values show little correlation with Ba and Eu concentrations. Leucogranite 06 has especially low Ba and Eu concentrations, while samples 07c, 09b and 10 have the highest concentrations of Ba and Eu. 74

Figure 3.5 – Chondrite-normalised major and trace element analyses of K-feldspar (top) and plagioclase (bottom). LILEs (Rb, Sr, Cs, Ba, and Eu), lithium, and yttrium show the most variation between samples for K-feldspar and plagioclase whilst remaining above the detection limit. 75

Figure 3.6 – Chondrite-normalised major and trace element analyses of muscovite (top) and biotite (bottom). LILEs (Rb, Sr, Ce, Ba, and Eu), Li, Cr, Y, Sn, and W show the most variation between samples for muscovite and biotite whilst remaining above the detection limit. 76

Figure 3.7 – mgli-feal potassium mica classification diagram of muscovite spot analyses. Values for mgli and feal are calculated in a.p.f.u. Samples sit towards the base of the muscovite zone. 77

Figure 3.8 – Muscovite grain Rb/Sr values against (a) Ba and (b) Sn (ppm). Rb/Sr values are negatively correlated with Ba concentration and positively correlated with Sn concentration. 78

Figure 3.9 – mgli-feal potassium mica classification diagram of biotite spot analyses. Values for mgli and feal are calculated in a.p.f.u. Samples sit between siderophyllite and annite zones. 79

Figure 3.10 – Biotite grain Rb/Sr values against (a) Ba and (b) Sn (ppm). Rb/Sr values are negatively correlated with Ba concentration and positively correlated with Sn concentration. 79

Figure 3.11 – Violin plots of calculated Ti-in-biotite temperatures for leucogranite samples using (a) EDS and (b) LA-ICP-MS datasets. Bold dashed lines mark the median temperature values, and dotted lines mark the upper and lower quartiles. The width of each plot corresponds to the probable frequency of data at a given value. 81

Figure 3.12 – Violin plots of calculated Ti-in-biotite temperatures for migmatite samples, and orthogneiss 10, using (a) EDS and (b) LA-ICP-MS datasets. Bold dashed lines mark the median temperature values, and dotted lines mark the upper and lower quartiles. The width of each plot corresponds to the probable frequency of data at a given value. 82

Figure 3.13 – Compositional profile of a garnet grain from leucogranite sample 01d in polished thin section. BSE image of the garnet shows longitudinal profile A-A’. 83

Figure 3.14 – Chondrite-normalised REE profiles for LA-ICP-MS spots analyses 1-4 on a garnet grain from leucogranite sample 01d. BSE image of the garnet show the location of the four spot analyses. 83

Figure 3.15 – Composite BSE image of a garnet porphyroblast from leucogranite sample 06, showing longitudinal profile A-A’. Compositional zoning along A-A’ (µm) is plotted against (a) garnet endmember proportions and (b) trace element concentrations (ppm). 85

Figure 3.16 – Chondrite-normalised REE profiles from leucogranite sample 06 garnet porphyroblast. Profiles from 28 spot analyses, approximately every 60 µm across ~1700 µm, from the outer edge of the core to the rim. 86

Figure 3.17 – a) Endmember profiles of a garnet grain from migmatite sample f02 in polished thin section. BSE image of the garnet shows longitudinal profile A-A’. b) Endmember profiles of a garnet grain from orthogneiss sample 10 in polished thin section. BSE image of the garnet shows longitudinal profile A-A’. 86

Figure 3.18 – Modelled TiO_2 activity and phase stability for pelitic bulk composition with 0.67 wt% TiO_2. Coloured dashed lines denote the phase boundaries for titanite (ttn), ilmenite (ilm), and rutile (rt). After Ashley and Law, 2015, used with permission from Springer Nature. 88

Figure 4.1 – Typical $\delta^{18}O$ values of geological reservoirs relevant to zircon growth and crystallisation. After Roberts and Spencer (2015) and King et al. (1998). **CC BY 3.0** 98

Figure 4.2 – CL images showing examples of zircon grain morphology and internal zonation for samples with oscillatory grey and black rims (type 1). a) Grain with irregular core from 01d, b) Fractured grain from 02a, c) Equant grain from 04b, d) Elongate fractured grain from f02. 106

Figure 4.3 – CL images showing examples of zircon grain morphology and internal zonation for samples with high-contrast dark and bright rims (type 2). a) Equant rounded grain from 07c, b) Grain from 09b with large bright core, c) Elongate grain with rounded core from sample 10, d) Grain with irregular rounded core from 11a. 107

Figure 4.4 – Leucogranite 01d U-Pb results with 2σ error. a) Tera-Wasserburg plot of Himalayan-aged zircon rims. b) Ordered common-Pb corrected $^{206}Pb/^{238}U$ ages. 108

Figure 4.5 – Migmatite 02a U-Pb results with 2σ error. a) Tera-Wasserburg plot of Himalayan-aged zircon rims. b) Ordered common-Pb corrected $^{206}Pb/^{238}U$ ages. 108

Figure 4.6 – Migmatite 02b U-Pb results with 2σ error. a) Tera-Wasserburg plot of Himalayan-aged zircon rims. b) Ordered common-Pb corrected $^{206}Pb/^{238}U$ ages. 109

Figure 4.7 – Leucogranite 03 U-Pb results with 2σ error. a) Tera-Wasserburg plot of Himalayan-aged zircon rims. b) Ordered common-Pb corrected $^{206}Pb/^{238}U$ ages. 109

Figure 4.8 – Migmatite 04a U-Pb results with 2σ error. a) Tera-Wasserburg plot of Himalayan-aged zircon rims. b) Ordered common-Pb corrected $^{206}Pb/^{238}U$ ages. 109

Figure 4.9 – Migmatite 04b U-Pb results with 2σ error. a) Tera-Wasserburg plot of Himalayan-aged zircon rims. b) Ordered common-Pb corrected $^{206}Pb/^{238}U$ ages. 110

Figure 4.10 – Leucogranite 06 U-Pb results with 2σ error. a) Tera-Wasserburg plot of Himalayan-aged zircon rims. b) Ordered common-Pb corrected $^{206}Pb/^{238}U$ ages. 110

Figure 4.11 – Migmatite 07a U-Pb results with 2σ error. a) Tera-Wasserburg plot of Himalayan-aged zircon rims. b) Ordered common-Pb corrected $^{206}Pb/^{238}U$ ages. 110

Figure 4.12 – Leucogranite 07b U-Pb results with 2σ error. a) Tera-Wasserburg plot of Himalayan-aged zircon rims. b) Ordered common-Pb corrected $^{206}Pb/^{238}U$ ages. 111

Figure 4.13 – Migmatite 07c U-Pb results with 2σ error. a) Tera-Wasserburg plot of Himalayan-aged zircon rims. b) Ordered common-Pb corrected $^{206}Pb/^{238}U$ ages. 111

Figure 4.14 – Migmatite 09b U-Pb results with 2σ error. a) Tera-Wasserburg plot of Himalayan-aged zircon rims. b) Ordered common-Pb corrected $^{206}Pb/^{238}U$ ages. 111

Figure 4.15 – Orthogneiss 10 U-Pb results with 2σ error. a) Tera-Wasserburg plot of Himalayan-aged zircon rims. b) Ordered common-Pb corrected $^{206}Pb/^{238}U$ ages. 112

Figure 4.16 – Migmatite 11a U-Pb results with 2σ error. a) Tera-Wasserburg plot of Himalayan-aged zircon rims. b) Ordered common-Pb corrected $^{206}Pb/^{238}U$ ages. 112

Figure 4.17 – Migmatite f02 U-Pb results with 2σ error. a) Tera-Wasserburg plot of Himalayan-aged zircon rims. b) Ordered common-Pb corrected $^{206}Pb/^{238}U$ ages. 112

Figure 4.18 – Orthogneiss f03 U-Pb results with 2σ error. a) Tera-Wasserburg plot of Himalayan-aged zircon rims. b) Ordered common-Pb corrected $^{206}Pb/^{238}U$ ages. 113

Figure 4.19 – Leucogranite f04 U-Pb results with 2σ error. a) Tera-Wasserburg plot of Himalayan-aged zircon rims. b) Ordered common-Pb corrected $^{206}Pb/^{238}U$ ages. 113

Figure 4.20 – Migmatite f13 U-Pb results with 2σ error. a) Tera-Wasserburg plot of Himalayan-aged zircon rims. b) Ordered common-Pb corrected $^{206}Pb/^{238}U$ ages. 113

Figure 4.21 – Histograms and kernel density estimate (KDE) plots for common-Pb corrected zircon rim $^{206}Pb/^{238}U$ ages for a) leucogranites, b) migmatites, and c) orthogneiss. Histogram bin widths are 0.5 Ma and KDE bandwidths are 0.2 Ma. 115

Figure 4.22 – Zircon rim $\delta^{18}O$ values compared to coinciding $^{206}Pb/^{238}U$ ages for a) leucogranites, b) migmatites, and c) orthogneiss. Error bars are 2σ for both $\delta^{18}O$ and age, however, for $^{206}Pb/^{238}U$ ages they are mostly smaller than the symbols. 116

Figure 4.23 – Violin plots of zircon rim $\delta^{18}O$ values for leucogranites. Bold dashed lines mark the median temperature values, and dotted lines mark the upper and lower quartiles. Dots show the values of individual rim measurements, while the width of each plot corresponds to the probable frequency of data at a given value. 117

Figure 4.24 – Violin plots of zircon rim $\delta^{18}O$ values for migmatites and orthogneiss. Bold dashed lines mark the median temperature values, and dotted lines mark the upper and lower quartiles. Dots show the values of individual rim measurements, while the width of each plot corresponds to the probable frequency of data at a given value. 117

Figure 4.25 – Zircon rim εHf values compared to coinciding $^{206}Pb/^{238}U$ ages for a) leucogranites, b) migmatites, and c) orthogneiss. Error bars are 2σ for both εHf and age, however, they are mostly smaller than the symbols. 118

Figure 4.26 – Zircon rim εHf values compared to coinciding $\delta^{18}O$ values for a) leucogranites, b) migmatites, and c) orthogneiss. Error bars are 2σ for both εHf and $\delta^{18}O$, however, for εHf they are mostly smaller than the symbols. 119

Figure 4.27 – Y concentration vs $^{206}Pb/^{238}U$ ages for zircon rims. Error bars are 2σ for both Y concentration and age, however, they are mostly smaller than the symbols. 119

Figure 4.28 – Eu/Eu* (Eu anomaly) vs $^{206}Pb/^{238}U$ ages for zircon rims. Eu/Eu* values <1 are considered 'negative' anomalies. 120

Figure 4.29 – Eu/Eu* (Eu anomaly) vs chondrite normalised Lu concentration ($Lu_{[n]}$) for zircon rims. Eu/Eu* values <1 are considered 'negative' anomalies. 120

Figure 4.30 – Ce, Th, and Y maps of monazite grains with simple or oscillatory zoning, with high-Ce, low-Th cores and mostly homogenous Y (type 1). Colour gradient depicts counts per second (cps). a) simple zoned monazite from leucogranite sample 01d. b) Oscillatory zoned monazite from migmatite 04a. c) Oscillatory zoned monazite from leucogranite 06. 121

Figure 4.31 – Ce, Th, and Y maps of monazite grains with irregular zoning, low-Th, and patchwork Y (type 2). Colour gradient depicts counts per second (cps). a) Irregular zoned monazite from migmatite 07c. b) Irregular zoned monazite from migmatite 09b. 122

Figure 4.32 – Leucogranite 01d monazite U-Th-Pb results with 2σ error. a) U-Th-Pb plot of Himalayan-aged spots. b) Ordered common-Pb corrected $^{208}Pb/^{232}Th$ ages. 124

Figure 4.33 – Migmatite 02a monazite U-Th-Pb results with 2σ error. a) U-Th-Pb plot of Himalayan-aged spots. b) Ordered common-Pb corrected $^{208}Pb/^{232}Th$ ages, with spots from grains 1 and 2 indicated. 124

Figure 4.34 – Migmatite 02b monazite U-Th-Pb results with 2σ error. a) U-Th-Pb plot of Himalayan-aged spots. b) Ordered common-Pb corrected $^{208}Pb/^{232}Th$ ages. 124

Figure 4.35 – Migmatite 04a monazite U-Th-Pb results with 2σ error. a) U-Th-Pb plot of Himalayan-aged spots. b) Ordered common-Pb corrected $^{208}Pb/^{232}Th$ ages. 125

Figure 4.36 – Migmatite 04b monazite U-Th-Pb results with 2σ error. a) U-Th-Pb plot of Himalayan-aged spots. b) Ordered common-Pb corrected $^{208}Pb/^{232}Th$ ages, with spots from grains 1-3 indicated. 125

Figure 4.37 – Migmatite 05b monazite U-Th-Pb results with 2σ error. a) U-Th-Pb plot of Himalayan-aged spots. b) Ordered common-Pb corrected $^{208}Pb/^{232}Th$ ages, with spots from grains 1-6 indicated. 125

Figure 4.38 – Leucogranite 06 monazite U-Th-Pb results with 2σ error. a) U-Th-Pb plot of Himalayan-aged spots. b) Ordered common-Pb corrected $^{208}Pb/^{232}Th$ ages. 126

Figure 4.39 – Migmatite 07c monazite U-Th-Pb results with 2σ error. a) U-Th-Pb plot of Himalayan-aged spots. b) Ordered common-Pb corrected $^{208}Pb/^{232}Th$ ages. 126

Figure 4.40 – Migmatite 09b monazite U-Th-Pb results with 2σ error. a) U-Th-Pb plot of Himalayan-aged spots. b) Ordered common-Pb corrected $^{208}Pb/^{232}Th$ ages, with spots from grains 1-10 indicated. 126

Figure 4.41 – Orthogneiss 10 monazite U-Th-Pb results with 2σ error. a) U-Th-Pb plot of Himalayan-aged spots. b) Ordered common-Pb corrected $^{208}Pb/^{232}Th$ ages, with spots from grains 1-3 indicated. 127

Figure 4.42 – Migmatite f02 monazite U-Th-Pb results with 2σ error. a) U-Th-Pb plot of Himalayan-aged spots. b) Ordered common-Pb corrected $^{208}Pb/^{232}Th$ ages. 127

Figure 4.43 – Leucogranite f04 monazite U-Th-Pb results with 2σ error. a) U-Th-Pb plot of Himalayan-aged spots. b) Ordered common-Pb corrected $^{208}Pb/^{232}Th$ ages. 127

Figure 4.44 – Migmatite f13 monazite U-Th-Pb results with 2σ error. a) U-Th-Pb plot of Himalayan-aged spots. b) Ordered common-Pb corrected $^{208}Pb/^{232}Th$ ages, with spots from grains 1 and 2 indicated. 128

Figure 4.45 – Stacked histogram of zircon rim $^{206}Pb/^{238}U$ ages coloured by sample melt reaction signatures (Bt = biotite-dehydration, Ms = muscovite-dehydration, Fluid = fluid-present). Bin widths are ~0.5 Ma, n = 177. 132

Figure 4.46 – Compiled zircon rim εHf values compared to coinciding $^{206}Pb/^{238}U$ ages. Error bars are 2σ for both εHf and age, however, they are mostly smaller than the symbols. KDEs of GHS and LHS zircon εHf values after Hopkinson et al. (2020) (**CC BY 3.0**), based on the compilation of Spencer et al. (2018). 135

Figure 4.47 – Compiled zircon rim εHf values compared to coinciding $\delta^{18}O$ values. Error bars are 2σ for both εHf and $\delta^{18}O$, however, for εHf they are mostly smaller than the symbols. GHS zone of εHf and $\delta^{18}O$ values (purple) based on leucogranites from Bhutan, after Hopkinson et al. (2017). 136

Figure 5.1 – T-XH_2O diagram at a fixed pressure of 0.95 GPa, calculated in Perple_X. Dotted blue lines mark the chosen "dry" (1.5 wt%) and "wet" (2.0 wt%) concentrations of H_2O. 144

Figure 5.2 – Phase equilibrium diagrams in the MnNCKFMASHT system of pelite compositions in Table 5.2, and charts of main phase stability curves for (a) 2.0 wt% H_2O and (b) 1.5 wt% H_2O, calculated in Perple_X. Also shown are P-T-t paths for the lower and middle-upper portions of the Badrinath Fm, with relative ages of fluid-present and fluid-absent melting. 146

Figure 5.3 – Schematic diagram of the tectonic evolution in the Garhwal GHS. 148

List of Tables

Table 2.1 – Samples collected from the Garhwal Himalaya, India. Sample IDs in **bold** are referred to throughout this text. The letter 'f' in sample ID indicates collection as a float sample. Coordinates are given in decimal degrees. 13

Table 2.2 – Mineralogical summary of key samples. Where present, chlorite is interpreted as a retrograde feature and is coloured in green to highlight this. The previous presence of sillimanite is inferred from muscovite-sericite clots in samples marked with '~' in pink. 16

Table 2.3 – Summary table of Kfs and Sil texture observed in migmatite samples, by latitude in descending order. Approximate modal % of Kfs and Sil are given, alongside textures present, melt% produced and inferred melt reaction. 66

Table 3.1 – Analytical techniques applied to samples discussed in this chapter. 68

Table 3.2 – Calculated Ti-in-biotite temperatures from EDS and LA-ICP-MS datasets for each sample. Rock types are abbreviated for leucogranite (L), migmatite (M), and orthogneiss (O). Column 'n' is the number of individual data points. 80

Table 4.1 – Analytical techniques applied to resin-mounted zircon and monazite grain separates. Entries of '~' indicate analyses with no ages younger than 45 Ma, interpreted as mixed or pre-Himalayan (Copley et al., 2010). 100

Table 5.1 – Summarised signatures of fluid-present and fluid-absent melting for various features and phases. 141

Table 5.2 – Concentrations (wt%) of relevant oxide phases in the average pelite (Forshaw & Pattison, 2021) and dry and wet pelite compositions, based on sample 08, used for modelling. 144

List of Abbreviations

Himalaya	
LHS	Lesser Himalayan Sequence
GHS	Greater Himalayan Sequence
THS	Tethyan Himalayan Sequence
MFT	Main Frontal Thrust
MBT	Main Boundary Thrust
MCT	Main Central Thrust
MCTZ	Main Central Thrust Zone
HHD	High Himalayan Discontinuity
STDS	South Tibetan Detachment System
ITSZ	Indus-Tsangpo Suture Zone
BSZ	Badrinath Shear Zone
MT	Munsiari Thrust
HHL	High Himalayan Leucogranite

Analytical & Chemical	
PPL	Plane Polarized Light
XPL	Cross Polarized Light
SEM	Scanning Electron Microscope
BSE	Backscatter Electron
EDS	Energy Dispersive X-ray Spectroscopy
LA-ICP-MS	Laser Ablation Inductively Coupled Plasma Mass Spectrometry
CL	Cathodoluminescence
SIMS	Secondary Ionization Mass Spectrometry
LASS	Laser Ablation Split Stream
KDE	Kernel Density Estimate
VSMOW	Vienna Standard Mean Ocean Water
CHUR	Chondritic Uniform Reservoir
LILE	Large Ion Lithophile Element
REE	Rare Earth Element
HREE	Heavy Rare Earth Element
LREE	Light Rare Earth Element

Mineral	
Ab	Albite
Act	Actinolite
Alm	Almandine
Aln	Allanite
Als	Aluminosilicate
An	Anorthite
And	Andalusite
Ap	Apatite
Bt	Biotite
Cal	Calcite
Chl	Chlorite
Dol	Dolomite
Fsp	Feldspar
Grs	Grossular
Grt	Garnet
Ilm	Ilmenite
Kfs	K-feldspar
Ky	Kyanite
Ms	Muscovite
Or	Orthoclase
Pl	Plagioclase
Prp	Pyrope
Qz	Quartz
Rt	Rutile
Sil	Sillimanite
Sps	Spessartine
Ttn	Titanite
Tur	Tourmaline

1 Introduction

Anatexis in orogenic systems has wide-reaching implications for the structure, mechanical strength, and later exhumation of the orogenic middle-crust (Rosenberg and Handy, 2005; Whittington and Treloar, 2002). Determining the specific melting reactions that occur and dominate within individual settings can provide a greater understanding of the system in question, as reactions can be tied to P-T-X_{H_2O} conditions, and the melt itself can be dated with accessory phase crystallisation ages. The melt reactions of metapelitic rock have been extensively studied (Patiño Douce and Harris, 1998; Gardien et al., 1995; Harris et al., 1993, 1995; Inger and Harris, 1992, 1993; Breton and Thompson, 1988), with three major melt-producing reactions identified; fluid-present incongruent melting, fluid-absent muscovite-dehydration melting, and fluid-absent biotite-dehydration melting (Figure 1.1). Each of these reactions have implications for the release, transport and final destination of particular elements, depending on the compositions of the reacting phases and whether peritectic phases are formed (Bea, 1996).

The textural and chemical signatures of melt-forming reactions are commonly preserved in migmatites and smaller bodies of leucogranite (Dyck et al., 2020; Gao et al., 2017; Patiño Douce and Harris, 1998). However, the identification of these signatures involves detailed petrographic observations and bulk-rock geochemical measurement. As such, a targeted approach of identifying the key textural and elemental fingerprints of various melt reactions in common rock-forming and

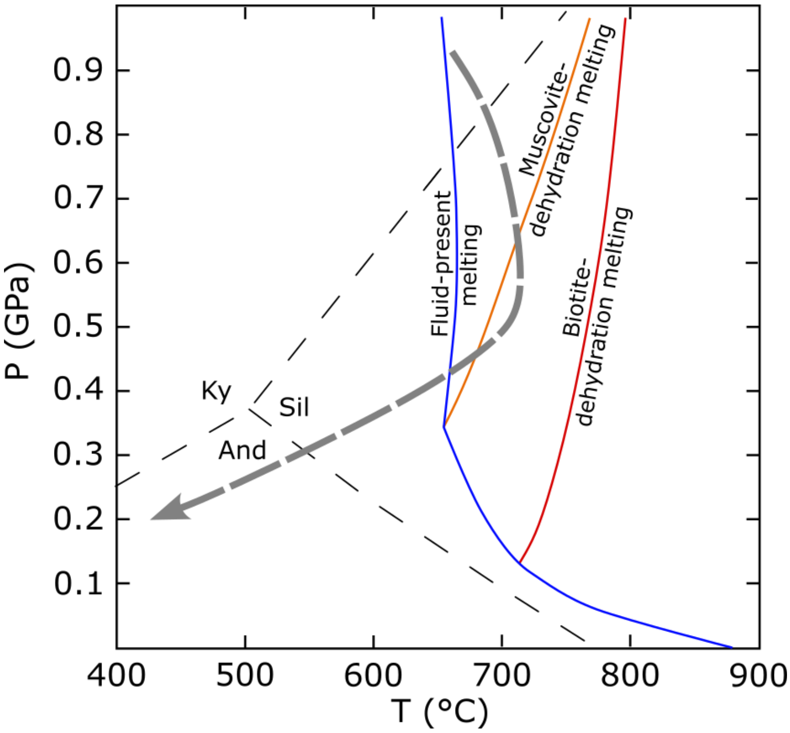

Figure 1.1 – P-T diagram of the main melt-forming reactions in pelitic systems. The grey arrow represents the P-T path of the Greater Himalayan Sequence (GHS). After Searle et al. (2009) and Nabelek (2019).

accessory phases may provide a useful tool for future work. Additionally, the timing of various melt reactions, especially relative to one another, may be used to further understand the evolution of the host orogenic system as a whole.

The Himalaya are the ideal natural laboratory for investigating continental collisional processes, as the relative age of the orogen, compared to the much older orogens like the Caledonian (~430 Ma) and Grenville (~1.1 Ga) (Weller et al., 2021; Gee et al., 2008; Rivers, 2012), removes the complication of overprinting geological events, or the loss of sub-million year detail in U-Th-Pb dating. The Himalayan orogenic belt is an active continent-continent collisional plate boundary, stretching ~2400 km from the Karakoram in the Kashmir region to Arunachal Pradesh in eastern India. This tectonic feature formed through the northward movement of the Indian subcontinent, closing the Neo-Tethys ocean, and colliding with the Eurasian continent at approximately 50 Ma (Copley et al., 2010; Hodges, 2000).

The Indian lithosphere has been thrust beneath the Eurasian plate, resulting in the uplift of the Tibetan Plateau, thickening of the continental crust to >70 km in some regions, and the formation of the Himalaya fold and thrust belt to accommodate crustal shortening (Nábělek et al., 2009; Hirschmiller et al., 2014). Buried sedimentary units along India’s northern margin were subject to metamorphism and subsequent partial melting (Dyck et al., 2019). By studying these rocks and their crystallised melt products, we can improve our understanding of the crust during continental collision and the role it plays in the development of orogenic belts.

1.1 Thesis objectives

This study uses migmatite and leucogranite samples from the Garhwal GHS to identify the melt forming reactions, the signatures they impart, and to interpret the timing of this melting in relation to Himalayan tectonic evolution and mid-crust exhumation. The key questions addressed in this thesis are:

1. What petrographic evidence of anatexis is present in these rocks and which melt forming reactions do they indicate?

The peritectic product phases of melt reactions vary (Patiño Douce and Harris, 1998; Inger and Harris, 1992, 1993), and as such, reactions can be inferred from mineral assemblages and textures of peritectic grains. The microstructural evolution of peritectic K-feldspar during muscovite-dehydration melting in pelites is established in Dyck et al. (2020); this will form the underlying criteria for melt texture comparison and interpretation.

2. What geochemical signatures do these melt reactions impart on rock-forming and accessory mineral phases?

Several studies have looked at whole-rock trace element concentrations in granites generated under fluid-present and fluid-absent conditions (Gao et al., 2017; Patiño Douce and Harris, 1998; Harris et al., 1993, 1995; Inger and Harris, 1993). However, targeting individual mineral phases within granites and migmatites may provide further insight into melt reactions and chemical inheritance from the protolith. Additionally, signatures recorded in phases that crystallise at known points within a P-T-t path, i.e. zircon, may provide time-resolved chemical conditions.

3. When did anatexis occur in relation to prograde metamorphism and exhumation, and what are the implications of this?

Previous studies in the Garhwal region have largely focused on either the leucogranite bodies in the uppermost Badrinath Formation (Iaccarino et al., 2017; Sachan et al., 2010; Stern et al., 1989), or the activation of structures like the BSZ (Benetti et al., 2021). As such, questions still remain around the timing of pro-grade melting (Prince et al., 2001) and the onset of muscovite-dehydration melting. Migmatites and in-source leucogranitic bodies of the central Badrinath Formation are more likely to record these processes than the migrated leucogranite higher up stratigraphy.

1.2 Major geological units of the Himalaya

The Himalaya is divided into three major lithotectonic units that are continuous along strike for the length of the orogenic belt; these are, from south to north, the Lesser Himalayan Sequence (LHS), Greater Himalayan Sequence (GHS), and Tethyan Himalayan Sequence (THS) (Kohn, 2014) (Figure 1.2a). Each of these units is bound by various thrust and normal faults, summarised in Figure 1.2b. The LHS is thrust on top of the unmetamorphosed Siwalik group of foreland sediments, along the Main Boundary Thrust (MBT), marking the first appearance of Himalayan metamorphism. The Siwalik group itself is separated from the Indo-Gangetic Plain by the Main Frontal Thrust (MFT). The GHS is emplaced above the LHS along the Main Central Thrust (MCT) or Main Central Thrust Zone (MCTZ). There is an internal boundary within the GHS, called the High Himalayan Discontinuity (HHD), which is thought to have formed as a mid-crustal rheological boundary (Waters, 2019; Montomoli et al., 2015). The THS is separated from the GHS by a sequence of extensional shear structures called the South Tibetan Detachment System (STDS). The THS is bound in the north by the Indus-Tsangpo Suture Zone (ITSZ), marking the surface expression of the Indian-Eurasian plate boundary.

The rocks of the LHS increase in metamorphic grade from greenschist facies along the MBT to middle-amphibolite facies towards the MCT. The GHS increases from middle-amphibolite facies at the MCT to lower-granulite facies around the HHD, with widespread partial melting, before typically decreasing in grade before the STDS. As such, the LHS-GHS sequence of metamorphic facies can be seen as ‘inverted’, with increasingly high-grade rocks emplaced above those of lower grades (Kohn, 2014). The THS ranges from lower amphibolite-facies along the STDS to largely unmetamorphosed sediments at its upper stratigraphic levels (Sen et al., 2022; Kohn, 2014).

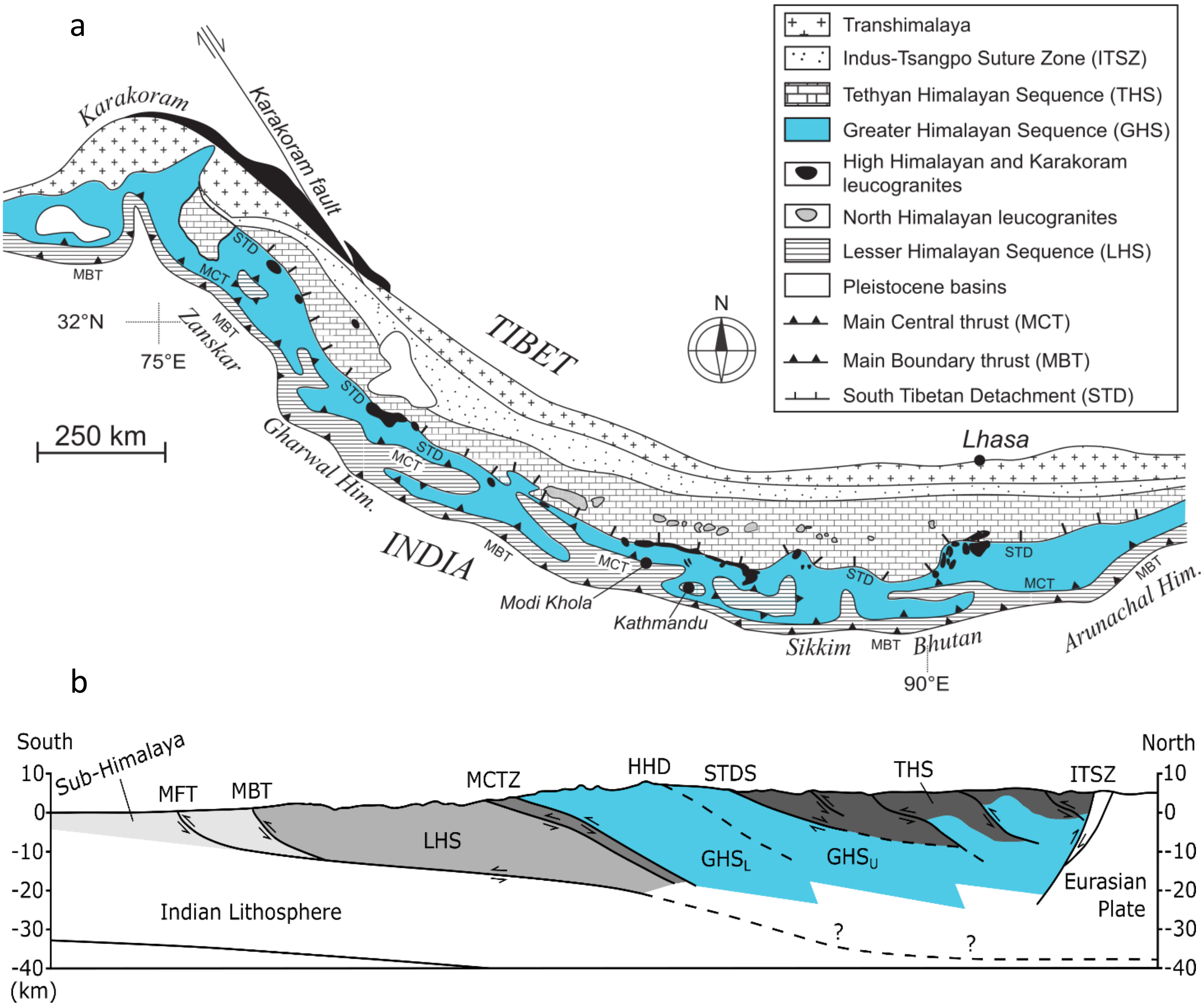

Figure 1.2 – Major lithotectonic units and structural features of the Himalayan orogen. a) Geological map of the Himalayan orogenic belt, after Weinberg (2016), used with permission from John Wiley & Sons. b) Schematic cross-section through the Himalaya, after Jessup (2013), used and edited with permission.

1.3 The GHS of the Garhwal Himalaya

In the Garhwal Himalaya (Uttarakhand, India), the GHS is divided in three units: the Joshimath Formation, the Pandukeshwar Formation, and the Badrinath Formation, as shown in Figure 1.3. The Joshimath Formation consists of pelitic gneisses and schists with the assemblages of quartz + biotite + plagioclase + garnet ± staurolite ± muscovite ± kyanite ± chlorite ± calcite ± graphite ± titanite ± rutile/ilmenite (Spencer et al., 2012a). Migmatites are present in the upper portions of the Joshimath Formation in eastern Uttarakhand (Paul, 1998). The Pandukeshwar Formation, also known as the Suraithota Formation (Jain et al., 2014), consists of medium- to fine-grained meta-arkose, quartzite, and meta-psammite interlayered with schists and amphibolite (Iaccarino et al., 2020; Spencer et al., 2012a). The Badrinath Formation, also known as the Bhapkund Formation (Jain et al., 2014), consists of migmatitic metapelites, leucogranite bodies and relatively minor calc-silicates. Metapelite assemblages are similar to the Joshimath Formation with the addition of sillimanite, while leucosomes and leucogranites consist of quartz + K-feldspar + plagioclase + muscovite ± garnet ± tourmaline (Spencer et al., 2012a; Paul, 1998).

The MCT is present as a ductile shear zone with pervasive mylonitization separating chlorite-biotite schists of the Munsiari Formation (LHS) and overriding kyanite gneisses of the GHS (Valdiya, 1979). The MCT is also referred to as the Vaikrita Thrust in this region, with the base of the shear zone marked by the Munsiari Thrust (MT). The HHD runs between the Pandukeshwar and Badrinath Formations as a thrust-sense shear zone, and is referred to as the Badrinath Shear Zone (BSZ) (Benetti et al., 2021).

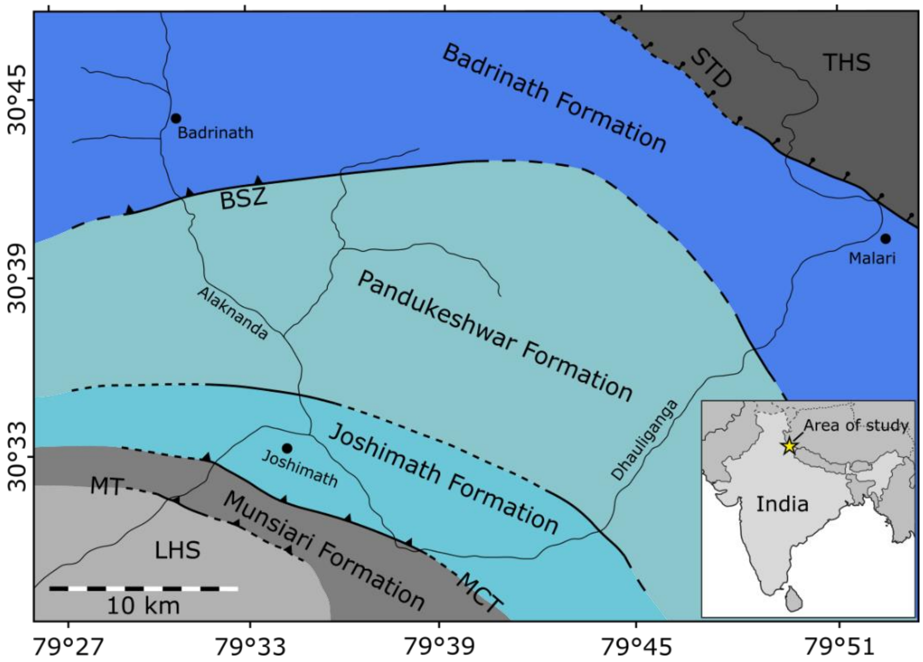

Figure 1.3 – Simplified geological map of the GHS in the eastern Garhwal, showing the Alaknanda and Dhauliganga valleys, after Spencer et al., 2012 and references therein, used with permission from John Wiley & Sons. Inset after Prince et al., 2001.

1.4 Partial melting in the GHS

Evidence of partial melting, such as migmatites and leucogranites, is most abundant in the upper GHS, with the emplacement of the High Himalayan Leucogranites (HHL) beneath the STDS as a network of interconnecting dykes and sills which commonly feed into larger bodies (Searle, 1999). Both fluid-present melting and fluid-absent muscovite-dehydration melting are likely to have contributed to the generation of these granites as the upper GHS experienced supra-solidus conditions, especially during active decompression (Figure 1.1).

Melting events in the Garhwal region are primarily attributed to fluid-present melting (Stern et al., 1989; Scaillet et al., 1990; Prince et al., 2001; Sachan et al., 2010; Kawabata et al., 2021), despite temperatures >750°C modelled during decompression for the upper GHS of the Garhwal (Spencer et al., 2012a; Iaccarino et al., 2017; Benetti et al., 2021), which would suggest temperatures were high enough for fluid-absent muscovite-dehydration melting. Specific melt reactions and their products are discussed further in Chapter 2.

Extensive decompression melting in the Garhwal GHS occurred between 22-18 Ma, as constrained by Rb-Sr and K-Ar dating of the Bhagirathi leucogranite (Stern et al., 1989) and zircon U-Pb dating of the Malari leucogranite (Sachan et al., 2010). However, leucogranites such as these represent the final emplacement of melt, whereas migmatites, where melt is formed in situ without migrating through the crust, yield melt ages older than 24 Ma (Singh, 2019; Prince et al., 2001).

1.5 Tectonic models and exhumation

Thermomechanical modelling of the Himalaya has been used to further understand the formation of Himalayan orogenic belt, the dynamics of partial melt rheology, and the exhumation of mid-crustal rocks. The outputs of these models have been tested against geological observations across the Himalaya and refined.

1.5.1 Critical taper and channel flow models

The critical taper or wedge model of fold-and-thrust belt formation (Kohn, 2008; Dahlen, 1990) is based on a competent underthrusting plate, with weak overriding material colliding with a strong hanging wall. In this setting, deformation is accommodated by foreland-propagated thrust sheets displacing the weak mid-upper crustal material. As seen with the MFT, MBT, and MCT, and the units they separate, this results in high-grade mid-crustal material thrust above low-grade material from higher structural levels (Figure 1.2b).

The channel flow model uses ductile extrusion to specifically account for the placement of the GHS (Beaumont et al., 2001; Grujic et al., 1996). In this setting, the occurrence of partial melting in the mid-crust results in a region of relatively low viscosity and low mechanical strength (Rosenberg and Handy, 2005; Vigneresse et al., 1996), which is forced upwards and southwards by the overarching collisional pressure gradient. This region of low viscosity that facilitates extrusion of the GHS is thought to have formed what is now the HHD (Montomoli et al., 2015).

These two models form non-mutually exclusive end-members for fold-and-thrust belt formation, with their influence over the system changing over time as the architecture of the orogen evolves (Cottle et al., 2015). It has been suggested that part of this evolution is the downwards shift in deformation centres, from early deformation concentrated in the upper GHS (41-28 Ma), to the HHD (27-16 Ma), to the MCT (<16 Ma) (Carosi et al., 2015, 2018; Iaccarino et al., 2015; Montomoli et al., 2015).

1.5.2 The timing and rate of GHS exhumation

The exhumation of the GHS is driven by the coupled tectonic forces of the northward moving Himalayan wedge and the downward collapse of the Tibetan Plateau (Maiti and Mandal, 2021). The gravitational collapse is a result of reducing convergence velocities of the Indian and Eurasian plates between 50-40 Ma, which is itself a consequence of crustal thickening (Copley et al., 2010). Surface erosion is thought to play only a minor role in the exhumation rates, as channel flow rates of supra-solidus mid-crustal rocks are not sensitive to enhanced surface erosion (Piccolo et al., 2018).

The thermomechanical model of GHS extrusion rates by Maiti and Mandal (2021) suggest that a wedge-extrusion system is established to depths of ~60 km at approximately 27 Ma, bounded by the STDS and HHD. Extrusion reaches peak velocities of 3.4 cm/yr at 22 Ma, while tectonic convergence rates drop to just 5 cm/yr (Copley et al., 2010). This extrusion translates to a rapid vertical exhumation component of 18 mm/yr. These rates are fairly short lived, however, with exhumation rates slowing significantly to ~5 mm/yr by 17 Ma, as the lower boundary of the wedge-extrusion system migrates southwards to the MCT. The changing relative velocities of this system from 27-17 Ma are summarised in Figure 1.4.

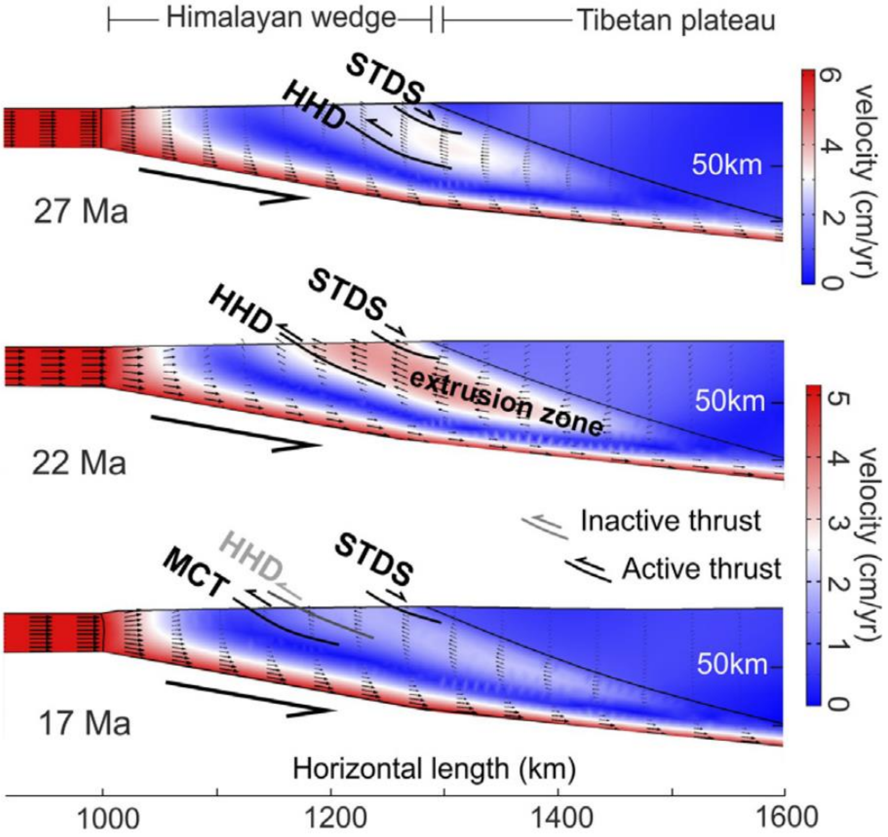

Figure 1.4 – Numerical modelling of GHS wedge-extrusion dynamics. Convergence velocities were 6-5.5 cm/yr at 27 Ma and 5 cm/yr at 22 and 17 Ma. From Figure 8 of Maiti and Mandal (2021). CC BY 4.0

The model predicts pro-grade (burial) conditions prior to ~27 Ma for the upper GHS, and slightly younger for the lower GHS the other side of the HHD, and peak exhumation at 22 Ma, which coincides with the oldest dates from leucogranites in the Garhwal (Sachan et al., 2010; Stern et al., 1989). Such predictions provide a context for better understanding the periods of melt formation in the Garhwal Himalaya.

1.6 Thesis structure

The questions expanded on in the introduction are explored in this thesis as follows:

Chapter 2 presents field observations and petrographic descriptions of key samples, identifying melt reaction types that are built upon in later chapters.

Chapter 3 links petrographic observations to major and trace element concentrations in feldspars, micas, and garnet, as well as Ti-in-biotite thermometry.

Chapter 4 presents the U-Th-Pb crystallisation ages of zircon and monazite from migmatites and leucogranites, alongside zircon Hf-O isotopes and trace element concentrations.

Chapter 5 is a synthesis of previous interpretations, summarising key findings of melt reaction signatures and exploring P-T-t pathways of the Garhwal GHS.

2 Fieldwork and sample descriptions: implications for determining melt reaction and percentage

2.1 Introduction

Petrographic observations can be used to determine the melt reactions which may have occurred in a particular sample. The presence and features of peritectic products of melt reactions are of particular interest as, by definition, they form during anatexis, whereas the melt itself may be extracted through percolation (Vigneresse et al., 1996; Rosenberg and Handy, 2005; Brown, 2007). Metapelitic rocks have well-understood melt reactions, which may occur by (1) fluid-saturated incongruent melting, (2) fluid-absent melting of muscovite, and (3) fluid-absent melting of biotite, each with distinct peritectic phases (Inger and Harris, 1992, 1993). Fluid-present melting produces only sillimanite or kyanite as a peritectic phase (reaction 1) (Patiño Douce and Harris, 1998), while fluid-absent Ms-dehydration melting produces both K-feldspar and sillimanite-kyanite peritectic phases (reaction 2) (Gardien et al., 1995; Patiño Douce and Harris, 1998; Pickering and Johnston, 1998), and fluid-absent Bt-dehydration melting produces peritectic K-feldspar, garnet, and ilmenite/rutile (reaction 3) (Breton and Thompson, 1988; Harris et al., 1995).

Fluid-present melting $\mathrm{Ms + Qz + Pl + H_2O = Als + Melt}$ (1)

Ms-dehydration melting $\mathrm{Ms + Qz + Pl = Kfs + Als + Melt}$ (2)

Bt-dehydration melting $\mathrm{Bt + Als + Qz + Pl = Kfs + Grt + Ilm/Rt + Melt}$ (3)

As such, the presence of peritectic K-feldspar in a migmatite or leucogranite is indicative of Ms-dehydration melting, while peritectic garnet and K-feldspar together are indicative of Bt-dehydration melting. Peritectic grains may be distinguished from melt-crystallised grains of the same phase by examining their textures. K-feldspar textures attributed to peritectic growth include the overgrowth and replacement of plagioclase, poikiloblastic grains, and porphyroblastic grains (Dyck et al., 2020). Garnet may be identified as peritectic by the presence of very fine, randomly oriented inclusions in the cores of grains, primarily of apatite (Dorais and Campbell, 2022; Dorais and Spencer, 2014; Taylor and Stevens, 2010).

The melt volume produced may be estimated by the relative proportions of product phases. For Ms-dehydration melting, the theoretical ratio of K-feldspar to sillimanite to melt is close to 8:5:10 (Dyck et al., 2020), and as such, a migmatite with a K-feldspar modal abundance of ~20% can be ascribed a total produced melt volume of ~25% before extraction. Issues may arise, however, from textural overprinting in systems with sequential melt-producing reactions, as peritectic sillimanite or kyanite formed through fluid-present melting may be indistinguishable from, or even overgrown by, later sillimanite/kyanite as a product of Ms-dehydration melting. As such, potential differences in geochemical signatures due to varying reactant phases and proportions, tied to textural observations, provide the best opportunity to interpret melt-reaction history.

In this chapter, I document the field and petrographic observations that underpin all future analyses and interpretations. Samples are then collated into groups based on shared mineralogy and textures that best document different melt reactions and melt volume percentages.

2.2 Fieldwork and sampling

Samples were collected in the Garhwal Himalaya, Uttarakhand, India, over 7 days in October 2018. I was accompanied by my supervisor, Dr Christopher Spencer, and assisted by Dr Aditya Akhara from the Wadia Institute of Himalayan Geology, Dehradun. Fieldwork was confined to the valleys of the Alaknanda River and a tributary called the Rishi Ganga. Sampling involved hiking from the town of Badrinath to camp in the Rishi Ganga at 3500 m altitude and travelling by taxi from Badrinath to Mana to hike further up the Alaknanda valley. Working at altitudes between 3000 and 4200 m presented challenges due to the limited time available for acclimatising. Outcrops were limited to the steep-faced valley walls and road cuttings, with float samples collected from rocky point bars in the Alaknanda and Rishi Ganga.

This fieldwork aimed to sample pelitic/semi-pelitic migmatites that had undergone various degrees of melting, from *in-situ* leucosomes to extensive interconnected former melt bodies, as well as leucogranites, that have presumably migrated from their source rock to higher structural levels. Localities displaying cross-cutting relationships of various melt bodies were also of particular interest. Sampling outcrops that fit these criteria would provide the best chance of generating a dataset of zircon isotope geochemistry and geochronology, along with petrographic observations, to interpret the history of melt generation in the region. All samples are listed in Table 2.1, with locality information and brief descriptions. Table 2.2 details the mineralogy of key samples referred to throughout this work. Sample locations are shown in Figure 2.1.

Sampling was permitted by the Wadia Institute of Himalayan Geology, an autonomous institution of the Department of Science & Technology, Government of India.

Table 2.1 – Samples collected from the Garhwal Himalaya, India. Sample IDs in ***bold*** *are referred to throughout this text. The letter 'f' in sample ID indicates collection as a float sample. Coordinates are given in decimal degrees.*

Sample ID	**Location**	**Locality No.**	**Latitude**	**Longitude**	**Rock type**	**Comments**
BAD01d	Badrinath - Hanuman Chatti	01	30.71693	79.49751	Leucogranite	Medium-grained in-source Grt-leucogranite. Grt & Bt form thin layering in line with host migmatite schlieren and schollen/rafts.
BAD02a	Rishi Ganga	02	30.74428	79.47037	Migmatite	Gneissose Tur-metatexite with disseminated 0.5 cm scale leucosomes. Leucosomes up to 20 x 10 cm.
BAD02b	Rishi Ganga	02	30.74428	79.47037	Migmatite leucosome	Leucosome pod within metatexite. Bt-rich schlieren sub-parallel with host, more prevalent towards the leucosome boundaries.
BAD03	Rishi Ganga	03	30.74440	79.46177	Leucogranite	Medium-grained Bt-leucogranite. The boundary between the leucogranite and host-migmatite is sharp.
BAD04a	Rishi Ganga	04	30.74426	79.45016	Migmatite	Schlieren diatexite with rafts. Sil-Bt selvedges are common along schollen/raft-leucosome transitions.
BAD04b	Rishi Ganga	04	30.74426	79.45016	Migmatite	Schollen diatexite with schlieren. Sil-Bt selvedges are common along schollen/raft-leucosome transitions.
BAD05a	Mana - Alaknanda	05	30.77444	79.48951	Migmatite	Fine-grained melanocratic migmatite. Thin (~1 cm) leucosome layers. Considered to be melt-extracted residuum.
BAD05b	Mana - Alaknanda	05	30.77444	79.48951	Migmatite	Medium-grained melanocratic migmatite. Thin (1-2 cm) leucosome layers. Considered to be melt-extracted residuum.
BAD06	Mana - Alaknanda	06	30.77517	79.48624	Leucogranite	Medium-grained Grt-Tur-leucogranite. Tur forms sub-parallel horizons in association with Qz.
BAD07a	Mana - Alaknanda	07	30.78055	79.47762	Migmatite	Schlieren diatexite. Sil-Bt selvedges line leucosome boundaries. Associated with 1-5 cm wide vein-structured leucocratic dykelets.
BAD07b	Mana - Alaknanda	07	30.78055	79.47762	Leucogranite	Medium-grained Tur-leucogranitic dyke, 2.5-3.0 m wide. Associated dykelet network cross-cutting host migmatite, up to 50 cm wide.
BAD07c	Mana - Alaknanda	07	30.78055	79.47762	Migmatite	Deformed melanocratic diatexite. Irregular leucosomes and Sil-Bt-rich selvedges.
BAD08	Hanuman Chatti	08	30.69918	79.50424	Migmatite/ Schist	Fine-grained schistose migmatite with folded vein-like leucosomes 1-4 mm wide in hand specimen (up to 5 cm wide at exposure).

BAD09a	Hanuman Chatti	09	30.70085	79.50388	Meta-arkose	Medium-grained bands of quartz-rich horizons with thin phyllosilicate layers and garnet.
BAD09b	Hanuman Chatti	09	30.70085	79.50388	Migmatite/ Schist	Medium-grained schistose migmatite with vein-like leucosomes 1-8 mm wide.
BAD10	Hanuman Chatti	10	30.69894	79.50621	Orthogneiss	Melanocratic Bt-Grt-orthogneiss with regular Qz-Fsp-augen up to 8 mm across. Sil + Ky are both present in thin section.
BAD11a	Joshimath	11	30.56328	79.56776	Migmatite	Deformed Bt-Grt-Tur metatexite. Folded, irregular leucosomes 3-8 mm wide.
BAD11b	Joshimath	11	30.56328	79.56776	Migmatite	Bt-Grt-Tur stromatic metatexite. Sub-parallel leucosome bands 1-5 mm wide with augen up to 10 mm wide.
BADf01	Rishi Ganga	A	30.74142	79.47026	Migmatite	Melanocratic migmatite, folded vein-like leucosomes with Tur phenocrysts. Considered to be melt-extracted residuum.
BADf02	Rishi Ganga	A	30.74142	79.47026	Migmatite	Schlieren diatexite with coarse-grained Tur-rich leucosome. Sil-Ms clots along the boundary between leucogranite and migmatite.
BADf03	Rishi Ganga	A	30.74142	79.47026	Orthogneiss	Mesocratic orthogneiss with discordant Qz-Fsp-augen and Bt banding.
BADf04	Rishi Ganga	A	30.74142	79.47026	Leucogranite	Tur-Bt-leucogranite, coarse-grained Qz + Fsp, with medium-grained micaceous areas.
BADf05	Rishi Ganga	A	30.74142	79.47026	Migmatite	Melanocratic migmatite, vein-like leucosomes with Tur phenocrysts. Considered to be melt-extracted residuum.
BADf06	Rishi Ganga	A	30.74142	79.47026	Orthogneiss	Mesocratic orthogneiss with discordant Qz-Fsp-augen and Bt banding.
BADf07	Rishi Ganga	A	30.74142	79.47026	Calc-silicate	Medium-grained Dol-Cal-Ab-Calc-silicate with Act porphyroblasts.
BADf08	Rishi Ganga	A	30.74142	79.47026	Leucogranite	Coarse-grained leucogranite with minor Bt, Tur and Grt.
BADf09	Rishi Ganga	A	30.74142	79.47026	Migmatite	Melanocratic migmatite, vein-like leucosomes with Tur phenocrysts and Grt. Considered to be melt-extracted residuum.
BADf10	Rishi Ganga	B	30.74233	79.45197	Leucogranite/ Migmatite	Melt extracted melanocratic migmatite paired with coarse-grained Bt-leucogranitic leucosome.

BADf11	Rishi Ganga	B	30.74233	79.45197	Leucogranite/ Migmatite	Melt-extracted melanocratic migmatite paired with medium-grained Tur-leucogranitic leucosome.
BADf12	Rishi Ganga	B	30.74233	79.45197	Migmatite	Schollen diatexite with schlieren. Sil-Bt selvedges are common along schollen/raft-leucosome transitions.
BADf13	Rishi Ganga	B	30.74233	79.45197	Leucogranite/ Migmatite	Schollen diatexite paired with very coarse Tur-leucogranite. Boundary lined with Tur & Qz.
BADf14	Rishi Ganga	C	30.74264	79.47013	Migmatite	Melanocratic Tur-migmatite with Sil clots 5-20 mm across visible on cleaved planes. Considered to be melt-extracted residuum.
BADf15	Rishi Ganga	C	30.74264	79.47013	Migmatite	Melanocratic Tur-migmatite with Sil clots 4-15 mm across visible on cleaved planes. Considered to be melt-extracted residuum.
BADf16	Mana - Alaknanda	D	30.77515	79.48786	Leucogranite	Medium-grained Tur-leucogranite with minor garnet.
BADf17	Mana - Alaknanda	E	30.77624	79.48262	Migmatite	Melanocratic migmatite, folded vein-like leucosomes with Tur phenocrysts. Considered to be melt-extracted residuum.
BADf18	Rishi Ganga	B	30.74233	79.45197	Leucogranite/ Orthogneiss	Banded Bt-Sil-orthogneiss paired with coarse-grained Tur-leucogranitic leucosome. There is a sharp contact between the two.

Table 2.2 – Mineralogical summary of key samples. Where present, chlorite is interpreted as a retrograde feature and is coloured in green to highlight this. The previous presence of sillimanite is inferred from muscovite-sericite clots in samples marked with '~' in pink.

Sample	**Rock type**	**Quartz**	**Plagioclase**	**K-feldspar**	**Biotite**	**Muscovite**	**Chlorite**	**Garnet**	**Sillimanite**	**Tourmaline**	**Ilmenite**	**Rutile**	**Zircon**	**Apatite**	**Monazite**
BAD01d	Leucogranite	x	x	x	x	x	x	x	~			x	x	x	x
BAD02a	Migmatite	x	x	x	x	x	x	x	x	x		x	x	x	x
BAD02b	Migmatite/ Leucosome	x	x	x	x	x	x	x				x	x	x	x
BAD03	Leucogranite	x	x	x	x		x					x	x	x	
BAD04a	Migmatite	x	x	x	x	x	x		x	x		x	x	x	x
BAD04b	Migmatite	x	x	x	x	x	x		x	x		x	x	x	x
BAD05b	Migmatite	x	x	x	x	x	x		x	x	x		x	x	x
BAD06	Leucogranite	x	x	x		x		x		x			x		x
BAD07a	Migmatite	x	x	x	x	x	x		x			x	x	x	
BAD07b	Leucogranite	x	x	x	x	x	x		x	x		x	x	x	x
BAD07c	Migmatite	x	x	x	x	x	x	x	x			x	x	x	x
BAD08	Migmatite	x	x	x	x	x	x	x	~	x	x		x	x	x
BAD09a	Meta-arkose	x	x		x	x	x	x		x	x		x	x	x
BAD09b	Migmatite	x	x		x	x	x	x			x		x		x
BAD10	Orthogneiss	x	x	x	x	x		x	x			x	x	x	x
BAD11a	Migmatite	x	x		x	x		x	~	x	x		x	x	x
BADf02	Migmatite	x	x	x	x	x		x	~	x		x	x	x	x
BADf03	Orthogneiss	x	x	x	x	x		x	x		x		x	x	x
BADf04	Leucogranite	x	x	x	x	x	x		x	x		x	x	x	x
BADf13	Migmatite	x	x	x	x	x	x		~	x	x		x	x	x

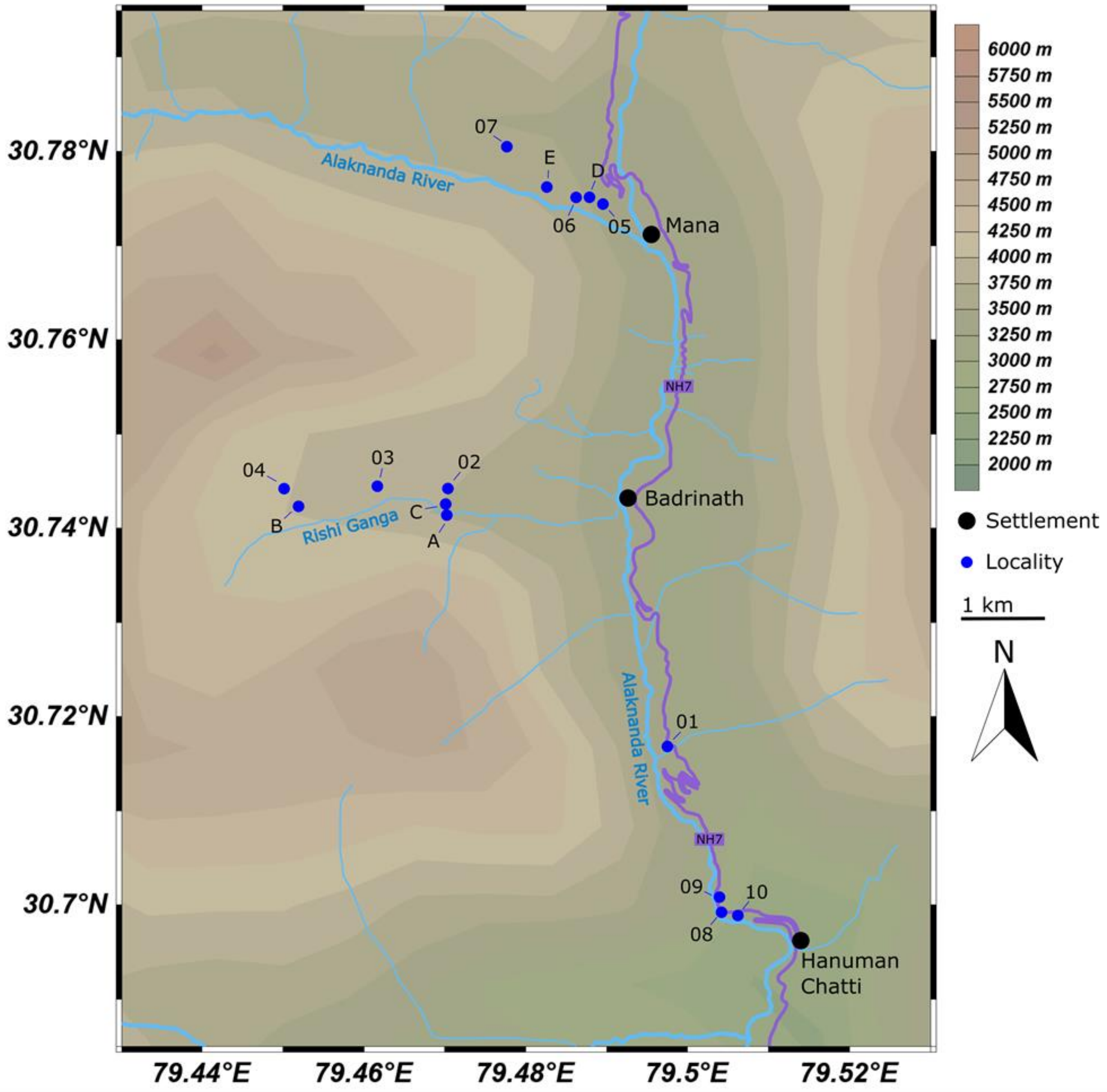

Figure 2.1 – Map of sampling localities along the Alaknanda and Rishi Ganga valleys, around Badrinath in the Garhwal Himalaya. Sample localities are marked in blue and labelled by number. Coordinates use the World Geodetic System (WGS84). Note that locality 11 is 15.5 km south-southeast of Hanuman Chatti, near Joshimath.

2.3 Methods

Samples are described using optical microscopy on polished thin sections to allow for SEM and laser-ablation analysis of the observed textures *in situ*, with typical thicknesses of 35-40 µm. As such, photomicrographs of minerals in thin sections throughout this chapter display higher-order interference colours than standard thin sections. Photomicrographs were taken with my phone camera down a microscope lens due to COVID-imposed time and lab pressures.

Whole-section Backscattered-Electron (BSE) imaging was used to assist optical microscopy in identifying phases and capturing textures due to the similar optical properties of feldspars in thicker than standard thin sections, and the limited field of view of microscope objectives. BSE images were collected using a tungsten-filament FEI Quanta 200 3D at the Open University and stitched together using the Oxford Instruments INCA software 'Montage' function.

2.4 Key sample descriptions and field relations by location

Sample descriptions are sorted by geographical location and then by sampling localities, as shown in Figure 2.1. Localities are grouped in this way as it corresponds to relative stratigraphic height within the Badrinath Formation, starting with samples from near Hanuman Chatti in the south and progressing up stratigraphy to Mana in the north. Locality 11 is part of the Joshimath Formation, with samples collected to compare with those from the Badrinath Formation.

2.4.1 Hanuman Chatti

The sampling localities around Hanuman Chatti lie within the transitional stratigraphic boundary between the Pandukeshwar and Badrinath Formations. This boundary has been identified as the Badrinath Shear Zone, primarily effecting the local metasediments of the Badrinath Formation (Benetti et al., 2021). Samples were retrieved *in situ* from the cliff face along the eastern side of the Alaknanda valley, adjacent to the NH7 highway. The outcrop along this section is composed of interbedded metapelites and metaquartzites.

2.4.1.1 Locality 08

Sampling locality 08 is west-northwest of Hanuman Chatti, where the NH7 bends northwards (30.69918°N, 79.50424°E) (Figure 2.1). The sampled exposure is a 30-50 cm wide band of metapelite bounded by metapsammites (Figure 2.2). The schistose metapelite unit contains bedding- and cleavage-parallel lenticular leucosomes, up to 60 cm across and 5 cm wide.

Sample BAD08 is an *in-situ* migmatite collected from the schistose metapelitic unit, with a fine-grained assemblage of muscovite + quartz + plagioclase + biotite, with minor amounts of K-feldspar + magnetite + garnet + apatite + tourmaline + ilmenite. Zircon and monazite are present as accessory phases. There is only minor chloritization of biotite. There is a sharp transition from schist to leucosome, composed of quartz + plagioclase + muscovite + K-feldspar (Figure 2.3). Quartz grains show undulose extinction throughout the sample.

K-feldspar is present in the schist and leucosome portions of the sample in groups of two or three grains within 3 mm of each other. Grains in the schist portions are rare, 250-600 µm across, and occur in small quartzofeldspathic domains. K-feldspar-muscovite grain boundaries are complex and lined with sericite (Figure 2.4a). In the leucosome, K-feldspar grains are more common and larger, with grains up to 1000 µm in length. Sparse plagioclase myrmekite grains, approximately 200 µm in diameter, are associated with the K-feldspar in both schist and leucosome (Figure 2.4b).

Regular anastomosing laths of muscovite dominate phyllosilicate domains with biotite disseminated evenly throughout. Muscovite also occurs as uncommon elongate strips of fine

Figure 2.2 – Locality 08 (30.69918°N, 79.50424°E). Sampled metapelitic unit of variable thickness (30-50 cm), with fabric-parallel lenticular leucosomes. On either side of this unit are interbedded metaquartzite and metapsammite units typical of the Pandukeshwar-Badrinath transition.

sericite intergrown with biotite and quartz along leucosome boundaries. Garnet occurs in the schist as rare, isolated grains, <500 µm in diameter. They have a distinct pink hue, with irregular grain boundaries and fractures. Tourmaline is present in quartzofeldspathic domains as rare euhedral grains, up to 1800 µm in diameter. These grains are strongly pleochroic with blue-green cores and olive-green rims, which appear black in hand specimen.

Figure 2.3 – Thin section image of migmatite sample 08, displaying the schistose texture present in the sample and vein-like leucosomes of Qz + Pl + Ms + Kfs.

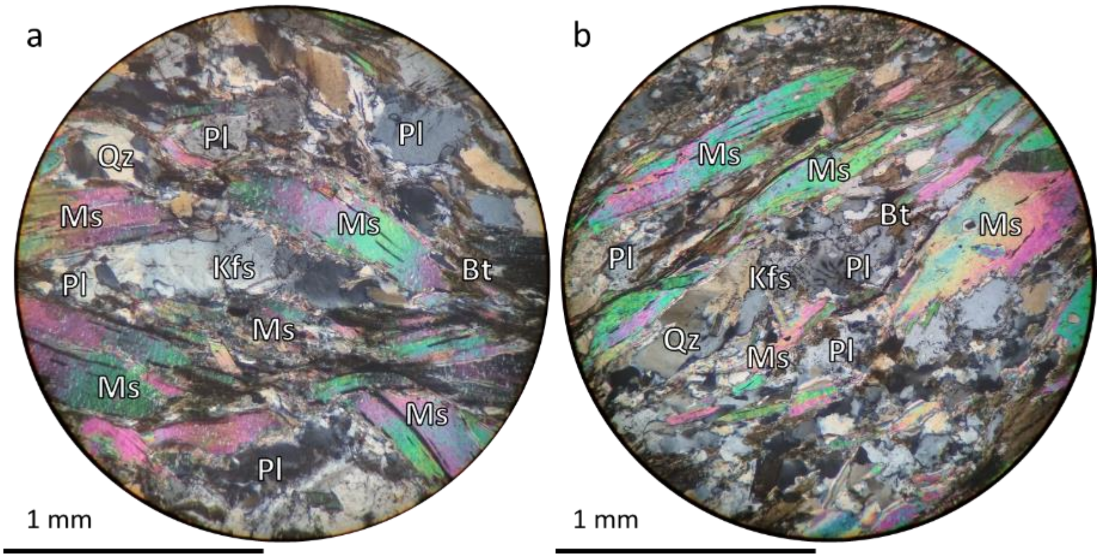

Figure 2.4 – Photomicrographs of feldspar textures in sample 08 (XPL). a) K-feldspar with complex sericitized boundary along contact with muscovite. b) Myrmekitic plagioclase adjacent to K-feldspar.

2.4.1.2 Locality 09

Sampling locality 09 is 200 m north of locality 08 along the NH7 (30.70085°N, 79.50388°E) (Figure 2.1). The exposure features interbedded metapelites, metapsammites, and metaquartzites; metapelitic beds are less prevalent than at locality 08 and are only 10-20 cm thick. Fabric-parallel leucosomes are present in the metapelitic units, similar to locality 08.

Sample BAD09a is an *in-situ* meta-arkose from a metapelite-metaquartzite unit boundary. This sample is composed of fine to medium-grained quartz + plagioclase + muscovite + biotite + garnet, with minor apatite + ilmenite + tourmaline. Zircon and monazite are present as accessory phases. Thin sections are dominated by quartzofeldspathic domains, which vary from 3-10 mm wide, while phyllosilicate domains range from 0.5-1.0 mm. There is only minor chloritization of biotite. Quartz grains show undulose extinction throughout the sample.

Garnet grains in the phyllosilicate domains are subhedral and up to 1.6 mm in diameter. They are elongated parallel to the fabric and have fractures that run perpendicular to this (Figure 2.5a). Biotite, muscovite, and apatite form pressure shadows. Garnets in the quartzofeldspathic layers are tabular skeletal relics that conform to the fabric (Figure 2.5b). Tourmaline is rare and only occurs in the quartzofeldspathic domains. Grains are <0.6 mm across and strongly pleochroic with olive green colouration.

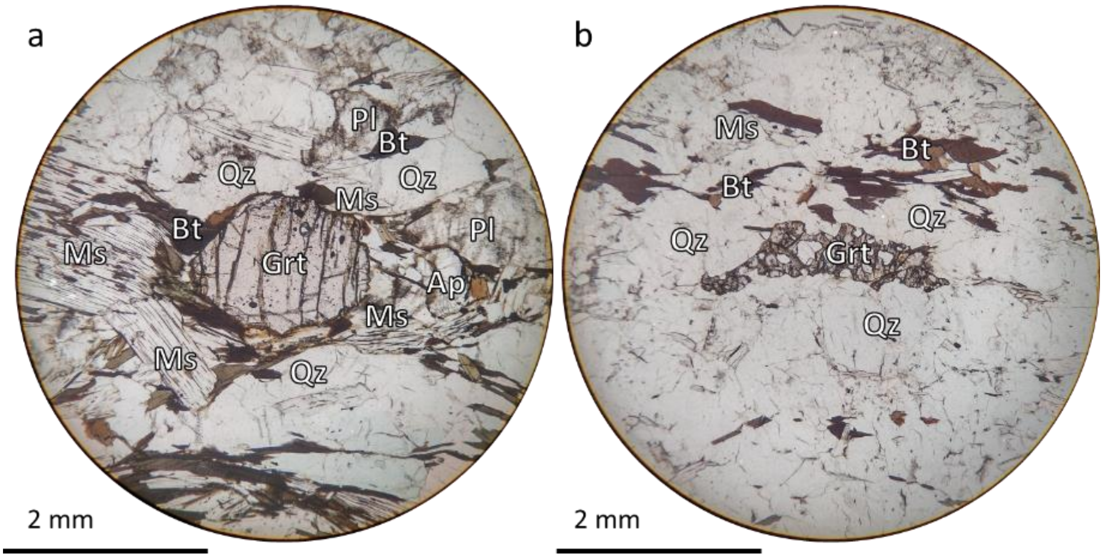

Figure 2.5 – Photomicrographs of garnet grains in sample 09a (PPL). a) Subhedral garnet in phyllosilicate domain with fractures perpendicular to fabric. b) Tabular relict garnet in quartzofeldspathic domain, in-line with fabric.

Sample BAD09b is an *in-situ* migmatite collected from a leucosome-bearing schistose metapelitic unit, with an assemblage of quartz + plagioclase + muscovite + biotite + garnet, with minor ilmenite. Zircon and monazite are present as accessory phases. As with sample BAD08, there is a sharp transition from the schist to the leucosome (Figure 2.6), composed of quartz + plagioclase + muscovite, with a few small biotite grains that have been highly chloritized. Quartz grains show undulose extinction throughout the sample.

Schist areas are medium-grained, with 4-5 mm wide compositional layering quartzofeldspathic and phyllosilicate domains. The leucosome is coarse-grained, with euhedral primary muscovite.

Plagioclase is partially sericitized. The schist-leucosome boundary is lined with medium-grained biotite and muscovite.

Garnet grains only occur in the phyllosilicate schist layers and are largely encased in biotite and muscovite. Grains are elongated with the fabric, 1-2 mm long and 0.6-0.8 mm wide, similar to sample BAD09a. They also have annealed fractures perpendicular to the fabric (Figure 2.7) and are rich in quartz inclusions.

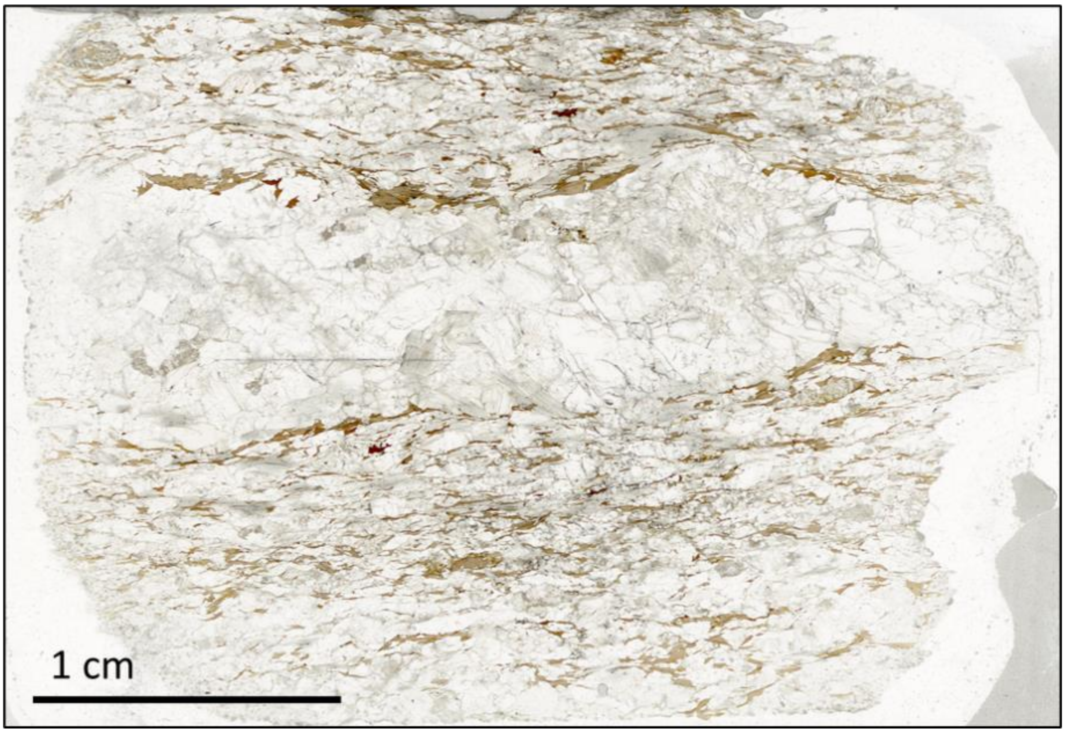

Figure 2.6 – Thin section image of migmatite sample 09b, displaying the schistose texture present in the sample and vein-like leucosomes of Qz + Pl + Ms.

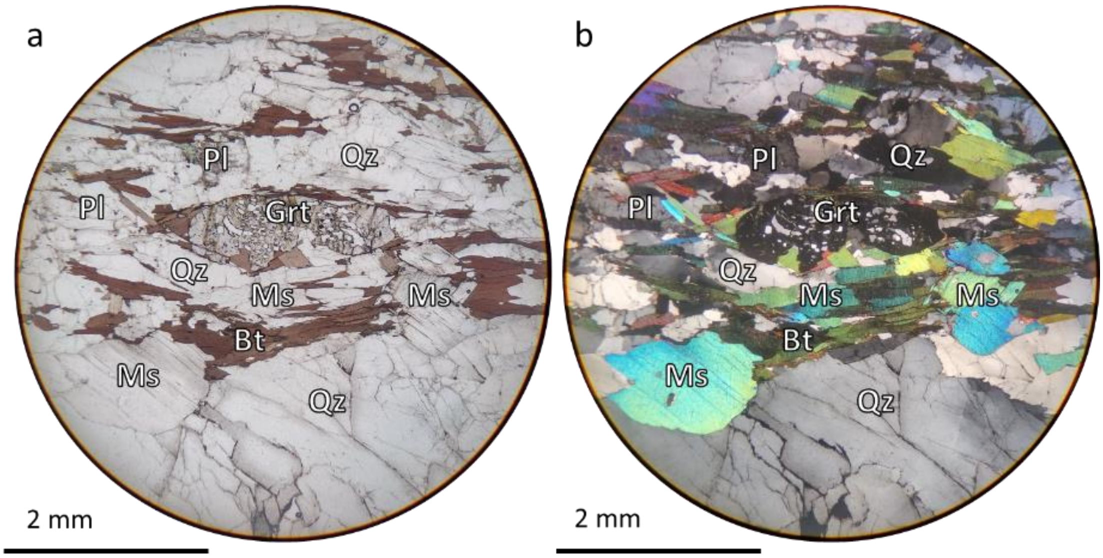

Figure 2.7 – Photomicrographs of a garnet in sample 09b. Garnet is in the phyllosilicate domain, elongated with the fabric and rich in quartz inclusions. Imaged in a) PPL and b) XPL.

2.4.1.3 Locality 10

Sampling locality 10 is 200m east-southeast of locality 08 along the NH7 (30.69894°N, 79.50621°E) (Figure 2.1). The sample exposure is a biotite-rich gneissose rock with lenticular leucocratic augen.

Sample BAD10 is an *in-situ* medium-grained orthogneiss with an assemblage of biotite + quartz + plagioclase + sillimanite + muscovite + garnet + K-feldspar. Apatite, rutile, zircon, and monazite are present as accessory phases. Quartzofeldspathic domains form asymmetric augen, up to 8 mm long and 4 mm wide, which disrupt phyllosilicate layers (Figure 2.8). Quartz grains show undulose extinction throughout the sample.

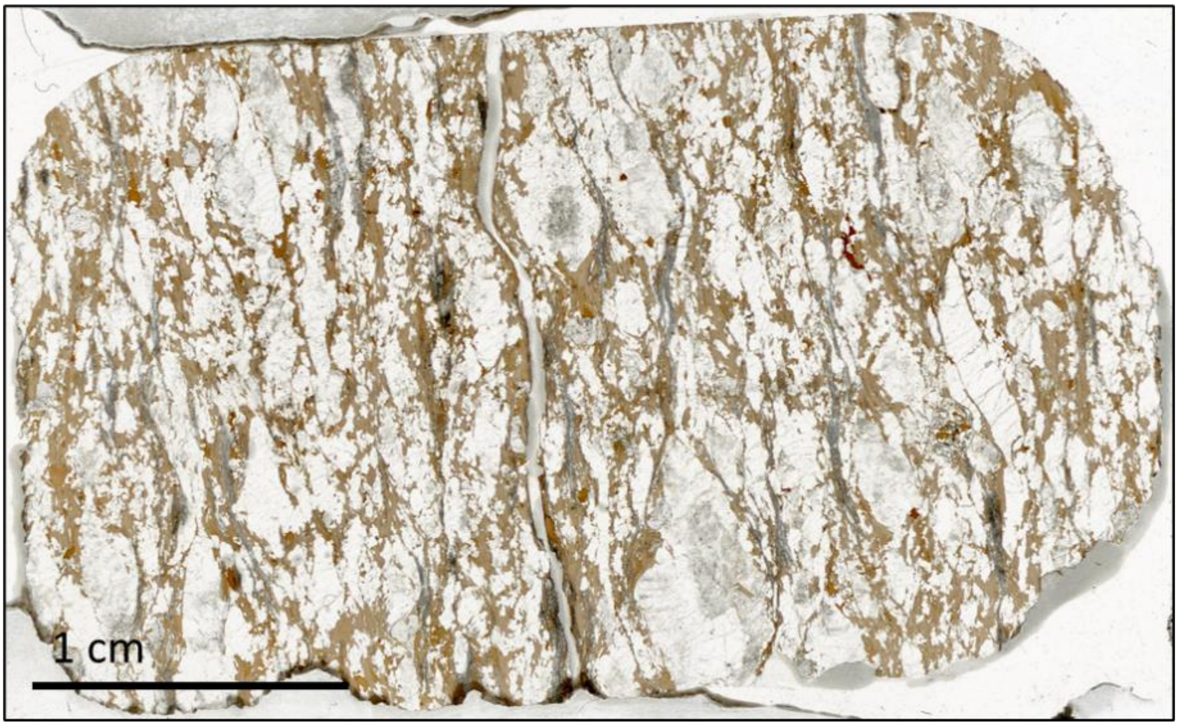

Figure 2.8 – Thin section image of orthogneiss sample 10, displaying feldspar augen and anastomosing biotite. Grey-coloured central regions of augen are antiperthitic K-feldspar intergrowths.

K-feldspar is present in two modes, as free grains and as intergrowths in antiperthite. The free grains of K-feldspar are tabular, ranging from 200-400 µm wide and 650-800 µm long, with complex sericitized boundaries with micas and contacts with plagioclase that commonly feature myrmekites (Figure 2.9a). Antiperthitic plagioclase intergrowths of K-feldspar form a network of irregular tabs up to 350 µm. This texture is only present in coarser plagioclase grains (> 1.5 mm) (Figure 2.9b).

Sillimanite is in the form of fibrolite clots with fine-grained muscovite intergrowths, up to 5.5 mm long and 200 µm wide within biotite-rich layers. Kyanite is also present as rare tabular grains, 150-500 µm long, either enclosed in plagioclase or at plagioclase-biotite grain boundaries (Figure 2.10). Garnet either forms subhedral grains ~1 mm in diameter with quartz inclusion-rich cores, or as skeletal relics with irregular replacement by quartz-biotite-rutile aggregates.

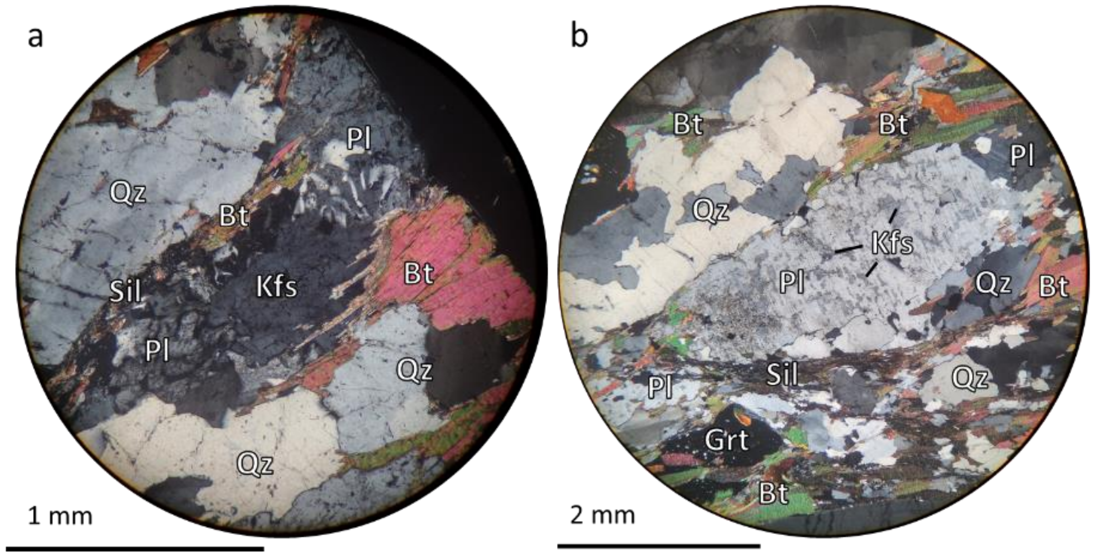

Figure 2.9 – Photomicrographs of feldspar textures in sample 10. a) Fine, tabular K-feldspar grain and myrmekitic plagioclase (XPL). b) Coarse plagioclase grain with antiperthitic K-feldspar intergrowths.

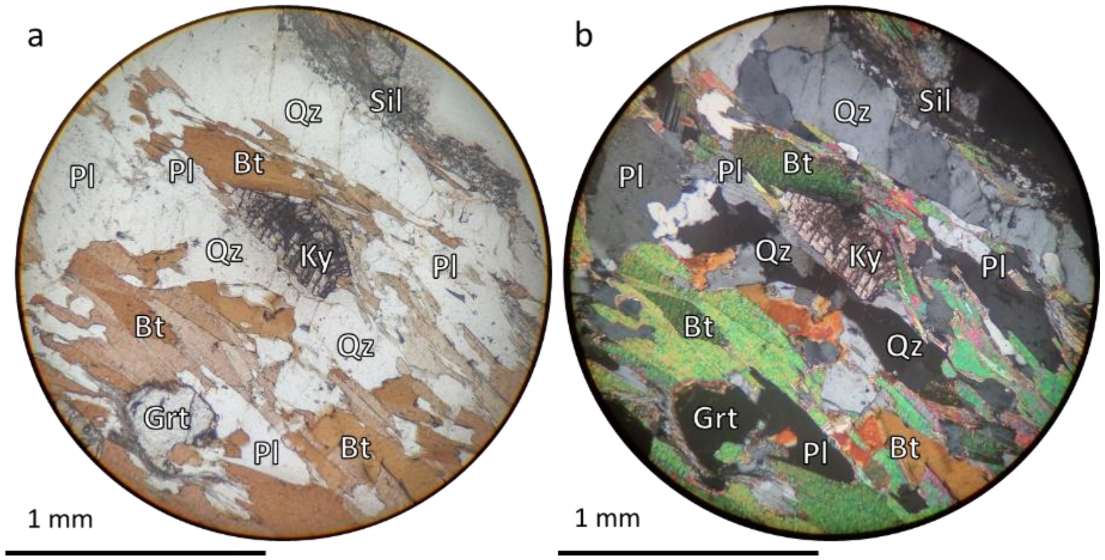

Figure 2.10 – Photomicrographs of kyanite, sillimanite, and garnet in sample 10. Sillimanite is present as fibrolite clots, while kyanite forms rare tabular grains. Imaged in a) PPL, and b) XPL.

2.4.2 Badrinath – Hanuman Chatti

2.4.2.1 Locality 01

Sampling locality 01 is approximately 4 km south of Badrinath along NH7, where the cliff and highway extend west into the valley (30.71693°N, 79.49751°E) (Figure 2.1). This locality lies wholly within the Badrinath Formation. Samples were retrieved *in situ* from the cliff face along the eastern side of the Alaknanda valley, adjacent to the NH7 highway. The outcrop along this section comprises leucosome-rich migmatites with schollen and schlieren, as well as metre-scale leucogranite bodies (Figure 2.11a). Boundaries between the melt and schollen are either gradational or lined with dark selvedges. Schlieren form closed folds within the melt (Figure 2.11b).

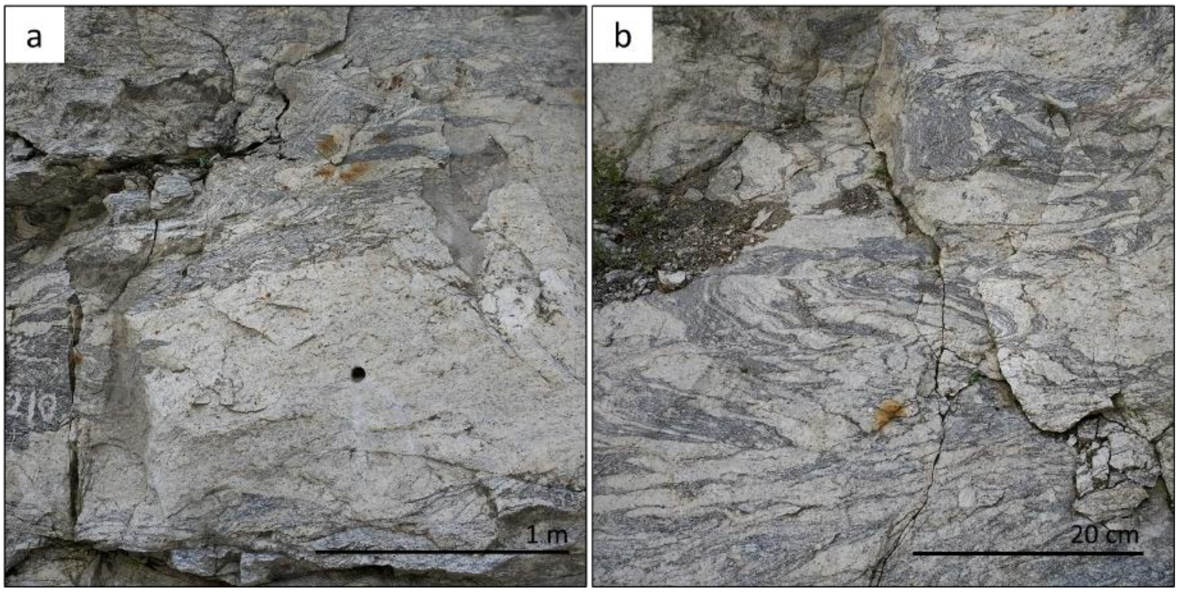

Figure 2.11 – Locality 01 (30.71693°N, 79.49751°E). a) Sampled leucogranite body within migmatite complex. b) Detail of melanocratic schlieren in migmatite surrounding the leucogranite.

Sample 01d is an *in-situ* medium-grained leucogranite collected from a 3 m wide granite body within a large migmatite complex of schollen and schlieren migmatites. It contains K-feldspar + quartz + plagioclase + garnet + muscovite + biotite, with apatite, zircon, and monazite present as accessory phases. Biotite is partially chloritized, with ~20% of grains affected. A weak planar fabric is present, with minerals generally elongated and aligned (Figure 2.12). Quartz grains show undulose extinction throughout the sample.

K-feldspar grains range between 0.8-3.5 mm across, the larger of which have perthitic albite exsolution lamellae, with irregular inclusions of quartz and plagioclase (Figure 2.13a). Plagioclase grains are 0.8-3.6 mm across and show partial sericitization. Myrmekitic plagioclase is common along K-feldspar-plagioclase grain boundaries.

Biotite grains have complex irregular boundaries with adjacent feldspars and quartz. Some biotite grains have sagenitic rutile growth, with the most affected grains also being extensively chloritized (Figure 2.13b). Muscovite is either present as grains 0.8-2.0 mm in length or as fine-grained sericite schlieren up to 6 mm long and 350 µm wide (Figure 2.13c). These sericite clots are associated with K-feldspar and fine-grained biotite. Garnets are highly elongated, one grain reaching 3.7 by 1.0 mm, with fractures perpendicular to their long axes that have partially annealed or show biotite/chlorite alteration (Figure 2.13d). Small inclusions of various morphologies (needle, blocky, prismatic), <50 µm long, run the central lengths of the garnets. Also present are inclusions of irregular lobate quartz.

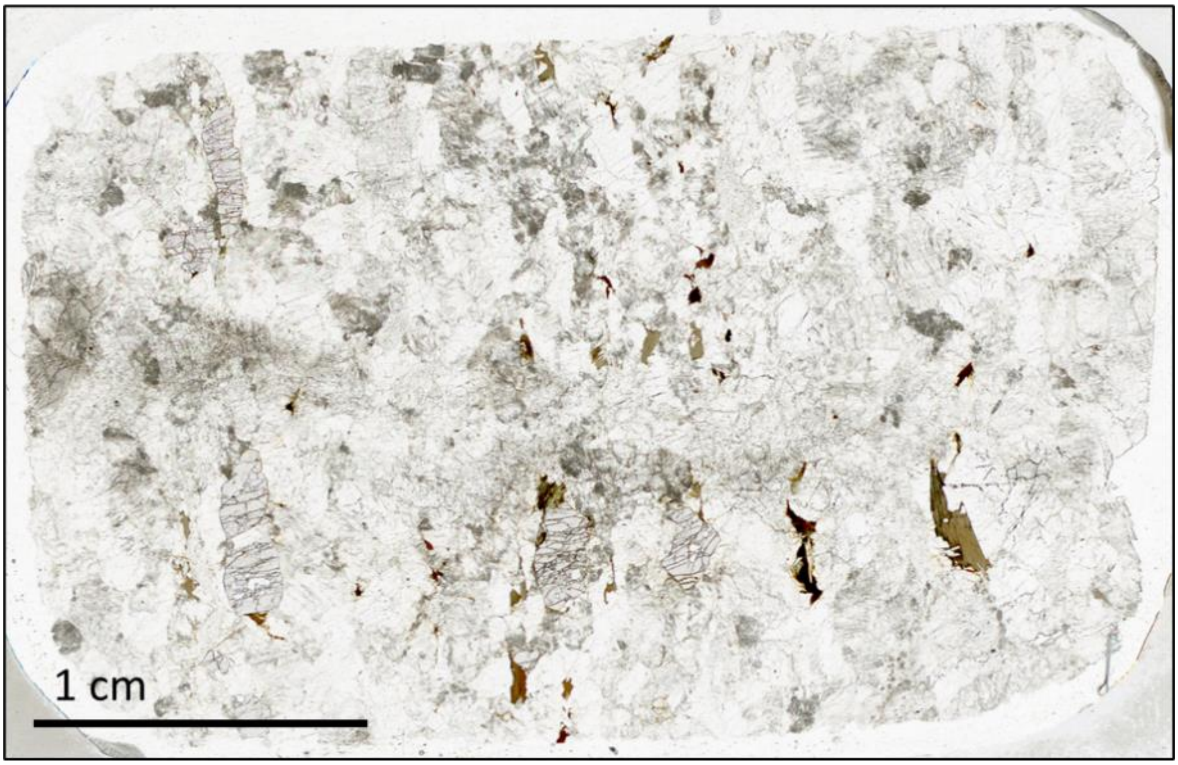

Figure 2.12 – Thin section image of leucogranite sample 01d, displaying fabric of aligned biotite schlieren and elongated garnet.

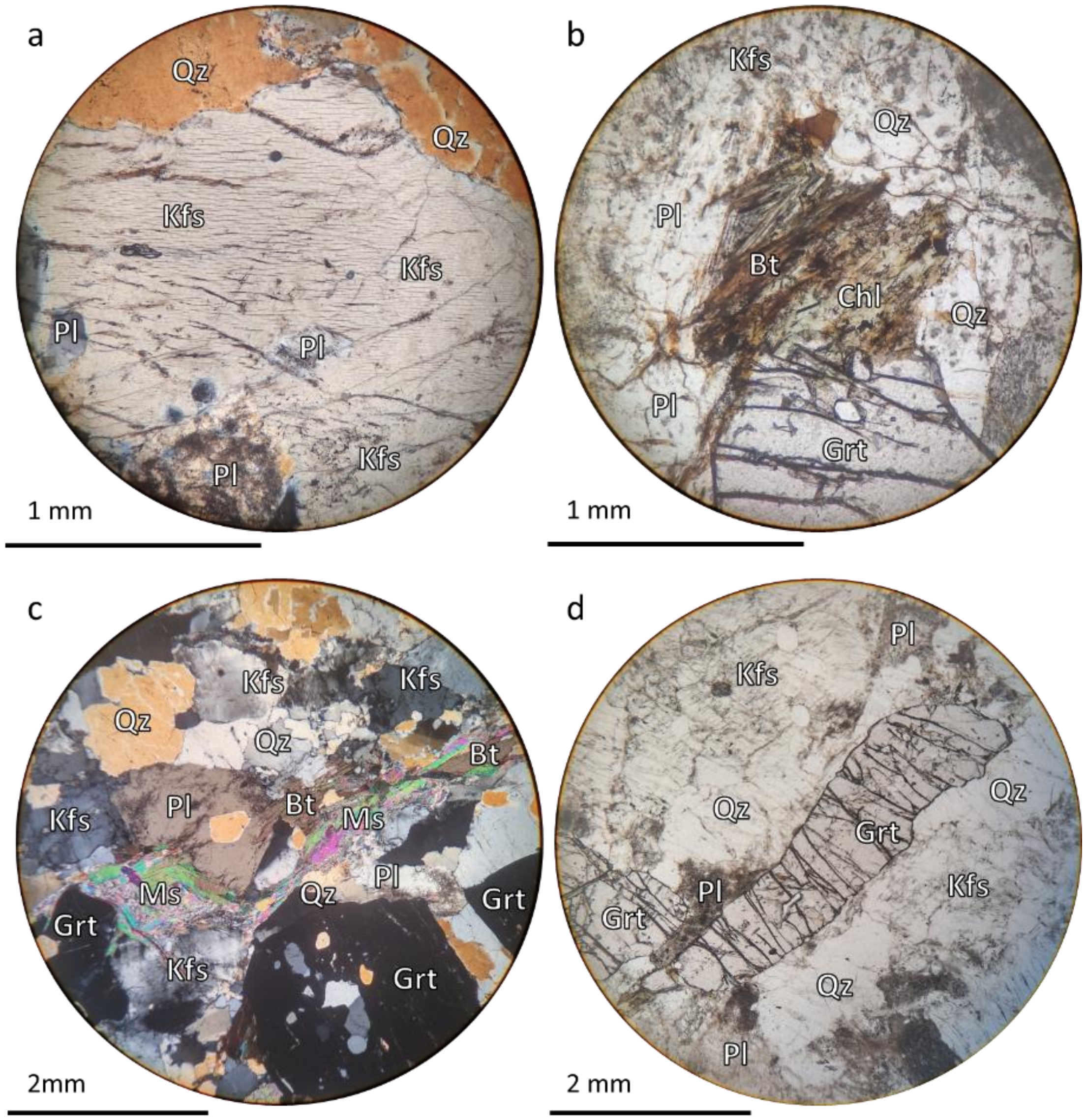

Figure 2.13 – Photomicrographs of various mineral textures in sample 01d. a) Coarse K-feldspar grain with perthitic albite exsolution lamellae. b) Partially chloritized biotite grain with sagenitic rutile growth. c) Muscovite-sericite schliere and clot. d) Highly elongated garnet grain with fractures perpendicular to its length.

2.4.3 Rishi Ganga

Sampling localities in the Rishi Ganga valley, west of Badrinath, are a mixture of *in situ* and float. Samples retrieved *in-situ* are from the cliff face along the northern side of the valley, while float samples, labelled with 'f', were collected either along the Rishi Ganga stream or from scree and boulders on the valley floor. Outcrops along the northern cliff section are migmatites and minor calc-silicates, with increasing proportions of leucosomes present at higher altitudes towards the western end of the valley.

2.4.3.1 Locality 02

Sampling locality 02 is 1.8 km west of Badrinath (30.74428°N, 79.47037°E) (Figure 2.1). The sampled exposure consists of gneissose metatexite with 0.5-1 cm lenticular leucosomes throughout, as well as leucosome pods up to 20 cm across (Figure 2.14). The edges of these pods are lined with biotite schlieren.

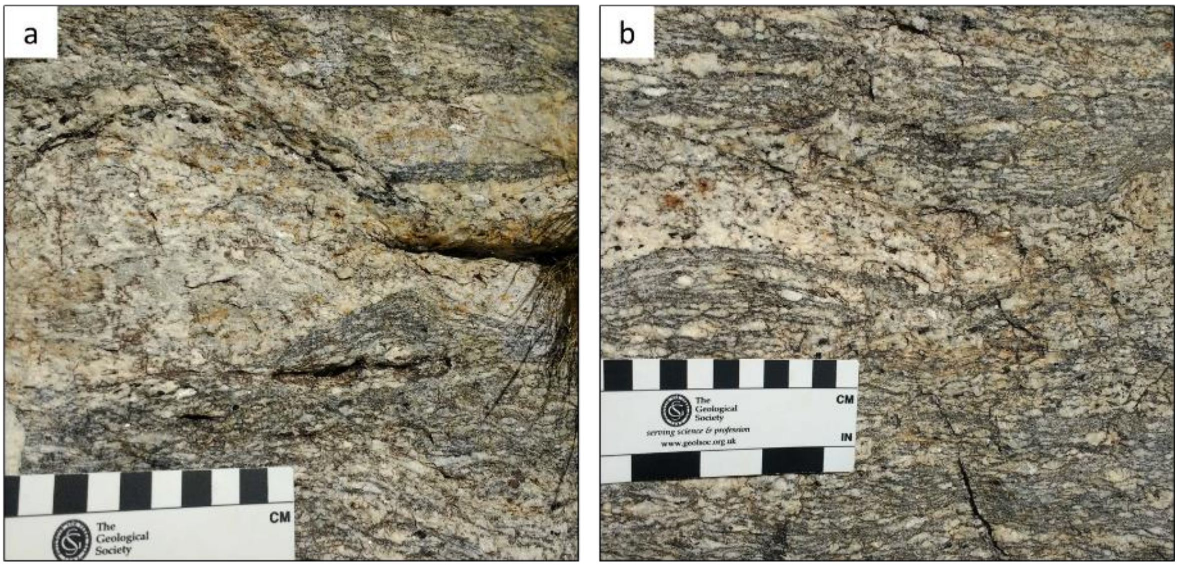

Figure 2.14 – Locality 02 (30.74428°N, 79.47037°E). a) Leucosome pod with tourmaline schliere, within gneissose migmatite. b) Lenticular leucosome within gneissose migmatite.

Sample 02a is an *in-situ* fine-grained metatexite with a gneissose fabric and medium-grained leucosomes (Figure 2.15). It consists of quartz + K-feldspar + plagioclase + biotite + sillimanite + muscovite + tourmaline, with apatite, zircon, and monazite present as accessory phases. Biotite grains within or adjacent to leucosomes have been extensively chloritized. Quartz grains show undulose extinction throughout the sample.

In the leucosomes, K-feldspar occurs as perthitic subhedral grains, 2-4 mm across, with rare grains > 5 mm. In the groundmass, K-feldspar forms sparse fine-grained aggregates around quartz, plagioclase, and biotite. Plagioclase shows albite twinning and partial sericitization, while grains adjacent to K-feldspar in leucosomes form myrmekites (Figure 2.16a).

Figure 2.15 – Thin section image of migmatite sample 02a, displaying elongate fibrolite clot (centre, top to bottom) and uncommon K-feldspar porphyroblasts >5mm (bottom left).

Fine-grained biotite and muscovite form disaggregated phyllosilicate bands. Biotite also occurs sporadically throughout quartzofeldspathic domains, and as sagenitic chlorite. Sillimanite forms fibrolite clots up to 18 mm long and 2 mm wide, with fine-grained K-felspar, quartz and sericite intergrowths (Figure 2.16b). Garnet is rare, with subhedral grains 0.8 mm in diameter associated with biotite and chlorite. Tourmaline is also rare, forming 0.75-1.25 mm grains adjacent to leucosomes, with strong olive-green to colourless pleochroism.

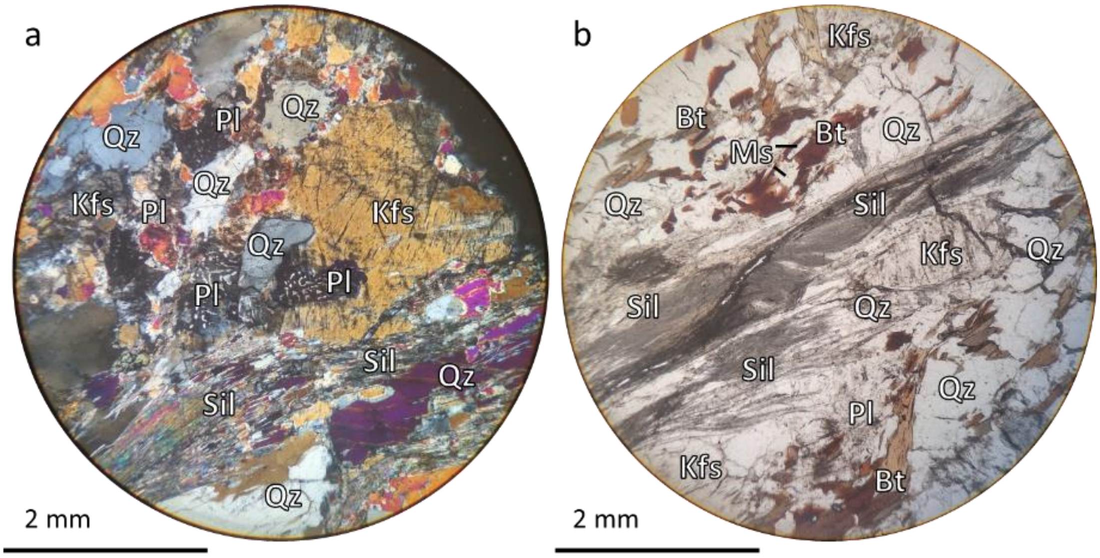

Figure 2.16 – Photomicrographs of feldspar and sillimanite textures in sample 02a. a) Medium-grain myrmekitic plagioclase and coarse-grains K-feldspar (XPL). b) Fibrolitic sillimanite with K-feldspar and quartz (PPL).

Sample 02b is an *in-situ* medium-grained migmatite leucosome sampled from one of the larger leucosome pods of locality 02. It is comprised of quartz + plagioclase + K-feldspar + chlorite/biotite + garnet + muscovite, with apatite, zircon, and monazite present as accessory phases. The leucosome is faintly foliated with bands of K-feldspar and phyllosilicate schlieren. Biotite is extensively chloritized, with few unaltered grains remaining. Quartz grains show undulose extinction throughout the sample.

K-feldspar forms perthitic grains with albite exsolution lamellae, typically 1-2 mm, and is partially sericitized. Some grains are poikiloblastic, with irregular quartz and plagioclase inclusions. Crosshatch twinning is present in smaller grains. Plagioclase forms 1.0-1.6 mm grains which are strongly sericitized. Myrmekitic plagioclase is common along boundaries with K-feldspar (Figure 2.17).

Chloritized biotite forms thin schlieren with small relict grains of muscovite. Chlorite is often sagenitic with fine rutile needles. Garnets are subhedral, 0.4-1.8 mm in diameter, with fractures lined with biotite and chlorite.

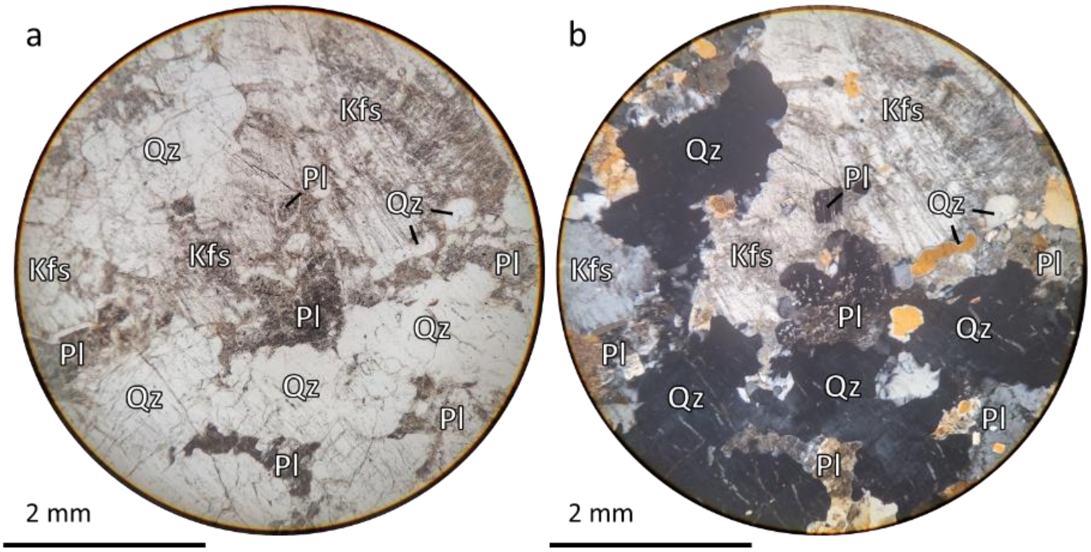

Figure 2.17 – Photomicrographs of feldspar textures in sample 02b. Medium-grained myrmekitic plagioclase adjacent to coarse perthitic K-feldspar. Plagioclase is strongly sericitized, while K-feldspar is preferentially sericitized along albite exsolution lamellae. Imaged in a) PPL, and b) XPL.

2.4.3.2 Locality 03

Sampling locality 03 is 0.8 km west of locality 02, 2.6 km west of Badrinath (30.74440°N, 79.46177°E) (Figure 2.1). The exposure is a 3.4 x 1.5 m lenticular leucogranite body with a sharp upper contact with the host migmatite (Figure 2.18). The lower contact is obscured by sediment and scree.

Figure 2.18 – Locality 03 (30.74440°N, 79.46177°E). Sampled lenticular leucogranite body, >3 m long, with sharp contact with host migmatite visible along its top edge.

Sample 03 is an *in-situ* medium-grained leucogranite taken from the leucogranite body from locality 03. It contains K-feldspar + plagioclase + quartz + biotite/chlorite + apatite, with zircon and allanite present as accessory phases. Biotite is partially chloritized, with ~40% of grains affected. Quartz grains show undulose extinction throughout the sample.

K-feldspar forms perthitic grains, typically 1.6-4.6 mm across (up to 7 mm), with albite exsolution blebs and lamellae. Some grains are poikiloblastic, with irregular plagioclase, quartz, and chlorite inclusions. Crosshatch twinning is present in smaller grains. Partial sericitization is prevalent around exsolution textures. Plagioclase forms 1.3-4.5 mm grains which are strongly sericitized. Boundaries with K-feldspar are irregular, with myrmekitic plagioclase and quartz.

Biotite and chlorite form fine-grained laths, 0.3-0.8 mm long, with irregular grain boundaries. Sagenitic rutile is common in both minerals (Figure 2.19a-b). Apatite makes up approximately 1% of the rock by volume, forming euhedral hexagonal and rounded grains 0.25-1.3 mm in diameter. Biotite, chlorite, and apatite often form clusters. Allanite is present as an accessory mineral, with rare grains up to 0.8 mm in length (Figure 2.19c-d).

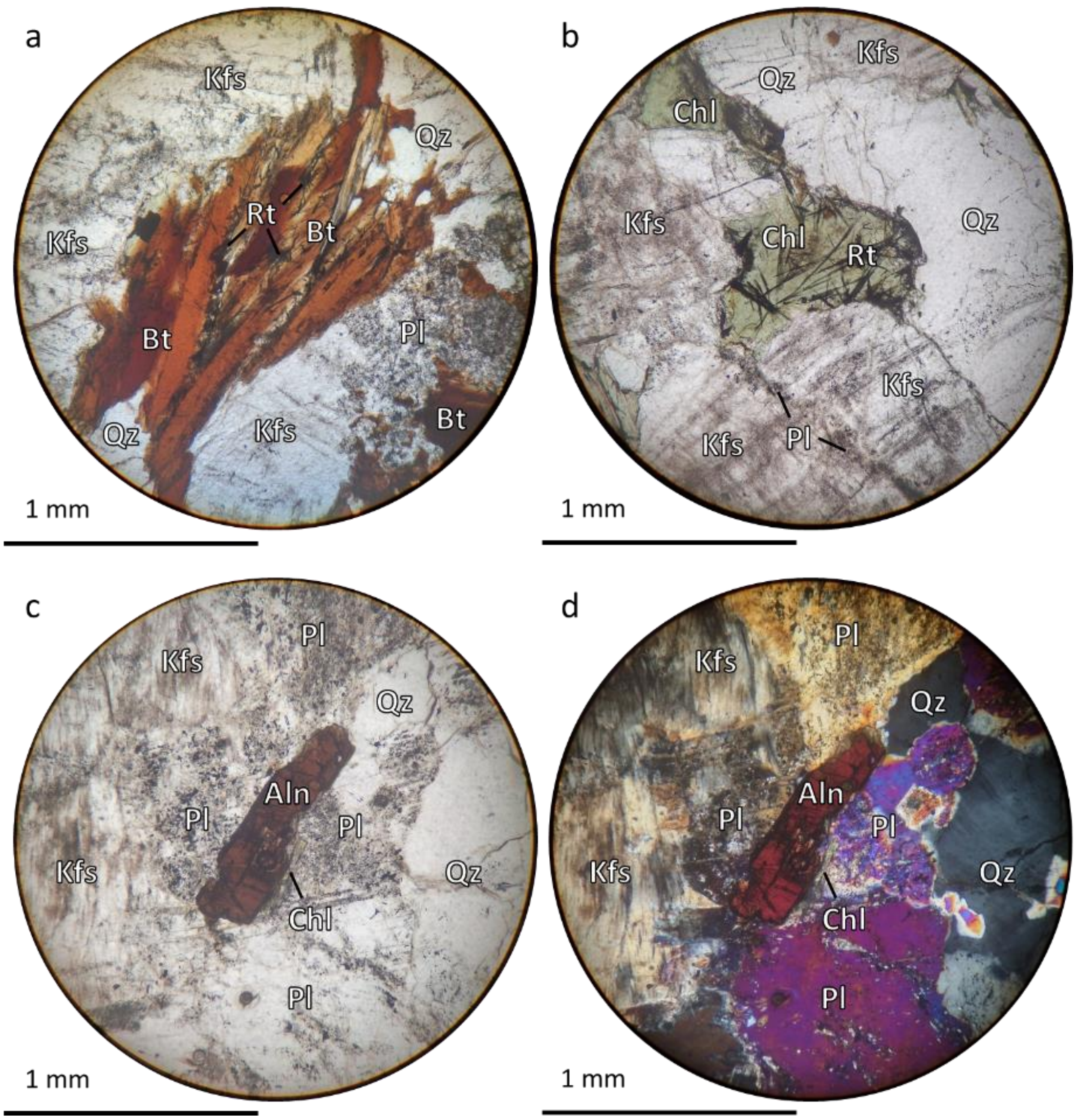

Figure 2.19 – Photomicrographs of various mineral textures in sample 03. a) Biotite laths with sagenitic rutile (PPL). b) Chlorite with sagenitic rutile (PPL). c) Rare allanite grain, 0.8 mm long (PPL). d) Rare allanite grain (XPL).

2.4.3.3 Locality 04

Sampling locality 04 is 1.2 km west of locality 03, 3.8 km west of Badrinath (30.74426°N, 79.45016°E) (Figure 2.1). The outcrop consists of transitional migmatites with varying proportions of leucosome to mesosome/schollen. Boundaries between rafts and melt are diffuse with schlieren and melanocratic selvedges.

Sample 04a is a medium-grained *in-situ* schlieren diatexite, consisting of K-feldspar + plagioclase + quartz + muscovite + biotite + sillimanite + tourmaline, with apatite, rutile, zircon, and monazite present as accessory phases. Phyllosilicate bands define schlieren, along with smaller grain-size quartz, K-feldspar, and albite than in the leucosome (Figure 2.20). Biotite is variably chloritized, with grains within the leucosomes showing greater alteration. Quartz grains show undulose extinction throughout the sample.

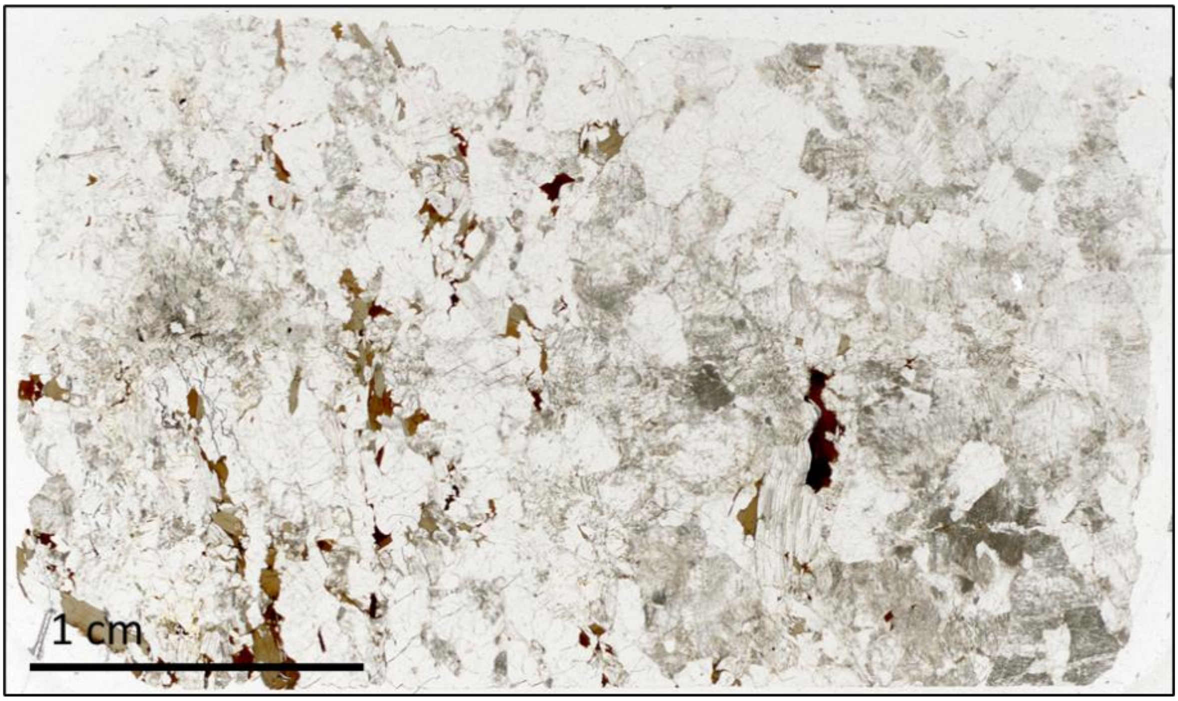

Figure 2.20 – Thin section image of migmatite sample 04a, displaying biotite schlieren and divide between fine-medium-grained mesosome (left) and coarse-grained leucosome (right).

K-feldspar in the leucosome is perthitic with albite lamellae and partially sericitized. Grains are commonly porphyroblastic, between 1.9-3.7 mm, with fine inclusions of plagioclase, quartz, and muscovite (Figure 2.21e). In schlieren/mesosome domains, K-feldspar form loose clusters, with grains 0.5-1.0 mm across. Complex sericite boundaries and quartz films occur along contacts with muscovite (Figure 2.21a). Plagioclase forms 1.6-4.4 mm highly sericitized grains in the leucosome. It is rare in the mesosome, with grains of 0.3-0.6 mm with K-feldspar overgrowths (Figure 2.21b).

Muscovite forms 1.3-4.3 euhedral laths in the leucosome, associated with K-feldspar and biotite. In the mesosome, grains are smaller, 0.5-1.0 mm, subhedral, and are sericitized along boundaries with K-feldspar. Biotite grains are mostly in the mesosome/schlieren, some up to 1.8 mm across. Grain boundaries are commonly irregular, especially for chloritized grains in the leucosome. Both biotite and chlorite can be sagenitic, with acicular rutile also occurring in quartz (Figure 2.21c-d). Sillimanite forms fibrous clots up to 2 mm long, with fine muscovite/sericite and K-feldspar inclusions. Tourmaline is rare and strongly pleochroic, with blue-green cores and brown-green rims. Grains in the leucosome are up to 1.7 mm across.

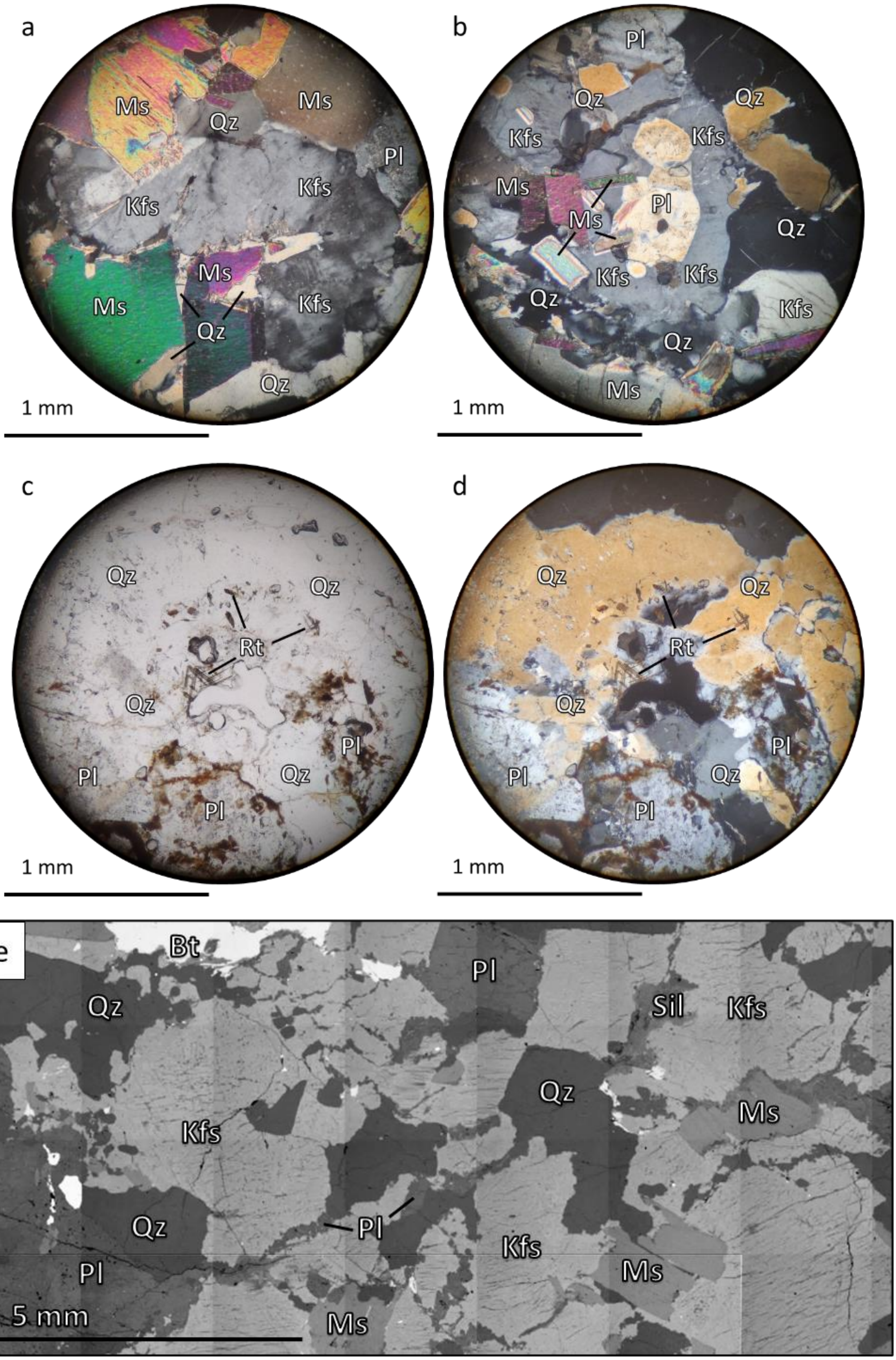

Figure 2.21 – Photomicrographs and BSE image of various mineral textures in sample 04a. a) Quartz films and sericite along muscovite boundaries with K-feldspar (XPL). b) Plagioclase with K-feldspar overgrowth/replacement in the mesosome (XPL). c) Acicular rutile inclusions in quartz (PPL). d) Acicular rutile inclusions in quartz (XPL). e) BSE image of perthitic K-feldspar porphyroblasts in the leucosome.

Sample 04b is a medium-grained *in-situ* schollen diatexite composed of K-feldspar + quartz + plagioclase + biotite + muscovite + sillimanite + tourmaline, with apatite, rutile, zircon, and monazite present as accessory phases. Schollen mesosomes and leucosomes form discrete domains with transition zones and schlieren (Figure 2.22). Biotite is variably chloritized, with grains within the leucosomes showing greater alteration. Quartz grains show undulose extinction throughout the sample.

Figure 2.22 – Thin section image of migmatite sample 04b, displaying leucosome (left) and mesosome schollen (right). Biotite marks the primary fabric of the mesosome and leucosome schliere (where disaggregated).

In the leucosome, K-feldspar forms partially sericitized medium-coarse grains up to 5.7 mm across. These porphyroblastic grains have perthitic albite lamellae and complex contacts with sericite/muscovite and sillimanite (Figure 2.23a-b). Grains commonly have inclusions of plagioclase, quartz, and sericitized muscovite. Plagioclase grains in the leucosome are partially sericitized, 1.2-1.9 mm across, and form sporadic myrmekites along boundaries with K-feldspar. In schollen mesosome domains, K-feldspar grains, typically 0.7-1.3 mm, form loose clusters with quartz, muscovite, and minor biotite, up to 12.3 mm long and 3.5 mm wide (Figure 2.23c-e). These grains show crosshatch twinning, perthitic albite, or neither of these features. Plagioclase is absent from the K-feldspar-quartz-muscovite clusters but occurs outside of them as fine-medium grains, 0.8-1.2 mm across, with partial sericitization. K-feldspar and plagioclase grains in the transitional mesosome are a mixture of the textures and grain sizes present in the leucosome and schollen domain, with the notable difference that the K-feldspar-quartz-muscovite clusters appear to be disaggregated.

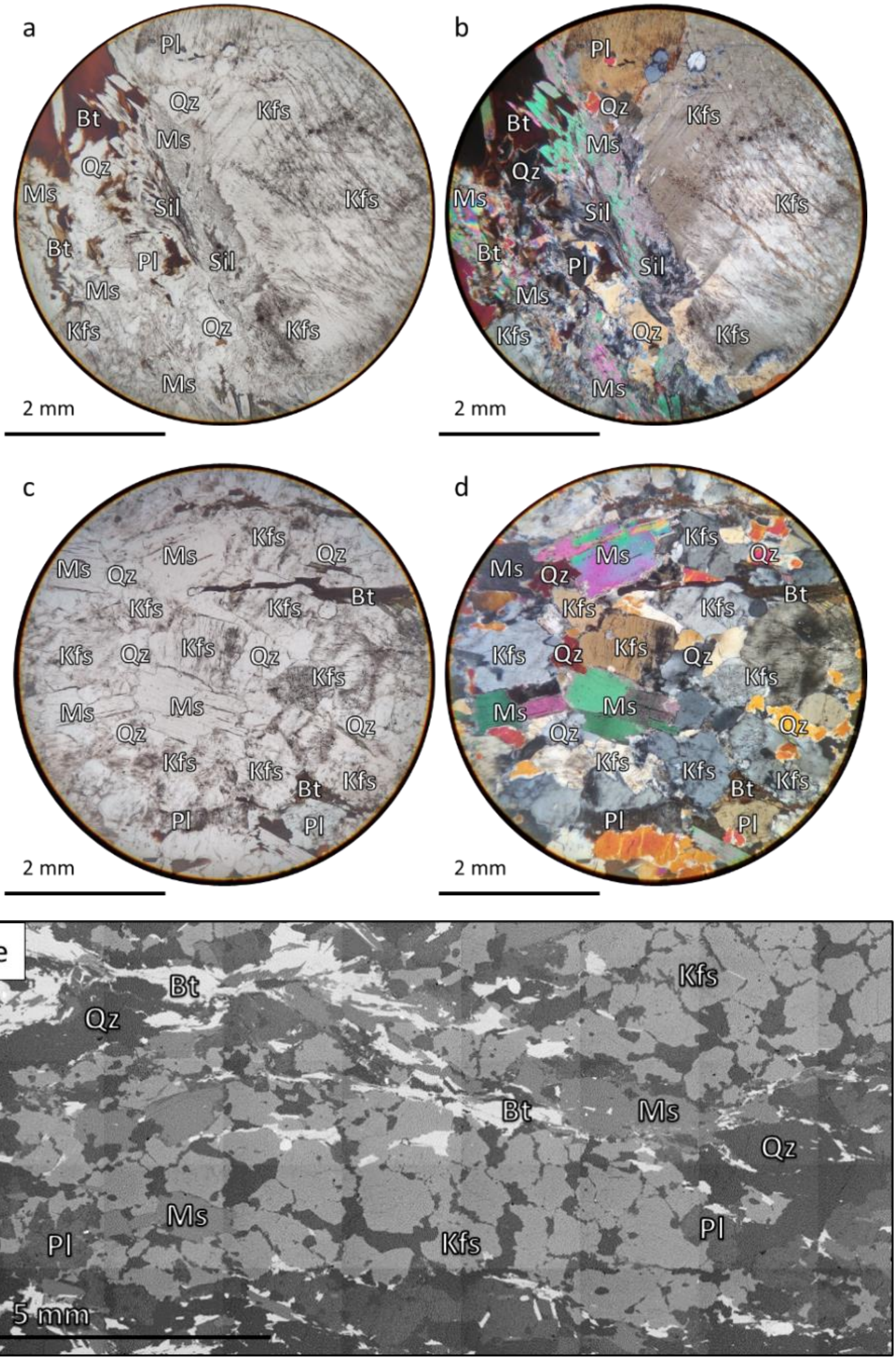

Figure 2.23 – Photomicrographs and BSE image of various mineral textures in sample 04b. a) Perthitic K-feldspar porphyroblast and sillimanite-sericite clot (PPL). b) Perthitic K-feldspar porphyroblast and sillimanite-sericite clot (XPL). c) Cluster of K-feldspar grains with muscovite and quartz (PPL). d) Cluster of K-feldspar grains with muscovite and quartz (XPL). e) BSE image of K-feldspar clusters (light grey) in the mesosome.

Biotite forms fine-medium grains, 0.5-1.6 mm, with irregular boundaries in schollen and schlieren. Sagenitic textures are common in both biotite and chlorite. Muscovite forms medium laths typically 1.0-1.4 mm long in the schollen and transitional mesosome, with thin sericite rims and quartz films along contacts with K-feldspar. In the leucosome, muscovite is medium-coarse, with grains up to 5.6 mm long. Intergrowths of sericite and sillimanite form fibrolitic clots that border perthitic K-feldspar. Tourmaline is rare and pleochroic, with small blue-green cores and brown-green rims. Grains in the leucosome are 0.5-1.4 mm.

2.4.3.4 Float Locality A

Sampling locality A is 0.3 km south of locality 02, 1.8 km west of Badrinath (30.74142°N, 79.47026°E) (Figure 2.1). Float samples were collected at this locality from a broad rocky bar in the Rishi Ganga stream. The catchment of these samples is relatively well-constrained due to the encircled nature of the valley.

Sample f02 is a medium-grained diatexite with coarse-grained leucosomes. It consists of quartz + muscovite + plagioclase + K-feldspar + tourmaline + apatite + biotite + garnet, with magnetite, zircon, and monazite present as accessory phases. The mesosome is rich in muscovite with K-feldspar-quartz-muscovite clusters and minor biotite, while the leucosome mostly lacks phyllosilicates, with a composition of quartz + plagioclase + tourmaline + K-feldspar + sericite (Figure 2.24). Quartz grains show undulose extinction throughout the sample.

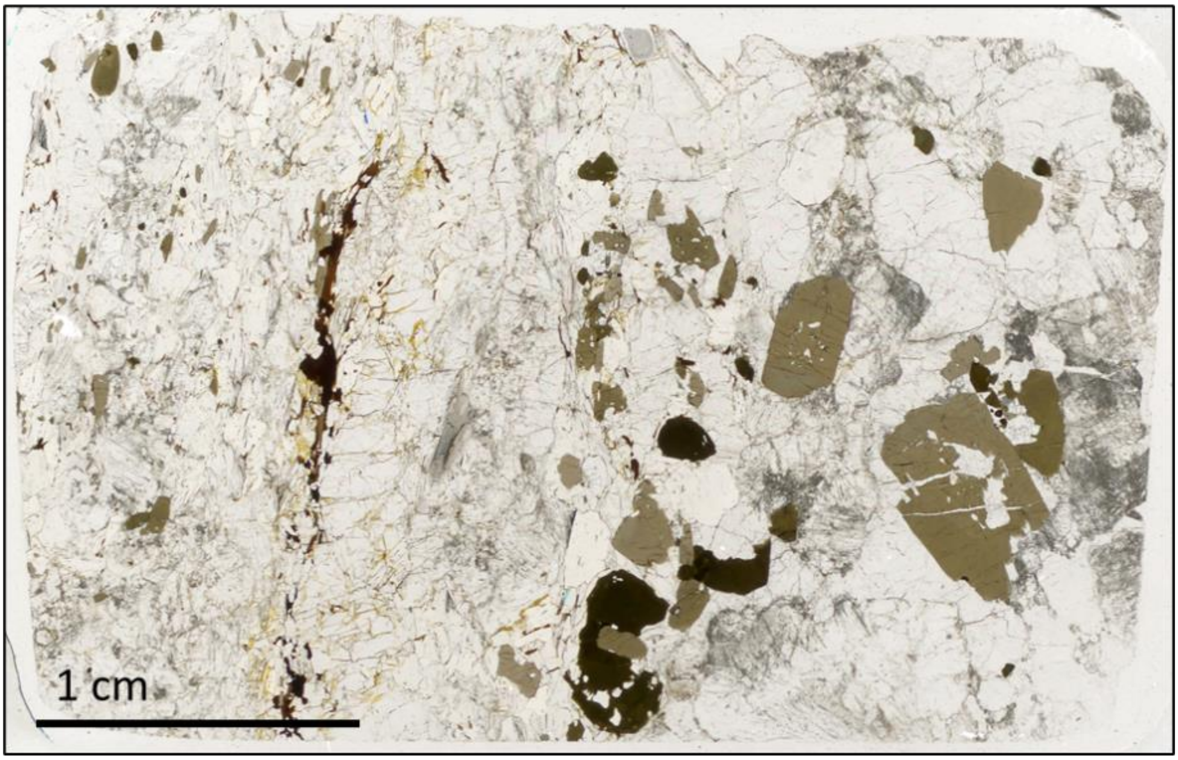

Figure 2.24 – Thin section image of migmatite sample f02, displaying medium-grained mesosome (left) and coarse-grained leucosome with pleochroic tourmaline (right).

In the mesosome, K-feldspar grains, typically 0.8-1.4 mm, form loose clusters with quartz and muscovite, with rare plagioclase grains with K-feldspar overgrowth (Figure 25a). Plagioclase grains are 0.5-1.6 mm, with partial sericitization and scattered myrmekitic grains along K-feldspar contacts. In the leucosome, K-feldspar forms medium perthitic grains, 3.3-4.5 mm, with inclusions of quartz and plagioclase, and also as groups of finer grains of disaggregated K-feldspar clusters from the mesosome. Plagioclase forms medium-coarse grains, 3.2-8.3 mm across, the largest showing antiperthitic blebs of K-feldspar.

Muscovite is present as fibrous sericite clots along the mesosome-leucosome boundary, up to 3.4 mm long. In the mesosome proper, muscovite is present either as 500-750 µm grains in the K-feldspar-quartz-muscovite clusters or as medium-grained laths, typically 1.6 mm long, in phyllosilicate bands, which are host to apatite and tourmaline. Biotite is only present in the mesosome as 0.4-1.5 mm laths, which have syntaxial overgrowth of muscovite (Figure 2.25b). Tourmaline forms euhedral prismatic grains up to 6.4 mm in the leucosome and up to 1.6 mm in the mesosome, associated with the phyllosilicate bands. Tourmaline is strongly pleochroic, with blue-green cores and olive-green rims. Garnet grains are rare, less than 600 µm in diameter, with irregular boundaries and associated with fine chlorite.

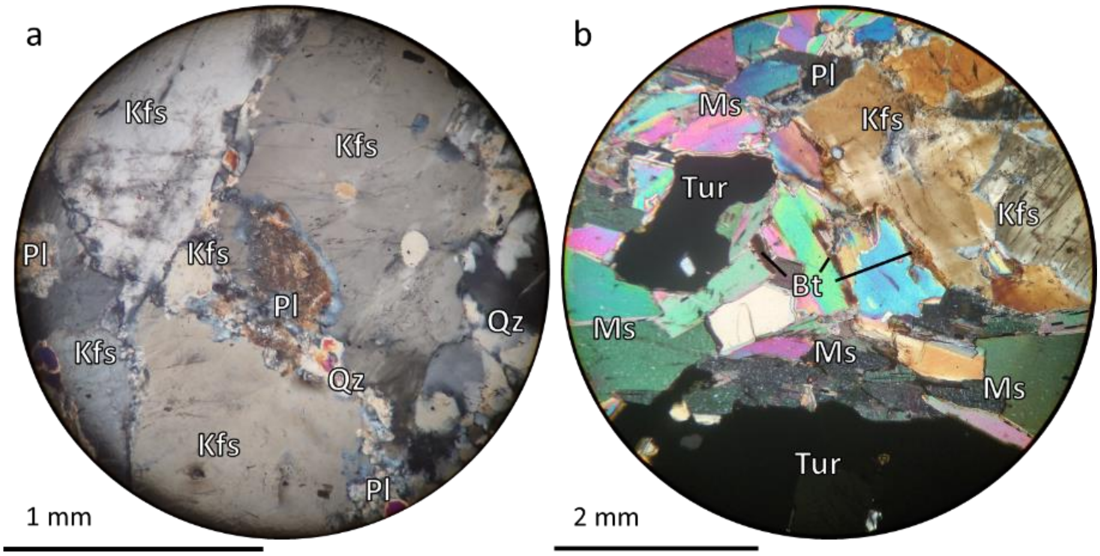

Figure 2.25 – Photomicrographs of feldspar and mica textures in sample f02. a) Plagioclase with K-feldspar overgrowth/replacement in the mesosome (XPL). b) Irregular biotite laths optically continuous with muscovite in phyllosilicate-rich domains (XPL).

Sample f03 is a medium-grained orthogneiss, consisting of K-feldspar + quartz + biotite + plagioclase + sillimanite + muscovite, with minor garnet + apatite. Zircon and monazite are present as accessory phases. Quartzofeldspathic domains form irregular augen, up to 20 mm long and 16 mm wide, but typically 12 x 5 mm, which disrupt phyllosilicate layers. Quartz grains show undulose extinction throughout the sample.

K-feldspar grains are typically rounded, 0.8-1.5 mm across, with either crosshatch twinning or very fine perthitic albite. Plagioclase grains are between 0.8-1.2 mm, with albite twinning. Myrmekitic plagioclase is common along K-feldspar contacts (Figure 2.26). Both feldspars are partially sericitized.

Phyllosilicate domains primarily consist of interlocking biotite laths, 0.8-1.4 mm long, which are host to garnets, <200 µm in diameter, and apatite, <350 µm in diameter. Muscovite grains are 0.5—1.2 mm long, with irregular boundaries along contacts with K-feldspar. Pockmarked grains occur in quartzofeldspathic domains, intergrown with K-feldspar (Figure 2.26). Sillimanite forms fibrolite clots with fine-grained muscovite intergrowths up to 5.0 mm long and 0.6 mm wide within phyllosilicate domains.

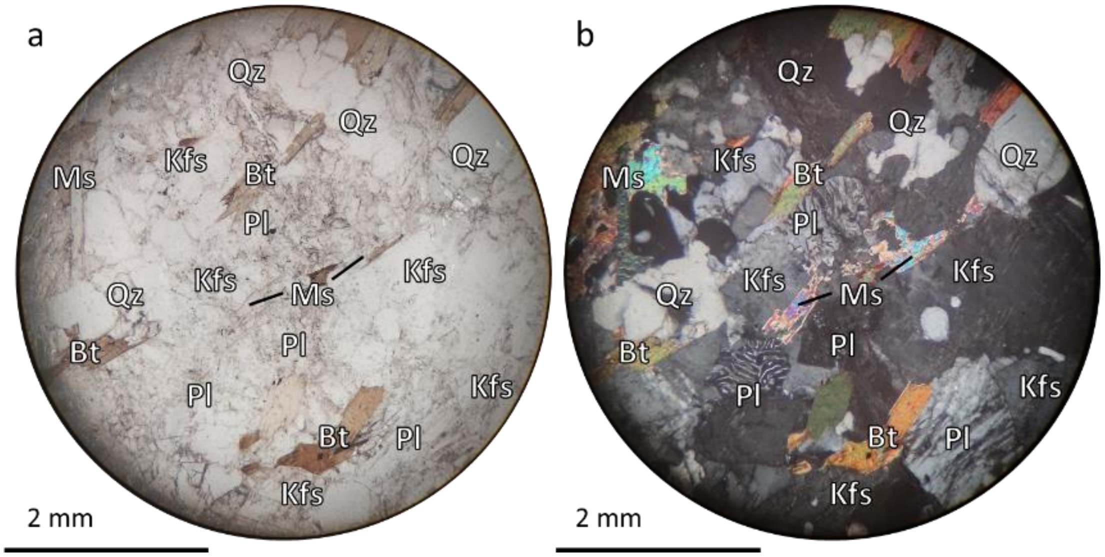

Figure 2.26 – Photomicrographs of feldspar and mica textures in sample f03. Myrmekitic plagioclase in contact with K-feldspar grain and pockmarked muscovite with irregular grain boundaries. Imaged in a) PPL, and b) XPL.

Sample f04 is a medium-grained leucogranite with an assemblage of plagioclase + quartz + K-feldspar + muscovite + biotite + tourmaline, with minor sillimanite. Apatite, zircon, and monazite are present as accessory phases. Biotite forms disaggregated schlieren strands with muscovite and sillimanite. Only a few biotite grains are affected by chloritization, constrained to the edges of biotite grains. Quartz grains show undulose extinction throughout the sample.

K-feldspar forms grains, typically 1.8-5.0 mm across, with perthitic albite exsolution lamellae (Figure 2.27e). Crosshatch twinning is common. Grains may have poikiloblastic zones with quartz and muscovite inclusions. Partial sericitization is prevalent around exsolution textures. Plagioclase forms 1.5-5.6 mm grains, with rare grains up to 12 mm, which are strongly sericitized. Boundaries with K-feldspar are irregular, with myrmekitic plagioclase, sericite, and quartz (Figure 2.27a-b).

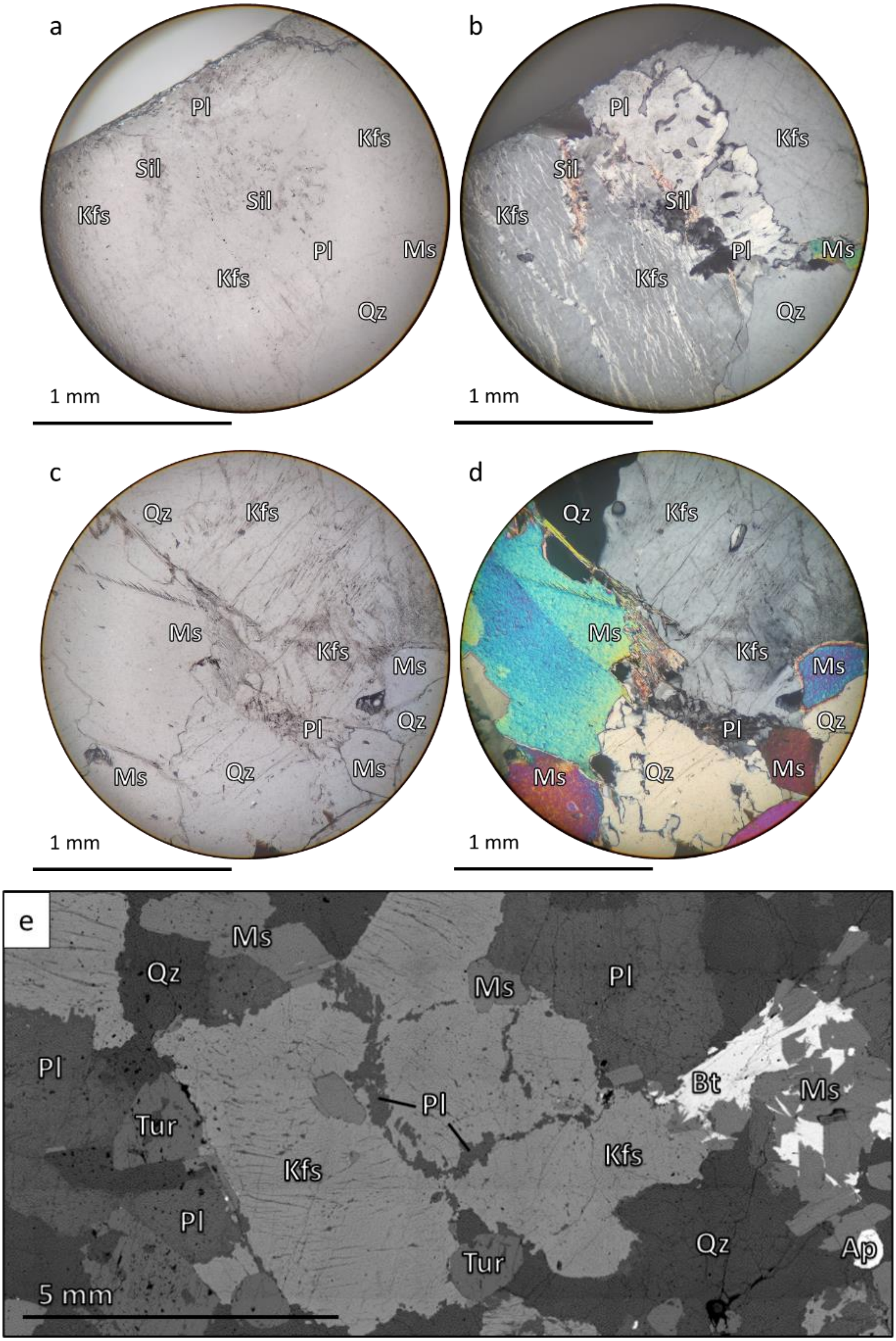

Figure 2.27 – Photomicrographs and BSE image of various mineral textures in sample f04. a) Myrmekitic plagioclase between perthitic K-feldspar (PPL). b) Myrmekitic plagioclase between perthitic K-feldspar (XPL). c) Muscovite with sericite and irregular grain boundaries with K-feldspar (PPL). d) Muscovite with sericite and irregular grain boundaries with K-feldspar (XPL). e) BSE image of K-feldspar porphyroblasts (light grey) and irregular plagioclase inclusions.

Muscovite is present either as fine laths, typically 0.6 mm across, interlocking with biotite in the strands of schlieren, or as subhedral medium grains, 0.9-2.9 mm across. Muscovite grain boundaries with K-feldspar are irregular, with interstitial sericite common (Figure 2.27c-d). Biotite only occurs as fine-medium grains, 0.4-2.5 mm across, in the schlieren, with irregular schlieren-external boundaries. Sillimanite is also only present in the schlieren as remnants of fibrolite clots within fine-grained muscovite. Tourmaline forms euhedral prismatic grains, 1.0-3.2 mm across in cross-section, that are strongly pleochroic with blue-green cores (not always present) and olive-green rims.

2.4.3.5 Float Locality B

Sampling locality B is 0.3 km southeast of locality 04, 3.6 km west of Badrinath (30.74233°N, 79.45197°E) (Figure 2.1). Here, float samples were collected from an alluvial fan at the base of a steep gully on the valley's north cliff face. As such, the catchment of these samples is well-constrained.

Sample f13 is a medium-grained schollen diatexite with a coarse-grained leucosome. The schollen mesosome consists of quartz + plagioclase + muscovite + biotite + K-feldspar, while the leucosome consists of quartz + plagioclase + K-felspar + tourmaline + muscovite (Figure 2.28). Apatite, zircon, and monazite are present as accessory phases in both domains. Biotite is rarely chloritized but constrained to the edges of grains where present. Quartz grains show undulose extinction throughout the sample.

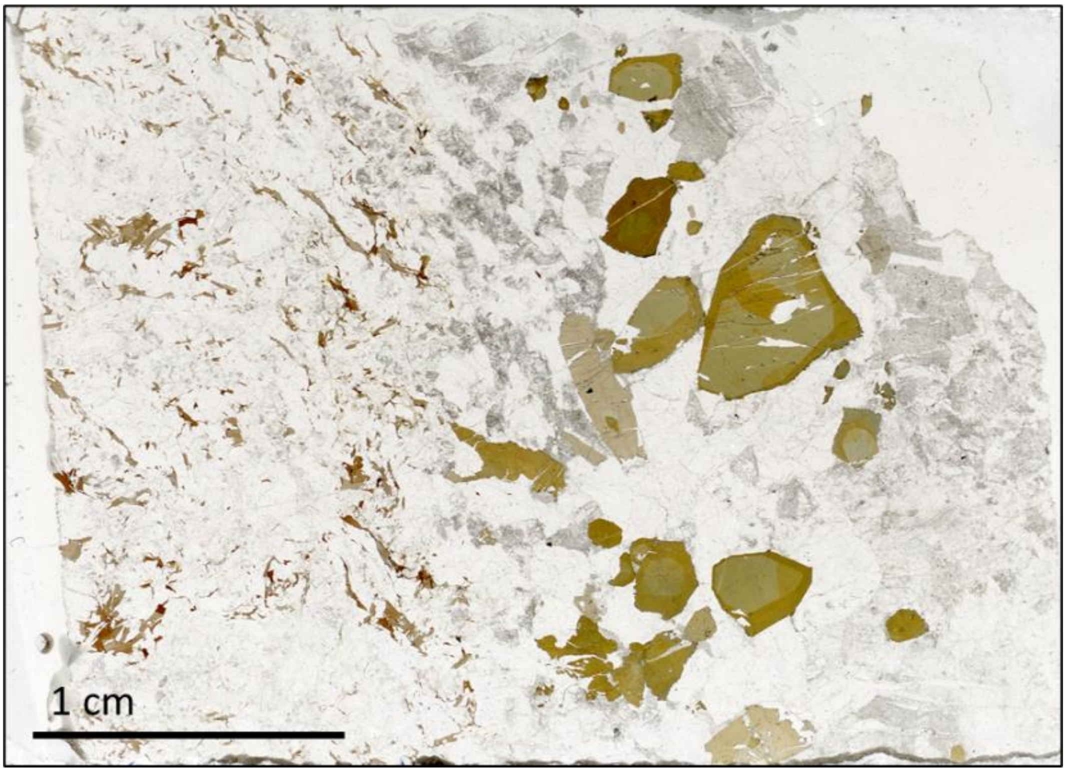

Figure 2.28 – Thin section image of migmatite sample f13, displaying medium-grained mesosome with biotite (left) and coarse-grained leucosome with pleochroic tourmaline (right).

In the leucosome, K-feldspar is present either as irregular strongly sericitized grains, 0.6-1.0 mm across, with crosshatch twinning and perthitic albite exsolution or as coarser 3.8-6.0 mm perthitic porphyroblasts with poikiloblastic quartz, muscovite with quartz films, and plagioclase inclusions (Figure 2.29a-b). Coarse perthite grains show partial sericitization, with myrmekitic plagioclase and sericitized muscovite along grain boundaries. Plagioclase forms 0.8-1.4 mm grains close to the mesosome-leucosome transition and sub-euhedral 2.0-6.6 mm grains further within the leucosome. Both display albite twinning and are strongly sericitized. In the mesosome, K-feldspar grains, 0.6-1.1 mm across, form irregular clusters with plagioclase and quartz up to 3.5 mm wide. Grains are partially sericitized, and myrmekitic plagioclase is common along grain boundaries. Plagioclase grains are typically 1 mm across, with albite twinning and partial sericitization.

Muscovite forms 0.8-4.0 mm laths in the leucosome, with irregular grain boundaries along plagioclase and K-feldspar, as well as sericite clots up to 3.5 mm long and 1 mm wide (Figure 2.29c-d). In the mesosome, muscovite laths are typically smaller, 0.6-1.9 mm across, also with irregular and sericitized grain boundaries with feldspars, and form sericite strands up to 4.2 mm long and <200 µm wide. Biotite is only present in the mesosome, with 0.3-0.8 mm laths with increasingly irregular grain boundaries towards the mesosome-leucosome transition. Tourmaline is present only in the leucosome, with widely variable prismatic grain sizes from 0.4 to 5.8 mm in cross-section, strong pleochroism, blue-green coloured cores and brown-green rims. Larger grains show further zoned colouration with an additional blue-green to brown-green rim overgrowth.

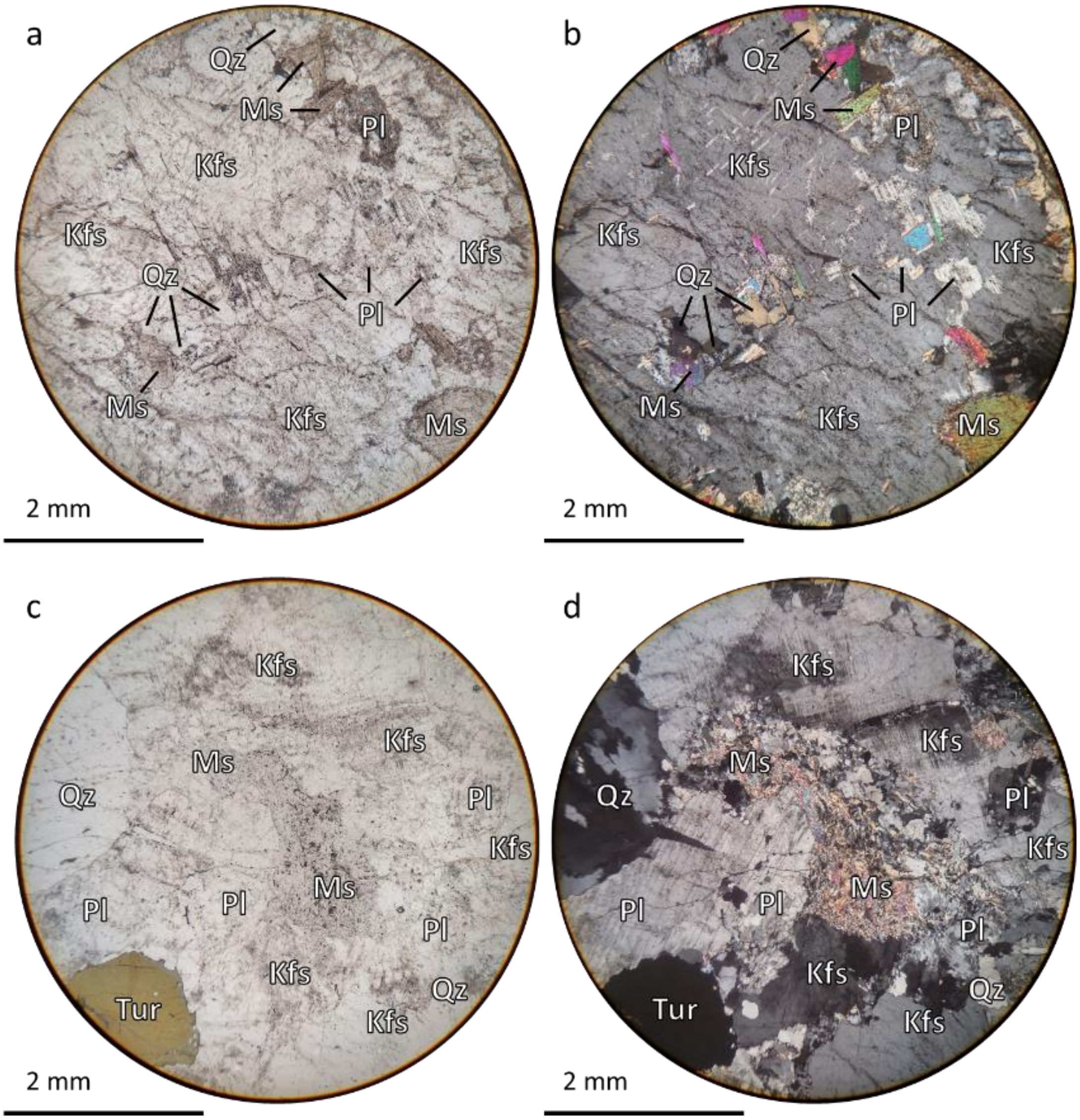

Figure 2.29 – Photomicrographs of feldspar and sericite textures in sample f13. a) Poikiloblastic K-feldspar, with inclusions of quartz, plagioclase, and muscovite with quartz films (PPL). b) Poikiloblastic K-feldspar, with inclusions of quartz, plagioclase, and muscovite with quartz films (XPL). c) Sericite clot between feldspar grains in the leucosome (PPL). d) Sericite clot between feldspar grains in the leucosome (XPL).

2.4.4 Mana – Alaknanda

Sampling localities in the Alaknanda valley, west of Mana, are a mixture of *in situ* and float; however, samples from float localities D and E were not used in this study. Samples retrieved *in situ* are from the cliff face along the northern side of the valley. Outcrops along the northern cliff section are migmatites and leucogranites, as well as minor calc-silicate units. The prevalence of leucogranite and the proportion of leucosome in migmatites increases at higher altitudes.

2.4.4.1 Locality 05

Sampling locality 05 is 0.5 km west of Mana (30.77444°N, 79.48951°E) (Figure 2.1). The exposure is a ~10 m wide alcove in the cliff face with surface mineralisation, beneath which is a strongly layered migmatite with alternating leucosome and mesosome bands 1-3 cm wide (Figure 2.30).

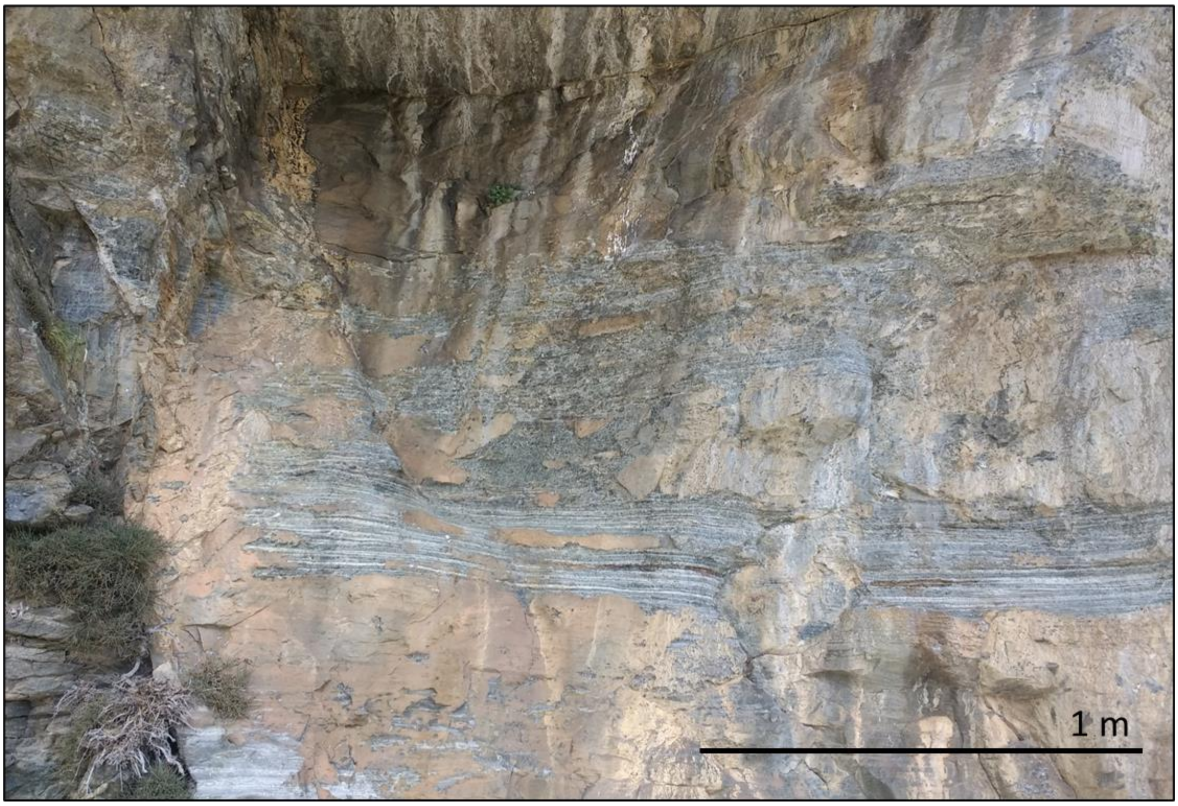

Figure 2.30 – Locality 05 (30.77444°N, 79.48951°E). Sampled strongly layered migmatite with alternative leucosomes and melanosomes. Surface mineralisation obscures most of the underlying migmatite.

Sample 05b is an *in-situ* medium-grained melanocratic migmatite sampled from the layered migmatites at locality 05. This sample comprises quartz + plagioclase + biotite + muscovite + K-feldspar + tourmaline + sillimanite, with apatite, ilmenite, zircon, and monazite present as accessory phases. K-feldspar, muscovite, tourmaline, and sillimanite are concentrated in the 1 cm wide leucosome domain, with less biotite. Biotite grains within the leucosome are strongly chloritized. Quartz grains show undulose extinction throughout the sample.

K-feldspar grains are 0.5-1.2 mm across and only present in leucosomes, with extensive muscovite alteration (Figure 2.31a-b). The remaining grains show either continuous extinction or crosshatch twinning, as well as irregular boundaries with plagioclase and partial sericitization. In the leucosome, plagioclase forms grains 0.5-1.2 mm across which are strongly sericitized with complex boundaries with K-feldspar and is also present as inclusions in muscovite-altered K-feldspar. Outside of the leucosome, plagioclase is typically coarser, 0.6-1.5 mm, with albite twinning and sericite alteration.

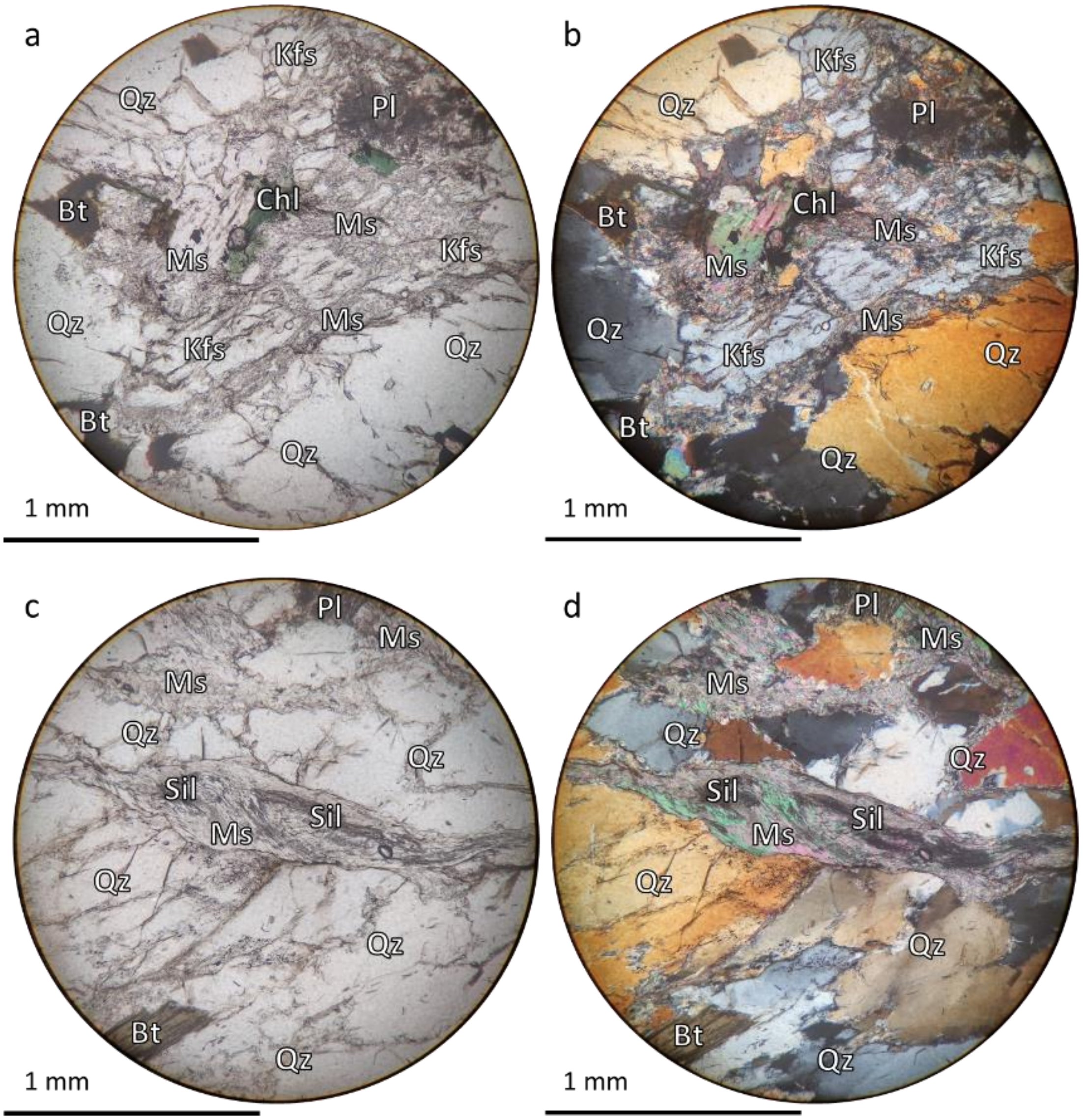

Figure 2.31 – Photomicrographs of various mineral textures in sample 05b. a) K-feldspar grain with extensive sericite alteration and replacement by muscovite (PPL). b) K-feldspar grain with extensive sericite alteration and replacement by muscovite (XPL). c) Sillimanite clot with sericite alteration (PPL). d) Sillimanite clot with sericite alteration (XPL).

Biotite forms fine laths, 0.2-0.8 mm long, with the small grains concentrated in and around the leucosome. Grains in the meso-melanosome are regular and form thin phyllosilicate domains. Muscovite in the leucosome forms either grains 0.7-1.1 mm across, or sericite clots with sillimanite, where it is up to 6 mm long and 300 µm wide (Figure 2.31c-d). Small muscovite grains are also present in biotite-rich areas in the meso-melanosome. Tourmaline is only present in the leucosome, with widely variable prismatic grain sizes, 0.5-2.8 mm in cross-section, strong pleochroism and blue-green colouration.

2.4.4.2 Locality 06

Sampling locality 06 is 0.8 km west of Mana (30.77517°N, 79.48624°E) (Figure 2.1). Samples were taken from 1-2 m diameter scree boulders directly downhill from a leucocratic scarp in the cliff to the north. The boulders are garnet-tourmaline leucogranite with sub-parallel tourmaline-rich horizons up to 0.5 cm wide and garnets with core-rim zoning, 1-8 mm in diameter (Figure 2.32).

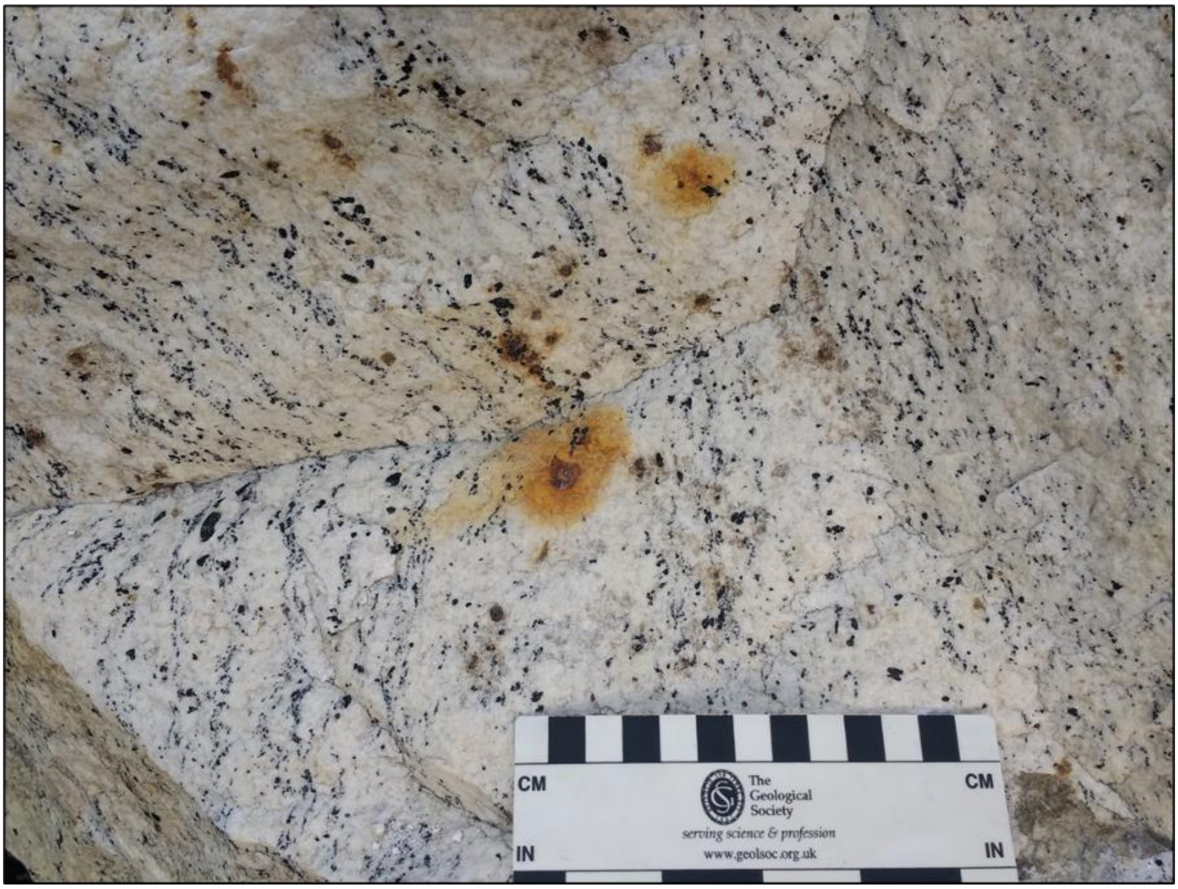

Figure 2.32 – Locality 06 (30.77517°N, 79.48624°E). Sampled boulder of garnet-tourmaline leucogranite, with sub-parallel tourmaline horizons and surface alteration halos around larger garnet grains.

Sample 06 is a medium-grained leucogranite taken from a boulder at locality 06, with garnet abundances and tourmaline-rich layers that are typical for the locality. The granite consists of plagioclase + quartz + K-feldspar + tourmaline + garnet, with minor muscovite (Figure 2.33). Zircon and monazite are present as accessory phases.

K-feldspar forms grains 1.2-2.4 mm across, rarely up to 6 mm, with perthite and crosshatch twinning both present. The larger grains are euhedral with quartz, plagioclase, and muscovite/sericite inclusions and full perthitic albite exsolution lamellae (Figure 2.34a-b). Plagioclase forms grains 0.9-

2.3 mm across with albite twinning common and as well as inclusion-poor grains up to 4.7 mm across with albite and simple twins. Myrmekitic plagioclase is common along boundaries with K-feldspar.

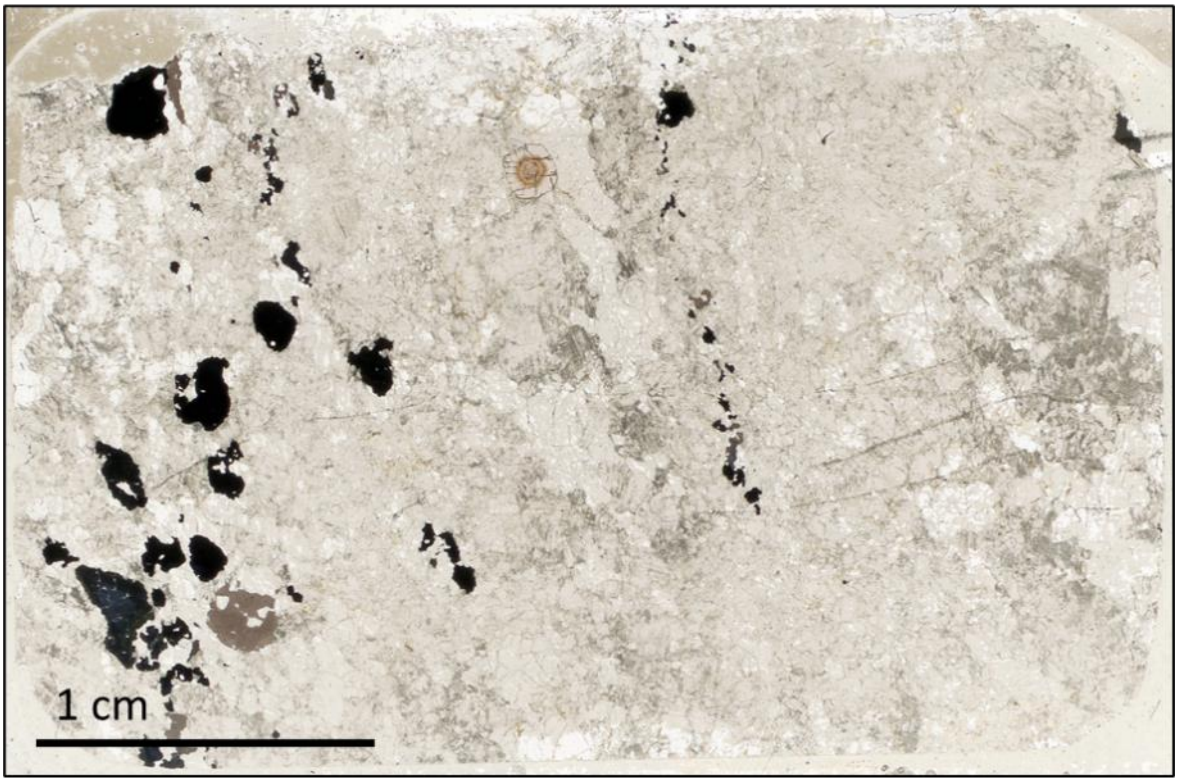

Figure 2.33 – Thin section image of leucogranite sample 06, displaying zoned pleochroic tourmaline (left) and euhedral garnet grain (centre-top).

Muscovite is present as a few small grains, 0.2-0.4 mm long, or as sericitized microporous vein perthite associated with particularly large K-feldspar grains. Tourmaline forms prismatic grains typically 0.4-1 mm in diameter in section and up to 3 mm in diameter and 10 mm long in hand specimen. These grains are strongly pleochroic with blue cores, dark blue rims, and a grey border (Figure 2.34c-d).

Garnets form sub- to euhedral grains, 2-8 mm in diameter, but typically 3-4 mm. There is distinct core-rim zoning, with orange-coloured cores and pale pink rims. Along core-rim boundaries is a zone of crystallographically oriented rutile needles, starting just inside the core region and extending to <100 µm into the rim (Figure 2.34e-f). The rims are typically inclusion poor, but some grains show irregular lobate quartz. BSE imaging of these garnets, isolated in resin mounts, reveals the cores to be rich in fine, randomly-oriented inculsions typically <10 µm in diameter (Figure 2.34g).

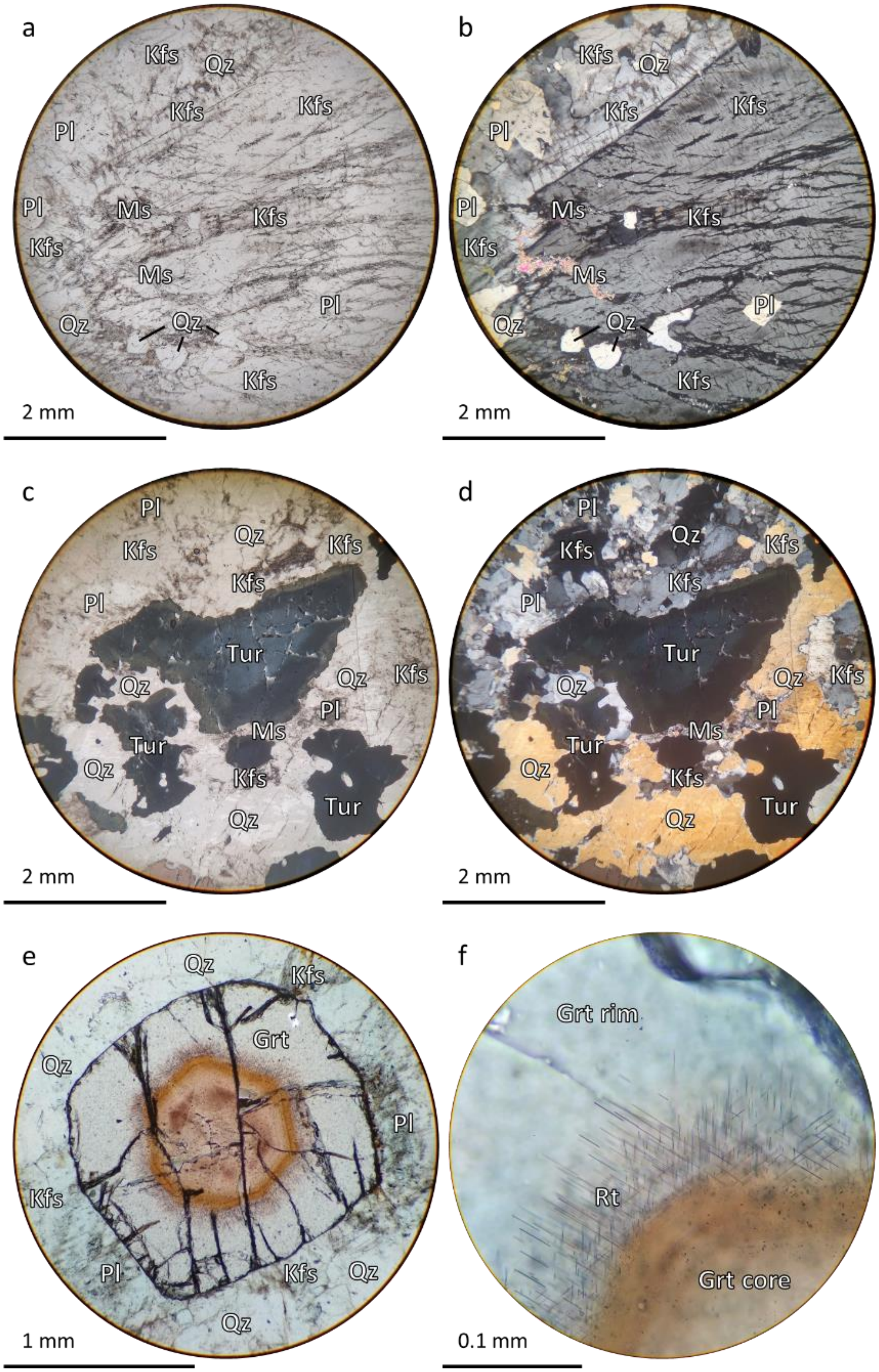

Figure 2.34 – Photomicrographs and BSE image of various mineral textures in sample 06. a) Coarse-grained euhedral K-feldspar with perthitic albite (PPL). b) Coarse-grained euhedral K-feldspar with perthitic albite (XPL). c) Coarse-grained tourmaline with core-rim zoning (PPL). d) Coarse-grained tourmaline with core-rim zoning (XPL). e) Euhedral garnet with distinct core (orange) and rim (PPL). f) Crystallographically oriented rutile needles at garnet core-rim boundary (PPL).

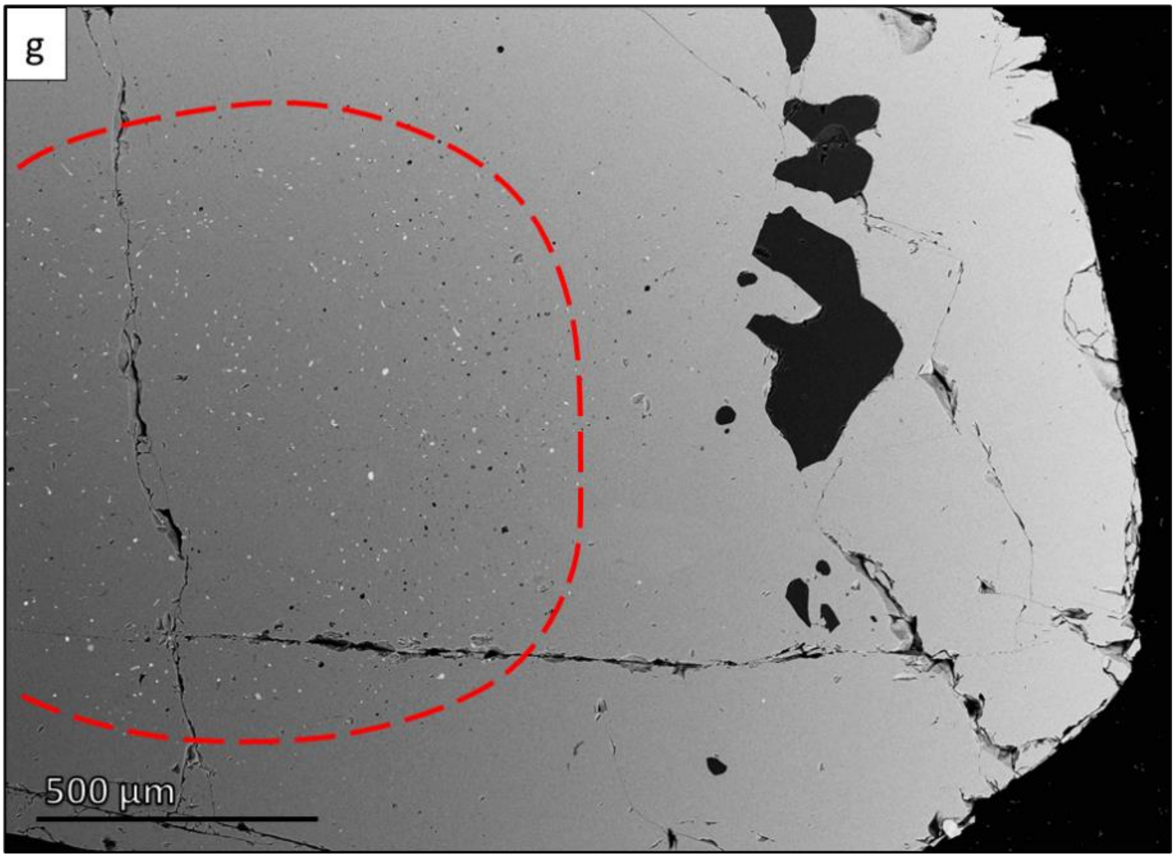

Figure 2.34 cont. – g) BSE image of a separated garnet grain in resin, from sample 06, with a core rich in randomly oriented micro-inclusions and irregular oblate quartz in the rim.

2.4.4.3 Locality 07

Sampling locality 07 is 1.8 km west-northwest of Mana (30.78055°N, 79.47762°E) (Figure 2.1). The locality is centred on a 2.5-3.0 m wide leucocratic dyke exposed at the base of the cliff on the north side of the Alaknanda valley. This exposure features diatexites crosscut by a leucogranite dyke and associated disseminated dykelets that vary in size down to the centimetre scale, where they become indistinguishable from migmatite leucosomes (Figure 2.35). Similar crosscutting leucocratic features are present higher up the face of the cliff.

Figure 2.35 – Locality 07 (30.78055°N, 79.47762°E). Sampled outcrop with central leucocratic dyke (inset – yellow) and disseminated dykelets (inset – blue), cross-cutting the host migmatite.

Sample 07a is a medium-grained *in-situ* schlieren diatexite sampled from the crosscut migmatite, proximal to centimetre-scale dykelets, consisting of quartz + plagioclase + K-feldspar + biotite + muscovite + sillimanite. Apatite, zircon, and rutile are present as accessory phases. Phyllosilicate bands with sillimanite define schlieren that breaks up the feldspar-dominated leucosome (Figure 2.36). Biotite is variably chloritized, with grains within the leucosomes showing greater alteration. Quartz grains show undulose extinction throughout the sample.

K-feldspar grains are typically 1.1-1.4 mm across with crosshatch twinning or perthite albite lamellae. Coarser grains, up to 2.5 mm in length, having microporous vein perthite. These grains form clusters up to 10 mm wide and longer than the width of a thin section with quartz, plagioclase, and muscovite (Figure 2.37a-b & e). Grains are only weakly sericitized, concentrated along perthitic and twinning structures. Plagioclase forms 0.6-1.2 mm grains that are strongly sericitized with albite twinning common. Irregular blebs of plagioclase are present as inclusions in K-feldspar in the clusters, with myrmekitic grains around the edges of the clusters. Plagioclase is more abundant away from these features.

Biotite forms 0.4-1.0 mm laths in phyllosilicate-rich schlieren and biotite-sillimanite selvedges along the edges of the K-feldspar clusters (Figure 2.37c-d). Chlorite is commonly sagenitic, while biotite is only rarely so. Muscovite as either 0.3-0.6 mm laths interlocking with biotite in schlieren, or as sericite clots with sillimanite, up to 9 mm long and 1.5 mm thick, or as pockmarked grains associated with K-feldspar alteration, up to 0.8 x 1.2 mm. Sillimanite is present as fibrolite in the previously mentioned clots, surrounded by sericite, within biotite-rich selvedges.

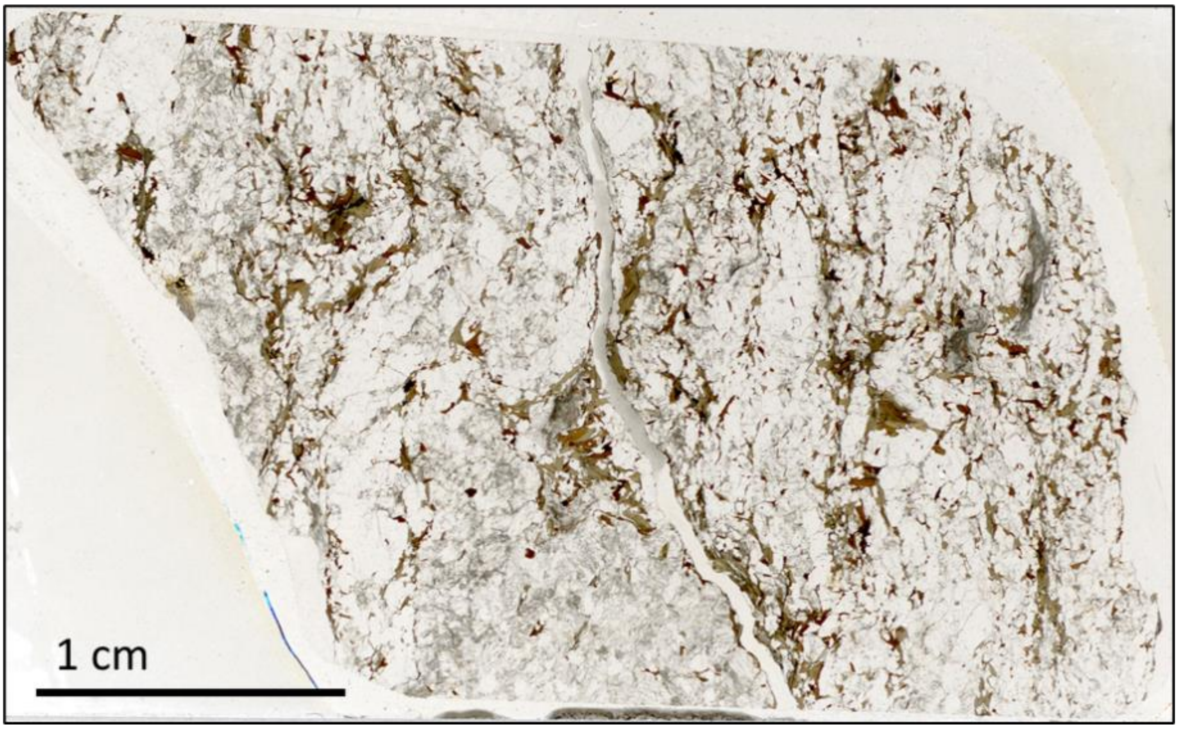

Figure 2.36 – Thin section image of migmatite sample 07a, displaying undulating sillimanite and phyllosilicate-rich layers between leucosomes.

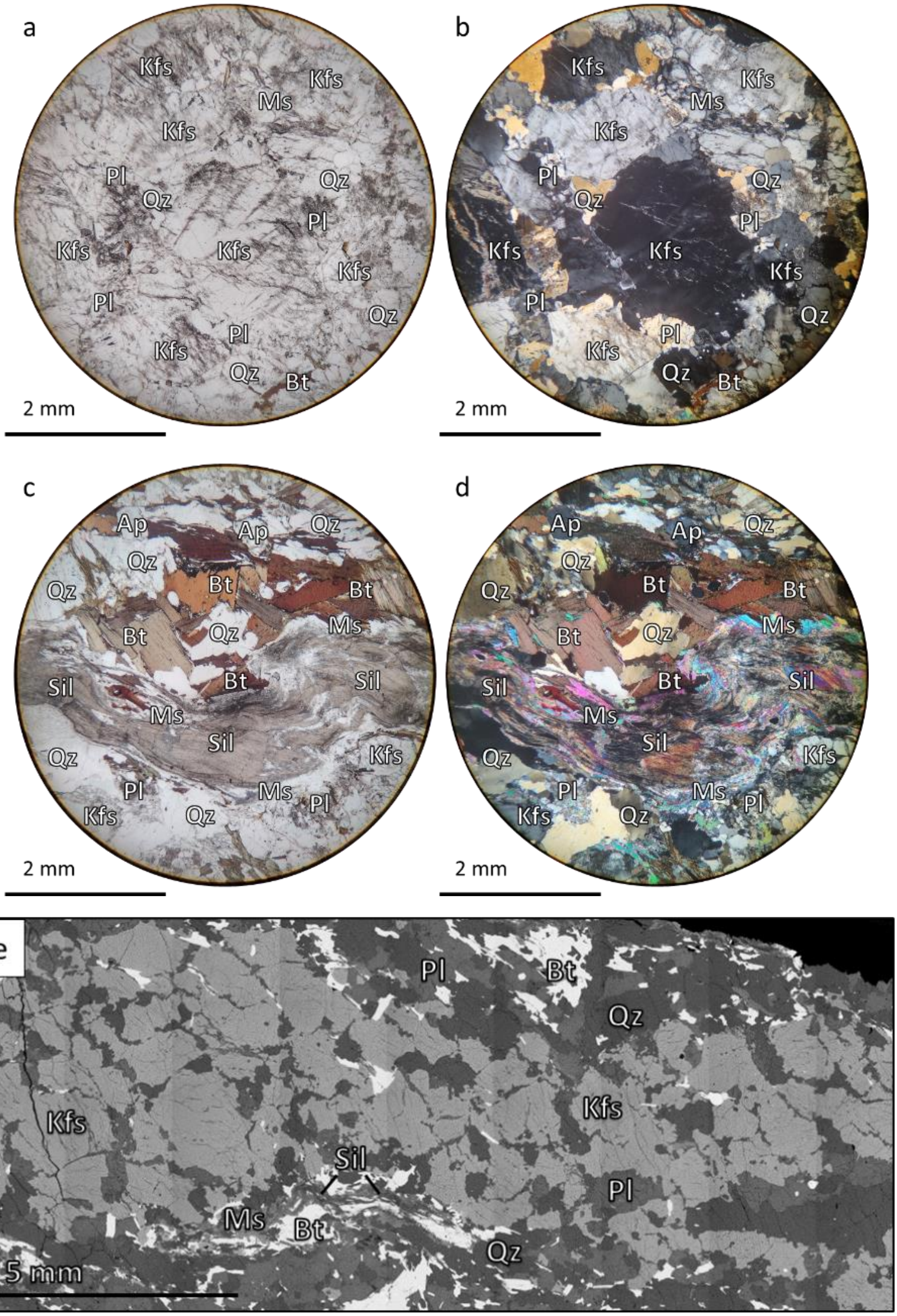

Figure 2.37 – Photomicrographs and BSE image of feldspar and sillimanite textures in sample 07a. a) Clusters of perthitic K-feldspar grains and irregular Pl + Qz + Ms (PPL). b) Clusters of perthitic K-feldspar grains and irregular Pl + Qz + Ms (XPL). c) Fibrolitic sillimanite and biotite selvedge along the edge of a K-feldspar cluster (PPL). d) Fibrolitic sillimanite and biotite selvedge along the edge of a K-feldspar cluster (XPL). e) BSE image of a lenticular K-feldspar cluster, >2 cm across, with sillimanite-biotite selvedge along its lower boundary.

Sample 07b is an *in-situ* medium-grained leucogranite taken from the leucogranite dyke. It contains K-feldspar + quartz + plagioclase + biotite + muscovite + tourmaline, with minor sillimanite. Apatite, zircon, monazite, and rutile are present as accessory phases. Biotite is partially chloritized, with ~20% of grains affected. Quartz grains show undulose extinction throughout the sample.

K-feldspar forms subhedral rectangular laths, 0.9-3.1 mm, with perthitic albite exsolution lamellae and crosshatch twinning common. Some grains form microporous vein perthite. Larger grains have inclusions of plagioclase, quartz, and muscovite (Figure 2.38a-b). Partial sericitization is prevalent along albite lamellae and contacts with muscovite and chlorite. Plagioclase grains are 0.9-2.5 mm across, strongly sericitized, and form complex boundaries with K-feldspar with myrmekitic plagioclase grains up to 530 µm across.

Biotite grains are irregular laths, typically 0.7 mm long, dispersed throughout the rock, often interlocking with muscovite. Chloritized grains are commonly sagenitic. Muscovite is present as (i) grains interlocking with biotite, typically 0.6 mm long, (ii) as sericite clots with sillimanite, up to 6.7 mm long and 0.3 mm wide, or (iii) as pockmarked grains, 0.9-1.8 mm across, associated with K-feldspar alteration (Figure 2.38c-d). Tourmaline forms pleochroic grains 0.4-1.5 mm across, that are brown-green in colour with rare blue-green cores. Sillimanite is present as both elongate fibrolite schlieren (Figure 2.38e) and prismatic crystals in the cores of sericite clots. The largest sillimanite grain is 400 x 35 µm.

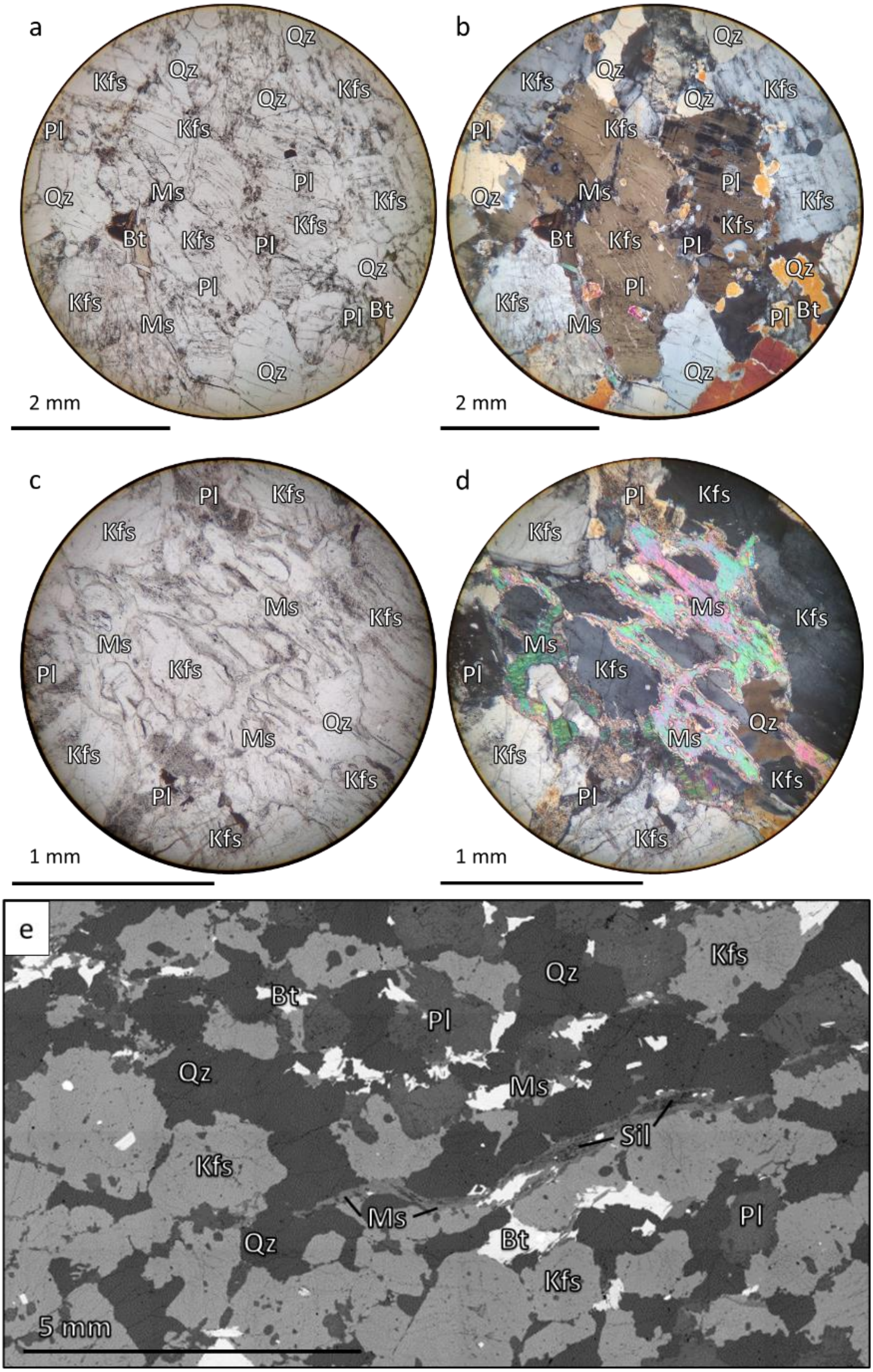

Figure 2.38 – Photomicrographs and BSE image of various mineral textures in sample 07b. a) Coarse-grain perthitic K-feldspar with inclusions of Pl + Qz + Ms (PPL). b) Coarse-grain perthitic K-feldspar with inclusions of Pl + Qz + Ms (XPL). c) Replacement of K-feldspar with muscovite (PPL). d) Replacement of K-feldspar with muscovite (XPL). e) BSE image of sillimanite schliere with sericite alteration.

Sample 07c is a medium-grained *in-situ* diatexite sampled from the crosscut migmatite, distal to centimetre-scale dykelets, consisting of plagioclase + quartz + biotite + sillimanite + K-feldspar + muscovite, with minor garnet. Apatite, zircon, monazite, and rutile are present as accessory phases. Biotite and sillimanite form melanocratic selvedges that line irregular medium- to coarse-grained leucosomes (Figure 2.39). There is only minor chloritization of biotite, predominantly of biotite adjacent to leucosomes. Quartz grains show undulose extinction throughout the sample.

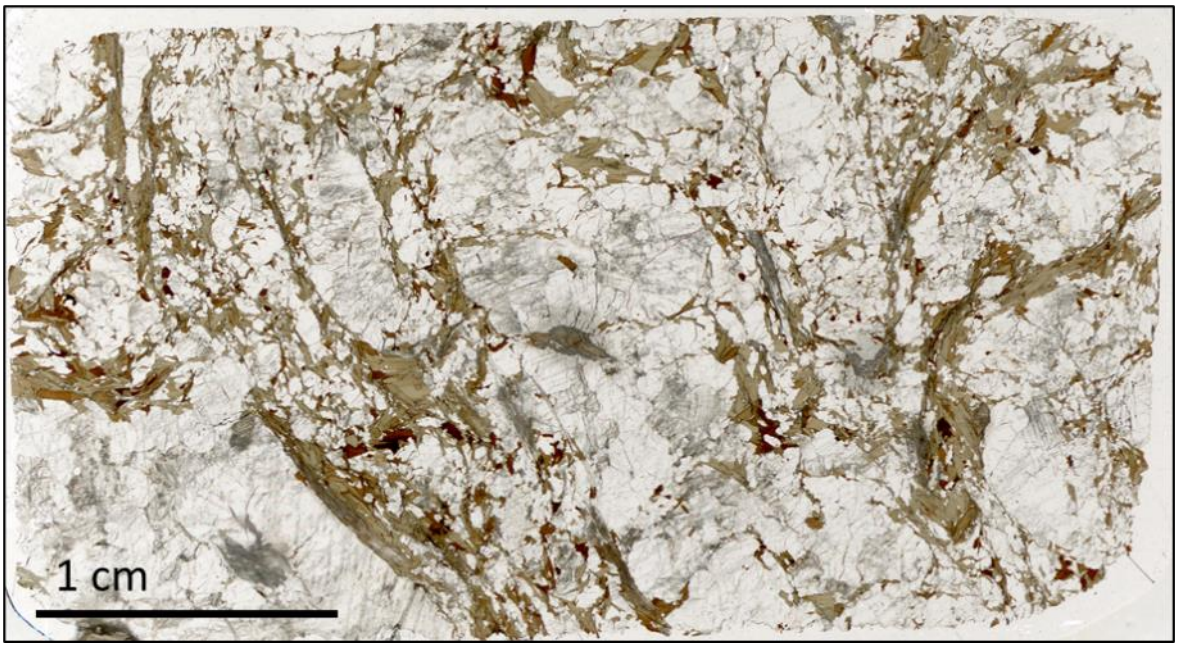

Figure 2.39 – Thin section images of migmatite sample 07c, displaying irregular leucosomes lined with sillimanite and biotite selvedges.

Only a few instances of K-feldspar are present in thin sections as subhedral 0.9-2.8 mm grains in the leucosomes. All grains are inclusion poor, with perthitic albite exsolution lamellae and partial sericitization along these features (Figure 2.40a-b). Plagioclase typically forms 1.1-3.5 mm subhedral grains, although there are also euhedral grains up to 9.2 mm across. Grains have inclusions of quartz, biotite, and sillimanite. Albite twins are common, and smaller grains are strongly sericitized. Myrmekitic plagioclase is present along grain boundaries with K-feldspar.

Biotite is largely absent from the leucosomes, apart from rare small xenocrystic grains, and concentrated in biotite-sillimanite selvedges and adjacent melanosomes. Biotite laths are typically 0.9-1.3 mm long, with sagenitic textures present in partially and fully chloritized grains. Muscovite is present only as <200 µm laths interlocked with biotite and as strong sericite alteration of feldspar. Garnet grains are rare, <300 µm in diameter, fractured and partially resorbed, with biotite and chlorite (Figure 2.40c-d). Sillimanite forms fibrolite clots with biotite and sericite up to 8 mm long (Figure 2.40e).

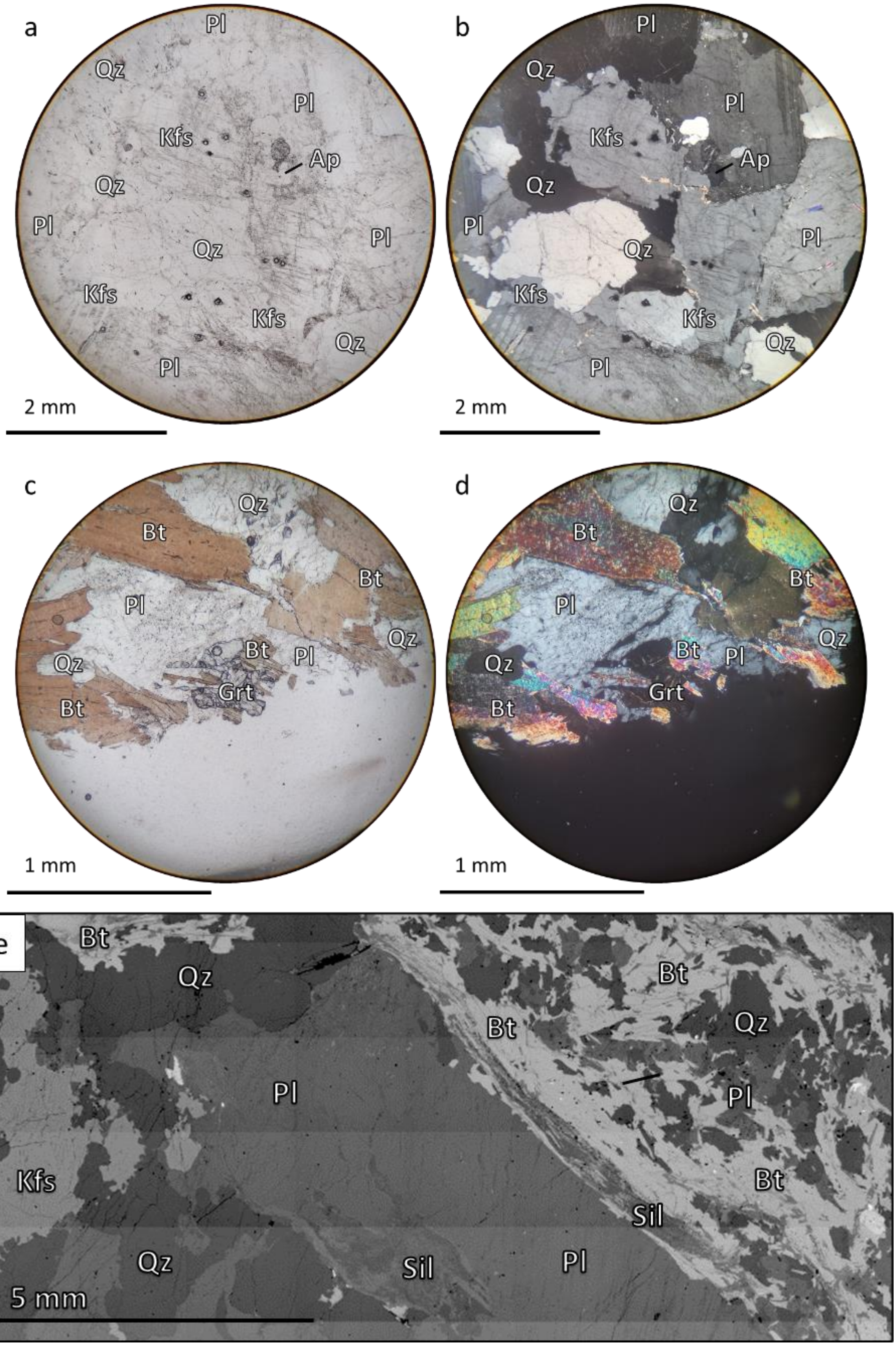

Figure 2.40 – Photomicrographs and BSE image of various mineral textures in sample 07c. a) Inclusion-poor perthitic K-feldspar in the leucosome (PPL). b) Inclusion-poor perthitic K-feldspar in the leucosome (XPL). c) Rare partially-resorbed garnet grain (PPL). d) Rare partially-resorbed garnet grain (XPL). e) Plagioclase phenocryst in a leucosome lined with a sillimanite and biotite selvedge.

2.4.5 Joshimath

2.4.5.1 Locality 11

Sampling locality 11 is to the north of Joshimath, across the Alaknanda River (30.56328°N, 79.56776°E), in the Joshimath Formation of the GHS. Samples were taken from >3 m diameter blocks along a section of road cutting. The blocks are a biotite-rich migmatite with irregular, folded leucosome up to 0.8 cm wide and garnets 2-5 mm in diameter.

Sample 11a is an *in-situ* metatexite from locality 11, with an assemblage of quartz + plagioclase + biotite + muscovite + garnet + tourmaline. Apatite, ilmenite, and zircon are present as accessory phases. The sample largely consists of medium-grained mesosome. Quartzofeldspathic domains, however, form highly irregular coarse-grained leucosomes bound by biotite-dominated phyllosilicate bands. There is little chloritization, and quartz grains show undulose extinction throughout the sample.

In the leucosomes, plagioclase grains are typically 1.2-3.2 mm across, with albite twinning common. Some grains up to 6.8 mm with inclusions of muscovite, quartz, and biotite (Figure 2.41a-b). Plagioclase in the mesosome forms grains 0.6-1.2 mm across, commonly with albite twinning, and is less abundant than in the leucosomes. Plagioclase shows partial sericitization in both domains.

Biotite forms fine irregular laths in the mesosome, typically 0.5-0.8 mm long, while in phyllosilicate domains, it forms medium laths 1.0-1.4 mm long with rare grains >2 mm. Chlorite is associated with sericite alteration and the grain boundaries of garnets. Muscovite grains in the mesosome form fine 0.3-0.9 mm laths with irregular boundaries with quartz and plagioclase. In phyllosilicate domains, muscovite forms 1.3-2.8 mm laths with irregular grain boundaries with leucosome plagioclase. Muscovite is also present towards the edges of leucosomes as rare muscovite/sericite clots between plagioclase grains with an aspect ratio of ~10:1 (Figure 2.41c-d).

Garnet is present in phyllosilicate domains as euhedral, pale pink grains, 2.1-4.5 mm in diameter, with quartz inclusions and atoll textures. Anhedral relict grains are also present in the mesosome, up to 850 x 350 µm, again with quartz inclusions. Tourmaline is also associated with the phyllosilicate domains and forms pleochroic euhedral grains 0.8-3.2 mm in cross-section, with an olive-green colouration.

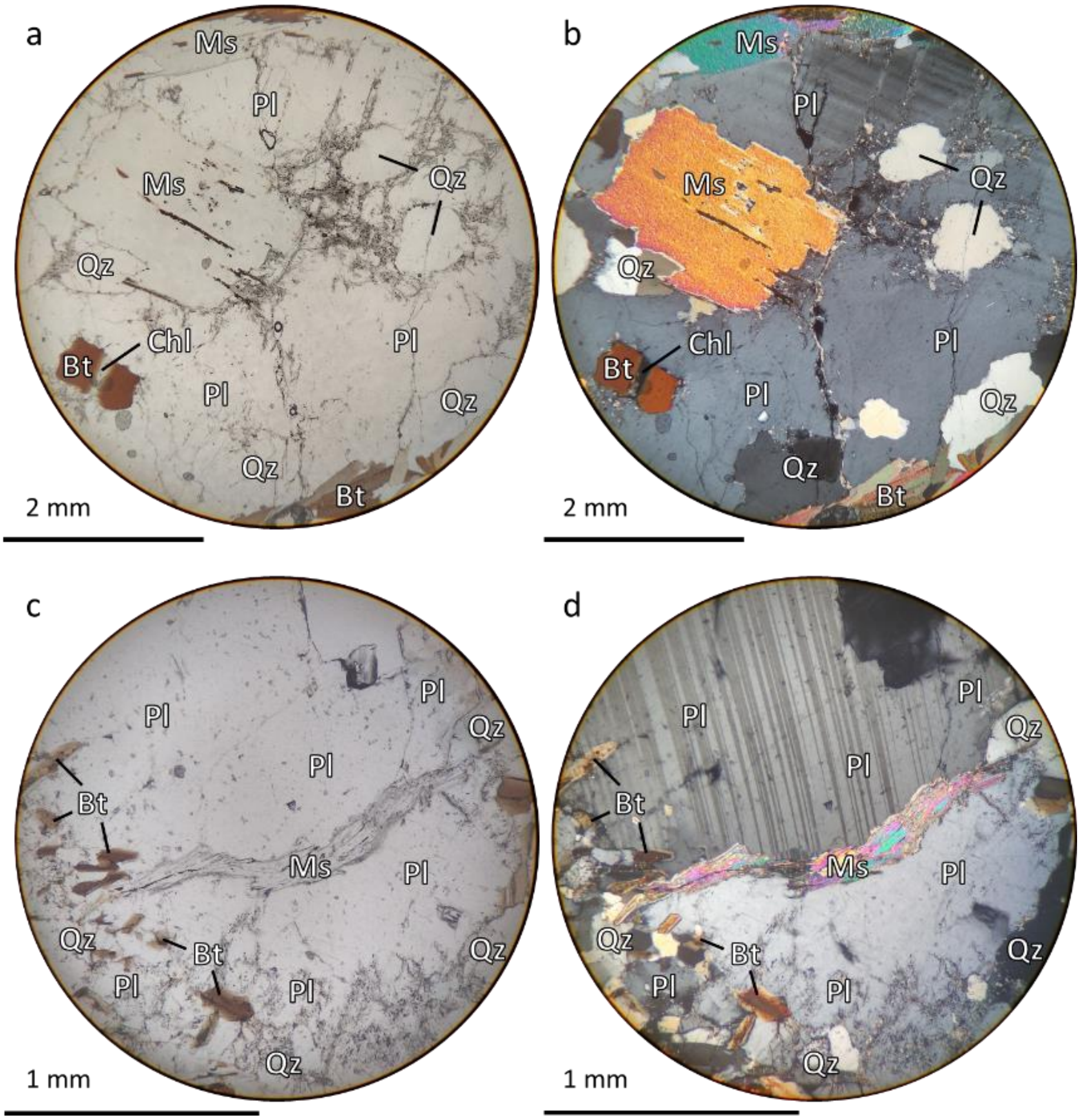

Figure 2.41 – Photomicrographs of plagioclase and muscovite textures in sample 11a. a) Coarse-grained plagioclase in the leucosome, with inclusions of Qz + Ms + Bt (PPL). b) Coarse-grained plagioclase in the leucosome, with inclusions of Qz + Ms + Bt (XPL). c) Muscovite-sericite clot between plagioclase grains in the leucosome (PPL). d) Muscovite-sericite clot between plagioclase grains in the leucosome (XPL).

2.5 Collation of textural observations

For textural purposes, observed sericite clots and schlieren are treated as evidence for former sillimanite. See section 2.6.3 for further details.

2.5.1 Textures in migmatites

2.5.1.1 K-feldspar as a minor component

Migmatite samples 05b, 07c, 08, 09b, and 11a share the common attribute of discrete leucosomes, either as veins or irregular deformed domains, while entirely lacking or having a low modal abundance (≤1%) of K-feldspar. Of these samples where K-feldspar is present, it occurs either only in leucosomes or additionally as fine, isolated grains in phyllosilicate-rich mesosomes.

Sillimanite in these samples varies between 0 and 5% modal abundance, with higher modal percentages associated with larger leucosome domains.

2.5.1.2 K-feldspar clusters and porphyroblasts

Samples 02a, 04a, 04b, 07a, f02, and f13 all have K-feldspar as a major component. K-feldspar is present as porphyroblastic grains >2 mm across in all of these samples (Figures 2.16a, 2.21e, 2.23a-b, 2.25a, 2.29, and 2.37a-b), with perthitic albite lamellae and inclusions of irregular quartz and embayed plagioclase. Four of the samples, 04b, 07a, f02, and f13, also have lenticular clusters of K-feldspar grains in quartzofeldspathic domains with plagioclase either greatly reduced in abundance within these lenses, or present as embayed inclusions (Figures 2.23c-e and 2.37e).

Sillimanite is also present in all of these samples but is texturally variable from low-aspect ratio clots (see sample 07a) in phyllosilicate domains to high-aspect ratio schlieren (see sample 02a) in leucosomes.

2.5.2 Textures in leucogranites

2.5.2.1 K-feldspar porphyroblasts

All leucogranite samples (01d, 02b, 03, 06, 07b, and f04) have K-feldspar grains that are larger than quartz, plagioclase, and K-feldspar grains in the groundmass. These larger grains are perthitic with albite lamellae, sometimes coarsened to vein-perthite, with inclusions of irregular quartz and embayed plagioclase (Figures 2.13a, 2.17, 2.27, 2.34a-b, and 2.38). These are largely indistinguishable from the porphyroblastic grains identified in many of the migmatite samples. As such, these grains are assumed to be at least partially inherited porphyroblasts, rather than igneous phenocrysts.

2.5.2.2 Sillimanite

Sillimanite is present in three of the six leucogranite samples as fibrolite (07b & f04) or sericite (01d) schlieren. Sample 07b also has a few prismatic sillimanite grains within fibrolite schlieren. The remaining three leucogranite samples (02b, 03, and 06) do not contain sillimanite, however, sample 02b is very closely associated with migmatite 02a, which does include sillimanite in its assemblage.

2.5.2.3 Garnet

Only two leucogranite samples contain garnet. Sample 01d garnets are elongate with fractures perpendicular to their length and a diverse population of inclusions, typically smaller than 50 µm, that run along the centre of the grains (Figure 2.13d). Also present are lobate quartz inclusions, which are randomly distributed throughout the grains. Sample 06 garnets are sub- to euhedral with strongly developed core-rim zoning. Cores appear orange in PPL and are rich in randomly oriented inclusions <10 µm in diameter, while the core-rim transition hosts crystallographically oriented rutile needles up to 100 µm in length (Figure 2.34e-g). Rims contain lobate quartz but are otherwise inclusion poor.

2.5.3 Textures in orthogneisses

The two orthogneiss samples (10 & f03) share broad textural features, such as strongly developed augen quartzofeldspathic domains broken-up by sillimanite-phyllosilicate domains. K-feldspar textures differ significantly, however, with sample 10 only containing a few isolated tabular grains, <800 µm long, and irregular tabs within antiperthitic plagioclase (Figure 2.9b), while sample f03 contains regular medium-grained K-feldspar (Figure 2.26). Sample f03 does not show K-feldspar clustering or porphyroblast growth with embayed plagioclase that is present in K-feldspar-rich migmatite samples. Both samples contain sillimanite as a major component, but sample 10 also contains kyanite (Figure 2.10).

2.6 Discussion

2.6.1 Evidence for different melt reactions

2.6.1.1 Fluid-present melting

Migmatite samples without peritectic K-feldspar are interpreted to have melted under fluid-present conditions by reaction 1 (Patiño Douce and Harris, 1998):

Fluid-present melting $$\text{Ms} + \text{Qz} + \text{Pl} + H_2O = \text{Als} + \text{Melt} \tag{1}$$

Migmatite samples identified in section 2.5.1.1 (samples 05b, 07c, 08, 09b, and 11a) either lack K-feldspar or contain it as a minor component with insufficient textural evidence to describe the grains as peritectic. The modal abundance of K-feldspar in these samples is also too low relative to the volume of leucosome present to satisfy the stoichiometric ratio of peritectic K-feldspar to melt (4:5) (Dyck et al., 2020).

2.6.1.2 Ms-dehydration melting

Migmatite and leucogranite samples with peritectic K-feldspar, and no peritectic garnet, are interpreted to have melted and formed under fluid-absent conditions by Ms-dehydration melting (reaction 2) (Gardien et al., 1995; Patiño Douce and Harris, 1998; Pickering and Johnston, 1998):

Ms-dehydration melting $$\text{Ms} + \text{Qz} + \text{Pl} = \text{Kfs} + \text{Als} + \text{Melt} \tag{2}$$

Migmatite samples identified in section 2.5.1.2 (samples 02a, 04a, 04b, 07a, f02, and f13) contain K-feldspar with identified peritectic features. These textures develop and grow in abundance with increasing melt production as described by Dyck et al. (2020) and are summarised in Figure 2.42.

The first appearance of K-feldspar during Ms-dehydration melting is along Pl-Pl and Pl-Qz boundaries, with preferred nucleation of K-feldspar on plagioclase in quartzofeldspathic domains. The relationship between the plagioclase grain and K-feldspar replacement is topotactic, with epitaxial K-feldspar nucleation (Dyck et al., 2020) and alkali ion exchange on the existing feldspar structure. Sample 04a displays topotactic replacement of plagioclase by K-feldspar.

Continued melt production preserves textures of K-feldspar growth in quartzofeldspathic domains, with plagioclase grains being selectively replaced by K-feldspar in the matrix (Dyck et al., 2020). This produces areas of K-feldspar clusters which exclude or partially exclude plagioclase grains. The peritectic grains continue to grow and clusters anneal (Erdmann et al., 2012) to form poikiloblasts with common inclusions of quartz and biotite (Dyck et al., 2020), as well as irregular embayed plagioclase. These clustered and annealed K-feldspar textures are present in sample 04b, 07a, f02, and f13.

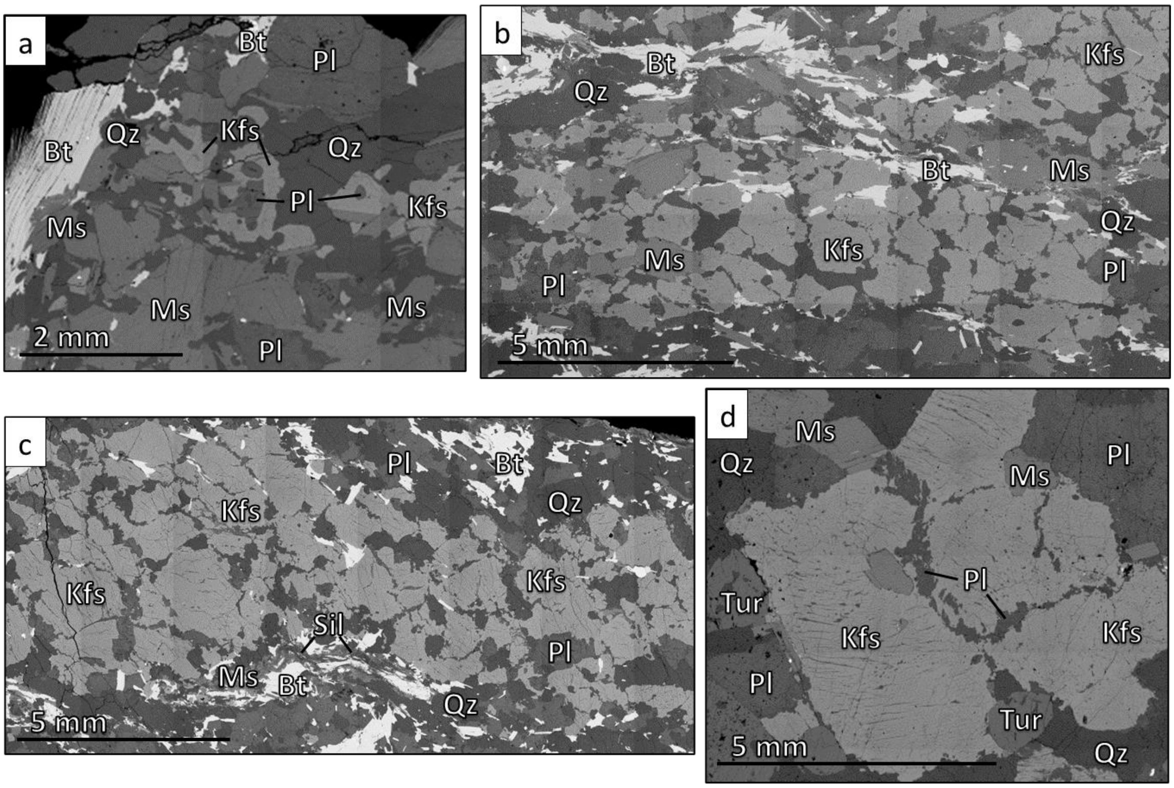

Figure 2.42 – BSE images of the textural evolution of peritectic K-feldspar during Ms-dehydration melting. a) Topotactic replacement of plagioclase with K-feldspar. b) Continued replacement of plagioclase, forming clusters of K-feldspar in the mesosome. c) K-feldspar grains in clusters anneal, forming poikiloblasts. d) Enhanced melt connectivity coarsens K-feldspar grains, forming porphyroblasts in the leucosome.

Further melting coarsens K-feldspar grains to form porphyroblasts, often with poikiloblastic cores, between 2-20 mm across (Dyck et al., 2020). K-feldspar porphyroblasts, most commonly present in leucosomes, are found in samples 02a, 04a, 04b, 07a, f02, and f13.

Sillimanite formed during Ms-dehydration melting is found either in phyllosilicate domains with relatively low aspect ratios (~5:1), described as clots and selvedges, or in leucosomes as schlieren with relatively high aspect ratios (>20:1) (Dyck et al., 2020).

Leucogranites may inherit peritectic K-feldspar and sillimanite from associated disaggregating migmatites and leucosome during melt amalgamation and migration (Brown, 2013). Leucogranite samples 01d, 02b, 03, 07b, and f04 feature K-feldspar grains that fit the interpretation of peritectic porphyroblasts with the growth of additional K-feldspar, generally of smaller grain size in the matrix, indicative of later melt crystallisation (Dyck et al., 2020). Sample 01d and 07b also have inherited high-aspect ratio sillimanite schlieren, with coarsened sillimanite forming prismatic grains in sample 07b.

2.6.1.3 Bt-dehydration melting

Samples with K-feldspar and garnet identified as peritectic are interpreted to have formed under fluid-absent conditions by Bt-dehydration melting (reaction 3) (Breton and Thompson, 1988; Harris et al., 1995):

Bt-dehydration melting Bt + Als + Qz + Pl = Kfs + Grt + Ilm + Melt (3)

Leucogranite 06 is the only sample that meets these criteria, with porphyroblastic K-feldspar grains, petrographically identical to those identified as peritectic in Ms-dehydration melting (section 2.6.1.2), and garnet with cores rich in very fine, randomly oriented inclusions (Dorais and Campbell, 2022; Dorais and Spencer, 2014; Taylor and Stevens, 2010). Garnets in leucogranite 01d do not display this texture. Lobate quartz inclusions in the rims of sample 06, and sporadically throughout garnets in sample 01d, suggest later igneous garnet crystallisation (Jung et al., 2022; Taylor and Stevens, 2010).

2.6.2 Evidence for melt proportions in migmatites

Sequential K-feldspar textures formed during Ms-dehydration melting can be linked to the relative volume of melt produced (Dyck et al., 2020). The first appearance of K-feldspar along Pl-Pl and Pl-Qz grain boundaries and the topotactic replacement of plagioclase occurs alongside low melt volumes, approximately 1-3% (Dyck et al., 2020). The formation of K-feldspar-rich areas of quartzofeldspathic domains, associated with K-feldspar clusters described here, and the growth of poikiloblastic grains are indicative of melt volumes of ~5-6% (Dyck et al., 2020). In migmatites with ≥8% melt, peritectic K-feldspar grains coarsen to form porphyroblasts due to increased mass transfer potential caused by crossing the liquid percolation threshold of 8% (Dyck et al., 2020; Rosenberg and Handy, 2005; Vigneresse et al., 1996).

Peritectic sillimanite formed during Ms-dehydration melting may also be linked to relative melt volumes. In migmatites below the percolation threshold of 8% melt, peritectic sillimanite forms as fibrolite clots with low aspect ratios (~5:1) in-line with foliation in phyllosilicate domains (Figure 2.37c-d) (Dyck et al., 2020), using mica as a template (Chinner, 1961). These often occur with fine intergrowths of matrix quartz. Where melt is ≥8%, sillimanite is not confined to phyllosilicate domains and may be present as foliation-defining schlieren with high aspect ratios (>20:1). Prismatic sillimanite may also form in fibrolite-rich domains (Dyck et al., 2020); however, this is not observed in the migmatites of this study.

Generated melt volumes beyond >8% have no further peritectic textural indicators, however, the modal abundance of peritectic K-feldspar may be compared to the idealized volume ratio of product phases (K-feldspar, sillimanite, and melt), which remains close to 8:5:10 (Dyck et al., 2020).

The occurrence of multiple different melt-percentage textures and a variety of K-feldspar and sillimanite textures may be indicative of disequilibrium or melting within an open system. Samples 04a and 04b are good examples of open system melt infiltration (conflicting melt volume textures).

For fluid-present melting, no studies have yet linked peritectic sillimanite textures and features to generated melt volumes. The assumption can be made, however, that sillimanite textures indicative of melt volumes greater or lower than the 8% percolation threshold in Ms-dehydration melting can be applied to a system melting under fluid-absent conditions. With this assumption, migmatites 08 and 11a can be attributed melt volumes of <8%, while sample 05b has ≥8%.

2.6.3 Deuteric textures

2.6.3.1 Sericite

Sericitization to some degree is observed in all samples, as widespread degradation of plagioclase and, to a lesser extent, K-feldspars, fine-grained muscovite alteration of fibrolite clots, and as coarser net-veining of K-feldspars to form pockmarked muscovite grains. These are retrograde hydration reaction textures that overprint the peak metamorphic and primary igneous assemblage (Que and Allen, 1996). Fluid released from the crystallisation of local melt, or from elsewhere in the system, may be invoked to facilitate these reactions. The presence of microporous vein perthite offers some constraints on this process, as perthite coarsening and micropore formation occur at temperatures ≤400-450°C (Worden et al., 1990), with later sericitization along these permeable structures.

2.6.3.2 Myrmekite

The formation of myrmekitic plagioclase is considered a metasomatic process occurring at a small scale along mineral intergrain boundaries (Hibbard, 1979). This includes wart and rim textures myrmekites. The process of myrmekitization releases potassium (Hatch et al., 1961), facilitating the formation of muscovite/sericite.

2.6.3.3 Chlorite

The movement of fluids through the upper GHS also causes chloritization, with the pseudomorphing of biotite by chlorite (Parneix et al., 1985). Chlorite minerals do not contain K in their structure; as such, the replacement of K-bearing biotite would also release potassium for sericitization. Biotite and chlorite are also observed with what is inferred to be inclusions of rutile needles, termed sagenite, or sagenitic biotite/chlorite. This texture forms through the precipitation of the Ti-phase during retrograde metamorphism (Shau et al., 1991), with excess Ti previously stable in biotite at peak PT conditions (Henry and Guidotti, 2002).

2.7 Summary

In summary, through detailed petrographic observation of the textures present, both the melt reactions and relative volume of melt produced for each sample have been interpreted. There is evidence for fluid-present, Ms-dehydration, and Bt-dehydration melting reactions havening occurred within the sampling area of the Badrinath Formation of the upper GHS, as *in situ* migmatites and amalgamated leucogranite bodies.

Peritectic K-feldspar and sillimanite textures in migmatite samples are summarised in Table 2.3, alongside estimated modal abundance of these two minerals, melt volume % produced, and melt reaction type.

Table 2.3 – Summary table of Kfs and Sil texture observed in migmatite samples, by latitude in descending order. Approximate modal % of Kfs and Sil are given, alongside textures present, melt% produced and inferred melt reaction.

Sample	**Modal %**		**Peritectic Kfs Textures**			**Sil Textures**		**Melt vol% produced**	**Melt Reaction Type**
	Kfs	**Sil**	**Pl replacement**	**Clusters/ poikiloblasts**	**Porphyro-blasts**	**Phyllosilicate domains**	**Schlieren**		
07a	34	4		x	x	x		≥8	Ms-dehydration
07c	2	5					x	≥8	Fluid-present
05b	1	2					x	≥8	Fluid-present
02a	30	4			x		x	≥8	Ms-dehydration
04a	26	3	x		x	x		≥8	Ms-dehydration
04b	28	4		x	x		x	≥8	Ms-dehydration
f13	8	2		x	x	x		≥8	Ms-dehydration
f02	15	2		x	x	x	x	≥8	Ms-dehydration
09b	0	0						?	Fluid-present
08	1	<1				x		<8	Fluid-present
11a	0	1				x		<8	Fluid-present

3 Major phase geochemistry and indicators of melt processes

3.1 Introduction

While the petrographic observation of peritectic products may provide information on previous melt reactions, the geochemical composition of product phases may be used to determine the composition and relative proportion of reactants consumed during melting, as they ultimately determine much of the major and trace element budget available during crystallisation (Harris et al., 1993, 1995). Trace element budgets dominated by accessory phases, e.g. Y, Zr, rare earth elements (REEs) (Brown, 2007), may also be influenced by melt reactions as the availability of accessory phase grains to the melt will vary depending on the breakdown of major phase hosts (Watt et al., 1996).

The large-ion-lithophile elements (LILEs) Rb, Sr, and Ba are of particular interest as melt reaction indicators, as these elements are predominantly hosted by the major phases involved in melt-producing reactions in schists and granites (Harris et al., 1995). Differences in the relative modal consumption of plagioclase, muscovite, and biotite in mica schists during melting result in leucosome or granite Rb/Sr of <2 for fluid-present melting and >5 for dehydration melting due to the varying Rb/Sr of each phase (Harris et al., 1993; Patiño Douce and Harris, 1998). Leucosomes or granite with relatively high concentrations of Ba, as a fluid-mobile element, are considered particularly indicative of fluid-present melting (Patiño Douce and Harris, 1998). Similarly, relatively high bulk concentrations of Ca, Zr, Hf, Th, and the light REEs and lower concentrations of Nb, Ta, and U indicate fluid-present melting (Gao et al., 2017).

Characterisation of major and trace element compositions of K-feldspar, muscovite, biotite, and garnet in migmatite and leucogranite in the studied samples provides further information for refining and interpreting melt reactions. The documentation of geochemical fingerprints may also remove the uncertainty of textural overprinting and provide easier identification of melt reactions in future work. Additionally, the use of major element data in geothermometry will also aid in the construction of P-T-t paths (see Chapter 5).

This chapter links the melt reactions and relative melt volumes interpreted from the petrographic observations, documented in chapter 2, to major and trace element geochemical compositions of feldspars, micas, and garnet. Geochemical characterisation, alongside temperatures calculated using Ti-in-biotite thermometry, provides further evidence for previous interpretations and insight to sample petrogenesis and the nature of regional anatexis.

3.2 Methods

Key samples described in Chapter 2 were further characterised using a combination of low-resolution energy-dispersive X-ray spectroscopy (EDS) maps, EDS point analyses for major elements, and laser ablation inductively coupled plasma mass spectrometry (LA-ICP-MS) spot analyses for trace elements. The primary targets were the major phases (feldspars, mica, and garnet); however, various accessory phases were also identified (apatite, rutile, xenotime, and zircon). Sequential analytical methods applied to each sample are outlined in Table 3.1.

Table 3.1 – Analytical techniques applied to samples discussed in this chapter.

Sample ID	Location	Rock type	EDS guide map	EDS point analysis	LA-ICP-MS spot analysis
BAD01d	Badrinath – Hanuman Chatti	Leucogranite	x	x	x
BAD02a	Rishi Ganga	Migmatite	x	x	
BAD02b	Rishi Ganga	Migmatite/ Leucosome	x	x	
BAD03	Rishi Ganga	Leucogranite	x	x	x
BAD04a	Rishi Ganga	Migmatite	x	x	
BAD04b	Rishi Ganga	Migmatite	x	x	x
BAD05b	Mana – Alaknanda	Migmatite	x		
BAD06	Mana – Alaknanda	Leucogranite	x	x	x
BAD07a	Mana – Alaknanda	Migmatite	x	x	x
BAD07b	Mana – Alaknanda	Leucogranite	x	x	x
BAD07c	Mana – Alaknanda	Migmatite	x	x	x
BAD08	Hanuman Chatti	Migmatite	x	x	
BAD09a	Hanuman Chatti	Meta-arkose	x	x	
BAD09b	Hanuman Chatti	Migmatite	x	x	x
BAD10	Hanuman Chatti	Orthogneiss	x	x	x
BAD11a	Joshimath	Migmatite	x		
BADf02	Rishi Ganga	Migmatite	x	x	x
BADf03	Rishi Ganga	Orthogneiss			
BADf04	Rishi Ganga	Leucogranite	x	x	x
BADf13	Rishi Ganga	Migmatite	x	x	x

Polished thin sections were cut and polished using standard preparation techniques but were left slightly thicker (35-40 µm) to allow for longer ablation periods during LA-ICP-MS analysis. Garnet grains were picked from partially crushed samples at various size fractions to recover intact grains, mounted in resin blocks according to their relative diameter, and polished to target the geographic cores of the grains more accurately. Thin sections and grain mounts were carbon-coated for all SEM imaging and EDS analysis. Before LA-ICP-MS analysis, the carbon coating was removed using diamond paste and isopropyl alcohol.

3.2.1 EDS guide maps

Whole-section EDS chemical maps were collected using a FEI Quanta 200 3D tungsten-filament SEM, fitted with an Oxford Instruments INCA EDS detector, at the Open University. The beam was set to a voltage of 20 keV and a current of 1.2 nA. EDS map sections were then stitched together using the Oxford Instruments INCA software 'Montage' function.

3.2.2 Major element analysis

The oxide weight per cent compositions of major phases in chosen samples were collected by point and line-analysis using a Zeiss Supra 55 VP field-emission SEM fitted with an Oxford Instruments X-Max 50 mm^2 EDS detector at the Open University. All analytical sessions were carried out between November 2021 and March 2022. The beam was set to a voltage of 20 keV and a current equivalent of 2.0 nA (60 µm aperture). Acquisitions were measured for 30 seconds of live-sensor time. EDS results are unnormalized and corrected for detector sensitivity loss using a natural almandine external standard, from the GEO MkII standard block made by P&H Developments ltd for EPMA analyses. This standard has a range of known major and minor element oxide wt% values from 37.17 – 0.20 wt%, allowing for evaluation of precision and accuracy across a wide range of oxide concentrations. Confidence in the precision of values is better than 0.3 oxide wt% (2σ). Full EDS major element data collection, reduction methods, and results can be found in Appendix A.

3.2.3 Trace element analysis

Trace element concentrations were collected by spot analysis using a HelEx II laser ablation cell together with an Agilent 8800 Triple Quadrupole ICP-MS at the Open University. The ICP-MS was tuned using NIST SRM 612 glass prior to each analytical session, which were carried out between June 2021 and April 2022. Spot analyses were run using a fluence of 3.63 J/cm^2, a repetition rate of 10 Hz, and a spot size of 50 µm, with each analysis collecting 30 seconds of background, 30 seconds of sample ablation, and 40 seconds of post-ablation washout. For feldspar analyses in samples 04b, 07c, 09b, and 10, a pre-ablation laser pulse was performed in order to improve laser-sample coupling, followed by a 10-second pause before collecting background measurements. Spots were analysed in batches of twenty, bracketed by two analyses of both 612 and BCR-2G standards.

Analyses were typically collected on a one spot per grain basis, however, in samples with few grains K-feldspar, or large porphyroblasts, multiple spots were collected.

Concentrations of 54 elements were collected to cover a broad range of geological interactions. Data reduction for spot analyses was processed using the Iolite software package for Igor Pro (Paton et al., 2011), with baseline signal subtraction and time-resolved spectra checked for inclusion signals and ablation issues. Only stable signal sections were used for concentration calculations. NIST SRM 612 used as the primary standard and BCR-2G as the secondary standard, excluding Na, Mg, Al, P, K, Ca, Ti, Mn, and Fe, where BCR-2G was used as the primary standard due to higher concentrations of these elements. Si was used as the standardisation element, values were taken from EDS measurements (either directly from the analysis site, or from averages of similar grains for each mineral phase where direct measurement was not possible. Indium concentrations were corrected for ^{115}Sn isobaric interference with the following equation:

$$\mathrm{In_{corrected}\ (ppm) = In_{measured}\ (ppm) - (0.0034*Sn\ (ppm))}$$

Accuracy and precision of BCR-2G analyses were compared to published values (Jenner and O'Neill, 2012) and were found to be in good agreement, with relative standard deviations of 3-5 % Full LA-ICP-MS standards analyses and trace element results can be found in Appendix B.

3.2.4 Thermometry

Major element data collected with both SEM EDS and LA-ICP-MS were used to calculate Ti-in-biotite temperatures using the Wu and Chen (2015) geothermometer:

$$\ln[T(°\mathrm{C})] = 6.313 + 0.224 \ln(X_{Ti}) - 0.288 \ln(X_{Fe}) - 0.449 \ln(X_{Mg}) + 0.15P$$

Where T is the temperature in degrees Celsius, P is the pressure in gigapascals, and Xj is the proportion of cation j in atoms per formula unit (a.p.f.u.), occupying octahedral sites, defined as $Xj = j/(\mathrm{Fe+Mg+Al^{VI}+Ti})$. The calibration can be applied to biotite within the chemical range X_{Fe} = 0.19-0.55, X_{Mg} = 0.23-0.67, and X_{Ti} = 0.02-0.14, on the basis of 11 oxygen per formula unit, and P-T range of 0.1-0.19 GPa and 450-840°C.

This calibration was selected as previous iterations of Ti-in-biotite thermometers were criticised for depending too strongly on the negative correlation between Mg/(Fe+Mg) and Ti with increasing temperature (Chambers and Kohn, 2012). The Wu and Chen (2015) calibration avoids this oversimplification by considering all major cations present in octahedral sites.

Ti-in-biotite thermometry results for EDS and LA-ICP-MS data sets can be found in Appendix C.

3.3 Results

3.3.1 K-feldspar

3.3.1.1 Major and minor elements

K-feldspar grains vary between 0.70 – 1.20 wt% Na_2O and 14.0 – 15.35 wt% K_2O, while CaO is below detection for all but one sample; K-feldspar in leucogranite 03 contains 0.16 wt% CaO on average. Concentrations of BaO in K-feldspar are comparable to Na_2O in samples 07c, 08, and 10; typically between 0.70-1.10 wt%, and ~0.20 wt% BaO is present in K-feldspar in samples 03, 07a, f02, f04, and f13. EDS maps of sample 05b also indicate 0.4-0.7 wt% BaO in K-feldspar. The variation between individual point analyses is shown on Figure 3.1. K-feldspar in leucogranite samples 01d, 03, and 06 cluster between $Or_{0.9\text{-}0.95}$ while leucogranite samples 07b, f04, and orthogneiss sample 10, are slightly more albitic, clustering around $Or_{0.9}$. Migmatite samples 02a, 02b, 04b, 08, and f13 K-feldspar sit between $Or_{0.9\text{-}095}$, while samples 04a and f02 cluster around $Or_{0.9}$. K-feldspar in migmatites 07a and 07c contain the highest albite component between $Or_{0.85\text{-}0.9}$. K-feldspar grains show significantly less compositional variation than the plagioclase in both leucogranites and migmatites.

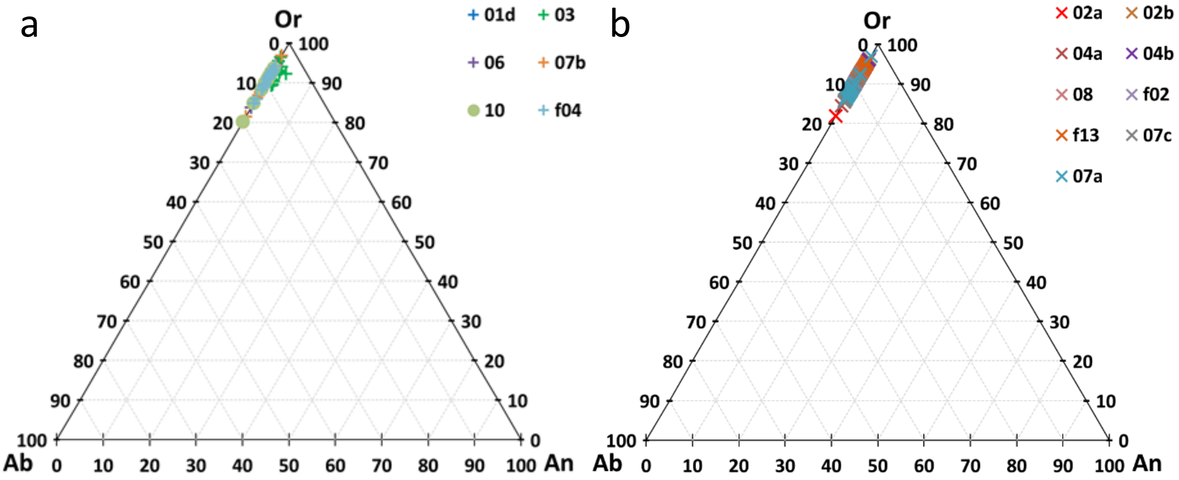

Figure 3.1 – Feldspar group ternary composition diagrams for individual EDS point analyses of K-feldspar grains in (a) leucogranites (including sample 10 orthogneiss), and (b) migmatites (including sample 09a meta-arkose). Endmember minerals are albite (Ab), anorthite (An), and orthoclase (Or).

3.3.1.2 Trace elements

Averaged measurements of elements above detection limit in K-feldspar are plotted in Figure 3.5, normalised to chondrite C1 values (Palme and O'Neill, 2014). Between samples, K-feldspar shows the most variation in LILE concentrations (Rb, Sr, Cs, Ba, and Eu), as well as Li and Y. Ba and Eu are investigated further as they are consistently above the limit of detection across K-feldspar analyses.

Barium concentrations in K-feldspar (between 650-2300 ppm) show negative correlations with Rb/Sr (Figure 3.2a). Notable outlying samples are leucogranite 06 with the highest Rb/Sr values (22.97-35.09) and lowest Ba concentrations (14.1-51.2 ppm), migmatite 07c with low Rb/Sr (1.05-1.73) and high Ba (5790-7200 ppm), and orthogneiss 10 with the lowest Rb/Sr (0.47-0.51) and variably high Ba (3380-12700 ppm), although these samples do still lie on the trend.

Europium concentrations (06-2.1 ppm) also show negative correlation with Rb/Sr (Figure 3.2b). Samples 06 and 10 again plot as outliers with high Rb/Sr, low Eu and low Rb/Sr, high Eu, respectively. Concentrations in migmatite 07c, however, are more closely associated with the main group of analyses.

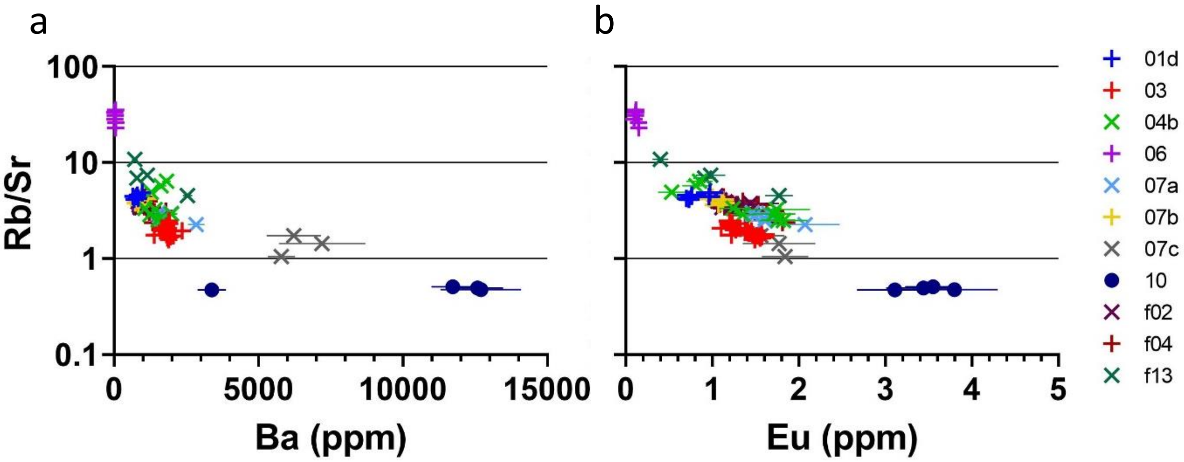

Figure 3.2 – K-feldspar grain Rb/Sr values plotted against (a) Ba and (b) Eu (ppm). Rb/Sr values are negatively correlated with both Ba and Eu concentrations. Leucogranite 06 is a high-Rb/Sr, low-Ba and Eu outlier, while samples 07c and 10 are low-Rb/Sr, high-Ba and Eu outliers.

3.3.2 Plagioclase

3.3.2.1 Major and minor elements

Plagioclase grains typically record 7.50 – 9.50 wt% Na_2O, 0.15 – 0.34 wt% K_2O, and 1.60 – 4.60 wt% CaO. The variability is shown on Figure 3.3. Leucogranite samples 01d, 07b, and f04 cluster around ~$An_{0.35}$ with a spread towards Ab (Figure 3.3a). Plagioclase in leucogranite sample 06 has higher albite content, clustering at ~$An_{0.2}$, while plagioclase in sample 03 sits at ~$An_{0.45}$. The spread present within each sample is due to zoning of plagioclase grains, with oligoclase ($An_{0.1-0.3}$) and andesine ($An_{0.3-0.5}$) cores and albite ($An_{0-0.1}$) rims. Plagioclase in orthogneiss sample 10 has a composition of $An_{0.35-0.45}$ and does not show core-rim zoning. Plagioclase in migmatite samples 04a, 04b, 08, 09b, and f02, and meta-arkose sample 09a, cluster between $An_{0.3-0.4}$ (Figure 3.3b), with samples 07a and 07c between $An_{0.35-0.4}$. Plagioclase in migmatites 02a, 02b, and f13 is more albitic, clustering between $An_{0.2-0.3}$. All migmatite samples show a core-to-rim decrease in the An component (i.e. increasing Ab).

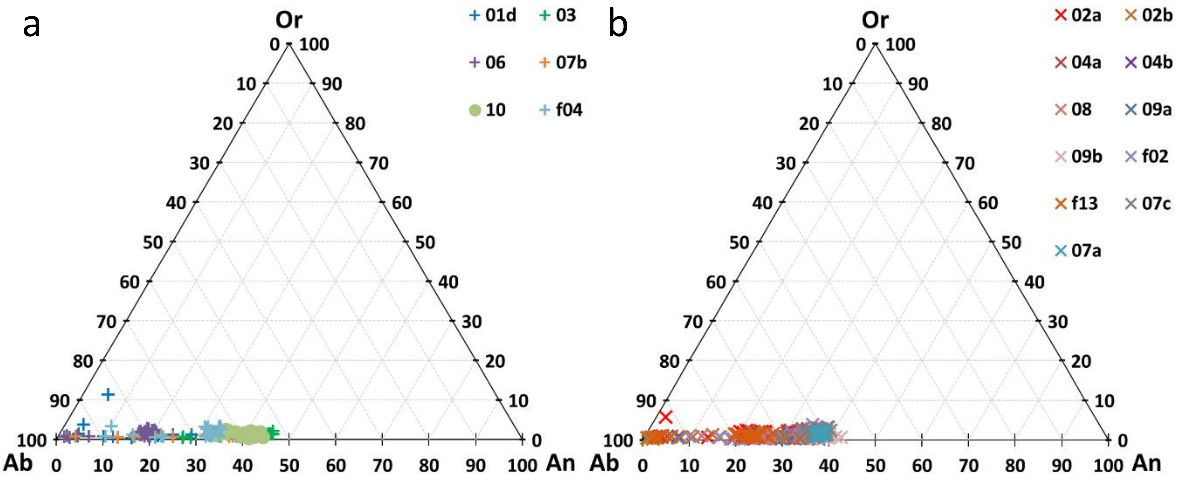

Figure 3.3 – Feldspar group ternary composition diagrams for individual EDS point analyses of plagioclase grains in (a) leucogranites (including sample 10 orthogneiss), and (b) migmatites (including sample 09a meta-arkose). Endmember minerals are albite (Ab), anorthite (An), and orthoclase (Or).

3.3.2.2 Trace elements

Averaged measurements of elements above detection limit in plagioclase are shown in Figure 3.5, normalised to chondrite C1 values (Palme and O'Neill, 2014). Between samples, plagioclase show the most variation in LILE concentrations (Rb, Sr, Cs, Ba, and Eu), as well as Li and Y. Ba and Eu concentrations are consistently above the detection limit.

Rb/Sr values show less variation between samples than in K-feldspar, as the overall variation is very small; between 4.46x10^{-4} and 5.58x10^{-1}. Distinctions can be made between samples, however, using the concentrations of Ba and Eu. The majority of samples have Ba concentrations of <65 ppm, whereas migmatite samples 09b and 07c, and orthogneiss 10, have elevated Ba concentrations typically >80 ppm (Figure 3.4a). The same grouping is present with concentrations of europium, with most samples containing <1.7 ppm Eu, while samples 07c, 09b, and 10 contain between 1.8-3.2 ppm Eu (Figure 3.4b). Leucogranite 06 is also distinguished from the other samples with very low Eu concentrations (<0.15 ppm).

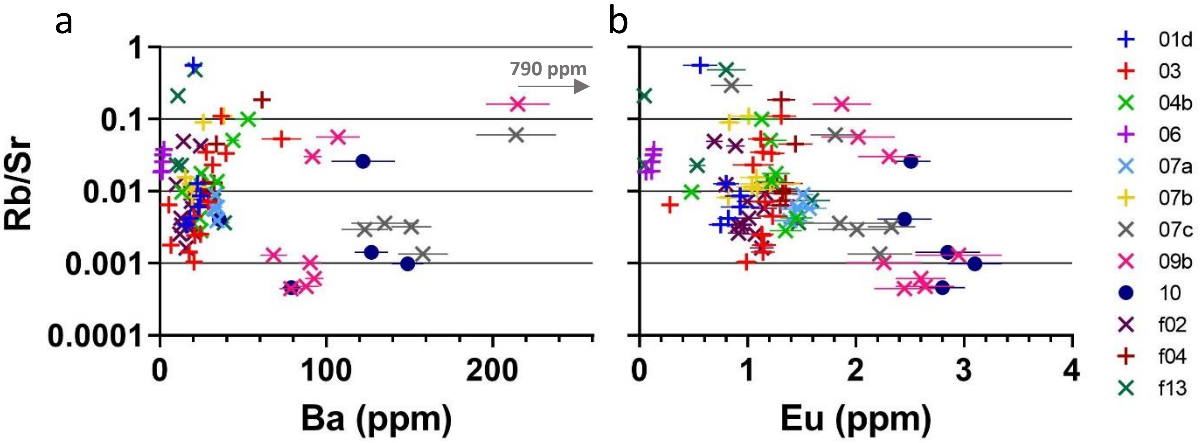

Figure 3.4 – Plagioclase grain Rb/Sr values against (a) Ba and (b) Eu (ppm). Rb/Sr values show little correlation with Ba and Eu concentrations. Leucogranite 06 has especially low Ba and Eu concentrations, while samples 07c, 09b and 10 have the highest concentrations of Ba and Eu.

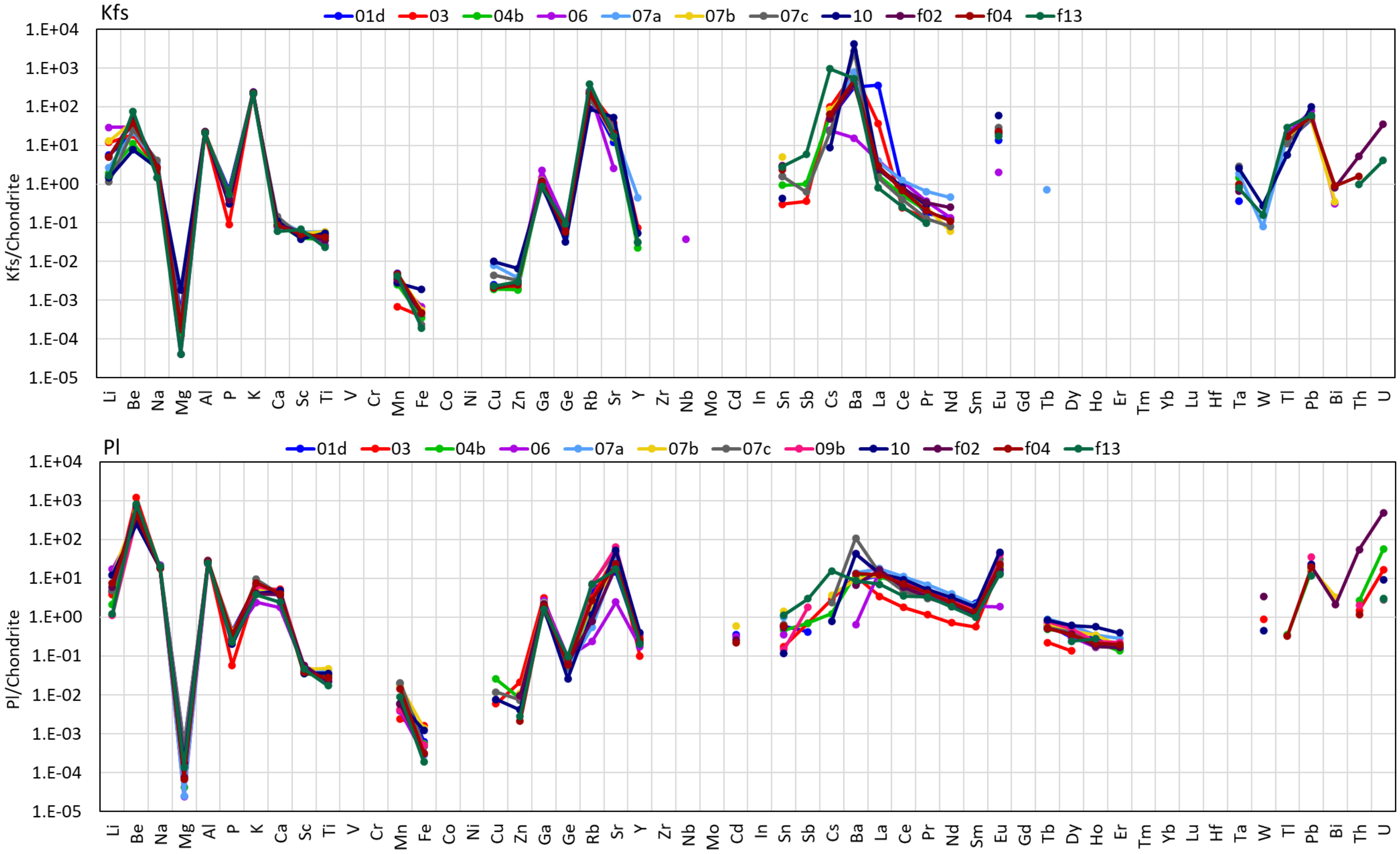

Figure 3.5 – Chondrite-normalised major and trace element analyses of K-feldspar (top) and plagioclase (bottom). LILEs (Rb, Sr, Cs, Ba, and Eu), lithium, and yttrium show the most variation between samples for K-feldspar and plagioclase whilst remaining above the detection limit.

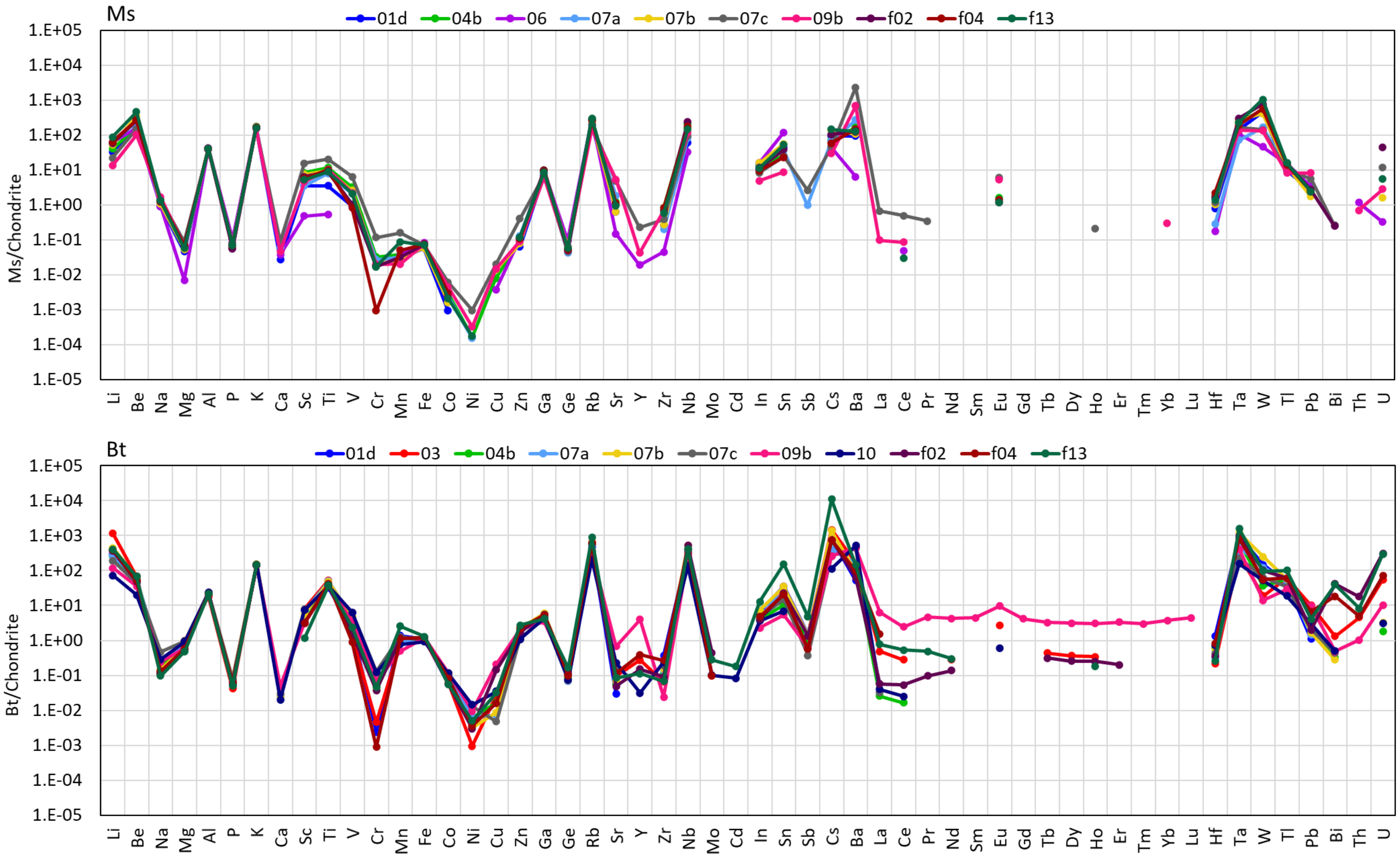

Figure 3.6 – Chondrite-normalised major and trace element analyses of muscovite (top) and biotite (bottom). LILEs (Rb, Sr, Ce, Ba, and Eu), Li, Cr, Y, Sn, and W show the most variation between samples for muscovite and biotite whilst remaining above the detection limit.

3.3.3 Muscovite

3.3.3.1 *Major and minor elements*

Major element oxides lie within typical ranges for muscovite in pelite (Forshaw and Pattison, 2021). Muscovite in samples 07c, 08, 09a, 09b, and 10, however, have detectable quantities of BaO; between 0.05-0.20 wt%. EDS maps of migmatite 05b and 11a also indicate up to 0.2 and 0.4 wt% BaO, respectively, in muscovite grains. These correlate either with the absence of K-feldspar (samples 05b, 09a, and 09b), or K-feldspar with elevated BaO wt% (samples 07c, 08, 10, and 11a).

3.3.3.2 *Trace elements*

The average concentrations of elements above detection limit in muscovite are plotted in Figure 3.6, normalised to chondrite C1 values (Palme and O'Neill, 2014). Between samples, muscovite shows most variation in the concentrations of LILEs, Li, and Y, as well as Sc, Cr, Ni, Cu, Sn, and W.

Laser-ablation measurements of Li allow for further classification using the *mgli-feal* a.p.f.u. notation (Mg – Li = *mgli*, Fe_{tot} + Mn + Ti - ^{VI}Al = *feal*) (Tischendorf et al., 2004). Muscovite analyses are tightly clustered towards the base of the muscovite field, around values of 0 for *mgli*, and -1.8 for *feal* (Figure 3.7).

Barium concentrations show a negative correlation with Rb/Sr (Figure 3.8a), similar to K-feldspar. Most samples cluster between Rb/Sr values of 57-160 and Ba concentrations of 220-720 ppm. Leucogranite 06 again plots as a high Rb/Sr (440-840), low Ba (9.2-25.7 ppm) outlier, with

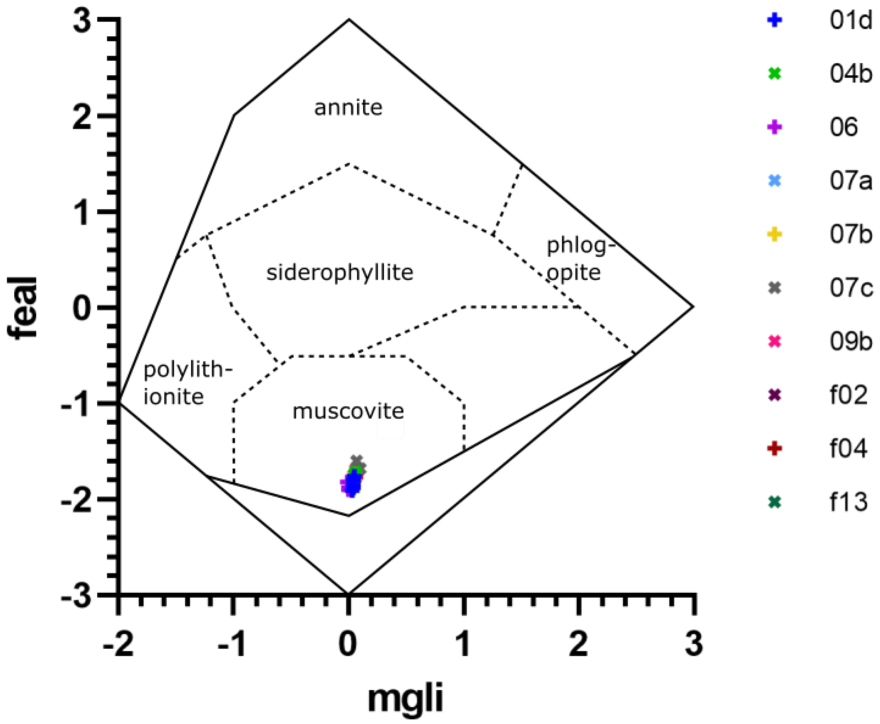

Figure 3.7 – mgli-feal potassium mica classification diagram of muscovite spot analyses. Values for mgli and feal are calculated in a.p.f.u. Samples sit towards the base of the muscovite zone.

migmatites 07c and 09b present as low Rb/Sr (6.4-15.4), high Ba (>1300 ppm) outliers. Tin (30-160 ppm), however, shows a positive correlation with Rb/Sr (Figure 3.8b). Muscovites in leucogranite 06 have high Sn concentrations (96-277 ppm), while muscovites in migmatites 07c and 09b have particularly low Sn concentrations at 34.7-46.6 and 12.7-16.4 ppm, respectively. Migmatite f13 also yielded two muscovite analyses that are particularly Sn-rich at 190 and 723 ppm, with relatively high Rb/Sr values of 64-217.

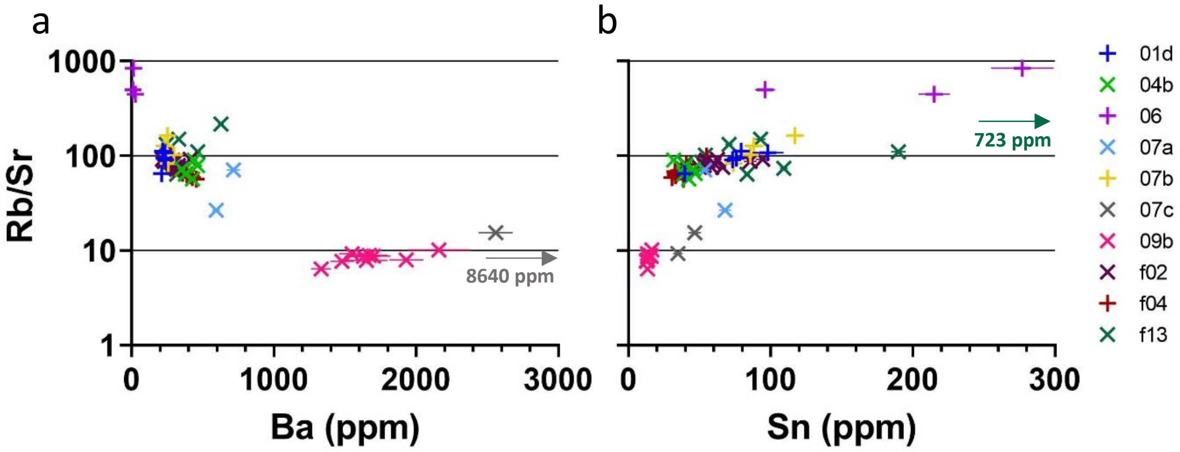

Figure 3.8 – Muscovite grain Rb/Sr values against (a) Ba and (b) Sn (ppm). Rb/Sr values are negatively correlated with Ba concentration and positively correlated with Sn concentration.

3.3.4 Biotite

3.3.4.1 Major and minor elements

Major element oxide results indicate biotite Al/Si and Fe/Mg typical of siderophyllite-annite compositions (Deer et al., 2013). Biotites are consistently between 2.0 – 4.0 wt% TiO_2, equating to 0.12 – 0.24 Ti a.p.f.u., with the exception of leucogranite sample 03, which has elevated values at ~4.4 wt% Ti, or 0.26 Ti a.p.f.u.

3.3.4.2 Trace elements

The average concentrations of elements above detection limit in biotite are plotted in Figure 3.6, normalised to chondrite C1 values (Palme and O'Neill, 2014). Between samples, biotite shows most variation in the concentrations of LILEs, Li, and Y, as well as Sc, Cr, Ni, Cu, Sn, and W.

Lithium measurements allow for classification of biotite grains using the *mgli-feal* a.p.f.u. notation (Mg – Li = *mgli*, Fe_{tot} + Mn + Ti - ^{VI}Al = *feal*) (Tischendorf et al., 2004). Analyses plot along the field boundaries of siderophyllite and annite, with values of 0.4-1.0 for *mgli* and 0.4-1.4 for *feal* (Figure 3.9). Biotites in migmatite 07c and orthogneiss 10 are the only two samples to plot entirely within the siderophyllite field.

Barium shows a negative correlation with Rb/Sr (Figure 3.10a), with most samples forming a cluster between Rb/Sr values of 1200-5600, and Ba concentrations of 100-480 ppm. Biotite in migmatites

07c, 09b, and orthogneiss 10 have higher Ba concentrations and lower Rb/Sr values. Tin is positively correlated with Rb/Sr (Figure 3.10b), with Sn concentrations of 10-70 ppm. Biotites in migmatite 09b and orthogneiss 10 are at the low end of the scale for both Rb/Sr and Sn. Biotites in migmatite f13 contain significantly higher Sn concentrations than biotite in other samples (172-406 ppm).

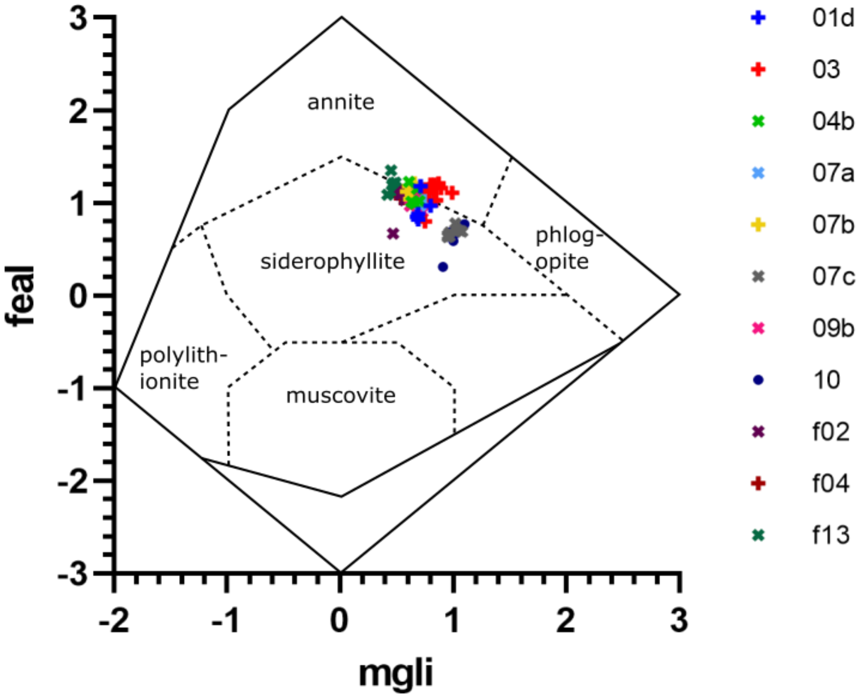

Figure 3.9 – mgli-feal potassium mica classification diagram of biotite spot analyses. Values for mgli and feal are calculated in a.p.f.u. Samples sit between siderophyllite and annite zones.

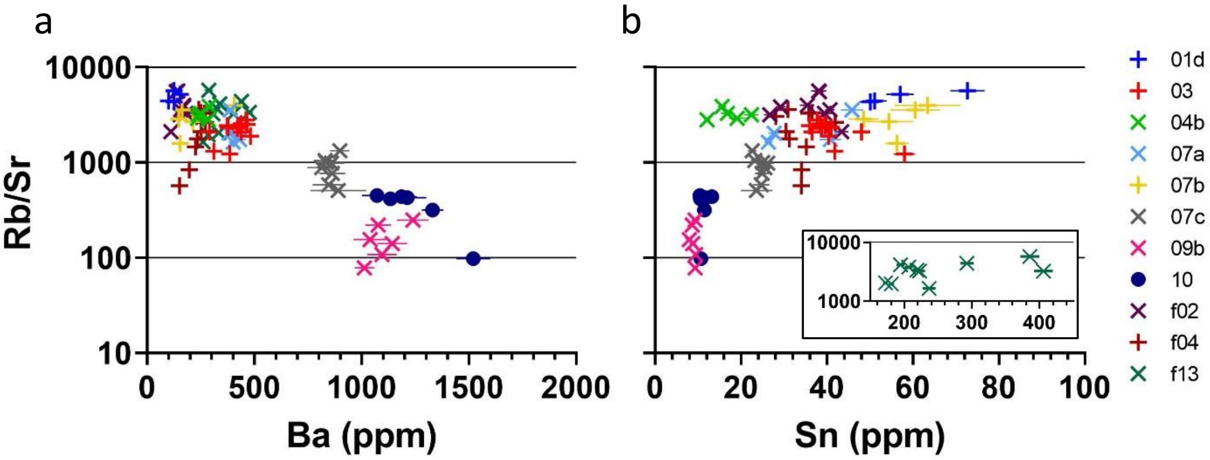

Figure 3.10 – Biotite grain Rb/Sr values against (a) Ba and (b) Sn (ppm). Rb/Sr values are negatively correlated with Ba concentration and positively correlated with Sn concentration.

3.3.4.3 Ti-in-biotite thermometry

Temperatures calculated using Ti-in-biotite calibration of Wu and Chen (2015) for EDS and LA-ICP-MS datasets for each sample are presented in Table 3.2. A pressure estimate of 1 GPa is used in the calibration, from peak calculated pressure conditions in the Badrinath Formation (Spencer et al., 2012a). Propagated error for the calibration is approximately ±65°C (Wu and Chen, 2015). EDS data for samples f02, f04, and f13 fell outside of the compositional calibration range, as did LA-ICP-MS data for sample f13. No LA-ICP-MS data were collected for samples 02a, 04a, or 08 (Table 3.1). Across all samples, temperatures range from 633–833°C, with a maximum variation within any given sample of 110°C. The sample with the highest mean temperature is f04 (799°C), while sample 07c has the lowest (670°C).

Table 3.2 – Calculated Ti-in-biotite temperatures from EDS and LA-ICP-MS datasets for each sample. Rock types are abbreviated for leucogranite (L), migmatite (M), and orthogneiss (O). Column 'n' is the number of individual data points.

Sample	**Rock type**	**Dataset**	**n**	**Temperature (°C)**			
				Max	Min	Mean	Stdev
01d	L	EDS	18	776	675	726	30
		LA-ICP-MS	4	742	696	717	18
02a	M	EDS	10	791	756	775	12
		LA-ICP-MS	-	-	-	-	-
03	L	EDS	11	745	720	730	7
		LA-ICP-MS	12	751	675	707	21
04a	M	EDS	15	787	738	760	14
		LA-ICP-MS	-	-	-	-	-
04b	M	EDS	7	771	742	760	10
		LA-ICP-MS	5	809	764	779	16
07a	M	EDS	9	784	760	776	7
		LA-ICP-MS	4	790	759	777	12
07b	L	EDS	11	807	790	797	6
		LA-ICP-MS	5	811	781	798	12
07c	M	EDS	42	690	633	670	13
		LA-ICP-MS	8	696	650	678	17
08	M	EDS	18	715	663	690	16
		LA-ICP-MS	-	-	-	-	-
09b	M	EDS	6	766	674	729	30
		LA-ICP-MS	6	804	707	756	29
10	O	EDS	18	715	655	681	15
		LA-ICP-MS	6	742	639	693	31
f02	M	EDS	-	-	-	-	-
		LA-ICP-MS	5	825	714	784	45
f04	L	EDS	-	-	-	-	-
		LA-ICP-MS	9	833	748	799	23

Leucogranite samples fall into two groups of higher and lower temperatures (Figure 3.11). Samples 01d and 03 have relatively low temperatures with median values of 700–740°C, while samples 07b and f04 have higher temperatures with median values of ~800°C. Variation between EDS and LA-ICP-MS datasets for each sample is primarily on the range of calculated temperatures, with the median value of sample 03 showing the largest difference of ~20°C.

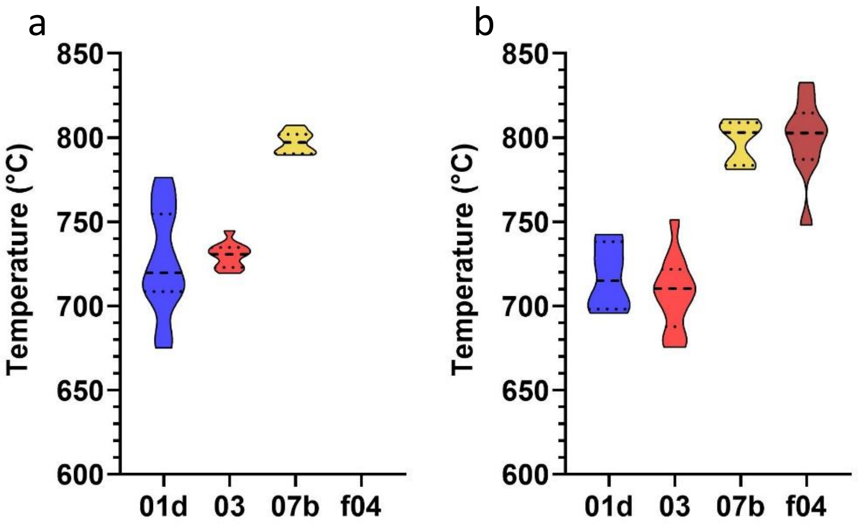

Figure 3.11 – Violin plots of calculated Ti-in-biotite temperatures for leucogranite samples using (a) EDS and (b) LA-ICP-MS datasets. Bold dashed lines mark the median temperature values, and dotted lines mark the upper and lower quartiles. The width of each plot corresponds to the probable frequency of data at a given value.

Migmatite samples largely fall into groups of higher and lower temperatures, with a couple of outliers (Figure 3.12). Samples 02a, 04a, 04b, and 07a all have median values of 750–780°C for both EDS and LA-ICP-MS datasets, while samples 07c and 08, as well as orthogneiss 10, have median values of <700°C. The temperature ranges of sample 09b overlap the two groups, with median values of ~750°C. Sample f02 has a notably high median value of 810°C, comparable to the high temperature leucogranites (07b and f04), while having the largest intrasample variation.

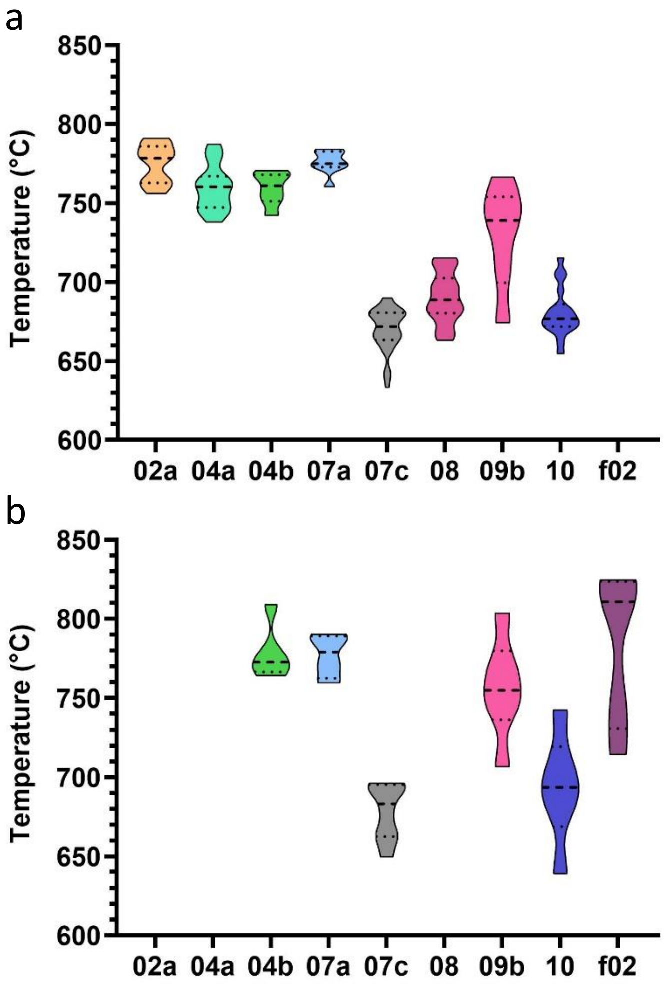

Figure 3.12 – Violin plots of calculated Ti-in-biotite temperatures for migmatite samples, and orthogneiss 10, using (a) EDS and (b) LA-ICP-MS datasets. Bold dashed lines mark the median temperature values, and dotted lines mark the upper and lower quartiles. The width of each plot corresponds to the probable frequency of data at a given value.

3.3.5 Garnet

Garnets are present in 12 out of 20 key samples (Table 2.2), but they are mostly rare, or occur as small, relict grains. However, leucogranite samples 01d and 06 provide exceptions to this, with common garnet porphyroblasts. This section focuses on the geochemistry of garnet in these two samples, with an overview of garnet endmember profiles in other samples.

3.3.5.1 Leucogranite 01d garnet

Garnet endmember profiling shows that the almandine component is fairly consistently ~0.75, with a central region, between 900-1500 µm, relatively enriched in spessartine (~0.135), alongside irregular quartz inclusions (Figure 3.13). In the outer-most 150 µm of the grain, almandine and pyrope components decrease sharply from 0.76 to 0.71 and 0.12 to 0.09, respectively, while spessartine increases from ~0.8 to ~0.17.

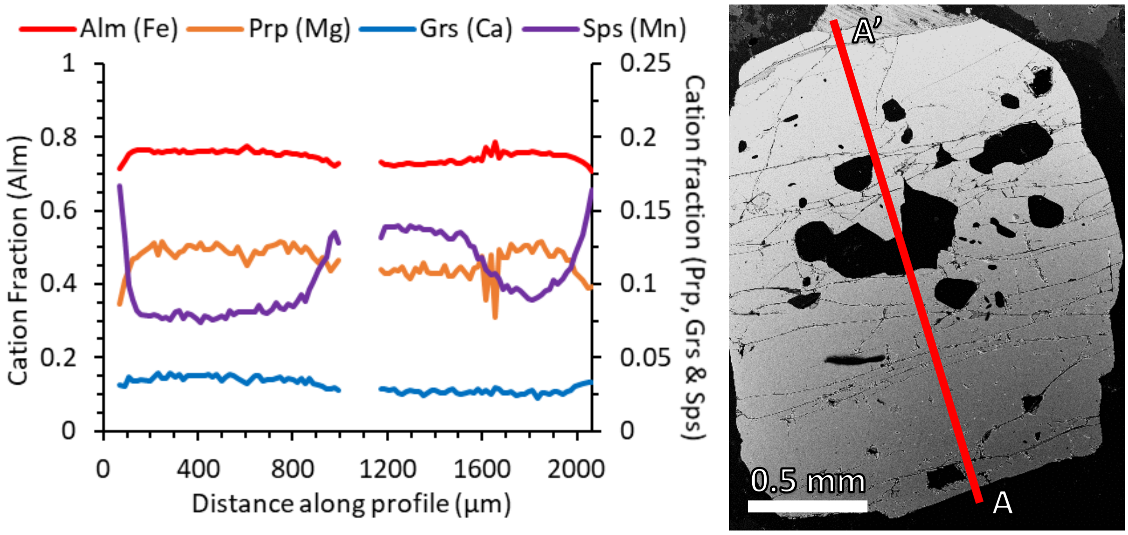

Figure 3.13 – Compositional profile of a garnet grain from leucogranite sample 01d in polished thin section. BSE image of the garnet shows longitudinal profile A-A'.

Chondrite-normalised REE profiles for four spot analyses along the long axis of the garnet grain are plotted in Figure 3.14. There is a slight increase in the abundance of the heavy rare earths (especially Ho-Lu) towards the rim of the grain. La, Ce, Pr, and Eu are frequently below detection.

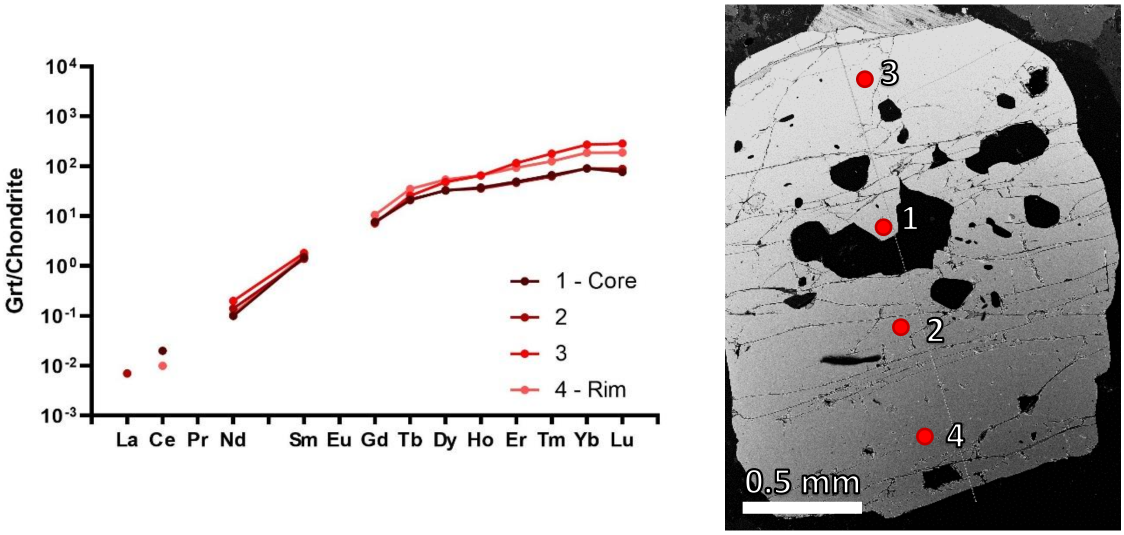

Figure 3.14 – Chondrite-normalised REE profiles for LA-ICP-MS spots analyses 1-4 on a garnet grain from leucogranite sample 01d. BSE image of the garnet show the location of the four spot analyses.

3.3.5.2 Leucogranite 06 garnet

Leucogranite sample 06 contains euhedral garnet grains with distinct core-rim zoning and inclusions of rutile needles (Figure 2.40e-f). Endmember profiles show significant change from core to rim, with (i) a notably high spessartine component (>0.46) in the core; (ii) an intermediate mantle zone of steadily decreasing spessartine (0.37-0.26) with increasing almandine and grossular; (iii) a rim of further decreasing spessartine (0.26-0.12) (Figure 3.15a).

The core region (1700-2850 µm) is also rich in randomly distributed inclusions, identified using qualitative EDS apatite, rutile, xenotime, and zircon, <10 µm across. The crystallographically oriented rutile needles coincide with the intermediate zone and are poorly imaged in BSE due to infrequent intersection with the polished surface. Apart from the rutile and occasional irregular quartz grains, the intermediate and rim zones are inclusion-poor. Endmember zoning is asymmetric, with a broader intermediate zone on one side of the core than the other (650-1700 µm, compared to 2850-3550 µm).

Zonation is also present in trace elements, with spot analyses taken every 60 µm across the garnet grain (Figure 3.15b). The core is too inclusion-rich to collect garnet-exclusive trace element concentrations. The intermediate zone of 0.37-0.26 spessartine coincides with elevated P, Nb, Sn, and Ta concentrations, which decrease with distance from the core. Ti concentrations are high (>1000 ppm) within the intermediate zone but decrease rapidly either side of it. Y concentration increases with distance from the core, before reaching its peak (1610 ppm) just before the rim zone of a decreasing spessartine component. Trace element zoning is asymmetric, as with endmember zoning.

Chondrite-normalised REE profiles for 28 spot sites from 0–1700 µm are in Figure 3.16. The gradient of the profiles increases with distance from the core, as light rare earth elements (LREEs) decrease in abundance and heavy rare earth elements (HREEs) increase. The peak abundance for HREE occurs at ~800 µm, coinciding with the peak in Y concentration, before decreasing.

3.3.5.3 Other garnet-bearing samples

Garnet-bearing migmatite samples 02b, 07c, and f02, all have flat major element profiles, with variation <0.07 for almandine, and <0.045 for other endmembers. Spessartine varies the most between samples, with average values of 0.17 for 02b, 0.21% for 07c, and 0.07 for f02. A garnet profile from sample f02 is shown in Figure 3.17a, it also shows rim spessartine enrichment up to 0.20.

Migmatite samples 08 and 09b, meta-arkose 09a, and orthogneiss 10, from the base of the Badrinath Formation, contain garnets with compositional zoning patterns with U-shaped spessartine profiles corresponding with a drop in other components, and a central region slightly elevated in spessartine. A garnet profile from sample 10 is shown in Figure 3.17b.

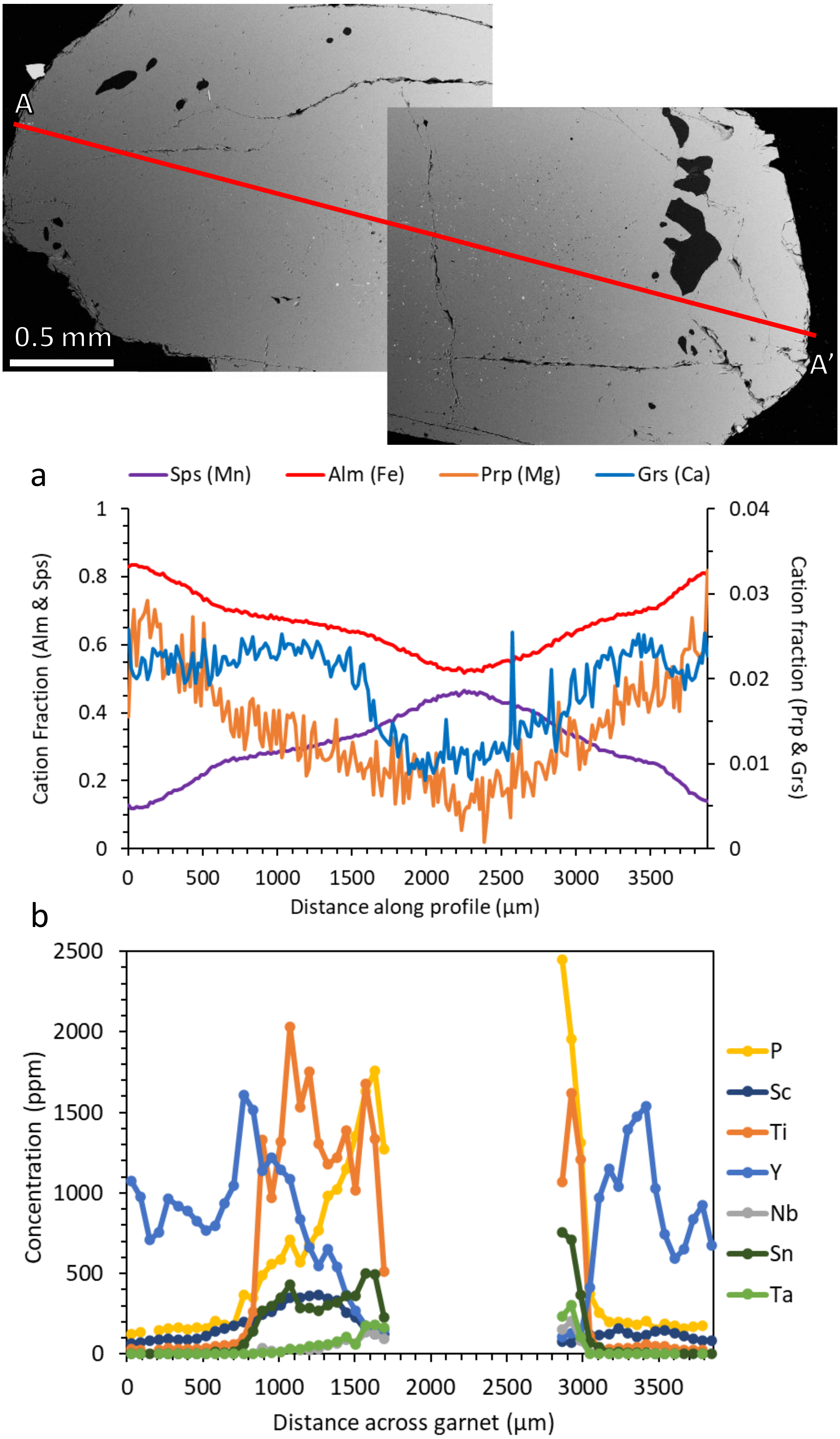

Figure 3.15 – Composite BSE image of a garnet porphyroblast from leucogranite sample 06, showing longitudinal profile A-A'. Compositional zoning along A-A' (µm) is plotted against (a) garnet endmember proportions and (b) trace element concentrations (ppm).

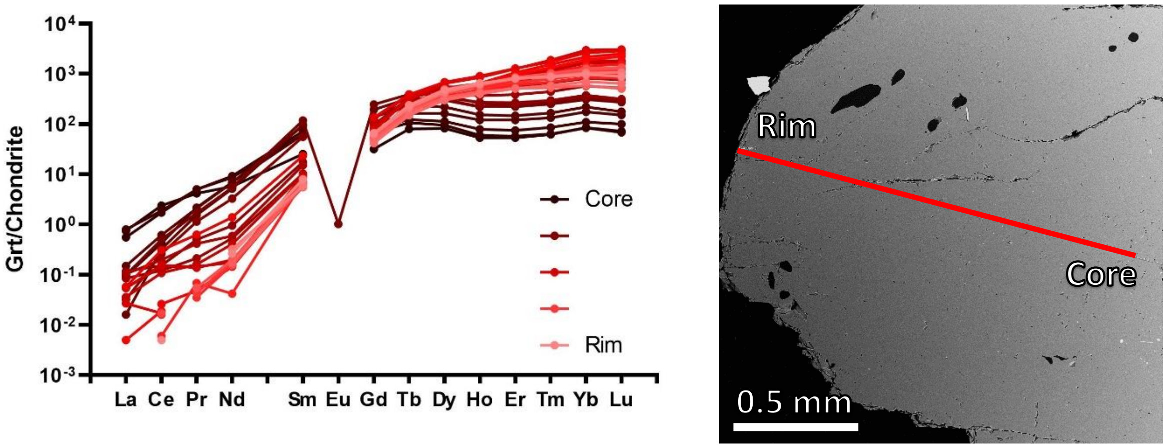

Figure 3.16 – Chondrite-normalised REE profiles from leucogranite sample 06 garnet porphyroblast. Profiles from 28 spot analyses, approximately every 60 µm across ~1700 µm, from the outer edge of the core to the rim.

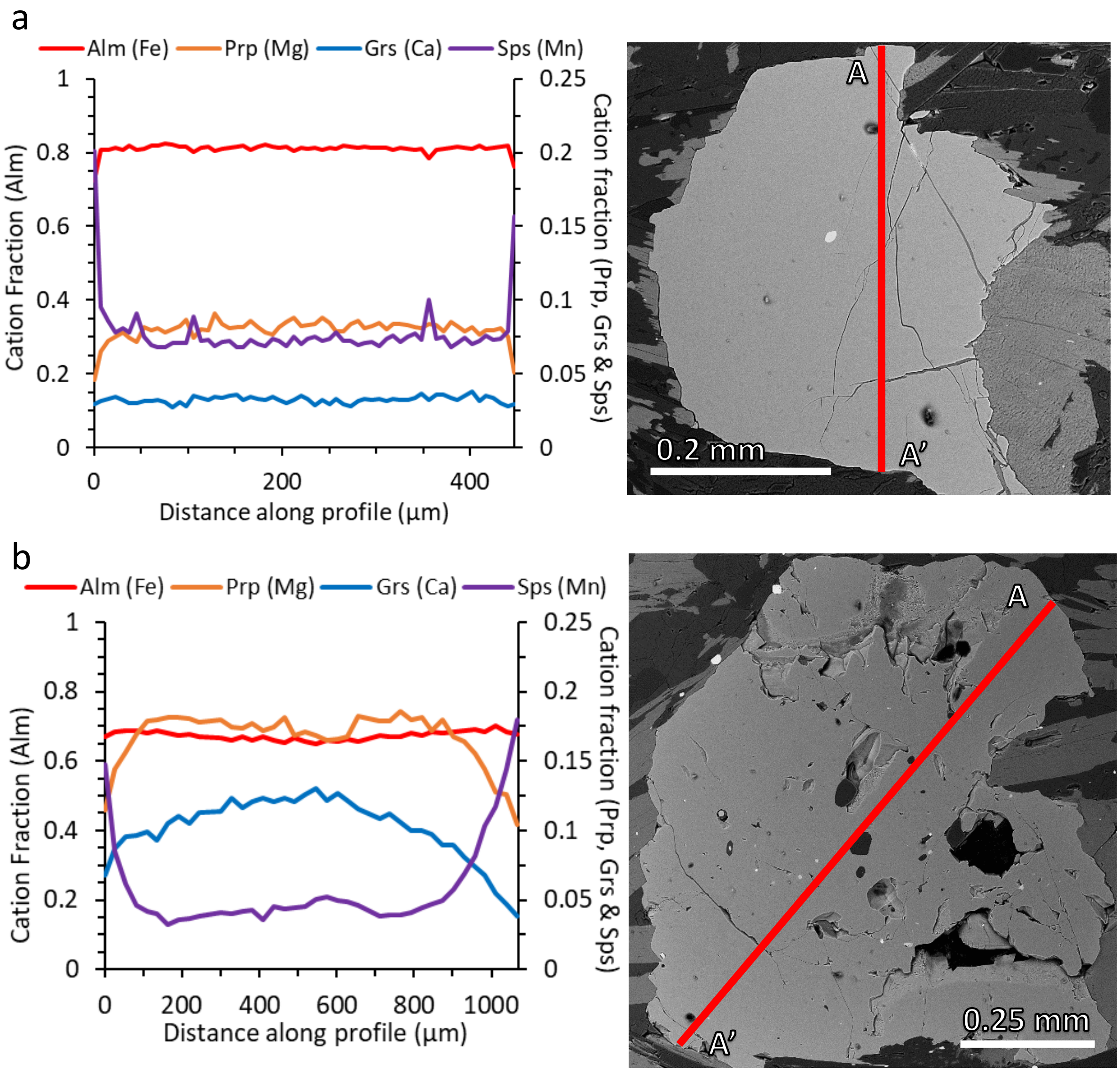

Figure 3.17 – a) Endmember profiles of a garnet grain from migmatite sample f02 in polished thin section. BSE image of the garnet shows longitudinal profile A-A'. b) Endmember profiles of a garnet grain from orthogneiss sample 10 in polished thin section. BSE image of the garnet shows longitudinal profile A-A'.

3.4 Discussion

3.4.1. EDS vs LA-ICP-MS datasets

Ti-in-biotite temperatures calculated for each sample using the EDS and LA-ICP-MS datasets are similar or show marginally greater variation in the LA-ICP-MS temperatures, even though the EDS dataset has an equal or greater number of individual datapoints for each sample, excluding leucogranite 03 and samples without EDS results (Table 3.2). Differences between the two datasets could be due to (i) analytical uncertainties associated with oxides/elements used in the calculation, (ii) differences in Ti concentrations with grain size and a difference in the grain size distribution of the grains analysed for the two datasets, or (iii) heterogeneity and/or inclusions within the volume of material analysed.

Uncertainties (2σ) for LA-ICP-MS data are on average 6% for Ti and 3-5% for major elements (Mg, Al, Fe, etc,) in biotite. Typical uncertainties of 6% for TiO_2 and 3.5-4.5% for other oxides equate to temperature variations of ±43°C when run through the temperature equation, while pressure variations of ±0.2 GPa equate to ±23°C. This results in a total calibration error of ±66°C. EDS uncertainties (2σ) for biotite are 3-6% for TiO_2, and <2% for MgO, Al_2O_3, SiO_2, and FeO. Typical uncertainties of 5% for TiO_2 and 2% for other oxides equate to temperature variations of ±27°C when run through the temperature equation, while pressure variations of ±0.2 GPa equate to ±23°C. This comes to a total calibration error of ±50°C, lower than the approximation of ±65°C by Wu and Chen (2015). The EDS temperature dataset, therefore, has the smaller overall 2σ value.

The 12 samples analysed with LA-ICP-MS are all medium- to coarse-grained migmatites, leucogranites, and orthogneiss, and as such, there are plenty of locations suitable for 50 µm diameter spots on biotite grains. EDS analyses also shows there is limited variation in major oxide concentrations within each sample (Figure 3.9). Therefore, any Ti concentration differences with grain size and/or grain size distributions are unlikely to play a major role in EDS vs LA-ICP-MS dataset variation.

Laser ablation analyses are on a 50 µm diameter spot, drilling ~30 µm deep into the polished thin section, of volume of approximately 6×10^4 µm^3, while the interaction volume of an electron beam at 20 keV in an Si-rich medium can be approximated as a sphere with radius of <2.5 µm (Goldstein et al., 2017), or 6.5×10^1 µm^3, three orders of magnitude smaller than the laser ablation volume. Petrographic observations of biotite found inclusions of ilmenite and sagenitic rutile to be relatively common throughout the sample set. While areas of inclusion-poor biotite were selected for laser ablation, the possibility of micro-inclusions being ablated cannot be entirely ruled out, and, therefore, may contribute to variation of the LA-ICP-MS results compared to the EDS.

3.4.2 What do Ti-in-biotite temperatures record?

The Ti-in-biotite thermometer of Wu and Chen (2015) provides a temperature for a given proportion of Mg to Ti, while also accounting for substitutions with Fe and Al^{VI}, within the calibration range. The calibration also requires the sample to be TiO_2-saturated, with either rutile or ilmenite present as an accessory phase. As such, the efficacy of the thermometer depends on the activity of TiO_2 (a_{TiO_2}) within a sample for given P-T conditions. For a pelite bulk composition with 0.67 wt% TiO_2, at pressures of 0.9-1.0 GPa and 650-700°C, the a_{TiO_2} is ~1.0 (Figure 3.18) (Ashley and Law, 2015), with the TiO_2 concentration used in this model below the average of 0.97 wt% calculated by Forshaw and Pattison (2021). EDS-map bulk values of 0.96-0.98 wt% TiO_2 were measured for schistose migmatite sample 08. The modelled a_{TiO_2} value drops rapidly, however, after the rutile-out boundary around temperatures >700°C for a pressure of 0.9-1.0 GPa (Ashley and Law, 2015; Meinhold, 2010), which may reduce the rate for Ti exchange in biotite, and artificially reduce calculated temperatures. It should be noted, however, that the Ti contents of micas often approximate expected compositions in equilibrium with rutile, even when rutile is not present, possibly indicating that pelites are generally near rutile-saturation (Chambers and Kohn, 2012).

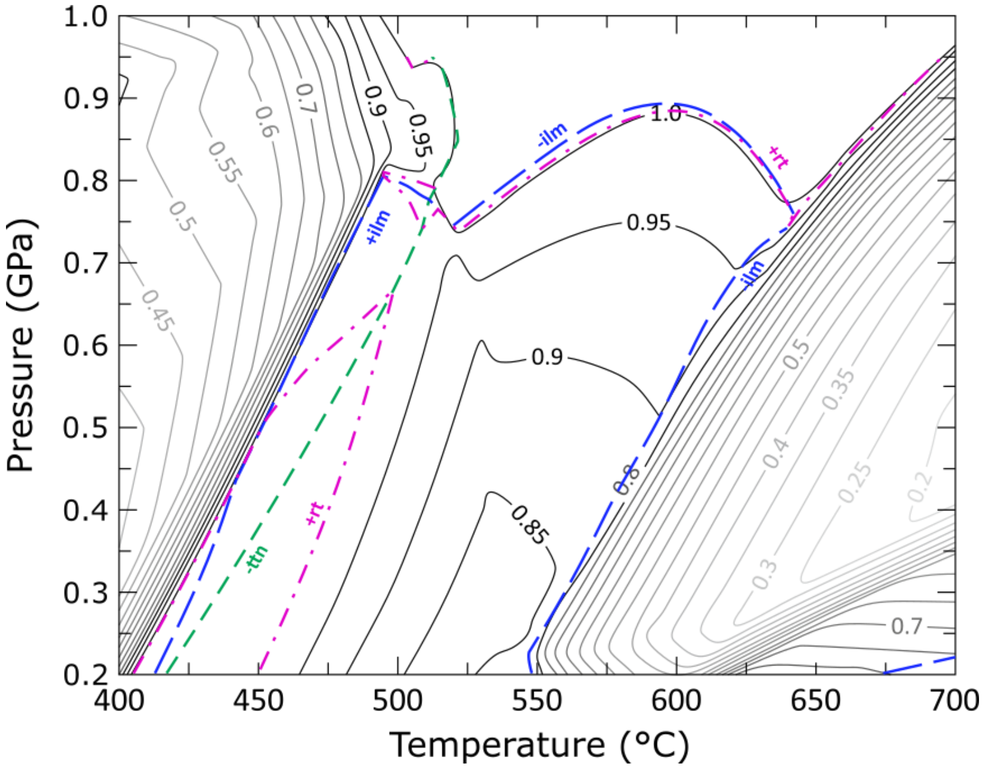

Figure 3.18 – Modelled TiO_2 activity and phase stability for pelitic bulk composition with 0.67 wt% TiO_2. Coloured dashed lines denote the phase boundaries for titanite (ttn), ilmenite (ilm), and rutile (rt). After Ashley and Law, 2015, used with permission from Springer Nature.

The a_{TiO_2} may also be reduced by the presence of melt, as modelling from granitoid and rhyolitic melt suggests a_{TiO_2} values of <0.5 relative to rutile saturation (Borisov and Aranovich, 2020; Schiller and Finger, 2019). As such, the Ti-in-biotite temperature may record the point at which the presence of interstitial melt reduces the effective transfer of Ti^{2+} and Mg^{2+} ions between biotite and the matrix. Leucogranite samples 01d, 03, 07b, and f04 have all been identified as having formed through muscovite-dehydration melting. The temperature difference of 70-80°C between the two groups, therefore, cannot be explained by differing melt reactions.

Temperatures calculated for migmatite samples largely reflect the groups identified as fluid-present and muscovite-dehydration melting (Chapter 2, section 2.6.1), with temperatures typically <750°C for fluid-present melting and >750°C for muscovite-dehydration melting. There is a difference of >50°C between the mean values of these two groups, greater than the calculated error for the EDS data and, therefore, likely to be representative of real differences between the two groups. These temperatures are also in agreement with all samples crossing the metapelite wet solidus at ~670°C and 1.0 GPa (Brown, 2007), with only samples containing peritectic K-feldspar reaching mean temperatures of <760°C, presumably undergoing muscovite-dehydration melting during decompression (Patiño Douce and Harris, 1998; Weinberg, 2016). The effect of melt on a_{TiO_2} could explain the ~100°C difference between migmatite samples 07a and 07c, from the same outcrop, but with muscovite-dehydration and fluid-present melt textures, respectively.

Calculated Ti-in-biotite temperatures may also be lowered by post-peak Fe-Mg diffusion between biotite and other ferromagnesian minerals, especially garnet, as retrograde exchange reactions increase the Mg concentration in biotite (Kohn and Spear, 2000). This effect is strongest where garnet and biotite are in contact, and as such, analyses of biotite grains in contact with garnet were not used for thermometry in this study, reducing the impact of retrograde processes on the calculated temperatures (Kohn and Spear, 2000). Further work is required to fully quantify the impact of Fe-Mg diffusion on Ti-in-biotite thermometry for these rocks.

The extent of Fe-Mg diffusion is also dependent on cooling rate during exhumation, with greater retrograde exchange occurring in slowly cooled systems (Frost and Chacko, 1989; Kohn and Spear, 2000). Exhumation of the GHS in the Garhwal Himalaya was relatively fast, with periods of exhumation rates >1 cm/year (Maiti and Mandal, 2021), as well as conductive cooling of the GHS beneath the South Tibetan Detachment (Spencer et al., 2012a). This likely reduced the impact of Fe-Mg exchange on rocks from the GHS. Retrograde Mg-loss in garnet is visible in the endmember profiles in Figure 3.17; however, migmatite samples 08 and f02 all show rim-depletion of pyrope while yielding some of the lowest and highest calculated temperatures in biotite, respectively. Retrograde Fe-Mg exchange is, therefore, unlikely to affect the overall results of the Ti-in-biotite thermometry but may be responsible for some of the variation within each sample.

The application of Ti-in-biotite thermometry to the migmatites and leucogranites appears to produce temperatures near to the expected peak conditions for each sample, with grouping that correlates with petrographic observations of fluid-present and muscovite-dehydration melting. This is despite the modelled drop in a_{TiO_2} at >700°C and 0.9-1.0 GPa, due to the instability of rutile, and the presence of any interstitial melt. The effect of Fe-Mg retrograde diffusion is likely to be relatively small due to fast exhumation and conductive cooling of the GHS, as well as through the careful selection of analytical sites.

3.4.3 Geochemical fingerprints of melt reactions

Plagioclase, muscovite, and biotite in a pelite each act as reservoirs of particular elements with high partition coefficients for that mineral, resulting in relative Rb/Sr that are low for plagioclase, moderate for muscovite, and high for biotite (Harris et al., 1995). Metamorphic fluid can also be characterised as enriched in fluid-mobile LILEs (Kessel et al., 2005). When a pelite melts, the distinct geochemical signatures of the minerals and any fluid involved are imparted onto peritectic minerals as well as those that form in and from the resulting melt (Harris et al., 1993, 1995; Patiño Douce and Harris, 1998; Gao et al., 2017). Here I discuss the geochemical signatures in sample groups identified with various melt-forming reactions through petrographic observations (Chapter 2).

3.4.3.1 Fluid-present melting

Migmatite samples 05b, 07c, 08, 09b, and 11a were all texturally identified as having undergone fluid-present melting (Chapter 2). These samples all show elevated concentrations of BaO in K-feldspar (0.4-1.1 wt% where present) and muscovite (~0.2 wt%), and low Rb/Sr in K-feldspar and micas. K-feldspar and plagioclase have elevated Ba and Eu concentrations, while muscovite and biotite have elevated Ba and low Sn concentrations. These data are in agreement with previous bulk-rock observations of relatively lower Rb/Sr and higher Ba and Eu concentrations in products of predominantly fluid-present melting (Harris et al., 1993; Gao et al., 2017). This geochemical signature is caused by a low consumption ratio of muscovite to plagioclase during melting (Harris et al., 1993), relatively enriching the melt and peritectic mineral phases with trace elements associated with plagioclase and aqueous fluid (Sr, Eu, and Ba), and relatively depleting the melt in mica-hosted trace elements (Rb and Sn) (Harris et al., 1995; Gao et al., 2017).

Garnets in samples 07c, 08, and 09b show major element homogenisation, with little variation in major cation concentrations across each grain, apart from retrograde enrichment of Mn in the rims (Banno and Chii, 1978). This enrichment is also present in garnet major element profiles from previous studies of the Badrinath and upper Pandukeshwar Formations (Spencer et al., 2012a). Given garnet grains in these samples are all typically <1 mm in diameter and mean Ti-in-biotite temperatures are >650°C, it is unlikely any significant major element growth zoning would be preserved as prograde metamorphism and exhumation would have taken cumulatively longer than 5 Ma (Spear, 2014; Caddick et al., 2010).

Orthogneiss sample 10 has the geochemical signatures of fluid-present melting as the migmatites and contains garnets with largely homogenised major element profiles and rim enrichment in Mn. Orthogneisses in the Garhwal GHS are Early Palaeozoic in age, with magmatic zircon rim ages of 510 - 416 Ma (Spencer et al., 2012b) and are thought to be the product of bimodal extensional magmatism, crustal thickening, or arc magmatism (Miller et al., 2001; Gehrels et al., 2003; Cawood et al., 2007). However, textural analysis of major phases suggests that some fluid-present melting occurred in this sample since its initial emplacement, and Ti-in-biotite thermometry yields mean calculated temperatures similar to those of fluid-present melting migmatites (~685°C), suggesting that Ti-Mg systematics in biotite were reset during prograde Himalayan metamorphism.

3.4.3.2 Ms-dehydration melting

Migmatite samples 02a, 02b, 04a, 04b, 07a, f02, and f14, and leucogranite samples 01d, 03, 07b, and f04 were all texturally identified as having undergone or formed through muscovite-dehydration melting (Chapter 2). K-feldspar shows slightly elevated concentration of BaO in samples 03, 07a, f02, f04, and f13 (~0.2 wt%), and concentrations below detection limits in other samples. The K-feldspar, muscovite, and biotite have higher Rb/Sr than fluid-present melting associated migmatites. K-feldspar and plagioclase have relatively depleted Ba and Eu concentrations, while muscovite and biotite have relatively low Ba and high Sn concentrations. This geochemical signature is the inverse of the fluid-present melt reaction signature. This association is interpreted as being caused by a relatively high ratio of muscovite to plagioclase consumption during melting, enriching the products in trace elements associated with muscovite (Rb and Sn), relative to those associated with plagioclase and fluid (Sr, Eu, and Ba) (Harris et al., 1993, 1995; Gao et al., 2017).

Within the muscovite-dehydration sample set, there is a spectrum of Rb/Sr values and correlating Ba concentrations in K-feldspar, muscovite, and biotite. Leucogranite 03 is at one end of the spectrum, around an average of 1.91 for Rb/Sr and 1850 ppm Ba, and leucogranite 01d at the other with an average of 4.44 for Rr/Sr and 786 ppm Ba (Figures 3.2a, 3.8a, and 3.10a). This spread in ratios and concentrations within muscovite-dehydration samples is also reported from bulk-rock compositions of Himalayan granites (group A) by Gao et al. (2017). This variation is likely to represent differences in the abundances of muscovite and plagioclase in the protolith, with the higher modal abundance of muscovite, relative to plagioclase, resulting in higher Rb/Sr values (Harris et al., 1993).

Garnets in migmatites 02b and f02 have homogenised major element profiles with little overall variation across each grain, excluding the rims of garnet in f02 (Figure 3.17a), which show garnet-enrichment in Mn (Banno and Chii, 1978). Mean Ti-in-biotite temperatures calculated for sample 02a (the host migmatite of sample 02b) and sample f02 of >770°C suggests homogenised garnets are to be expected (Spear, 2014; Caddick et al., 2010), alongside observations from previous studies (Spencer et al., 2012a).

Compositional zoning is preserved, however, in garnet from leucogranite 01d (Figure 3.13), with a spessartine core of ~0.135 and mantle of ~0.08. REE analysis across this compositional zoning (Figure 3.14) shows similar abundance and profile patterns to garnets crystallised from melt in leucogranites from Leo Pargil (Thöni et al., 2012). This observation, alongside petrographic observations of elongated grains (Figure 2.14d), and inclusions of lobate quartz along the centre of the grains, strongly indicate that these garnet grains grew within the leucogranite melt (Jung et al., 2022; Taylor and Stevens, 2010) and were subject to shearing, due to proximity to the Badrinath Shear Zone (BSZ) along the Badrinath-Pandukeshwar Formation boundary (Benetti et al., 2021).

Calculated temperatures for the muscovite-dehydration migmatites are in agreement with phase equilibrium modelling of migmatites from Malari, also in the Badrinath/Bhapkund Formation, of 750-775°C at 1.0 GPa (Iaccarino et al., 2017).

3.4.3.3 Bt-dehydration melting

Leucogranite 06 is the only sample identified as having formed through biotite-dehydration melting (Chapter 2). Results show the lowest relative concentrations of Ba alongside the highest Rb/Sr values in K-feldspar and muscovite of any sample analysed, as well as the lowest Eu concentrations in K-feldspar and plagioclase, and in K-feldspar and muscovite, and some of the highest Sn concentrations in muscovite. This geochemical signature is distinct compared with the spectrum of values recorded in muscovite-dehydration samples and would require input from reactants with higher initial Rb/Sr values. Biotite is the primary candidate as it is a major reservoir of Rb in mica schist, while being depleted in Sr relative to muscovite and plagioclase (Harris et al., 1995). This geochemical signature, therefore, suggests the participation of biotite as reactant during melting, and supports previous evidence of peritectic garnet indicating biotite-dehydration melting as a major contributor to this leucogranite.

The garnets in leucogranite 06 were petrographically identified as having inclusion-rich peritectic cores and overgrowths with crystallographically oriented rutile needles and lobate quartz inclusions, suggesting later growth within a melt. Results of garnet major element profiles show growth zoning, with a decreasing spessartine component from core to rim. The core has a spessartine fraction of 0.46-0.37, notably higher than garnets previously reported from this region (Spencer et al., 2012a). Trace element data was not retrievable from the core due to the abundance of inclusions <10 µm across. The intermediate mantle zone shows spessartine decrease slowly from 0.37-0.26, alongside elevated concentrations of Ti, Sn, and Sc, with decreasing P, Nb, and Ta, and increasing Y (Figure 3.15b). This occurs across the region with rutile needles.

The aim of the laser ablation analyses was to determine the composition of the garnet in this region. Spot analyses with coupled Ti and Nb concentrations in time-resolved element profiles (indicative of rutile) were discarded from the dataset, to avoid analyses with significant rutile contamination. The remaining points suggested Ti concentrations of >1000 ppm in the garnet itself. Similarly, analyses with P concentrations coupled with Ca or rare earth elements (indicative of apatite and/or monazite) were discarded to reduce the contamination from phosphate mineral inclusions.

The rim has the lowest spessartine component (0.26-0.12) with sustained Y concentrations of >500 ppm. The zoning of Y reflects overall abundance in the chondrite-normalised REE profiles, with an initially flat pattern of HREEs near the core that increase in concentration towards a maximum at the intermediate mantle and rim zone boundary before decreasing again (Figure 3.16). This zoning is described in granite-hosted peritectic garnets from Mkhondo Valley Metamorphic Suite, Eswatini (formerly Swaziland), and explained as peritectic garnet growth rates being faster than the rate of HREE-rich accessory phase dissolution in the melt; thus peritectic crystal growth is in disequilibrium with the melt (Taylor and Stevens, 2010).

Crystallographically oriented rutile needles in garnet are associated with temperature of >800°C, as the compatibility of Ti in garnet is increased with temperature and later exsolves during cooling (Hwang et al., 2007; Proyer et al., 2013; Axler and Ague, 2015), aligning the $(103)_{Rt}$ and $(111)_{Grt}$ planes (Hwang et al., 2016). This suggests locally higher temperature conditions are responsible for the onset of biotite-dehydration melting in the source of leucogranite 06, in order to support high initial Ti concentrations in the garnet.

3.4.4 Volumes and spatial relationships of melting

The highest volume % melt production, either as leucosomes (Table 2.3) or mobilised leucogranite, is recorded in samples with petrographic and geochemical signatures indicative of muscovite-dehydration. Trends in calculated Ti-in-biotite temperatures agree with this observation as muscovite-dehydration is associated with higher temperatures than fluid-present melting. Fluid-present melting is also unlikely to form large mobilised melt bodies as the fluid-present solidus forms a negative slope in P-T space along the prograde path, making unlikely that melt can leave the protolith (Harris et al., 1995).

Samples from the boundary of the Badrinath and Pandukeshwar Formations, migmatites 08 and 09b, and orthogneiss 10, display petrographic and/or geochemical signatures that indicate fluid-present melting. The BSZ is likely responsible for the availability of aqueous fluid in this region, and as such, inducing melt in the over-lying migmatites and orthogneiss. Fluid-present melting is not solely controlled by stratigraphic height or proximity to a shear zone, as migmatite samples 05b and 07c share these signatures but were collected NW of Mana, some ~8 km north of the shear zone, approximately halfway up the stratigraphy of the Badrinath Formation (Spencer et al., 2012a). Migmatite 11a, from the Joshimath Formation, also has fluid-present melting signatures.

3.5 Summary

Sample groups previously identified as having petrographic textures suggestive of fluid-present, muscovite-dehydration, and biotite-dehydration melting, each have appropriate major phase geochemical signatures. Fluid-present melting is characterised by low Rb/Sr values, low Sn concentrations in micas, and high Ba and Eu concentrations in feldspars, while muscovite-dehydration melting has high Rb/Sr, high Sn in micas, and low Ba and Eu in feldspars. Biotite-dehydration melting shares the same signatures as muscovite-dehydration, but with even higher Rb/Sr and lower Ba and Eu concentrations in feldspars. These signatures are ultimately attributed to the ratio of mica and plagioclase in the protolith that were consumed during melting (Harris et al., 1993, 1995; Gao et al., 2017).

Temperatures calculated using the Ti-in-biotite thermometer indicate lower temperatures for migmatites with fluid-present melting signatures (<750°C) and higher temperatures for those with muscovite-dehydration signatures (>750°C). There is typically a difference of 70-80°C between the two groups, consistent with temperatures determined through independent phase equilibrium modelling from the upper and lower Badrinath Formation (Iaccarino et al., 2017; Benetti et al., 2021). Further work is necessary to determine the relationship between Ti-in-biotite temperatures and a_{TiO_2}, especially in the presence of a melt or fluid. However, retrograde Fe-Mg exchange is unlikely to have a significant impact on calculated temperatures from typical metapelites of the GHS.

Garnets in migmatites have mostly flat major element concentration profiles in line with previous studies (Spencer et al., 2012a), which is to be expected for 1-2 mm-sized garnets residing at peak temperatures of >650°C for >5 Ma (Spear, 2014; Caddick et al., 2010). Garnets in leucogranite samples, however, record major element profiles that suggest growth zoning. Garnets from 01d show typical chondrite-normalised REE profiles suggestive of garnet crystallisation in a leucogranitic melt, while garnets in sample 06 have peritectic cores which continued to grow in a melt, temporarily under disequilibrium conditions with other HREE-bearing phases. The exsolution of acicular rutile in garnets from leucogranite 06 suggests peak temperatures of >800°C (Proyer et al., 2013).

4 The timing, conditions, and sources of melt generation

4.1 Introduction

In previous chapters, petrographic textures of leucogranites, migmatites, and orthogneiss from the Garhwal Himalaya were linked to major phase geochemistry and to melt-forming reactions, both fluid-present and fluid-absent. However, source contributions (apart from proximal sources retained in migmatites), conditions during melting, and the relative timing of melt reactions are yet to be determined. The presence of partial melt strongly affects rock strength, and in turn affects the evolution of mountain belts. As such, knowing what is melting, how much is melting and when it is melting is important for constraining tectonic evolution and for this to be accomplished, data must be examined from accessory phases that record this information during anatectic processes.

In this chapter, I examine U-Th-Pb crystallisation ages of zircon and monazite, together with trace elements and combined Hf-O isotopes in zircon, to temporally constrain partial melting events and inform source-melt chemistry. These results, in conjunction with melt reactions ascribed to samples through petrographic examination and major phase geochemistry, will delineate the evolution of melt generation in the Garhwal GHS.

4.1.1 Zircon

Zircon ($ZrSiO_4$) makes for an exceptional tool in geochronology as it is found as an accessory phase in most felsic igneous rocks (Roberts and Spencer, 2015), and U is somewhat compatible with its crystal structure, while Pb is excluded (Hoskin and Schaltegger, 2003; Watson et al., 1997). As such, the majority of Pb measured in zircon will be radiogenic in origin, as opposed to non-radiogenic 'common' Pb, allowing for greater precision in U-Pb dating techniques. However, in systems where Pb has been incorporated into zircon, or grains measured are particularly young and therefore low in radiogenic Pb, corrections can be applied to bring the isotopic ratios of ^{206}Pb, ^{207}Pb, ^{235}U, and ^{238}U back into agreement with each other, or concordance (Vermeesch, 2021), such as the Stacey-Kramers two-stage isotope evolution model (Stacey and Kramers, 1975). U-Th-Pb isotopes in zircon also have a closure temperature typically >800°C and are, therefore, unlikely to be reset by post-anatectic processes (Lee et al., 1997).

It is important to know when zircon crystallises because melt generation, migration, and crystallisation is a long-lived process, while zircon dates only provide a snapshot in time. In migmatitic systems, the bulk of zircon crystallisation occurs post-solidus at the point of Zr-saturation, dependent on temperature and bulk composition (Yakymchuk and Brown, 2014; Boehnke et al., 2013). Zircon will initially dissolve in most anatectic melts, with Zr-saturation being reached with increasing Zr concentration and decreasing temperature, resulting in the precipitation of zircon both as new grains and as rim overgrowth on entrained zircon (Yakymchuk and Brown, 2014). Zircon that has precipitated from a melt or fluid in this way can be texturally identified, using cathodoluminescence (CL) imaging, by characteristic regular internal polygonal, oscillatory, or sector zoning with largely euhedral crystal forms (Rubatto, 2017).

Oxygen and hafnium isotopes in zircon record source rock information. Oxygen isotopes in zircon are stable (i.e. independent of age) and are resistant to diffusion (Watson and Cherniak, 1997). The isotopic ratio of oxygen is presented as δ^{18}O, with ^{18}O/^{16}O values normalised to Vienna Standard Mean Ocean Water (VSMOW). The δ^{18}O value of a magma will reflect that of the source rock(s), and in turn, the δ^{18}O value of zircon reflects that of the magma it crystallised from (Valley et al., 2005). Various geological reservoirs of oxygen isotopes are well constrained, with values for the 5.3 ±0.6 ‰ for the mantle, 8-10 ‰ for continental crust, and 10-15 ‰ for sediments (Figure 4.1) (Roberts and Spencer, 2015; King et al., 1998), with δ^{18}O values effectively increasing with the degree of sedimentary recycling. For Hf isotopes, ^{176}Hf/^{177}Hf is compared to the chondritic uniform reservoir (CHUR), in the εHf notation (Blichert-Toft and Albarède, 1997; Patchett and Tatsumoto, 1981). This is used to date the timing of extraction of the source rock from the mantle (Vervoort and Kemp, 2016). Combined Hf-O isotope analysis, alongside U-Th-Pb dating, of the same growth domain, e.g. rim or core, can be used in granitic rock to reveal the relative proportions of mantle and crustal contributions during melting (Kemp et al., 2006, 2007). Granites from the GHS in Bhutan show no input from the mantle and are derived entirely from sediments and continental material (Hopkinson et al., 2017).

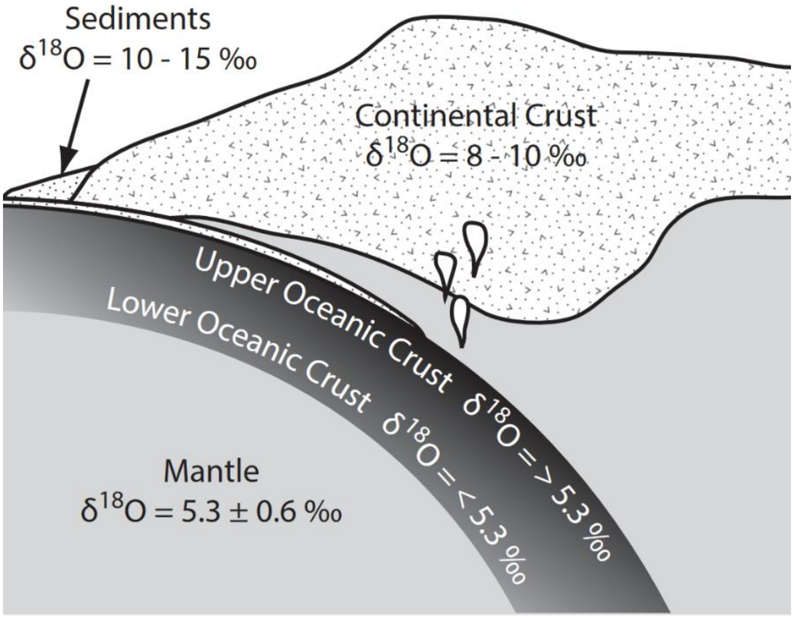

Figure 4.1 – Typical δ^{18}O values of geological reservoirs relevant to zircon growth and crystallisation. After Roberts and Spencer (2015) and King et al. (1998). CC BY 3.0

Zircon can be used to gain information on the chemical and physical conditions of the host environment at the point of crystallisation, as the trace element budget of the system is reflected in the trace element budget of zircon (Claiborne et al., 2010). Ti concentration may be used to constrain the temperature of crystallisation via Ti-in-zircon thermometry, as Ti substitution in zircon is primarily temperature dependent (Ferry and Watson, 2007). Y concentrations in zircon are influenced by the presence or absence of garnet, the other main Y-reservoir commonly coexisting with zircon in pelitic rocks (Rubatto, 2002). Chondrite-normalised Ce and Eu anomalies are useful proxies for oxidation state, with relatively enriched Ce and Eu implying oxidising conditions (Trail et al., 2012). In conjunction, these measurements are powerful tools to aid in the contextualisation of zircon crystallisation and its various isotopic values.

4.1.2 Monazite

Monazite ((Ce, La, Th, Nd)PO_4) is another accessory phase that is widely used as a geochronometer, as it readily incorporates Th and U during crystallisation, while excluding Pb (Montel et al., 1996). Monazite is known to form in rocks of pelitic bulk composition during prograde metamorphism (sub-solidus) (Rubatto et al., 2001), where it is expected to largely dissolve and re-precipitate during anatexis and melt crystallisation (Yakymchuk and Brown, 2014). As such, monazite from migmatites and leucogranites in this study are likely to record the timing of melt crystallisation. Previous studies of monazite in leucogranites from the Himalaya have found semi-continuous crystallisation of monazite over ~12 Ma, interpreted as pulsed melt emplacement (Lederer et al., 2013).

4.2 Methods

Of the twenty key samples described in Chapter 2, eighteen were selected for zircon and monazite separation and mounting. Sequential analyses of oxygen (SIMS), U-Th-Pb (LA-ICP-MS), and Hf isotopes and trace element concentrations (specifically Ti, Y, Nb, REEs, Hf, Th, and U) (LASS) were performed on mounted zircon grains. Analyses were ordered in this way as the oxygen isotope measurements were the least destructive, followed by U-Th-Pb dating, which then allowed for targeted analysis of Himalaya-aged rims for Hf isotope and trace element measurements . Monazite U-Th-Pb data was also collected from fourteen of these samples. Zircon and monazite analyses for each sample are summarised in Table 4.1.

Table 4.1 – Analytical techniques applied to resin-mounted zircon and monazite grain separates. Entries of '~' indicate analyses with no ages younger than 45 Ma, interpreted as mixed or pre-Himalayan (Copley et al., 2010).

Sample ID	**Rock Type**	**Mount**	**Zircon**				**Monazite**
			$\delta^{18}O$	**U-Th-Pb**	**εHf**	**Trace**	**U-Th-Pb**
BAD01d	Leucogranite	T1620	x	x	x	x	x
BAD02a	Migmatite	T1620	x	x	x	x	x
BAD02b	Migmatite/ Leucosome	T1620	x	x	x	x	x
BAD03	Leucogranite	T1622	x	x	x	x	
BAD04a	Migmatite	T1620	x	x	x	x	x
BAD04b	Migmatite	T1620	x	x	x	x	x
BAD05b	Migmatite	T1623	~	~	~	~	x
BAD06	Leucogranite	T1622	x	x	x	x	x
BAD07a	Migmatite	T1622	x	x	x	x	
BAD07b	Leucogranite	T1622	x	x	x	x	
BAD07c	Migmatite	T1622	x	x	x	x	x
BAD08	Migmatite	–					
BAD09a	Meta-arkose	–					
BAD09b	Migmatite	T1623	x	x	x	x	x
BAD10	Orthogneiss	T1623	x	x	x	x	x
BAD11a	Migmatite	T1623	x	x	x	x	
BADf02	Migmatite	T1621	x	x	x	x	x
BADf03	Orthogneiss	T1621	x	x			~
BADf04	Leucogranite	T1621	x	x	x	x	x
BADf13	Migmatite	T1621	x	x	x	x	x

4.2.1 Zircon and monazite separation

For each sample, ~1 kg or up to half the sample's total weight, whichever was lower, was crushed for heavy-mineral separation. Samples were initially prepped using a hardened steel manual splitter and Fritsch jaw crusher to produce rock fragments <10 mm across. At this point, twelve garnet grains were removed from leucogranite sample 06 for mounting in resin. Samples were then sieved, and sample fractions >250 µm were manually crushed using an agate pestle and mortar. Preparation areas and tools were brushed down and cleaned with isopropyl alcohol between each sample.

Heavy minerals were isolated in the mineral separation laboratory at the University of Portsmouth. Each sample was processed using the Holman Wilfley gravity separation table, with subsequent removal of magnetic grains using a covered neodymium magnet and heavy-liquid density separation (sodium polytungstate solution). Zircon and monazite were identified and picked from the remaining heavy fraction using optical microscopy and mounted on four 1" epoxy resin rounds (T1620-T1623) alongside grains of Plešovice (Sláma et al., 2008), Penglai (Li et al., 2010), and Qinghu (Li et al., 2013) zircon standards.

4.2.2 Imaging

Greyscale panchromatic cathodoluminescence (CL) images of zircon were taken using a MIRA3 TESCAN fitted with a Cathodoluminescence Detector through a contractor at the Guangzhou Institute of Geochemistry, Chinese Academy of Sciences. The imaging was completed in one analytical session, from the 2nd-3rd of August 2019, with a working distance of 16 mm and a voltage of 7 kV.

Semi-quantitative compositional maps of monazite grains were collected using a field-emission Zeiss Supra 55 VP fitted with an Oxford Instrument X-Max 50 mm^2 EDS detector at the Open University. Analytical sessions for mounts T1620, T1621, and T1622 were carried out between the 13th and 17th of May 2021, while T1623 grains were imaged between the 22nd and 24th of September 2021. The beam was set to a voltage of 20 keV and a current equivalent of 2.0 nA (60 µm aperture). Each grain map took approximately 1 hour and 45 minutes.

4.2.3 SIMS zircon oxygen isotope analysis

Oxygen isotopic compositions of zircon rims, identified using CL images, were measured using a CAMECA IMS 1280 secondary ion mass spectrometer (SIMS) at the Guangzhou Institute of Geochemistry, Chinese Academy of Sciences. Samples were gold-coated to prevent surface charging. The primary Cs^+ ion beam was set to a voltage of 10 keV and current of 2-3 nA, with a spot diameter of 10-15 µm. Analytical sites were pre-sputtered for 30-35 seconds to remove local Au-coating. Analytical sessions were carried out in early August 2019. Oxygen-18 and oxygen-16 ions were detected simultaneously in two faraday cups. This analytical method is described in detail by Yang et al. (2018), with a six-month long-term precision for Qinghu zircon of 0.44 ‰. Oxygen isotope mass fractionation and drift were monitored by analysing primary zircon standard Penglai ($\delta^{18}O$ = 5.31 ± 0.1 ‰) (Li et al., 2010) every 5 unknowns. Secondary zircon standard Qinghu ($\delta^{18}O$ = 5.40 ± 0.2 ‰) (Li et al., 2013) was analysed every 10 unknowns to assess the quality of mass fractionation and drift correction. Analyses of secondary standard Qinghu yielded mean $\delta^{18}O$ values of 5.55 ± 0.50 ‰, 5.50 ± 0.40 ‰, 5.45 ± 0.40 ‰, and 5.57 ± 0.36 ‰ (2σ) for resin mounts T1620-T1623, respectively.

Oxygen isotope measurements are reported in the conventional $\delta^{18}O$ notation of measured $^{18}O/^{16}O$ values normalised to Vienna Standard Mean Ocean Water (VSMOW) $^{18}O/^{16}O$ value of 0.0020052 (Baertschi, 1976) and presented in per mil (‰) with the following formula:

$$\delta^{18}O_{Sample} = \left[\frac{(^{18}O/^{16}O)_{Sample}}{0.0020052} - 1\right] \times 1000\ (‰)$$

For full zircon oxygen isotope analysis standard measurements, see Appendix D.

4.2.4 Zircon laser ablation U-(Th)-Pb analysis

U-(Th)-Pb isotopes were measured in zircon rims on top of the sites of SIMS measurements of oxygen isotopes. Au-coating was removed from the resin mounts prior to this analysis. Samples were ablated using a Resonetics RESOltuion M-50A-LR incorporating a Compex 102 excimer laser and measured using an Agilent 7700s quadrupole ICP-MS, with high-purity Ar as the plasma gas (flow rate of 0.98 L/min) at Curtin University, Australia. Spot analyses were run using a fluence of 1.7 J/cm^2, a repetition rate of 7 Hz, and a spot size of 23 µm, with each analysis collecting 30 seconds of background. The sample cell was flushed by He and N_2 with flow rates of 0.68 L/min and 2.8 mL/min, respectively. Elements measured on the quadrupole were monitored for 0.01 seconds each, with the exception of ^{204}Pb, ^{206}Pb, ^{207}Pb, ^{208}Pb (all 0.03 seconds), ^{232}Th (0.0125 seconds), and ^{238}U (0.0125 seconds). Reference material analyses bracketed every 22 unknowns.

The primary reference material used for U-Pb dating was zircon standard 91500 (1062.4 ± 0.4 Ma) (Wiedenbeck et al., 1995), while Plešovice (337.13 ± 0.37 Ma) (Sláma et al., 2008), GJ-1 (601.92 ± 0.7 Ma) (Jackson et al., 2004), and OG1 (3465.4 ± 0.6 Ma) (Stern et al., 2009) were used as secondary age standards. During this analytical session, 91500 yielded a $^{206}Pb/^{238}U$ weighted average age of 1062.6 ± 2.4 Ma (MSWD = 0.63, n = 20), Plešovice yielded a $^{206}Pb/^{238}U$ weighted average age of 341.8 ± 0.5 Ma (MSWD = 2.1, n = 19), GJ-1 yielded a $^{206}Pb/^{238}U$ weighted average age of 616.3 ± 1.0 Ma (MSWD = 1.2, n = 20), and OG1 yielded a $^{206}Pb/^{238}U$ weighted average age of 3491 ± 1.7 Ma

(MSWD = 11, n = 20). Calculated average ages and uncertainties of the secondary standards overlap within 2.4 % of the accepted values. Time-resolved mass spectra were reduced in Iolite (Paton et al., 2011) with baseline signal subtraction and time-resolved spectra checked for inclusion signals and ablation issues. The Iolite U_Pb_Geochronology3 data reduction module was used to propagate uncertainty and correct for laser-induced elemental fractionation (Paton et al., 2010). For full zircon U-(Th)-Pb analysis standard measurements, see Appendix D.

Reported zircon ^{206}Pb/^{238}U dates were corrected using the Stacey-Kramers two-stage isotope evolution model (Stacey and Kramers, 1975). This assumes discordance is solely caused by common Pb contamination (Vermeesch, 2021). This assumption can be made as Pb diffusion is unlikely to have occurred from either metamorphic overprinting or from accumulated fission damage due to the relative age of the samples and the absence of metamict zircon rim morphologies (Mezger and Krogstad, 2004). Uptake of radiogenic Pb during crystallisation cannot be corrected (Andersen et al., 2019), but the effect of this is assumed to be small due to the incompatibility of Pb in zircon.

4.2.5 Zircon laser ablation split-stream Lu-Hf isotopes and trace element analysis

Trace element composition and Lu-Hf isotopes were measured in zircon rims on top of the 23 µm ablation mark left by U-(Th)-Pb analysis, using laser ablation split-stream (LASS) at Curtin University, Australia. Samples were ablated using the same laser conditions as U-(Th)-Pb analysis, except for a 33 µm spot size. Half the split was sent to a Nu Instruments Plasma II MC-ICP-MS with Ar as the plasma gas (flow rate of 0.98 L/min) for Lu-Hf isotopic measurements, where masses for ^{172}Yb. ^{173}Yb, ^{175}Lu, ^{176}Hf+Yb+Lu, ^{177}Hf, ^{178}Hf, ^{179}Hf, and ^{180}Hf were measured simultaneously. The other half was sent to an Agilent 7700s quadrupole ICP-MS, with high-purity Ar as the plasma gas (flow rate of 0.98 L/min) for trace element measurements (Ti, Y, Zr, Nb, La, Ce, Pr, Nd, Sm, Eu, Gd, Dy, Yb, Lu, Hf, Th, and U). Reference material analyses bracketed every 22 unknowns.

For Lu-Hf measurements, zircon standard Mudtank (0.282507 ± 0.000008) (Fisher et al., 2014) was used as the primary reference to monitor accuracy and precision of internally corrected Hf isotope ratios (^{179}Hf/^{177}Hf = 0.7325). 91500 (0.282306 ± 0.000008) (Woodhead and Hergt, 2005), Plešovice (0.282482 ± 0.000013) (Sláma et al., 2008), R33 (0.282764 ± 0.000014) (Fisher et al., 2014), and GJ-1 (0.282000 ± 0.000005) (Morel et al., 2008) were used as secondary standards. During the analytical session, Mudtank yielded a corrected ^{176}Hf/^{177}Hf average ratio of 0.282503 ± 0.000039 (MSWD = 0.77, n = 19), 91500 yielded a corrected ^{176}Hf/^{177}Hf average ratio of 0.282276 ± 0.000049 (MSWD = 0.82, n = 19), Plešovice yielded a corrected ^{176}Hf/^{177}Hf average ratio of 0.282458 ± 0.000037 (MSWD = 0.9, n = 10), R33 yielded a corrected ^{176}Hf/^{177}Hf average ratio of 0.282698 ± 0.000038 (MSWD = 0.71, n = 19), and GJ-1 yielded a corrected ^{176}Hf/^{177}Hf average ratio of 0.282001 ± 0.000041 (MSWD = 0.71, n = 19). Average corrected values of the secondary standards are within

0.025 % of the accepted values. The raw values were reduced using Iolite (Paton et al., 2011), with isobaric interference of ^{176}Yb with ^{176}Hf and accuracy of mass bias corrections based on analysed stable isotope ratios of standard assessed using the workflow of Spencer et al. (2020). The mean ^{178}Hf/^{177}Hf values of the standards Mudtank, 91500, Plešovice, R33, and GJ-1 were 1.46720 ± 0.00007, 1.46720 ± 0.00009, 1.46720 ± 0.00007, 1.46720 ± 0.00007, and 1.46720 ± 0.00008, while the mean ^{180}Hf/^{177}Hf values were 1.88690 ± 0.00042, 1.88702 ± 0.00044, 1.88699 ± 0.00043, 1.88703 ± 0.00043, and 1.88700 ± 0.00040, respectively. These ratios are in accordance with the natural stable Hf isotope ratios of 1.46717 for ^{178}Hf/^{177}Hf and 1.88666 for ^{180}Hf/^{177}Hf (Blichert-Toft and Albarède, 1997).

Hf isotope measurements were corrected using the ^{206}Pb/^{238}U ages to report the initial value in the conventional εHf notation of measured ^{176}Hf/^{177}Hf values normalised to the CHUR ^{176}Hf/^{177}Hf value of 0.282785 (Bouvier et al., 2008), with the following formula:

$$\varepsilon Hf_{Sample} = \left[\frac{(^{176}Hf/^{177}Hf)_{Sample}}{(^{176}Hf/^{177}Hf)_{CHUR}} - 1\right] \times 10^4$$

Trace element concentrations used NIST SRM 610 glass as the primary standard and NIST SRM 612 as the secondary standard. Si was used as the index standardisation element. Accuracy and precision of NIST SRM 612 analyses were accessed using published values (Gao et al., 2002) and were found to be in relatively good agreement for LASS analysis of a 33 µm spot, with relative standard deviations of 12-20 %. For full zircon Lu-Hf isotopes and trace element LASS analysis standard measurements, see Appendix D.

4.2.6 Monazite laser ablation U-Th-Pb analysis

U-Th-Pb isotopes were measured on monazite grains using an ESI/NWR193UC laser and TV2 ablation cell, with He in the cell and Ar make-up gas with carrier gas flow rate of 0.6 L/min, and Nu Instruments Attom SC-ICP-MS (Ar flow rate of 0.7 L/min) at the Geochronology and Tracers Facility, British Geological Survey, UK. Two sessions were carried out in April 2022. Spot analyses were run using a fluence of 3 J/cm^2, a repetition rate of 10 Hz, and a spot size of ~11 µm, with each analysis collecting 30 seconds of background after 30 seconds of wash-out. Element isotopes ^{163}Dy and ^{172}Yb were measured for 0.0052 seconds, ^{206}Pb for 0.0104 seconds, ^{207}Pb and ^{235}U for 0.0208 seconds, ^{208}Pb for 0.0312 seconds, and ^{232}Th for 0.0156 seconds.

The primary reference material used for Pb/U and Th/Pb was monazite standard Bananeira (497.6 ± 1.6 Ma) (Kylander-Clark et al., 2013), while 44069 (421.9 ± 12.0 Ma) (Luo et al., 2020) and FC1 (55.6 ± 0.3 Ma) (Cottle et al., 2012) were used as secondary standards. During analytical sessions one and two, Bananeira yielded a ^{208}Pb/^{232}Th weighted average age of 507.1 ± 3.8 Ma (MSWD =

0.47, n = 33) and 506.8 ± 5.5 Ma (MSWD = 0.12, n = 14), 44069 yielded a ^{208}Pb/^{232}Th weighted average age of 436.8 ± 4.7 Ma (MSWD = 1.6, n = 17) and 421.8 ± 4.7 Ma (MSWD = 1.0, n = 15), and FC1 yielded a ^{208}Pb/^{232}Th weighted average age of 53.2 ± 0.6 Ma (MSWD = 3.3, n = 23) and 53.6 ± 0.7 Ma (MSWD = 1.0, n = 14). Calculated average ages and uncertainties of the secondary standards overlap within 4.65 % of the accepted values. Sample data were reduced using a mean of the ratios approach calculated in the Attolab time-resolved analysis software. No downhole correction is applied to the U-Th-Pb ratios. Fractionation is assumed to be similar between standards and samples. To avoid inaccurate normalisation, the mean of the ablation period (excluding the initial 2-3 seconds to allow for Pb contamination on the surface) is used for both standards and samples. For full monazite U-Th-Pb analysis standard measurements, see Appendix E.

Reported monazite ^{208}Pb/^{232}Th dates were corrected using the Stacey-Kramers two-stage isotope evolution model (Stacey and Kramers, 1975). As with zircon, the assumptions of this correction can be made due to the relatively young age of the samples and incompatibility of Pb in monazite. However, excess ^{206}Pb from the decay of ^{230}Th cannot be easily corrected. Therefore, interpretation and discussion of the monazite ages relies on the ^{208}Pb/^{232}Th dates only.

4.3 Results

4.3.1 Zircon zoning

CL images of the four resin grain mounts (T1620-T1623) show the internal zoning of 1,601 zircon grains across eighteen samples. Two broad groups of zircon rims were discernible: those with oscillatory grey and black rims, getting brighter towards the outer edge of the grain (Figure 4.2), and those with high-contrast rims of an inner dark-grey band and outer bright white band with a sharp contact between the two (Figure 4.3). Samples with zircon grains in the first group, which will be referred to as type 1 zircon, are leucogranite samples 01d, 03, 06, 07b, and f04, and migmatite samples 02a, 02b, 04a, 04b, 07a, f02, and f13. Samples with high-contrast zircon rims, referred to as type 2 zircon, are migmatite sample 05b, 07c, 09b, and 11a, as well as orthogneiss sample 10.

Zircons within these two groups also share external morphologies. Samples with type 1 zircon rims largely form euhedral bipyramidal crystals, 150-200 µm long, although they are commonly fractured. There is, however, a mix of elongate and equant crystals, with samples f02, f04, and f13 forming especially elongate grains. Type 2 zircon rims largely form rounded, subhedral grains, between 100-150 µm long, and are typically more equant than elongate.

The cores of zircon grains are commonly complex with bright and dark oscillatory and sector zoning present across both groups. In samples with type 1 zircon rims, core-rim boundaries are regular with minor pitting. Sample 01d has complex composite cores with irregular growth, and some grains in samples f02, f04, and f13 appear to lack inherited cores. In samples with type 2 zircon rims, cores are rounded, much like the subsequent rim growth.

CL images of analysed zircon grains for each sample with sequential analytical locations marked can be seen in Appendix D.

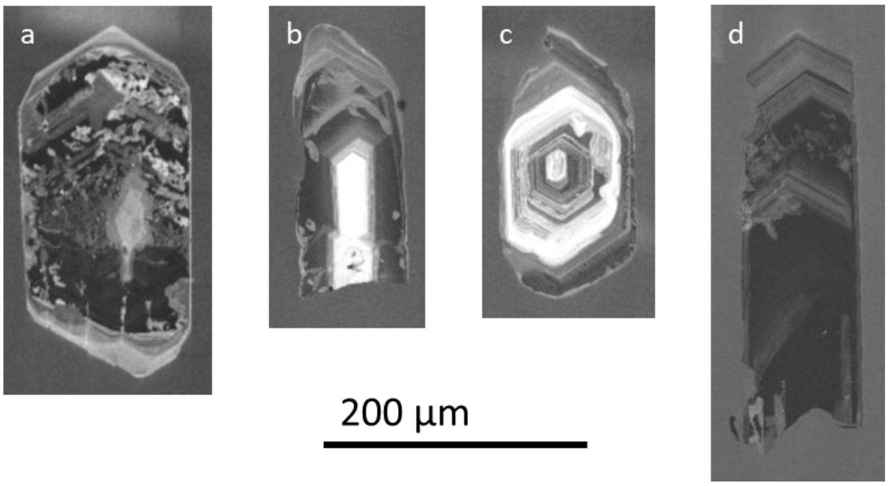

Figure 4.2 – CL images showing examples of zircon grain morphology and internal zonation for samples with oscillatory grey and black rims (type 1). a) Grain with irregular core from 01d, b) Fractured grain from 02a, c) Equant grain from 04b, d) Elongate fractured grain from f02.

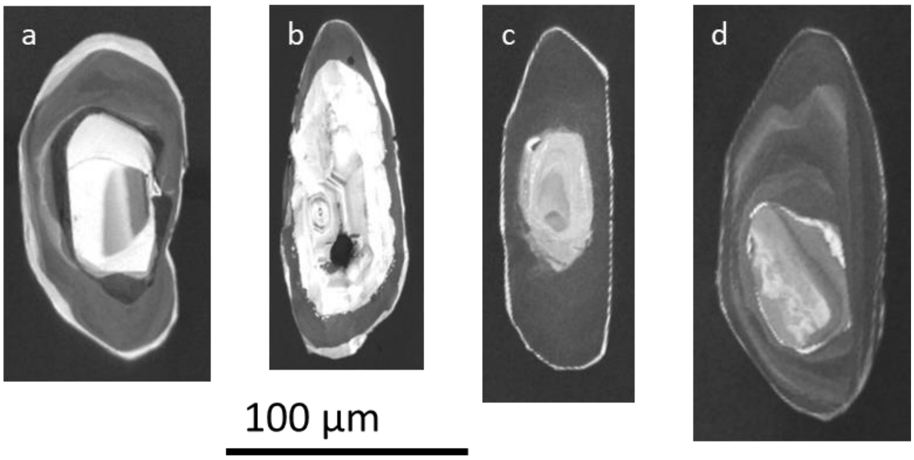

Figure 4.3 – CL images showing examples of zircon grain morphology and internal zonation for samples with high-contrast dark and bright rims (type 2). a) Equant rounded grain from 07c, b) Grain from 09b with large bright core, c) Elongate grain with rounded core from sample 10, d) Grain with irregular rounded core from 11a.

4.3.2 Zircon chemistry

Only the isotopic and trace element results for zircon analyses relevant to the Himalayan orogen (determined as those with $^{206}Pb/^{238}U$ ages younger than 45 Ma (Copley et al., 2010)) are presented here.

Full combined results for analysis of each zircon grain (U-Th-Pb, $\delta^{18}O$, εHf, and trace elements) are presented in Appendix D.

4.3.2.1 U-(Th)-Pb isotopes

After visual checking of the analysis pits, 178 analyses across 17 samples produce $^{206}Pb/^{238}U$ dates relevant to the timescales of the Himalayan orogen. Calculated ages were corrected for common Pb using the Stacey-Kramers two-stage isotope evolution model (Stacey and Kramers, 1975). Uncertainties on $^{206}Pb/^{238}U$ dates are typically ±0.2-0.6 Ma (2σ).

The $^{206}Pb/^{238}U$ corrected dates for each sample are summarised as follows:

- Leucogranite **sample 01d** – 25.3-15.7 Ma from 21 spots across 18 grains (Figure 4.4). Eighteen of these spots yielded ages younger than 18.3 Ma.
- Migmatite **sample 02a** – 35.5-17.4 Ma from 11 spots across 11 grains (Figure 4.5).
- Migmatite leucosome **sample 02b** – 31.6-24.3 Ma from 5 spots across 5 grains (Figure 4.6).
- Leucogranite **sample 03 –** 21.2-14.8 Ma from 19 spots across 19 grains (Figure 4.7).
- Migmatite **sample 04a** – 20.1-14.6 Ma from 6 spots across 6 grains (Figure 4.8).
- Migmatite **sample 04b** – 21.2-18.9 Ma from 5 spots across 4 grains (Figure 4.9).
- Leucogranite **sample 06** – 16.9-14.6 Ma from 3 spots across 3 grains (Figure 4.10).
- Migmatite **sample 07a** – 2 spots across 2 grains dated 18.8 and 13.8 Ma (Figure 4.11).

- Leucogranite **sample 07b** – 18.8-12.8 Ma from 5 spots across 5 grains (Figure 4.12).
- Migmatite **sample 07c** – 33.6-19.3 Ma from 14 spots across 14 grains (Figure 4.13).
- Migmatite **sample 09b** – 21.7-16.5 Ma from 6 spots across 6 grains (Figure 4.14).
- Orthogneiss **sample 10** – 33.4-16.0 Ma from 20 spots across 20 grains (Figure 4.15). Nineteen of these yielded ages older than 20 Ma.
- Migmatite **sample 11a** – 2 spots across 2 grains dated 22.1 and 21.6 Ma (Figure 4.16).
- Migmatite **sample f02** – 23.8-17.9 Ma from 22 spots across 21 grains (Figure 4.17).
- Orthogneiss **sample f03** – 1 spot dated 32.7 Ma (Figure 4.18).
- Leucogranite **sample f04** – 19.7-13.8 Ma from 21 spots across 21 grains (Figure 4.19).
- Migmatite **sample f13** – 21.7-12.3 Ma from 15 spots across 15 grains (Figure 4.20). Twelve of these yielded ages between

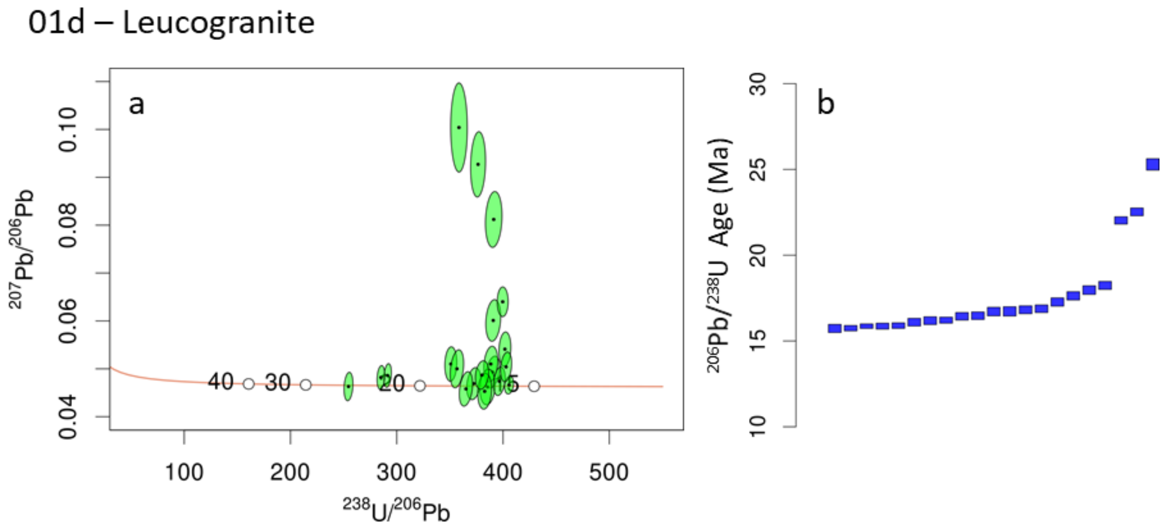

Figure 4.4 – Leucogranite 01d U-Pb results with 2σ error. a) Tera-Wasserburg plot of Himalayan-aged zircon rims. b) Ordered common-Pb corrected ^{206}Pb/^{238}U ages.

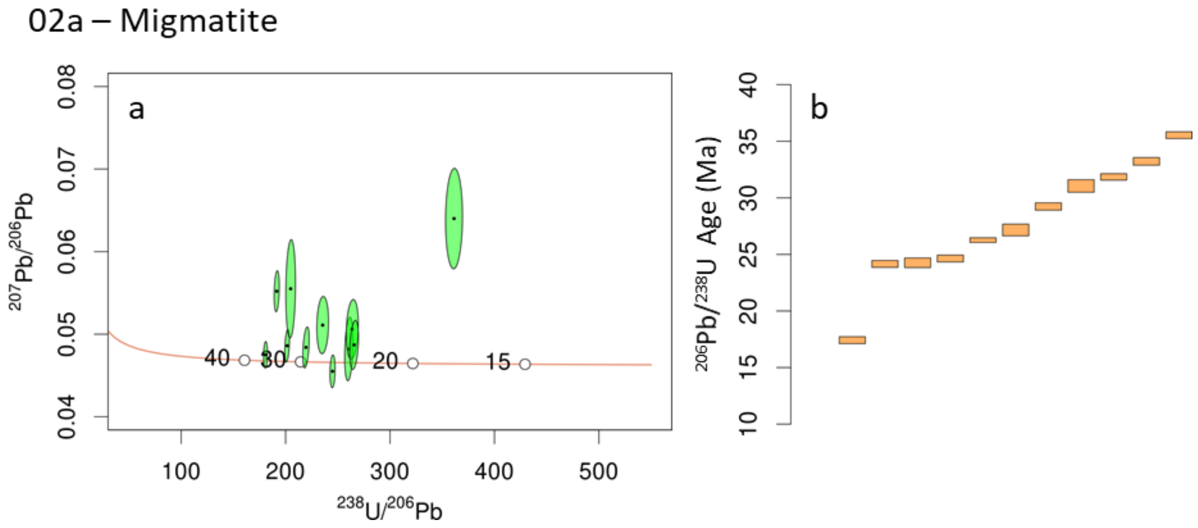

Figure 4.5 – Migmatite 02a U-Pb results with 2σ error. a) Tera-Wasserburg plot of Himalayan-aged zircon rims. b) Ordered common-Pb corrected ^{206}Pb/^{238}U ages.

02b – Migmatite

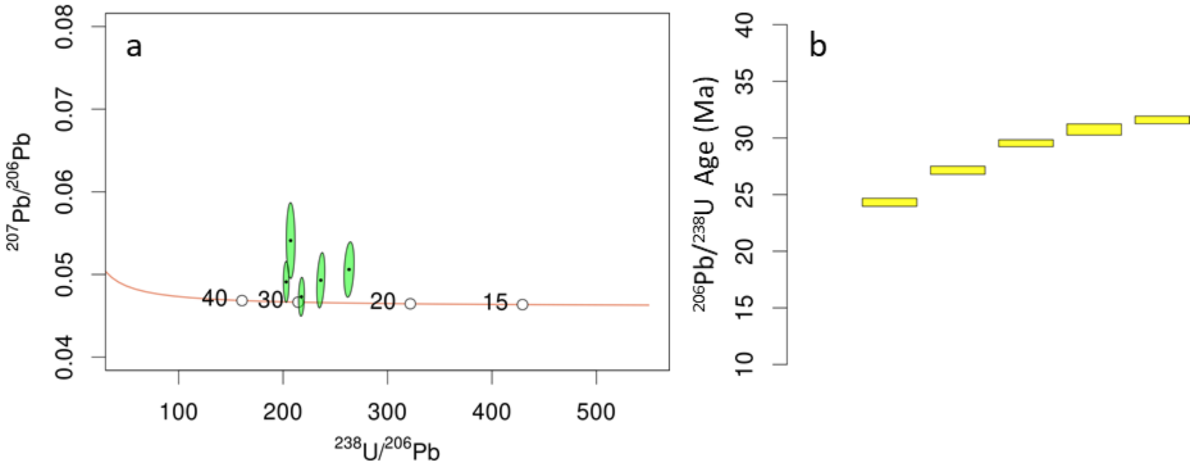

Figure 4.6 – Migmatite 02b U-Pb results with 2σ error. a) Tera-Wasserburg plot of Himalayan-aged zircon rims. b) Ordered common-Pb corrected ^{206}Pb/^{238}U ages.

03 – Leucogranite

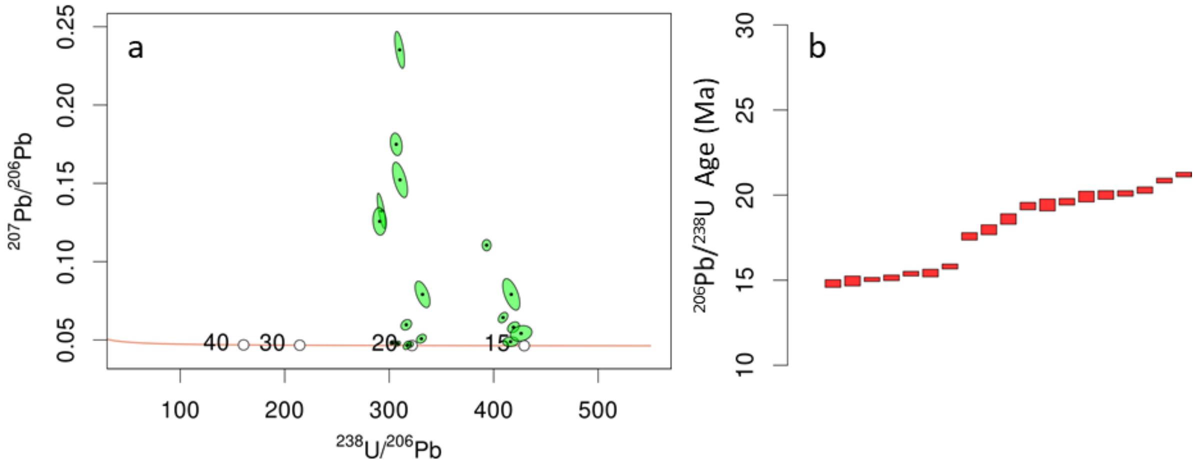

Figure 4.7 – Leucogranite 03 U-Pb results with 2σ error. a) Tera-Wasserburg plot of Himalayan-aged zircon rims. b) Ordered common-Pb corrected ^{206}Pb/^{238}U ages.

04a – Migmatite

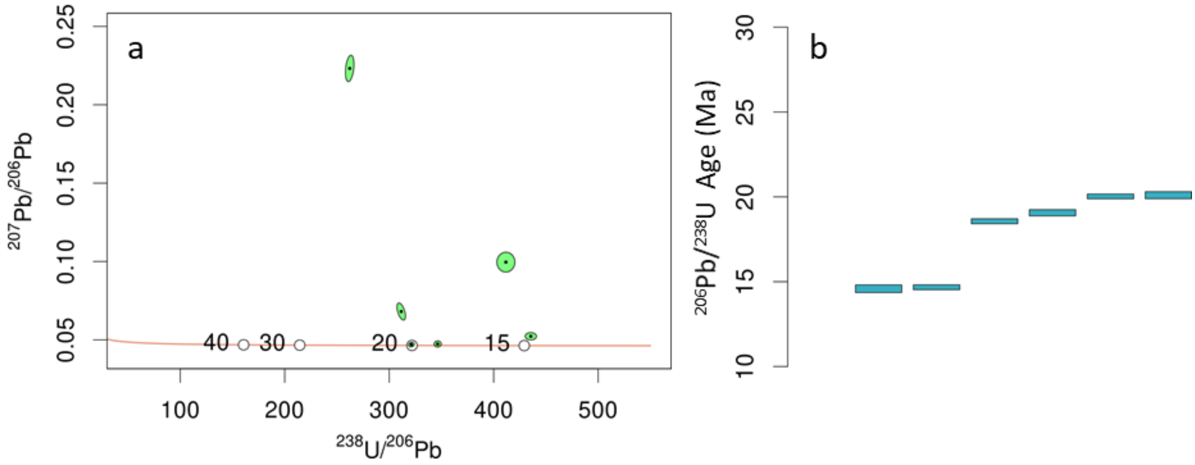

Figure 4.8 – Migmatite 04a U-Pb results with 2σ error. a) Tera-Wasserburg plot of Himalayan-aged zircon rims. b) Ordered common-Pb corrected ^{206}Pb/^{238}U ages.

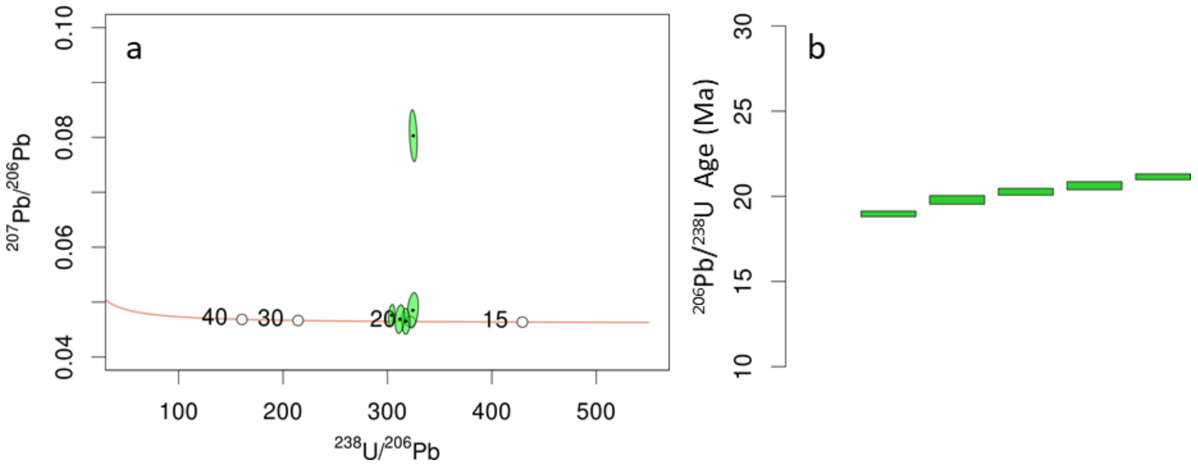
04b – Migmatite

Figure 4.9 – Migmatite 04b U-Pb results with 2σ error. a) Tera-Wasserburg plot of Himalayan-aged zircon rims. b) Ordered common-Pb corrected $^{206}Pb/^{238}U$ ages.

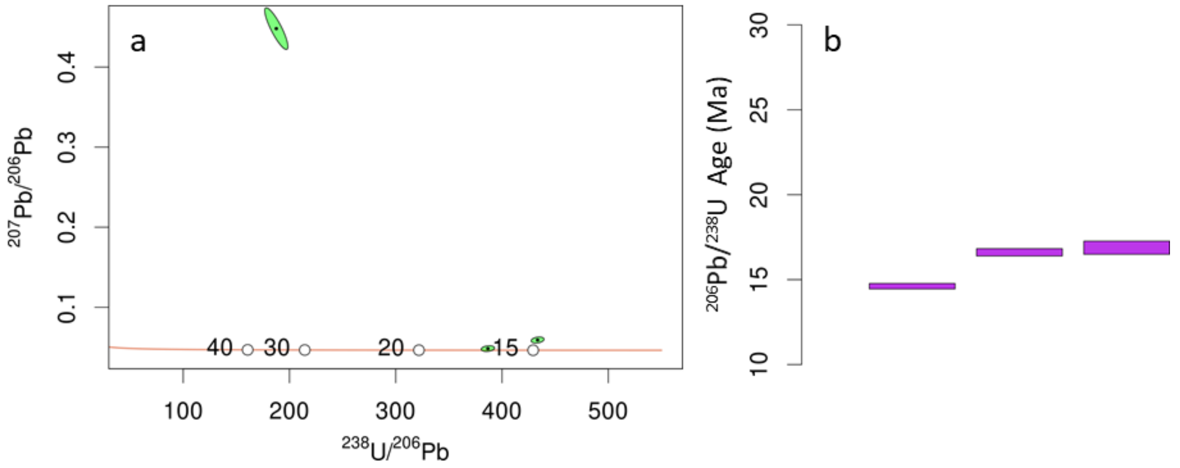
06 – Leucogranite

Figure 4.10 – Leucogranite 06 U-Pb results with 2σ error. a) Tera-Wasserburg plot of Himalayan-aged zircon rims. b) Ordered common-Pb corrected $^{206}Pb/^{238}U$ ages.

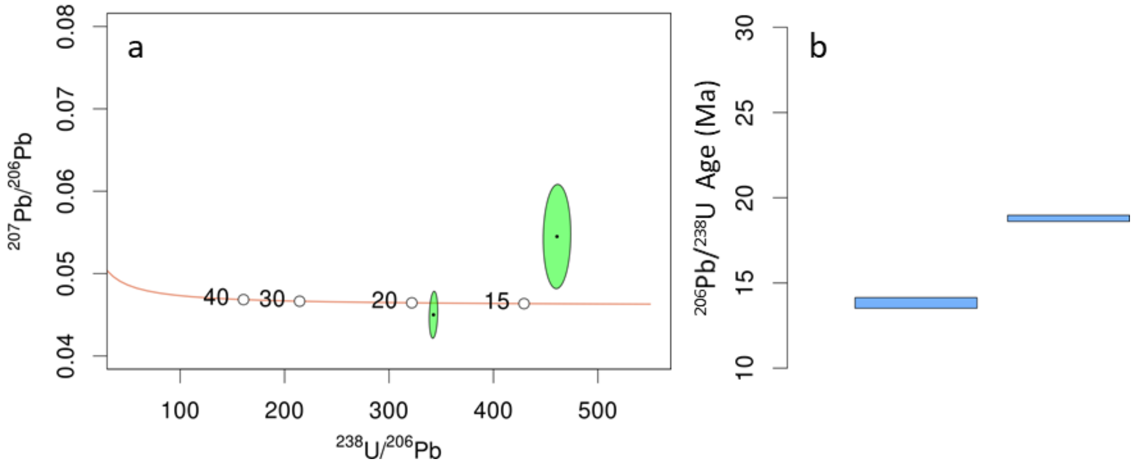
07a – Migmatite

Figure 4.11 – Migmatite 07a U-Pb results with 2σ error. a) Tera-Wasserburg plot of Himalayan-aged zircon rims. b) Ordered common-Pb corrected $^{206}Pb/^{238}U$ ages.

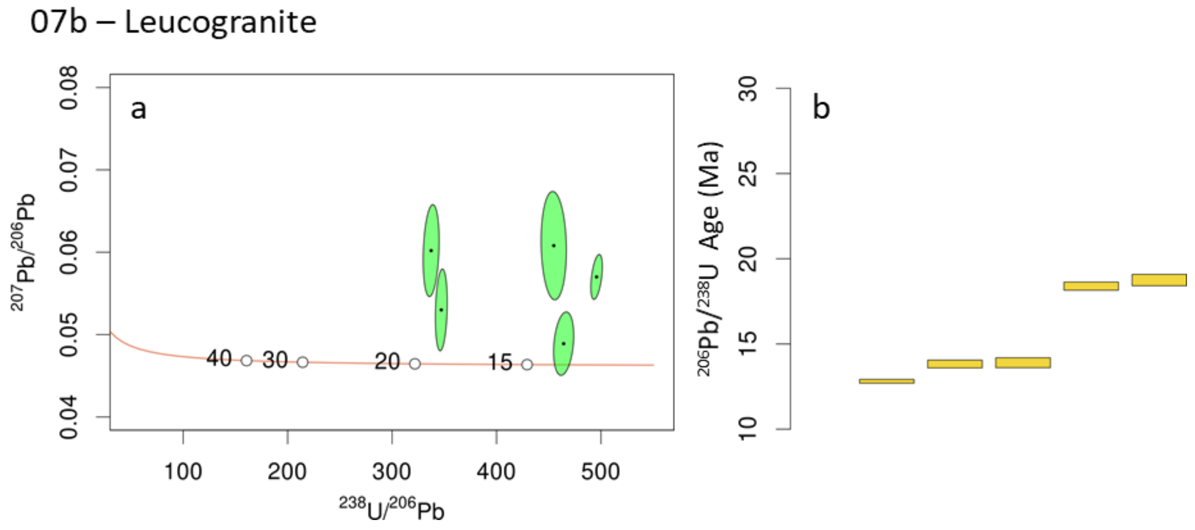

Figure 4.12 – Leucogranite 07b U-Pb results with 2σ error. a) Tera-Wasserburg plot of Himalayan-aged zircon rims. b) Ordered common-Pb corrected $^{206}Pb/^{238}U$ ages.

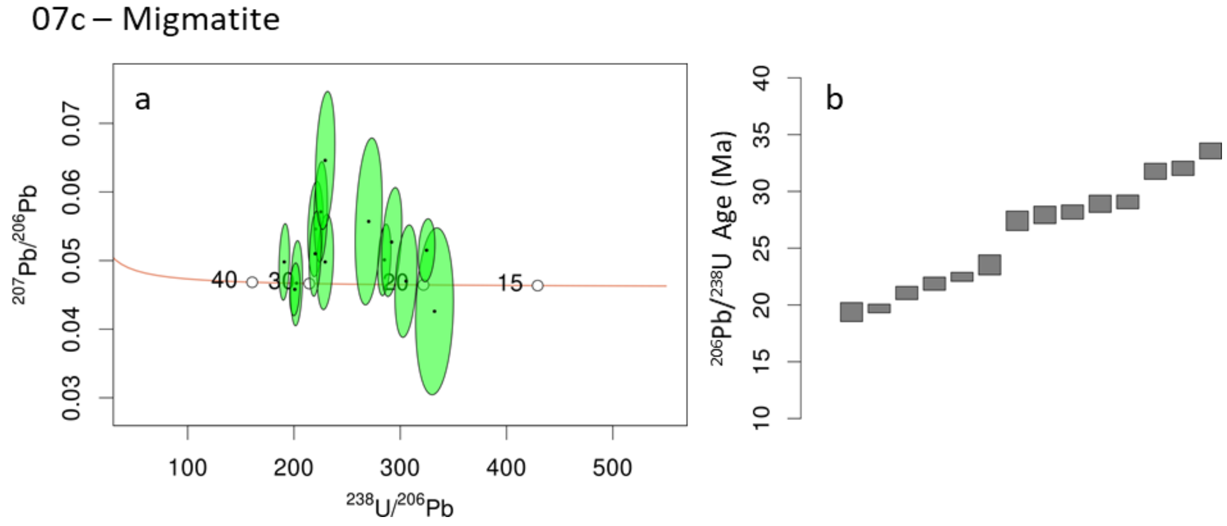

Figure 4.13 – Migmatite 07c U-Pb results with 2σ error. a) Tera-Wasserburg plot of Himalayan-aged zircon rims. b) Ordered common-Pb corrected $^{206}Pb/^{238}U$ ages.

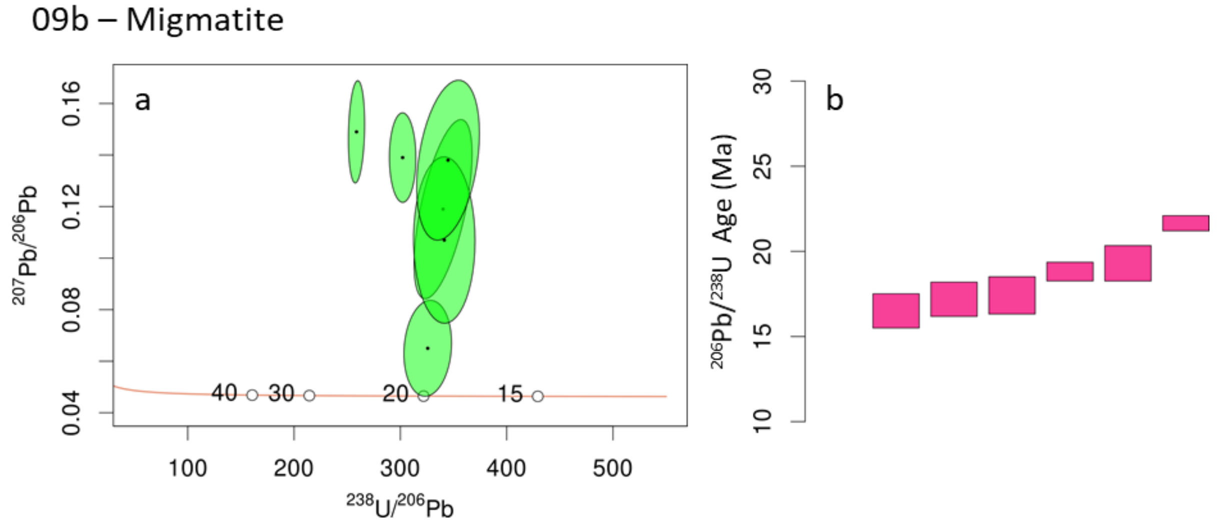

Figure 4.14 – Migmatite 09b U-Pb results with 2σ error. a) Tera-Wasserburg plot of Himalayan-aged zircon rims. b) Ordered common-Pb corrected $^{206}Pb/^{238}U$ ages.

10 – Orthogneiss

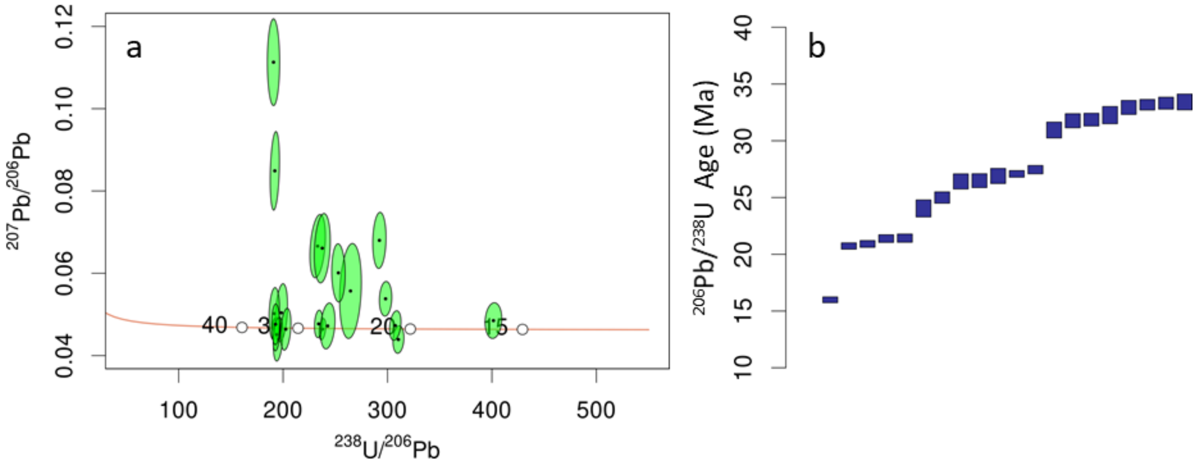

Figure 4.15 – Orthogneiss 10 U-Pb results with 2σ error. a) Tera-Wasserburg plot of Himalayan-aged zircon rims. b) Ordered common-Pb corrected ^{206}Pb/^{238}U ages.

11a – Migmatite

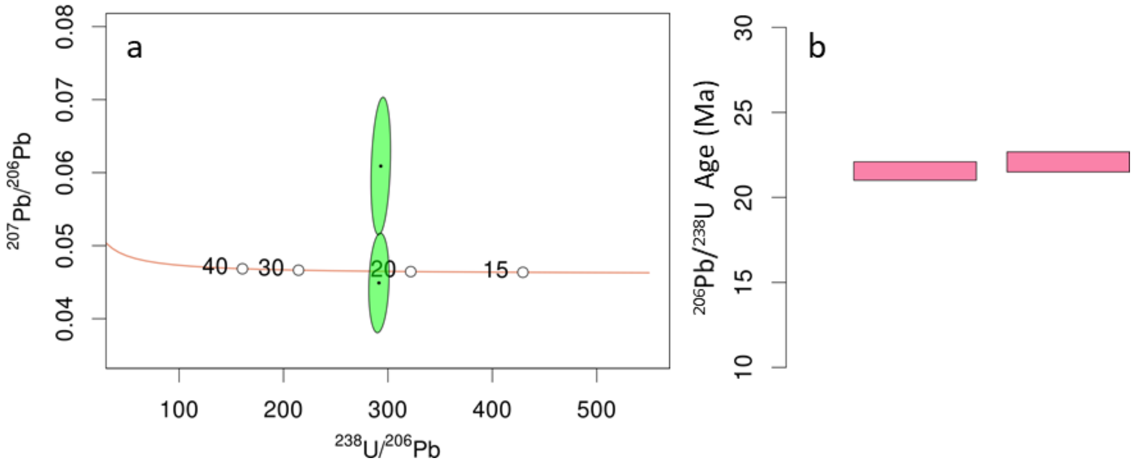

Figure 4.16 – Migmatite 11a U-Pb results with 2σ error. a) Tera-Wasserburg plot of Himalayan-aged zircon rims. b) Ordered common-Pb corrected ^{206}Pb/^{238}U ages.

f02 – Migmatite

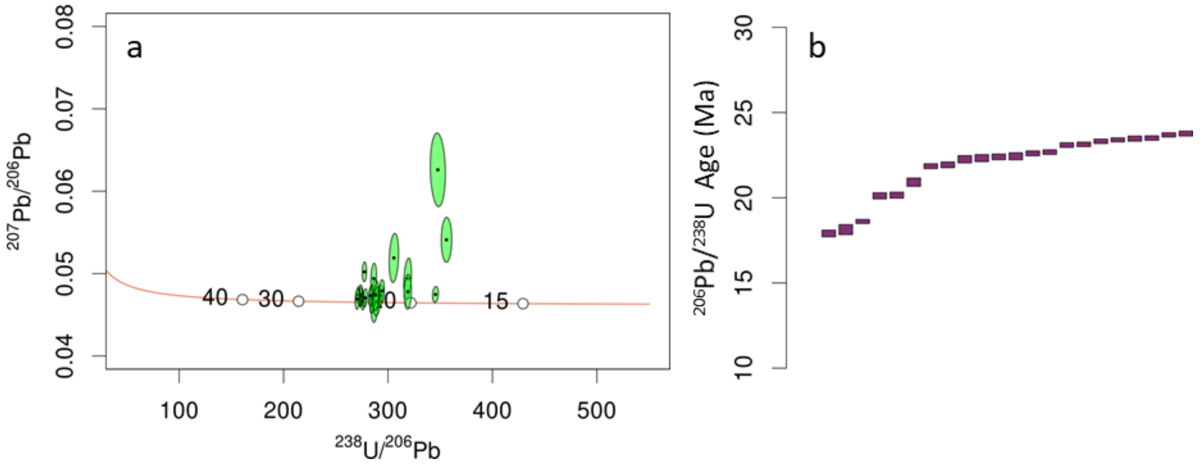

Figure 4.17 – Migmatite f02 U-Pb results with 2σ error. a) Tera-Wasserburg plot of Himalayan-aged zircon rims. b) Ordered common-Pb corrected ^{206}Pb/^{238}U ages.

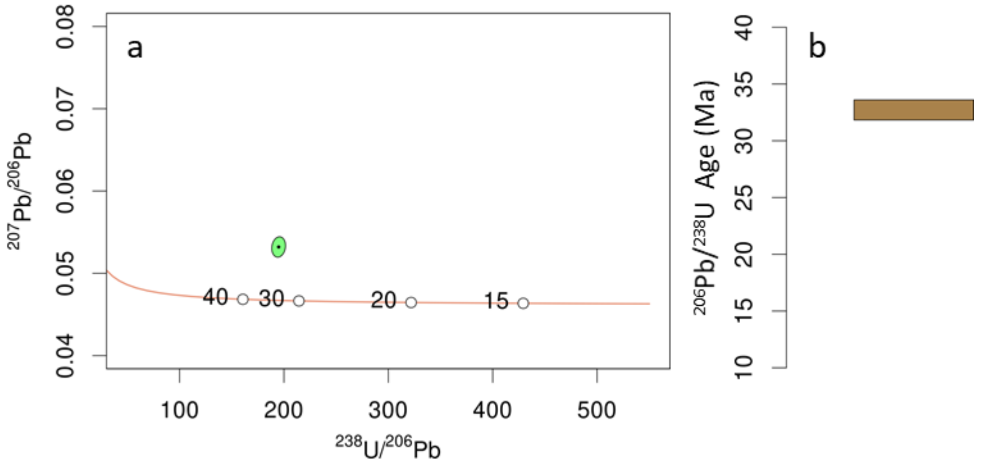
f03 – Orthogneiss

Figure 4.18 – Orthogneiss f03 U-Pb results with 2σ error. a) Tera-Wasserburg plot of Himalayan-aged zircon rims. b) Ordered common-Pb corrected ^{206}Pb/^{238}U ages.

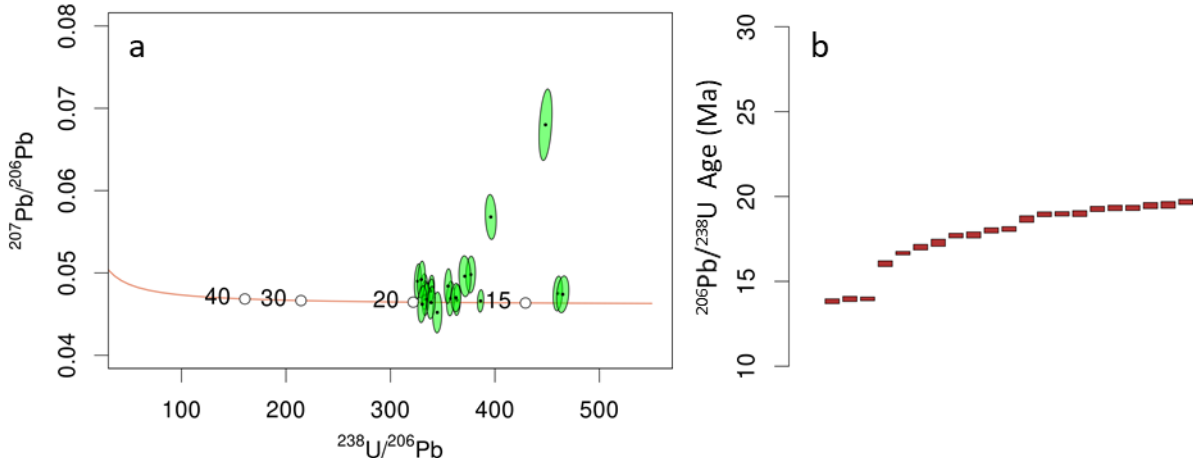
f04 – Leucogranite

Figure 4.19 – Leucogranite f04 U-Pb results with 2σ error. a) Tera-Wasserburg plot of Himalayan-aged zircon rims. b) Ordered common-Pb corrected ^{206}Pb/^{238}U ages.

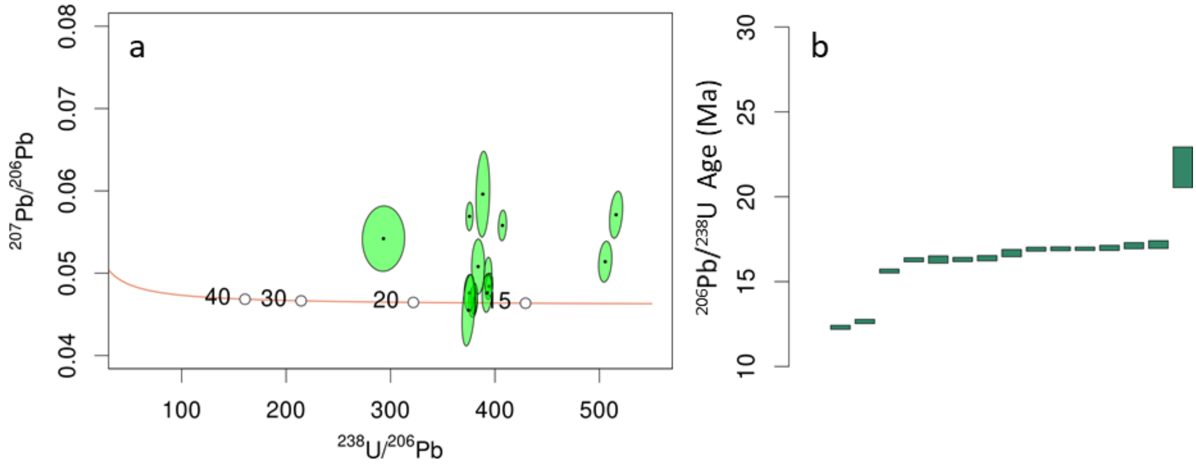
f13 – Migmatite

Figure 4.20 – Migmatite f13 U-Pb results with 2σ error. a) Tera-Wasserburg plot of Himalayan-aged zircon rims. b) Ordered common-Pb corrected ^{206}Pb/^{238}U ages.

The age data were grouped by lithology as histograms with bin widths of 0.5 Ma and kernel density estimates (KDEs) (Vermeesch, 2012) with bandwidths of 0.2 Ma. Leucogranite zircon rims date between ~23 Ma and ~13 Ma (n=69), with KDE peaks at 19.5 Ma and 16.5 Ma (Figure 4.21a). Migmatite zircon rims date to a broader range than the leucogranites, between ~35 Ma and ~12 Ma (n=88), with an increased abundance of rims dated between 25 Ma and 16 Ma, and a KDE peak at ~17 Ma (Figure 4.21b). Orthogneiss zircon rim dates are sparse between ~33 Ma and ~16 Ma (n=21); there are not enough data to distinguish between continuous growth or discrete episodes (Figure 4.21c).

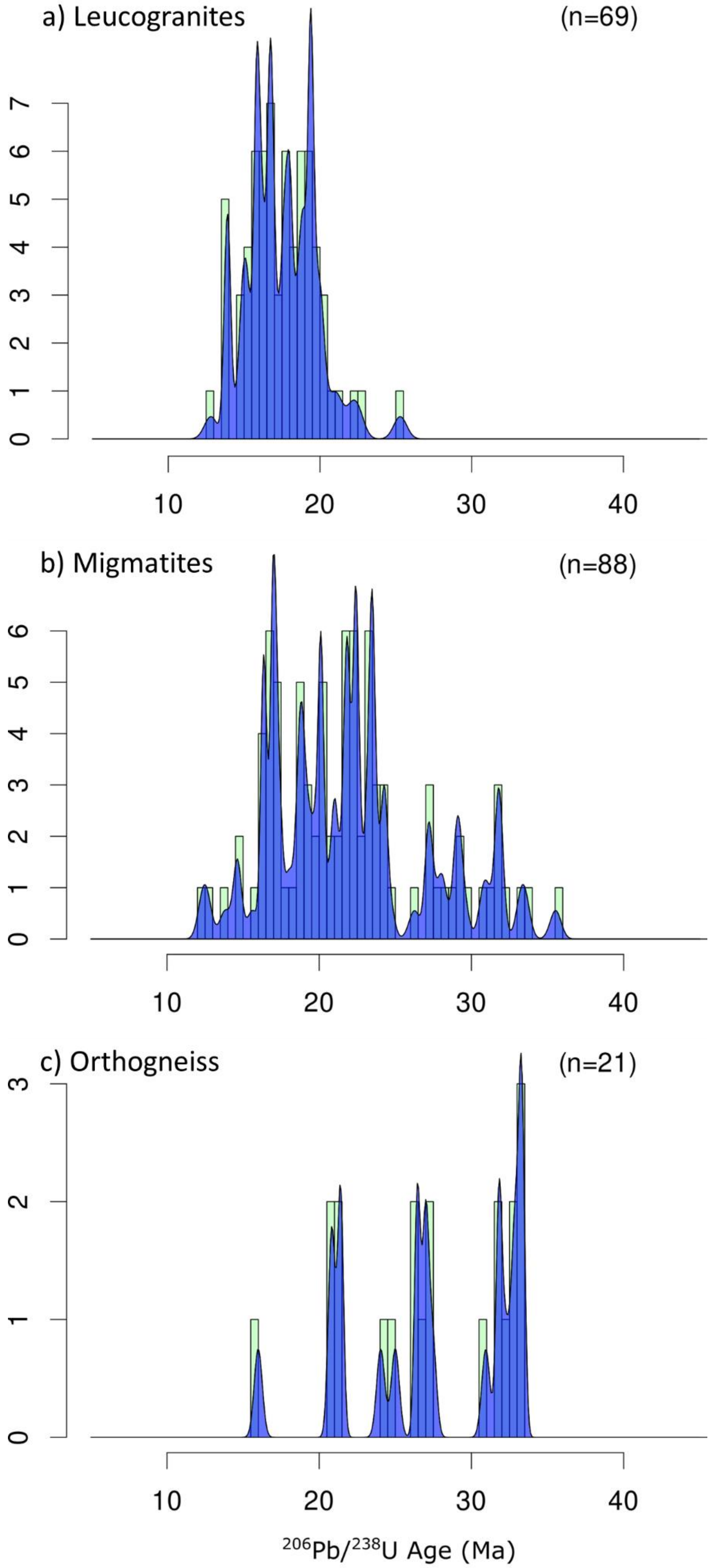

Figure 4.21 – Histograms and kernel density estimate (KDE) plots for common-Pb corrected zircon rim $^{206}Pb/^{238}U$ ages for a) leucogranites, b) migmatites, and c) orthogneiss. Histogram bin widths are 0.5 Ma and KDE bandwidths are 0.2 Ma.

4.3.2.2 Oxygen isotopes ($\delta^{18}O$)

All measured δ^{18}O values lie between 8.01-11.17 ‰, with typical error of ±0.35-0.50 ‰ (2σ). When plotted against the coinciding U-Th-Pb analysis for each grain, no overall trend with age for each rock type or individual samples appears (Figure 4.22).

a) Leucogranites

b) Migmatites

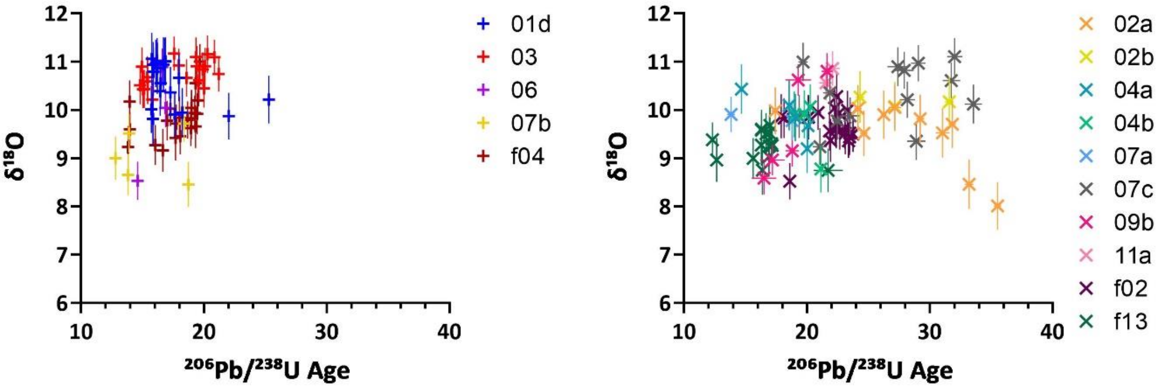

c) Orthogneiss

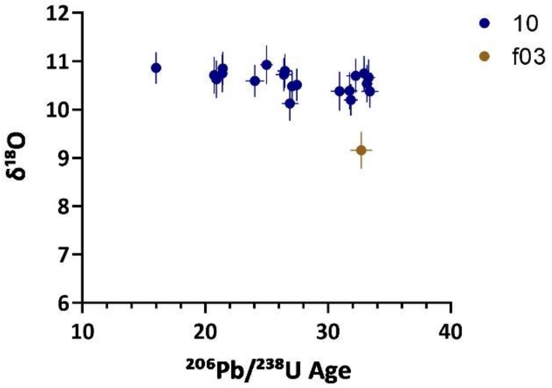

Figure 4.22 – Zircon rim δ^{18}O values compared to coinciding ^{206}Pb/^{238}U ages for a) leucogranites, b) migmatites, and c) orthogneiss. Error bars are 2σ for both δ^{18}O and age, however, for ^{206}Pb/^{238}U ages they are mostly smaller than the symbols.

Oxygen isotope values of zircon in leucogranites are spread between 8.5 ‰ to 11.2 ‰ (Figure 4.23). Samples 01d and 03 have relatively high median δ^{18}O values of ~10.7 ‰, while 07b has a relatively low value of ~9.0 ‰. Sample 06 has high variability (~8.5-10.9 ‰) across its three points, with a median value of 10.0 ‰, and sample f04 has a similarly high variability (~9.2-11.0 ‰) with a median of 9.8 ‰.

Migmatite zircon δ^{18}O values vary from 8.0 ‰ to 11.1 ‰ (Figure 4.24), with median of values 9.2-10.7 ‰. Samples 07c, 09b, 11a, and orthogneiss 10 stand apart from the other migmatites as they have individual values >10.5 ‰, however, 07c and 09b are highly variable with value of 9.2-11.1 ‰ and 8.6-10.8 ‰, respectively.

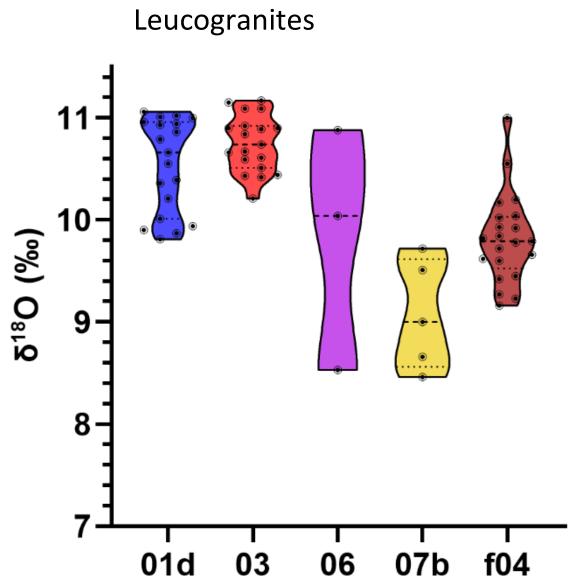

Figure 4.23 – Violin plots of zircon rim δ18O values for leucogranites. Bold dashed lines mark the median temperature values, and dotted lines mark the upper and lower quartiles. Dots show the values of individual rim measurements, while the width of each plot corresponds to the probable frequency of data at a given value.

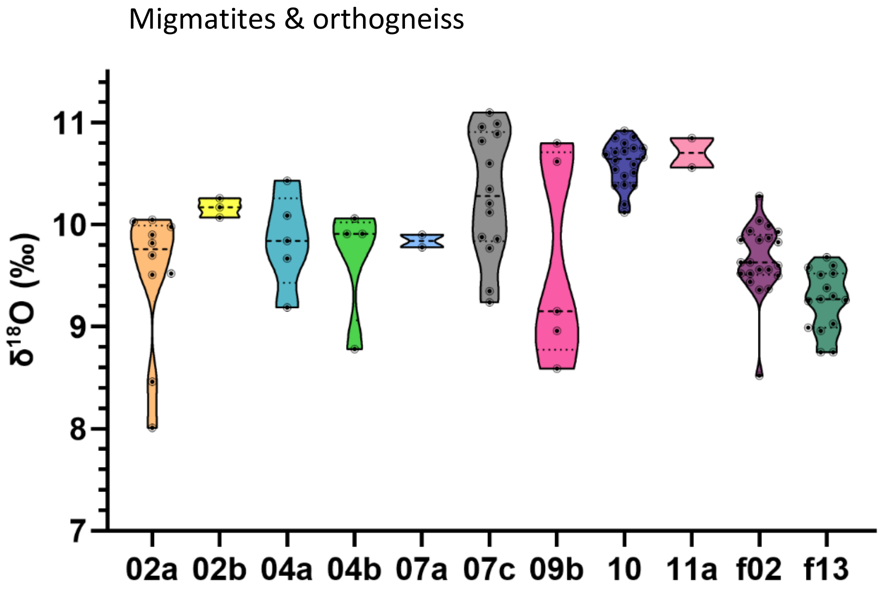

Figure 4.24 – Violin plots of zircon rim δ18O values for migmatites and orthogneiss. Bold dashed lines mark the median temperature values, and dotted lines mark the upper and lower quartiles. Dots show the values of individual rim measurements, while the width of each plot corresponds to the probable frequency of data at a given value.

4.3.2.3 Hafnium isotopes (εHf) and trace elements

All εHf values lie between -25.57 and 2.31, with typical error of ±0.25-0.45 (2σ), although all except two grains have εHf values lower than -6.73. A plot of εHf against the coinciding U-Th-Pb age shows no overall trend nor does the plot of εHf against $\delta^{18}O$ values for each rock type or individual samples (Figures 4.25 & 4.26).

Trace element concentrations have relative errors of 3-7 % for Y, Zr, Nb, HREEs, Hf, Th, and U, while Ti and LREEs have relative errors of >20 %. Concentrations of Ti are typically very low, with a median value of 1.86 ±0.79 ppm across all samples, with 25th and 75th percentiles at 1.14 and 3.68 ppm, respectively. Concentrations of Y show greater variation and overall abundance in grains with $^{206}Pb/^{238}U$ ages younger than ~24 Ma (Figure 4.27).

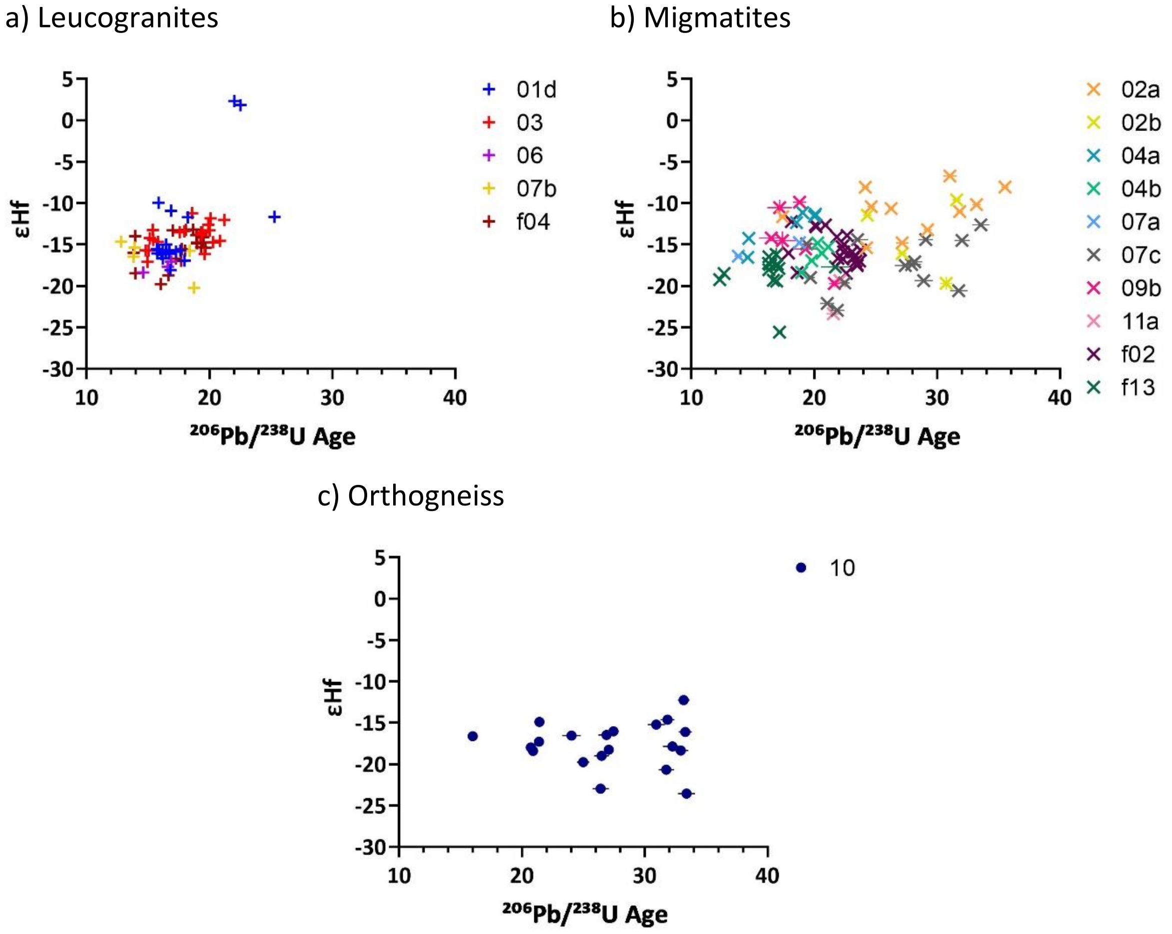

Figure 4.25 – Zircon rim εHf values compared to coinciding $^{206}Pb/^{238}U$ ages for a) leucogranites, b) migmatites, and c) orthogneiss. Error bars are 2σ for both εHf and age, however, they are mostly smaller than the symbols.

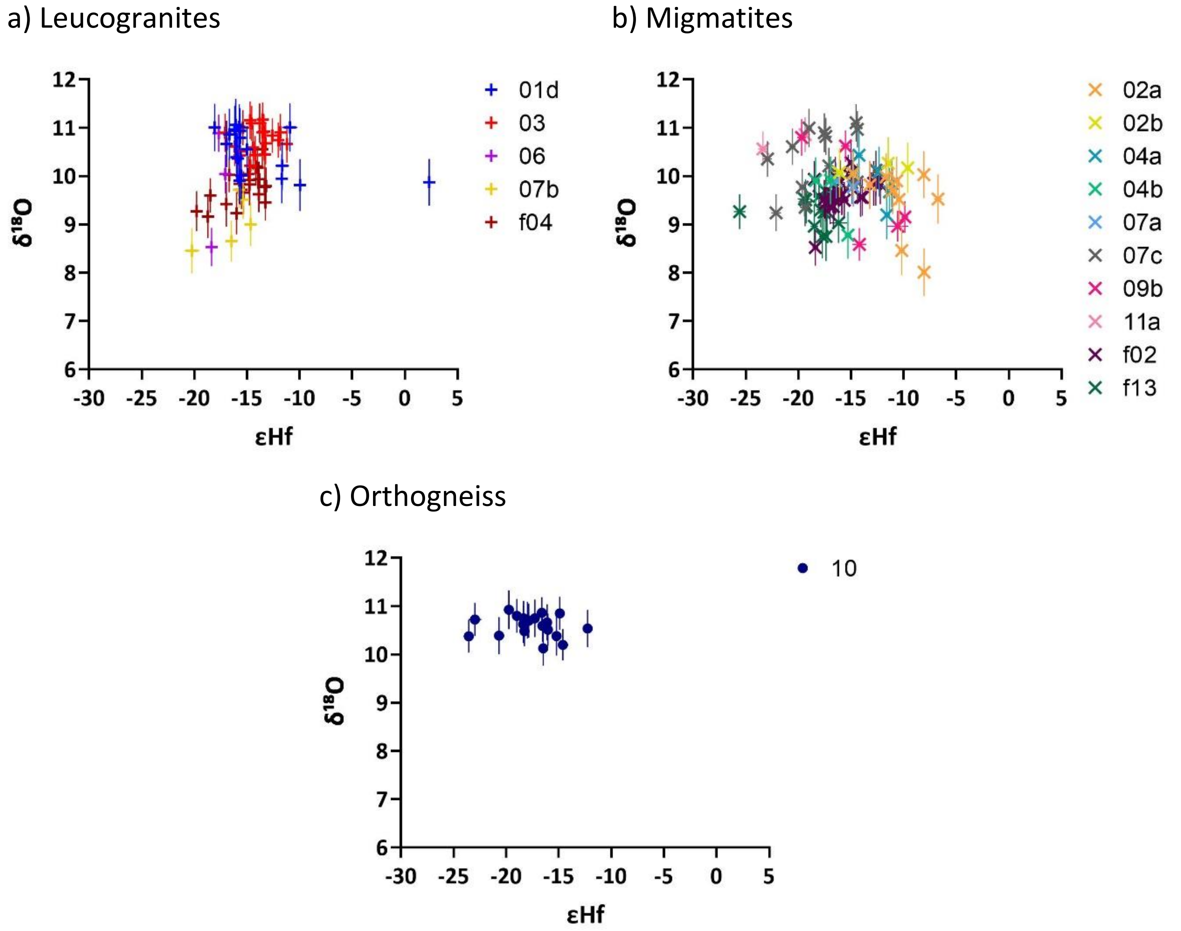

Figure 4.26 – Zircon rim εHf values compared to coinciding $\delta^{18}O$ values for a) leucogranites, b) migmatites, and c) orthogneiss. Error bars are 2σ for both εHf and $\delta^{18}O$, however, for εHf they are mostly smaller than the symbols.

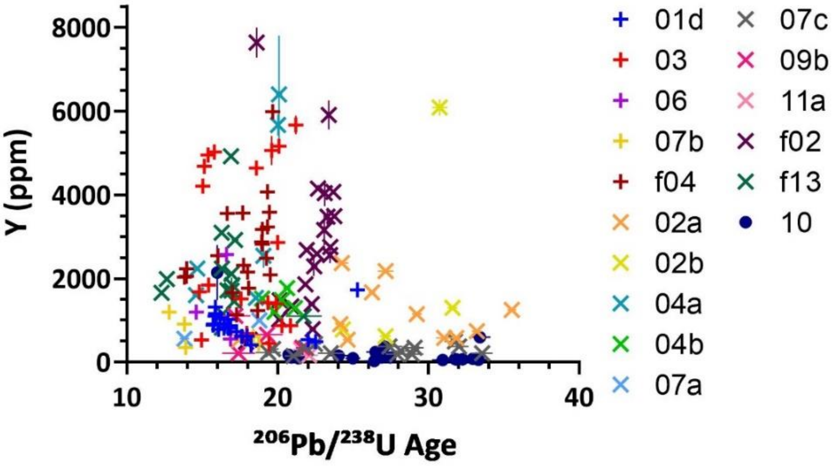

Figure 4.27 – Y concentration vs $^{206}Pb/^{238}U$ ages for zircon rims. Error bars are 2σ for both Y concentration and age, however, they are mostly smaller than the symbols.

Leucogranite samples 01d, 03, 06, 07b and f04, and migmatite samples 02a, 02b, 04a, 04b, 07a, f02, and f13 have strongly negative Eu/Eu* anomalies, typically <0.2, while migmatite samples 07c, 09b, and 11a, and orthogneiss 10, have variable Eu/Eu* anomalies, typically >0.2 and <1.2 (Figure 4.28). Zircon grains with Eu/Eu* anomalies <0.2 are also have higher abundances of HREEs (Gd, Dy, Yb, & Lu) compared to grains with Eu/Eu* anomalies >0.2 (Figure 4.29). Plots of zircon REE concentrations normalised to C1 chondrite values (Palme and O'Neill, 2014) for each sample are presented in Appendix D.

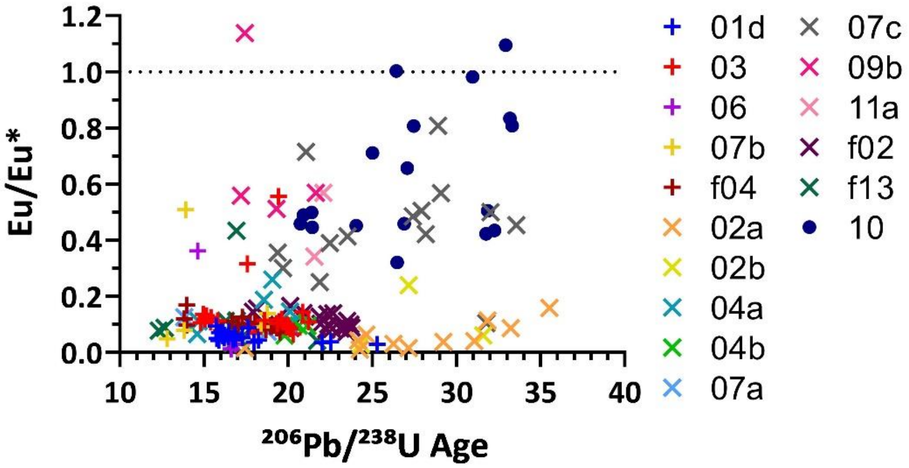

Figure 4.28 – Eu/Eu (Eu anomaly) vs ^{206}Pb/^{238}U ages for zircon rims. Eu/Eu* values <1 are considered 'negative' anomalies.*

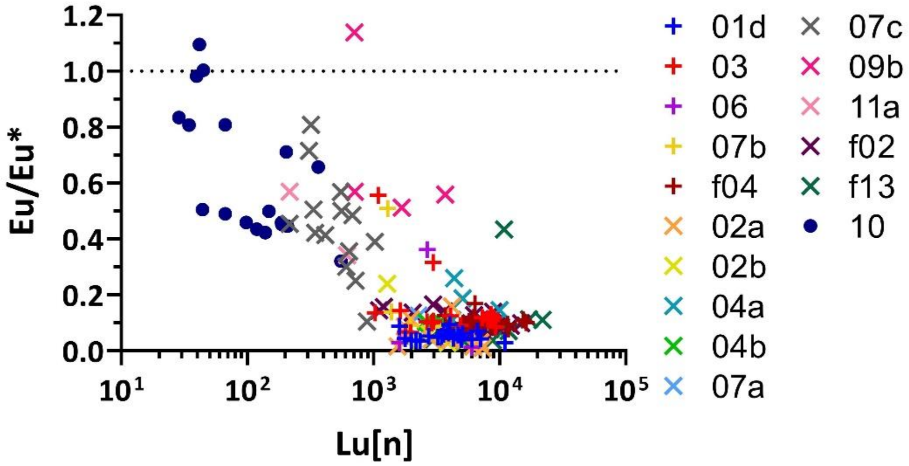

Figure 4.29 – Eu/Eu (Eu anomaly) vs chondrite normalised Lu concentration (Lu$_{[n]}$) for zircon rims. Eu/Eu* values <1 are considered 'negative' anomalies.*

4.3.3 Monazite zoning

EDS maps of Ce, Th, and Y concentrations in 42 grains across the four resin grain mounts (T1620-T1623) show the internal chemical zoning present in monazite from fourteen samples (Table 4.1).

Two broad groups of chemical zone types are recorded: those with simple and oscillatory zoning, prevalent in Ce and Th maps, typically with high-Ce, low-Th cores (Type 1 monazite) (Figure 4.30), and those with irregular, patchwork zoning, prevalent in Ce and Y maps, and low Th abundance (Type 2 monazite) (Figure 4.31).

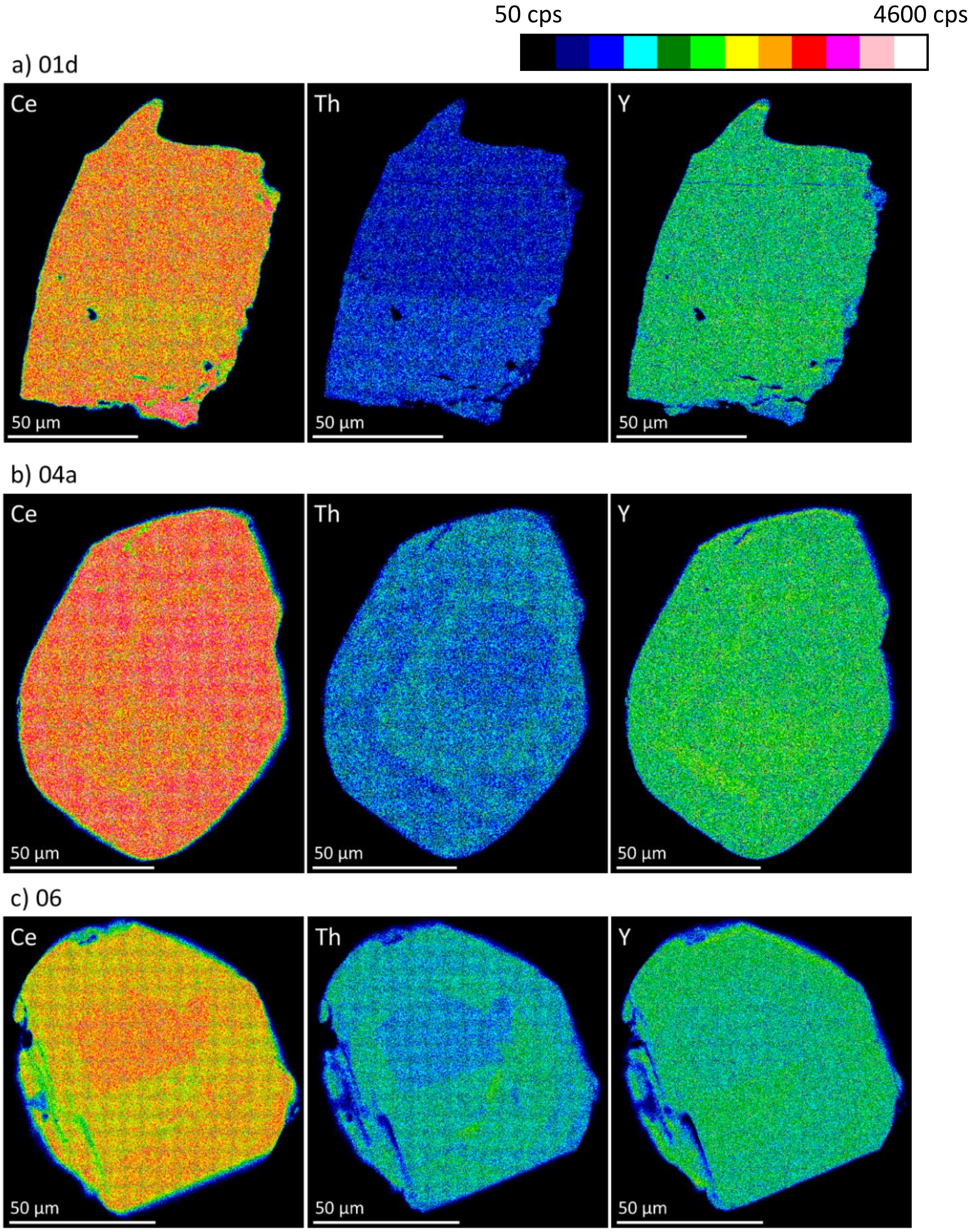

Figure 4.30 – Ce, Th, and Y maps of monazite grains with simple or oscillatory zoning, with high-Ce, low-Th cores and mostly homogenous Y (type 1). Colour gradient depicts counts per second (cps). a) simple zoned monazite from leucogranite sample 01d. b) Oscillatory zoned monazite from migmatite 04a. c) Oscillatory zoned monazite from leucogranite 06.

Samples with type 1 monazite grains are leucogranites 01d, 06, and f04, migmatites 02a, 02b, 04a, 04b, f02, and f13, although the monazite from migmatite 02b has a high-Th core, and orthogneiss f03. Sample with type 2 monazite grains are migmatite samples 05b, 07c, and 09b, and orthogneiss 10. Sample 05b also has sector zoned grains.

Images of all analysed monazite grains with annotated locations of analytical spots are presented in Appendix E.

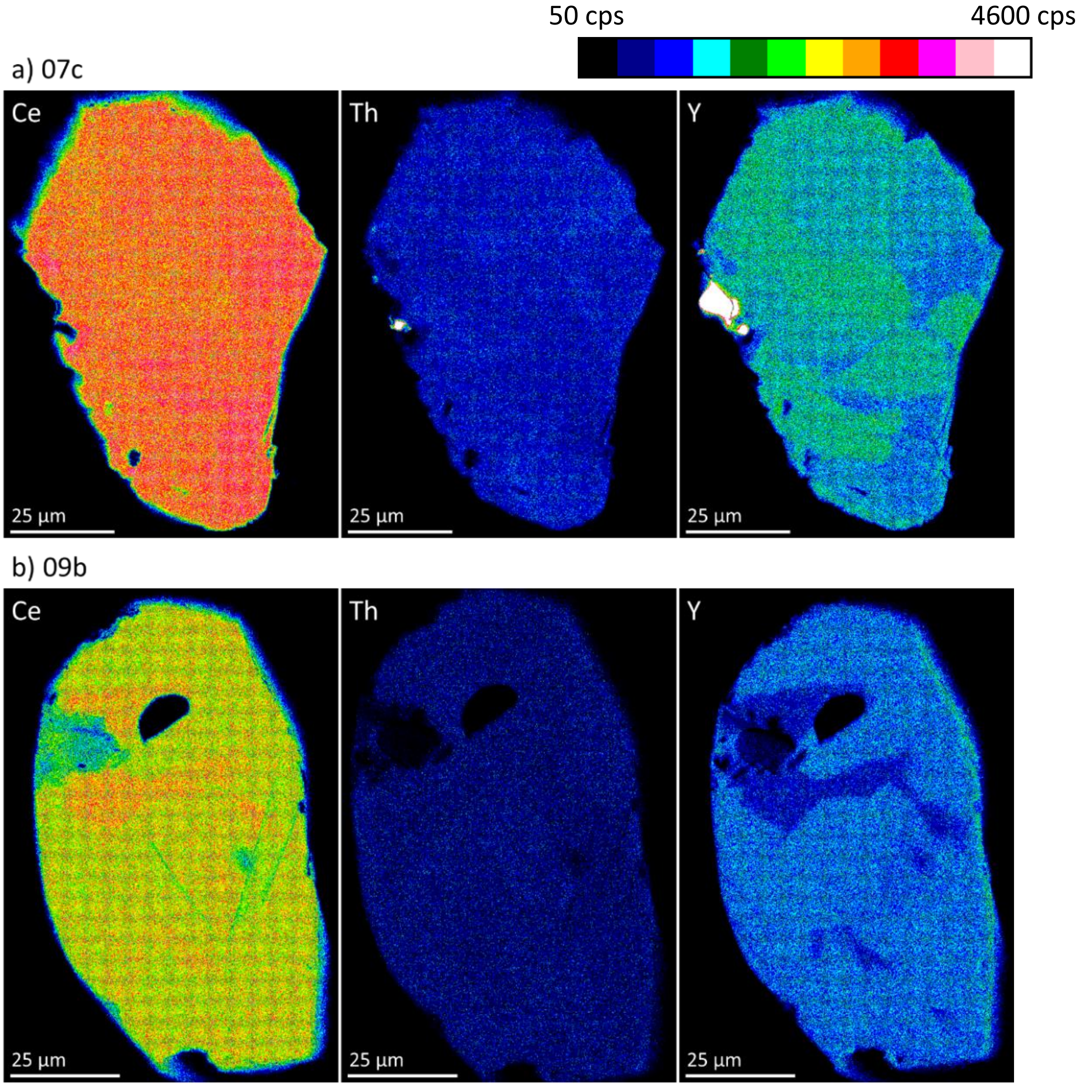

Figure 4.31 – Ce, Th, and Y maps of monazite grains with irregular zoning, low-Th, and patchwork Y (type 2). Colour gradient depicts counts per second (cps). a) Irregular zoned monazite from migmatite 07c. b) Irregular zoned monazite from migmatite 09b.

4.3.4 Monazite U-Th-Pb analysis

Presented here are U-Th-Pb isotope results for monazite analyses relating to the Himalayan orogeny, as defined by ^{208}Pb/^{232}Th ages younger than 45 Ma. Full results for analysis of each monazite grain are presented in Appendix E.

A total of 242 analyses were carried out across 14 samples, of which, 228 analyses across 13 samples yield ^{208}Pb/^{232}Th dates relevant to the timescales of the Himalayan orogen. Calculated ages are corrected for common Pb using the Stacey-Kramers two-stage isotope evolution model (Stacey and Kramers, 1975). Uncertainties on ^{208}Pb/^{232}Th dates are typically ±1.2-1.8 Ma (2σ).

The ^{208}Pb/^{232}Th corrected dates for each sample are summarised as follows:

- Leucogranite **sample 01d** – 1 grain between 22.5-19.0 Ma across 10 spots (Figure 4.32).
- Migmatite **sample 02a** – 2 grains, one between 33.9-23.6 Ma across 8 spots, and one between 26.6-21.7 Ma across 6 spots (Figure 4.33).
- Migmatite leucosome **sample 02b** – 1 grain between 27.6-23.5 Ma across 11 spots (Figure 4.34).
- Migmatite **sample 04a** – 1 grain between 22.9-21.6 Ma across 11 spots (Figure 4.35)
- Migmatite **sample 04b** – 3 grains, all between 26.5-21.2 Ma across 17 spots (Figure 4.36)
- Migmatite **sample 05b** – 6 grains, all between 25.4-19.8 Ma across 31 spots (Figure 4.37).
- Leucogranite **sample 06** – 9 grains, all between 25.8-16.8 Ma across 40 spots (Figure 4.38).
- Migmatite **sample 07c** – 1 grain between 32.9-26.9 Ma across 9 spots (Figure 4.39).
- Migmatite **sample 09b** – 10 grains, one between 33.3-30.5 Ma across 6 spots, and nine between 20.9-16.3 Ma across 40 spots (Figure 4.40).
- Orthogneiss **sample 10** – 3 grains, all 23.4-16.8 Ma across 15 spots (Figure 4.41). Only one spot is younger than 19 Ma.
- Migmatite **sample f02** – 1 grain between 25.1-23.9 Ma across 4 spots (Figure 4.42).
- Leucogranite **sample f04** – 1 grain between 22.8-18.0 Ma across 15 spots (Figure 4.43).
- Migmatite **sample f13** – 2 grains, one between 29.4-28.2 across 2 spots with an inherited core, and one between 24.2-21.6 Ma across 3 spots (Figure 4.44).

01d – Leucogranite

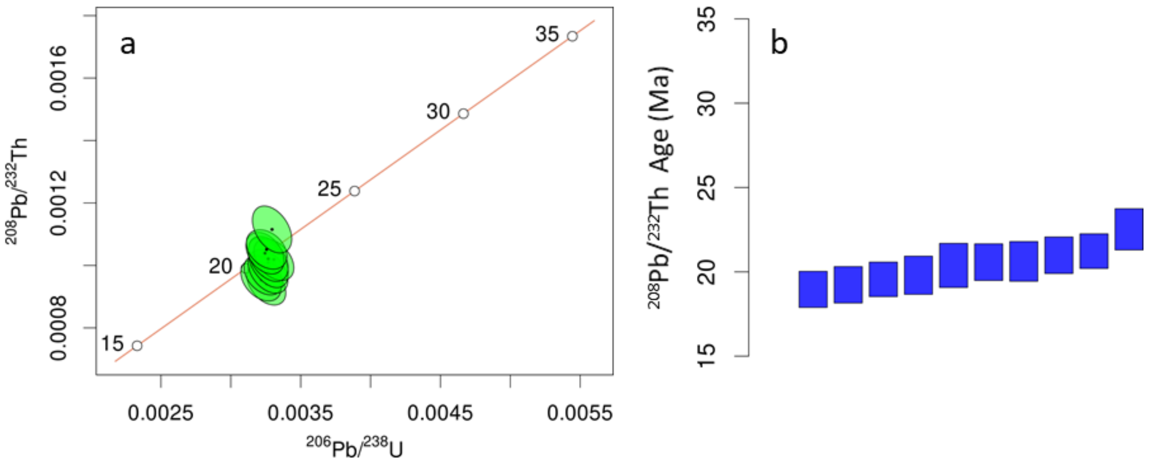

Figure 4.32 – Leucogranite 01d monazite U-Th-Pb results with 2σ error. a) U-Th-Pb plot of Himalayan-aged spots. b) Ordered common-Pb corrected $^{208}Pb/^{232}Th$ ages.

02a – Migmatite

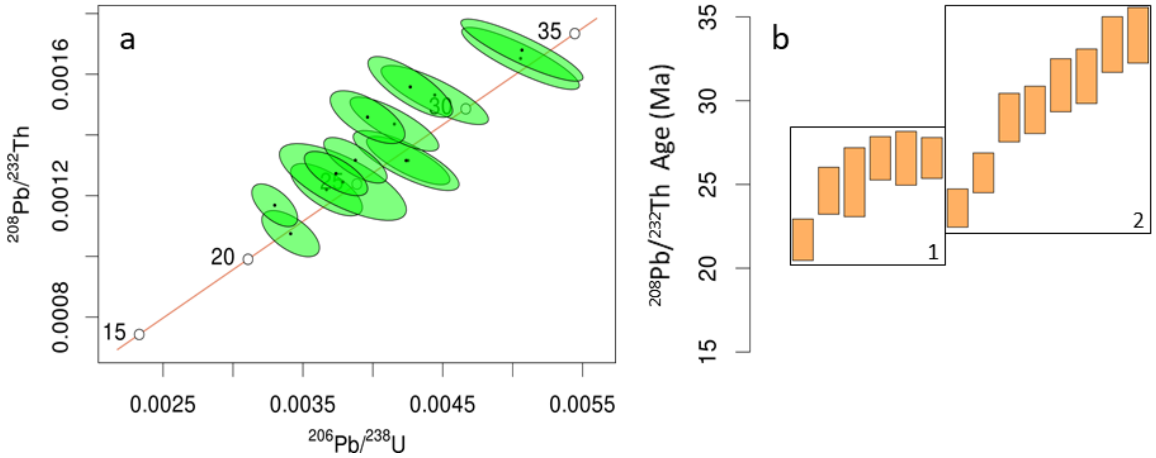

Figure 4.33 – Migmatite 02a monazite U-Th-Pb results with 2σ error. a) U-Th-Pb plot of Himalayan-aged spots. b) Ordered common-Pb corrected $^{208}Pb/^{232}Th$ ages, with spots from grains 1 and 2 indicated.

02b – Migmatite

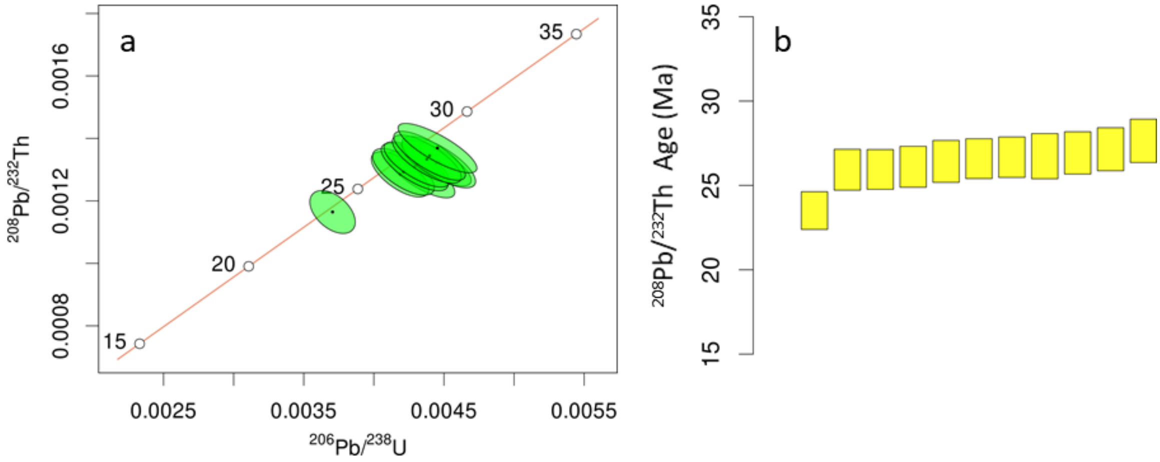

Figure 4.34 – Migmatite 02b monazite U-Th-Pb results with 2σ error. a) U-Th-Pb plot of Himalayan-aged spots. b) Ordered common-Pb corrected $^{208}Pb/^{232}Th$ ages.

04a – Migmatite

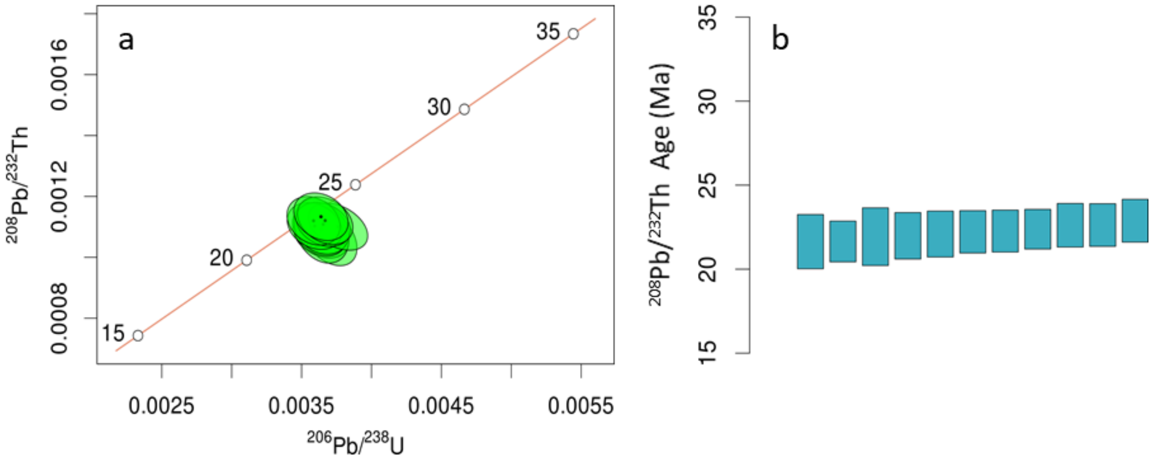

Figure 4.35 – Migmatite 04a monazite U-Th-Pb results with 2σ error. a) U-Th-Pb plot of Himalayan-aged spots. b) Ordered common-Pb corrected ^{208}Pb/^{232}Th ages.

04b – Migmatite

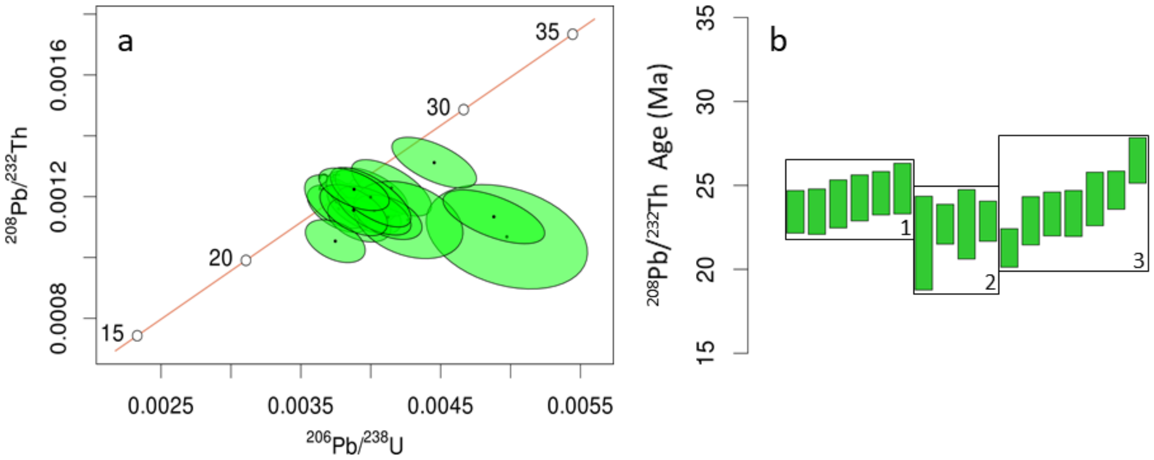

Figure 4.36 – Migmatite 04b monazite U-Th-Pb results with 2σ error. a) U-Th-Pb plot of Himalayan-aged spots. b) Ordered common-Pb corrected ^{208}Pb/^{232}Th ages, with spots from grains 1-3 indicated.

05b – Migmatite

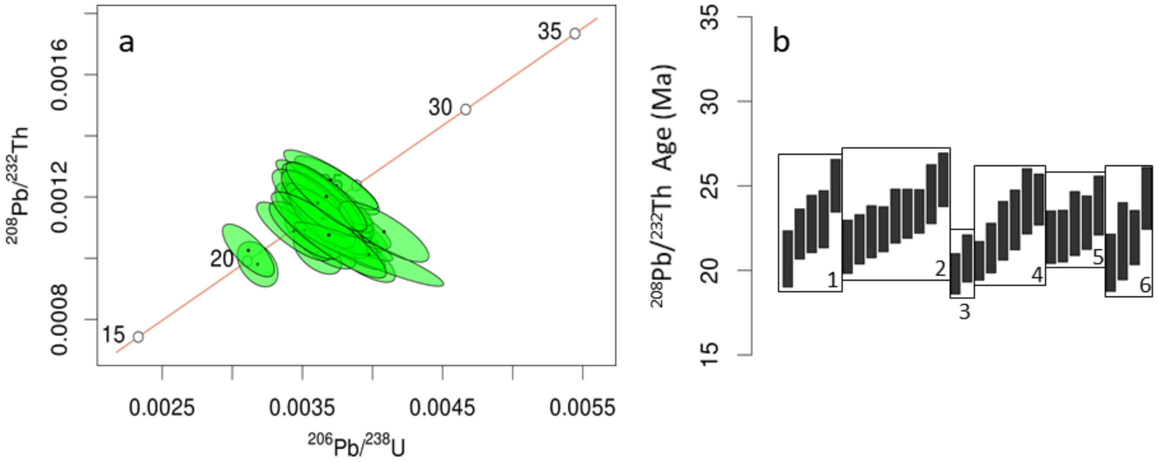

Figure 4.37 – Migmatite 05b monazite U-Th-Pb results with 2σ error. a) U-Th-Pb plot of Himalayan-aged spots. b) Ordered common-Pb corrected ^{208}Pb/^{232}Th ages, with spots from grains 1-6 indicated.

06 – Leucogranite

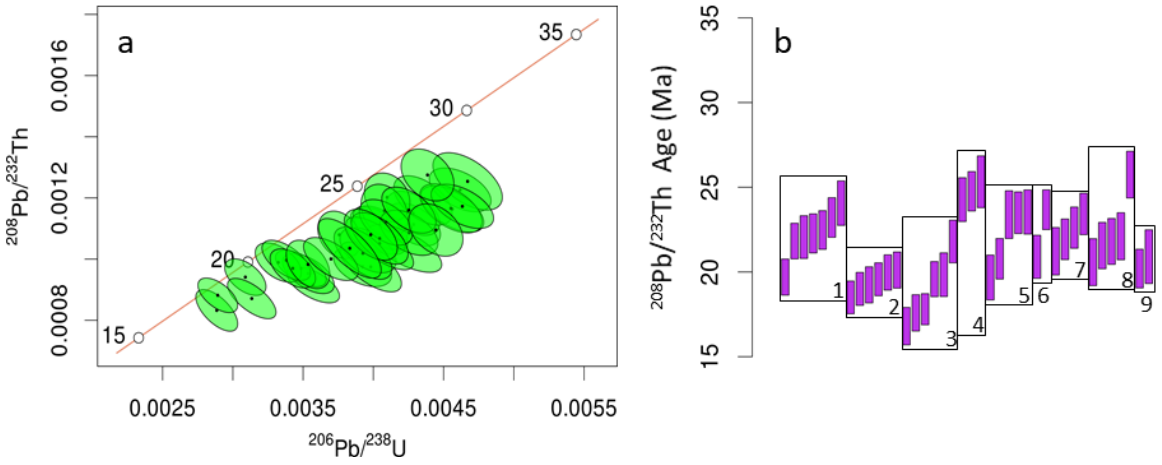

Figure 4.38 – Leucogranite 06 monazite U-Th-Pb results with 2σ error. a) U-Th-Pb plot of Himalayan-aged spots. b) Ordered common-Pb corrected ^{208}Pb/^{232}Th ages.

07c – Migmatite

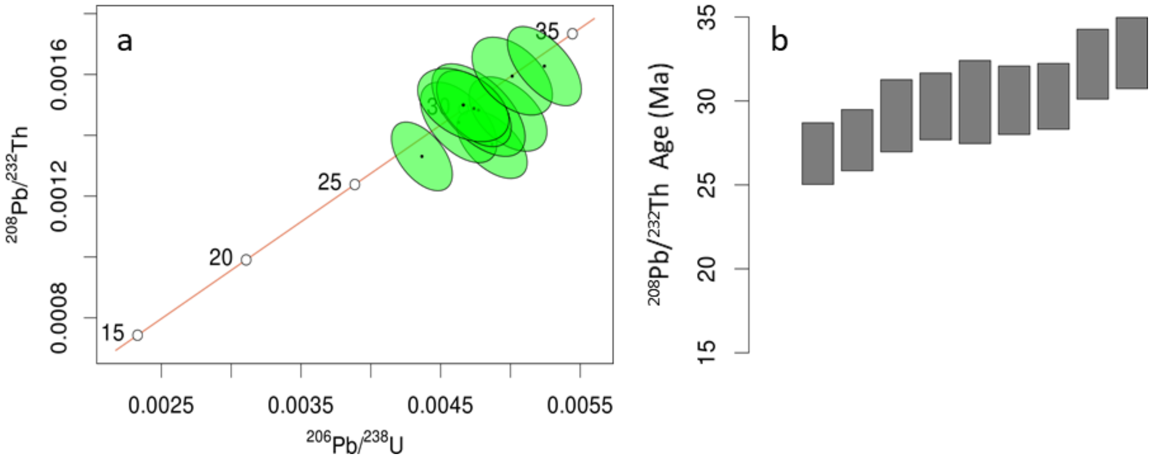

Figure 4.39 – Migmatite 07c monazite U-Th-Pb results with 2σ error. a) U-Th-Pb plot of Himalayan-aged spots. b) Ordered common-Pb corrected ^{208}Pb/^{232}Th ages.

09b – Migmatite

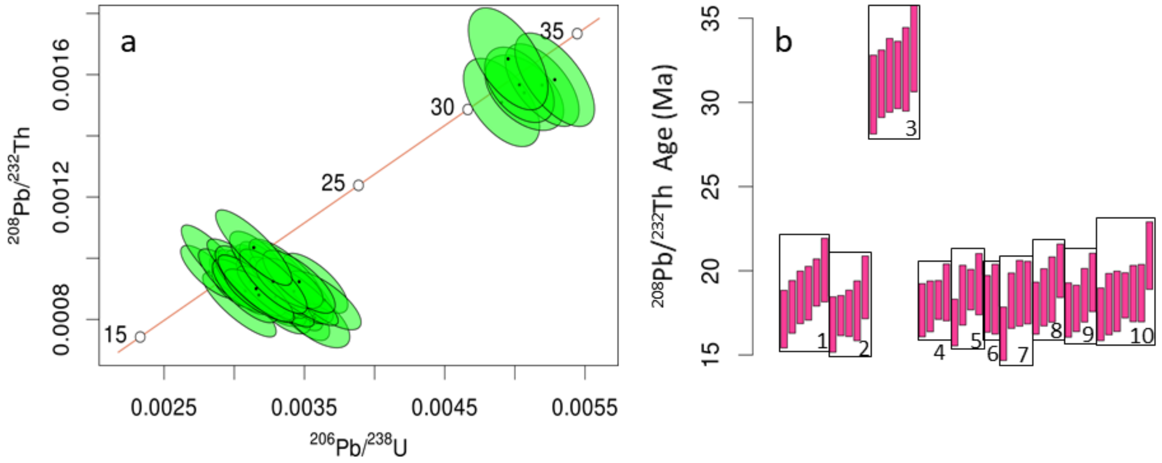

Figure 4.40 – Migmatite 09b monazite U-Th-Pb results with 2σ error. a) U-Th-Pb plot of Himalayan-aged spots. b) Ordered common-Pb corrected ^{208}Pb/^{232}Th ages, with spots from grains 1-10 indicated.

10 – Orthogneiss

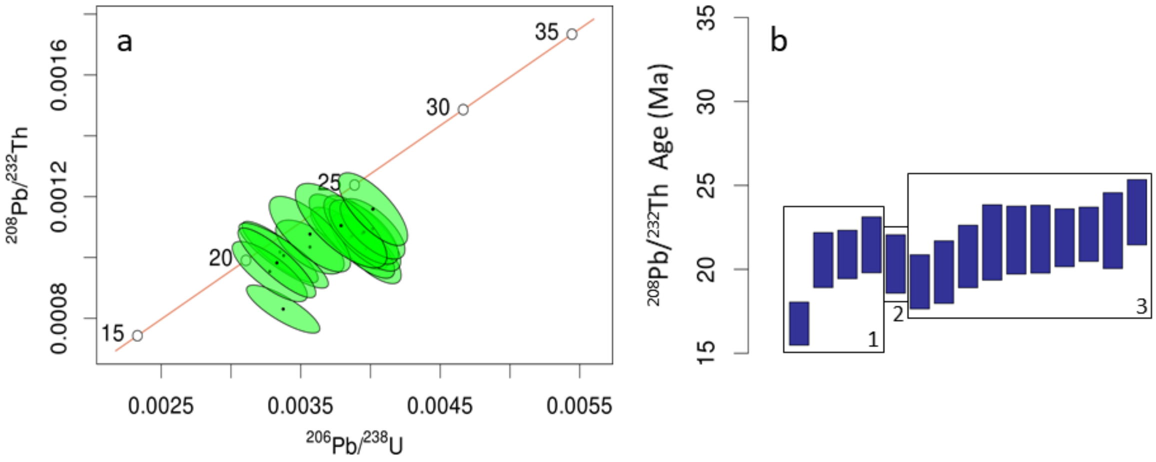

Figure 4.41 – Orthogneiss 10 monazite U-Th-Pb results with 2σ error. a) U-Th-Pb plot of Himalayan-aged spots. b) Ordered common-Pb corrected $^{208}Pb/^{232}Th$ ages, with spots from grains 1-3 indicated.

f02 – Migmatite

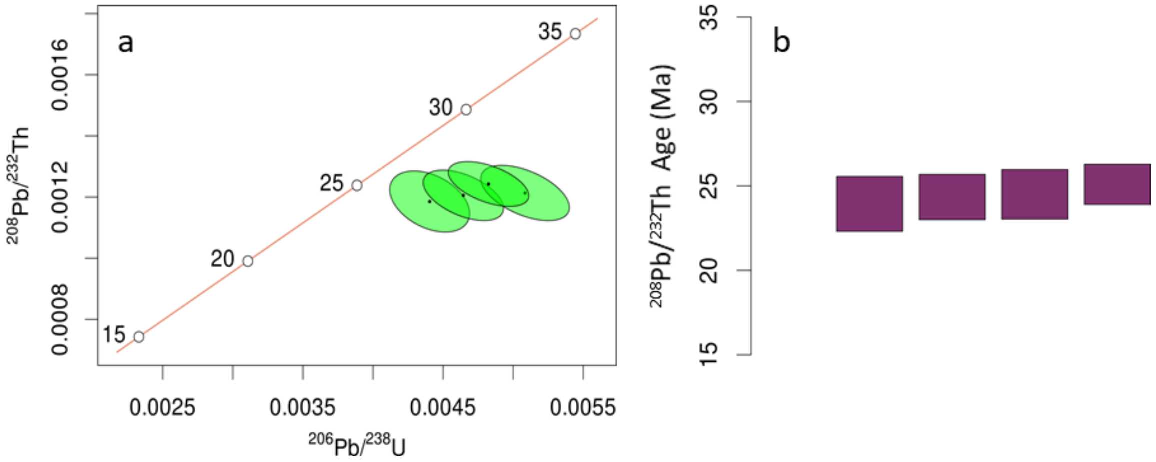

Figure 4.42 – Migmatite f02 monazite U-Th-Pb results with 2σ error. a) U-Th-Pb plot of Himalayan-aged spots. b) Ordered common-Pb corrected $^{208}Pb/^{232}Th$ ages.

f04 – Leucogranite

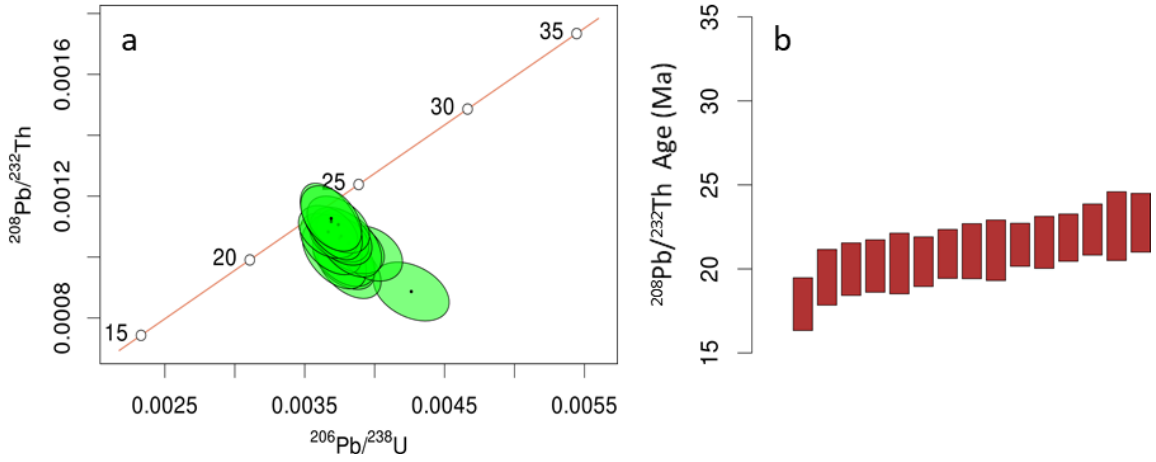

Figure 4.43 – Leucogranite f04 monazite U-Th-Pb results with 2σ error. a) U-Th-Pb plot of Himalayan-aged spots. b) Ordered common-Pb corrected $^{208}Pb/^{232}Th$ ages.

f13 – Migmatite

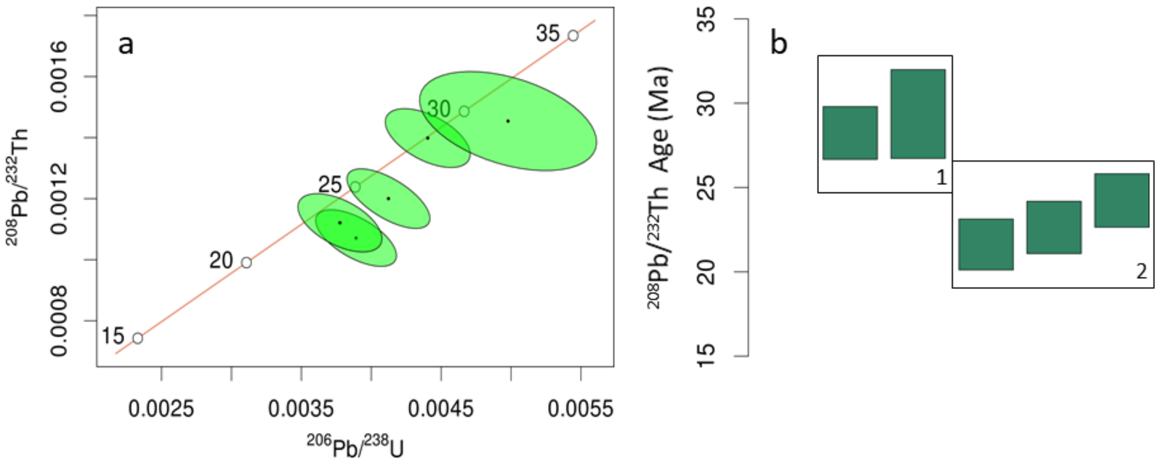

Figure 4.44 – Migmatite f13 monazite U-Th-Pb results with 2σ error. a) U-Th-Pb plot of Himalayan-aged spots. b) Ordered common-Pb corrected $^{208}Pb/^{232}Th$ ages, with spots from grains 1 and 2 indicated.

4.4 Discussion

4.4.1 Growth of zircon and monazite

For crystallisation of zircon and monazite to occur, the melt must first become saturated with respect to Zr and LREEs (Watson and Harrison, 1983; Rapp and Watson, 1986). Zircon and monazite will initially dissolve in anatectic melt, which increases the concentrations of Zr and LREEs until the point of saturation. Modelling of zircon and monazite in supra-solidus pelitic systems show that monazite dissolves far more readily than zircon under conditions of ~750°C and 1.0 ± 0.1 GPa, and consequently older cores are less likely to be preserved (Yakymchuk and Brown, 2014). Zircon, with slower dissolution rates compared to monazite, may also partially depend on reducing temperatures to reach saturation under these conditions, as the saturating concentration of Zr decreases with decreasing temperature (Boehnke et al., 2013). Ti-in-zircon thermometry (considered to record the temperature at which zircon crystallises) generally seems to record temperatures 35-50°C below peak temperature estimates in granitoid rocks (Schiller and Finger, 2019).

4.4.1.1 Causes of chemical zoning in zircon and monazite

The textures present in both type 1 and type 2 zircon rims are typical of grains crystallised or grown from a melt or fluid-rich system (Rubatto, 2017). The dark CL rim growth in both groups likely signifies high concentrations of U (& Th) relative to Dy (and other REEs), which causes CL properties to be suppressed (Rubatto and Gebauer, 2000). The opposite is the case for the bright external rim growth in type 2 zircon. As such, darker domains can be recognised as high-U zircon growth, with oscillations present in these domains likely caused by kinetic effects of local supersaturation and disequilibrium (Hoskin and Schaltegger, 2003; Hoskin, 2000), as opposed to separate melting events. The thin, U-poor type 2 overgrowths, however, are more commonly associated with sub-solidus growth with reduced U availability (Rubatto, 2017). The rounded boundary between the high- and low-U zones also suggests a period of dissolution, before low-U zircon precipitation, likely formed via post-anatectic recrystallisation with a fluid.

The textures of type 1 and type 2 monazite grains, seen in Ce-Th-Y maps (Figures 4.29 and 4.30), can also be used to group samples with common features. The two groups, those with simple or oscillatory zoning in Ce and Th, and those with irregular and rare sector zoning in Y and low Th concentrations, match the grouping of type 1 and type 2 zircon rims. Samples with type 1 zircon and monazite are associated with petrographic and elemental features identified as forming during fluid-absent melting, while samples with type 2 zircon and monazite are associated with other observations relating the fluid-present melting (see Chapter 3).

The two types of chemical zoning in the monazite grains are mostly easily distinguished by the presence or absence of Th zoning. Potential causes for Th zonation in monazite are poorly constrained, however, in high-grade metamorphic rocks, monazite is generally thought to control the Th budget (Williams et al., 2022). Low concentrations of Th relative to Y, in samples associated with fluid-present melting (05b, 07c, 09b, 10) would suggest either low bulk-rock Th concentration, or poor Th availability during monazite growth. Low-Th monazite in the Sestri-Voltaggio Zone, Italy, and the Protivanov Formation, Czech Republic, is explained as in-source authigenic growth (Cabella et al., 2001; Čopjaková et al., 2011; Catlos, 2013), without the presence of interconnected melt to deliver Th to the crystallising grain. As such, low melt interconnectivity, or total volumes, could be responsible for restricting Th availability to monazite as it grew in these samples.

4.4.1.2 Conditions during zircon crystallisation

Ti concentrations in zircon are commonly used for Ti-in-zircon thermometry (Ferry and Watson, 2007), to constrain temperatures of zircon crystallisation and thereby infer melt temperatures. However, the accommodation of ablation spots in the relatively narrow Himalayan-aged growth rims has resulted in high relative errors (30-50 %) for typically low concentrations (~2 ppm). When propagated with uncertainties in a_{TiO_2} and pressure, the error on calculated temperatures is greater than ±100°C. Therefore, zircon crystallisation temperatures were not determined for these samples.

Zircon and garnet are both reservoirs of Y and commonly coexist in metamorphic and anatectic rocks. Therefore, the concentration of Y in zircon can be used to infer the local presence or breakdown of garnet (Rubatto, 2002). Concentration of Y in zircon from all samples plotted against $^{206}Pb/^{238}U$ ages show an increase in the overall variability and abundance of Y in zones younger than 25 Ma (Figure 4.27), matching the sharp increase in the volume of zircon of this age in migmatites. Grains or zones older than 25 Ma typically contain between 5 and 1500 ppm Y, while younger grains or zones contain between 150 and ~7000 ppm Y. The increase in Y concentration is likely caused by the resorption of garnet, releasing Y and HREEs into the matrix and melt (Pyle and Spear, 1999). This agrees with petrographic observations of garnet instability and resorption in migmatite samples 02b, 07c, 08, 09b, f02 and orthogneiss 10 (see Chapter 2).

The normalised-REE profiles of zircon from all samples are fairly typical of magmatic grains, with HREE-enrichment, positive Ce anomalies, and largely negative Eu anomalies (Trail et al., 2012; Rubatto, 2002; Hinton and Upton, 1991; Murali et al., 1983). Zircon in samples identified as having experienced fluid-present (07c, 09b, 10, 11a) and fluid-absent (01d, 02a, 02b, 03, 04a, 04b, 06, 07a, 07b, f02, f04, f13) melting preserve different REE records; zircon in fluid-present melting samples record reduced negative Eu anomalies and decreased overall HREE abundance compared with those in samples where melting was facilitated by mica dehydration (Figure 4.28 & 4.29). Ce and Eu anomalies in zircon can record the oxidation state of a melt, with oxidising conditions resulting in positive Ce anomalies and positive (or reduced negative) Eu anomalies due to the increased compatibility of Ce^{4+} and Eu^{3+} with zircon (Trail et al., 2012). However, there is no distinction between Ce anomalies in samples that record fluid-present or fluid-absent melting, suggesting melt is somewhat oxidised irrespective of the activity of fluids during melting. The reduction of the strength of the negative Eu anomaly in samples that record fluid-present melting may instead be explained by increased availability of Eu in the melt compared to samples that record fluid-absent melting with the presence of peritectic K-feldspar (Patiño Douce and Harris, 1998; Pickering and Johnston, 1998; Gardien et al., 1995) during zircon crystallisation, as K-feldspar is a known Eu sink (Rubatto, 2002; Hinton and Upton, 1991; Murali et al., 1983).

4.4.2 The timing of anatexis and implications for Himalayan tectonics

Zircons rims in leucogranite samples that were previously associated with fluid-absent melting signatures (Chapter 2), date from 23 to 13 Ma, with the primary peak at ~19.5 Ma (Figure 4.21a). Migmatite zircon rims, split fluid-absent muscovite-dehydration melting signatures (02a, 02b, 04a, 04b, 07a, f02, and f13), and those with fluid-present melting signatures (07c, 09b, and 11a). Both groups record zircon growth from 35 to 15 Ma, however, most of these rims record ages between 25 and 16 Ma (Figure 4.21b). Zircon rims from orthogneiss sample 10, also associated with fluid-present melting signatures, yield a broad spread of ages between 34 and 16 Ma (Figure 4.21c).

Leucogranite zircon rim dates coincide with the modelled age of rapid GHS exhumation from 22 to 17 Ma, as a result of wedge-extrusion during India-Asia convergence at velocities of ~5 cm/year (Maiti and Mandal, 2021; Copley et al., 2010) (see Chapter 1 for more details). This conforms with the common interpretation of leucogranite formation in the GHS during widespread decompression melting (Patiño Douce and Harris, 1998; Weinberg, 2016). Migmatite samples from the Garhwal predate the formation of leucogranites and the onset of exhumation at 22 Ma, as suggested by Maiti and Mandal (2021). The regional increase in partial melting at this time, therefore, is a potential trigger for the initiation of exhumation, with a significant decrease in the mechanical strength of the GHS occurring with the formation melt fractions of 1-7 % by volume (Rosenberg and Handy, 2005; Vigneresse et al., 1996). This also coincides with increasing Y concentrations in zircon (Figure 4.27), suggesting decreasing garnet stability coincided with increasing anatectic melt volumes. The oldest of the zircon rims, between 36 and 25 Ma, in migmatite samples 02a, 02b, 07c, and orthogneiss 10, correspond to previous dating of peak metamorphism in GHS of the Garhwal of 37-25, with most ages around 33.9 ± 1.2 Ma (Kawabata et al., 2021; Catlos et al., 2007).

The prevalence through time of the three melt reactions identified in samples from this study (fluid-present, and fluid-absent muscovite- and biotite-dehydration) can be examined by grouping zircon ages by melt reaction associated with each sample (Figure 4.45). Fluid-present melting occurs intermittently between 34 and 16 Ma and is the dominant melt reaction type prior to ~25 Ma. After this, muscovite-dehydration melting becomes the dominant reaction type, coinciding with the overall increase in zircon volume, contributing to most of the age peaks present between 19.5 and 16.5 Ma (Figure 4.21a-b). Biotite-dehydration melt signatures are only present in one sample. However, the ages recorded by zircon in this sample coincide with the timing of muscovite-dehydration reactions in other samples at 16.5 Ma. The relationship between zircon population and the onset of decompression and rapid exhumation at ~22 Ma (Maiti and Mandal, 2021) is primarily attributed to samples that record muscovite-dehydration textures and chemistry. Hence, from these data we can infer that muscovite-dehydration melting is regionally the most important melt-forming reaction with regard to its implications for collisional tectonics. Additionally, the prevalence of fluid-present melting textures and chemistry from 34 to 25 Ma indicates the intersection of the fluid-present solidus with the prograde P-T path at generally lower temperatures (Harris et al., 1995), during peak metamorphic conditions of the Garhwal GHS (Kawabata et al., 2021; Catlos et al., 2007).

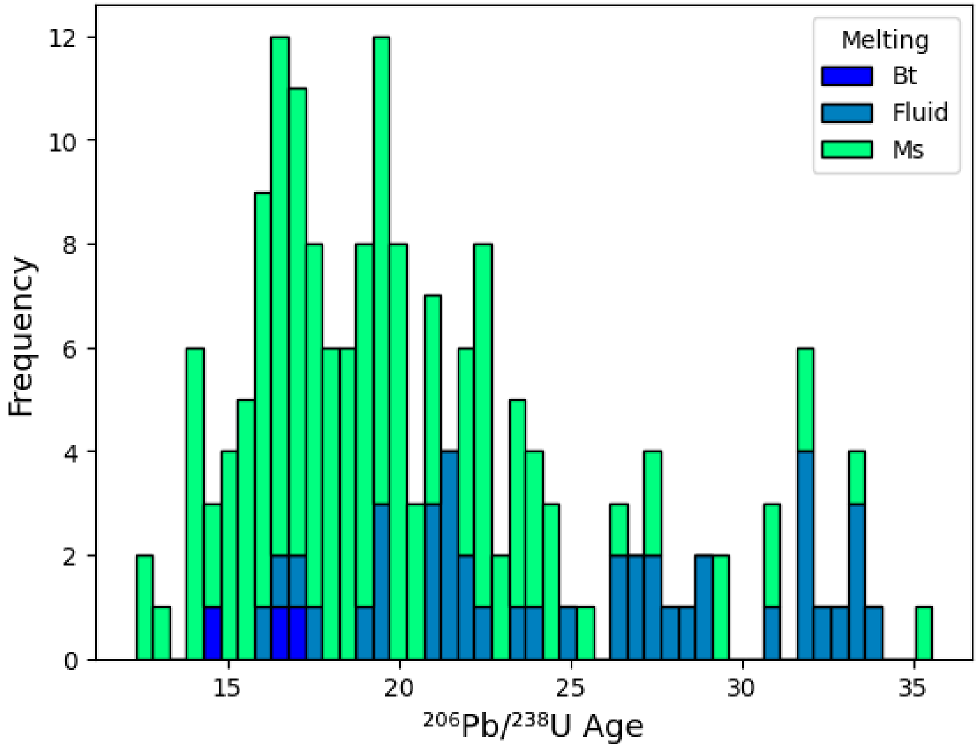

Figure 4.45 – Stacked histogram of zircon rim $^{206}Pb/^{238}U$ ages coloured by sample melt reaction signatures (Bt = biotite-dehydration, Ms = muscovite-dehydration, Fluid = fluid-present). Bin widths are ~0.5 Ma, n = 177.

Monazite age peaks in the leucogranites predate the zircon peaks, at 21-20 Ma, just before the sharp increase in zircon rim crystallisation. For migmatites, monazite age peaks also predate zircon peaks, typically by ~2 Ma, between 26.5-21.5 Ma. This suggests anatectic melt became saturated in LREE prior to saturation in Zr, with monazite dissolving more readily than zircon and therefore more rapidly saturating the melt (Yakymchuk and Brown, 2014). Sample 09b has a notably younger peak age of monazite growth at ~18.5 Ma. This may be explained by the proximity of locality 09 to the Badrinath Shear Zone, with supra-solidus conditions and monazite formation at ~19 Ma reported by Benetti et al. (2021).

Grain textures and corrected age ranges and peak KDE ages of zircon and monazite for each sample, where present, are summarised in Table 4.2.

Table 4.2 – Summarised textures and ages of zircon rims and monazite grains for each sample. Textures are abbreviated, for zircon: Type 1 - Eu. = euhedral, Osc. = oscillatory, Type 2 - R. = rounded, HCont. = high-contrast. For monazite: Type 1 - S. = simple, Osc. = oscillatory, Type 2 - Sec. = sector, Irr. = irregular, L-Th = low Th.

Sample ID	**Rock Type**	**Zircon**		**Monazite**	
		Texture	**$^{206}\text{Pb}/^{238}\text{U}$ ages**	**Texture**	**$^{208}\text{Pb}/^{232}\text{Th}$ ages**
BAD01d	Leucogranite	Eu. Osc.	25.3-15.7 Ma, ~16 Ma peak	S.	22.5-19.0 Ma, ~20.5 Ma peak
BAD03	Leucogranite	Eu. Osc.	21.2-14.8 Ma, ~20 & ~ 15 Ma peaks	-	-
BAD06	Leucogranite	Eu. Osc.	16.9-14.6 Ma	Osc.	25.8-16.8 Ma, ~20 Ma peak
BAD07b	Leucogranite	Eu. Osc.	19.1-13.0 Ma	-	-
BADf04	Leucogranite	Eu. Osc.	19.7-13.8 Ma, ~19 Ma peak	Osc.	22.8-18.0 Ma, ~21 Ma peak
BAD02a	Migmatite	Eu. Osc.	35.5-17.4 Ma, ~ 24 Ma peak	Osc.	33.9-21.7 Ma, ~26.5 Ma peak
BAD02b	Migmatite/ Leucosome	Eu. Osc.	31.6-24.3 Ma	Osc.	27.6-23.5 Ma, ~26.5 Ma peak
BAD04a	Migmatite	Eu. Osc.	20.1-14.6 Ma, ~20 Ma peak	Osc.	22.9-21.6 Ma
BAD04b	Migmatite	Eu. Osc.	21.1-19 Ma	S./Osc.	26.5-21.3 Ma, ~23 Ma peak
BAD05b	Migmatite	-	-	Irr./Sec., L-Th	25.4-19.8 Ma, ~22 Ma peak
BAD07a	Migmatite	Eu. Osc.	18.8-13.8 Ma	-	-
BAD07c	Migmatite	R. HCont.	33.6-19.4 Ma, ~28.5 & ~19.5 Ma peaks	Irr., L-Th	32.9-26.9 Ma
BAD09b	Migmatite	R. HCont.	21.6-16.5 Ma, ~17 Ma peak	Irr., L-Th	33.3-16.3 Ma, ~18.5 Ma peak
BAD11a	Migmatite	R. HCont.	22.1-21.6 Ma	-	-
BADf02	Migmatite	Eu. Osc.	23.8-17.9 Ma, ~23 Ma peak	S.	25.1-23.9 Ma, ~24.5 Ma peak
BADf13	Migmatite	Eu. Osc.	21.9-12.3 Ma, ~16.5 Ma peak	S./Osc.	29.4-21.6 Ma
BAD10	Orthogneiss	R. HCont.	33.4-16.0 Ma, ~26.5 & ~21 Ma peaks	Irr., L-Th	23.4-16.8 Ma, ~21.5 Ma peak

4.4.3 Isotopic signatures transferred from source to melt

The $\delta^{18}O$ values of a magmatic zircon are inherited from the source rock (Valley et al., 2005). Greater variability in $\delta^{18}O$ values is typically recorded in zircons from migmatite samples, up to 2 ‰, compared to the 1 % typically recorded in leucogranite samples. GHS leucogranites ultimately come from migmatitic sources, however, so another factor must be responsible for the difference in range. Migmatites are by definition heterogeneous, often with distinct melanosomes and leucosomes, and thermodynamic modelling of major elements suggests that the extraction, mobilisation, and amalgamation of leucosomes reduces heterogeneity (Koblinger and Pattison, 2017). This heterogeneity likely also applies to O isotopes, as they remain largely unaffected by high-temperature process and fractionation (Valley et al., 2005), and as such, coalesced bodies of leucogranite typically yield narrower ranges of zircon $\delta^{18}O$ values. Migmatite samples 07c, 09b, 11a, and orthogneiss 10, associated with fluid-present melting, all have zircon $\delta^{18}O$ values >10.5 ‰ (Figure 4.24), whilst migmatites associated with fluid-absent melting do not. Similarly to major phase geochemistry, higher $\delta^{18}O$ values in zircon could be attributed to differing proportions of plagioclase and mica consumed during melting (Harris et al., 1993), as plagioclase has higher $\delta^{18}O$ values than muscovite in the same sample, by approximately 1 ‰ (O'Neil and Taylor Jr., 1969).

Hf isotopes are a routinely measured isotopic signature that can be used to identify the source of anatectic melt, as a metasedimentary package, such as the GHS, will impart its Hf signature onto zircon crystallised within that melt (Scherer et al., 2007). Two potential metasedimentary units that could feasibly contribute to Himalayan leucogranites are the host GHS and underlying LHS, which each typically have εHf values of -5 to -40, with a KDE peak at -14.5, and -20 to -40, with a KDE peak at -25, respectively (Spencer et al., 2018). The distribution of εHf values with age from zircon rims of this study suggests that the GHS is the only contributing metasedimentary source unit (Figure 4.46). This is not unexpected, given the host metapelites and migmatites of the Badrinath Formation (upper GHS) is separated from lower GHS and LHS of the Garhwal Himalaya by the ~9 km thick Pandukeshwar Formation meta-arkose and quartzite (Spencer et al., 2012a). Our data differs from the findings in Bhutan, which showed increasing LHS component contributions in leucogranites between 17 and 12 Ma (Hopkinson et al., 2020), and where the thick intervening quartzite does not exist.

Hf isotopes in zircon can also be used to date the extraction of the source material from the mantle (Vervoort and Kemp, 2016). Age of mantle differentiation (T_{DM}) for the source material can be estimated using εHf upper and lower bounds of approximately -8 and -25, and a typical continental crust $^{176}Lu/^{177}Lu$ value of 0.015 (Griffin et al., 2004). This results in T_{DM} ages between ~1550 Ma and

~2600 Ma, with a similar spread of εHf values and corresponding T_{DM} ages to GHS leucogranites from Bhutan (Hopkinson et al., 2017).

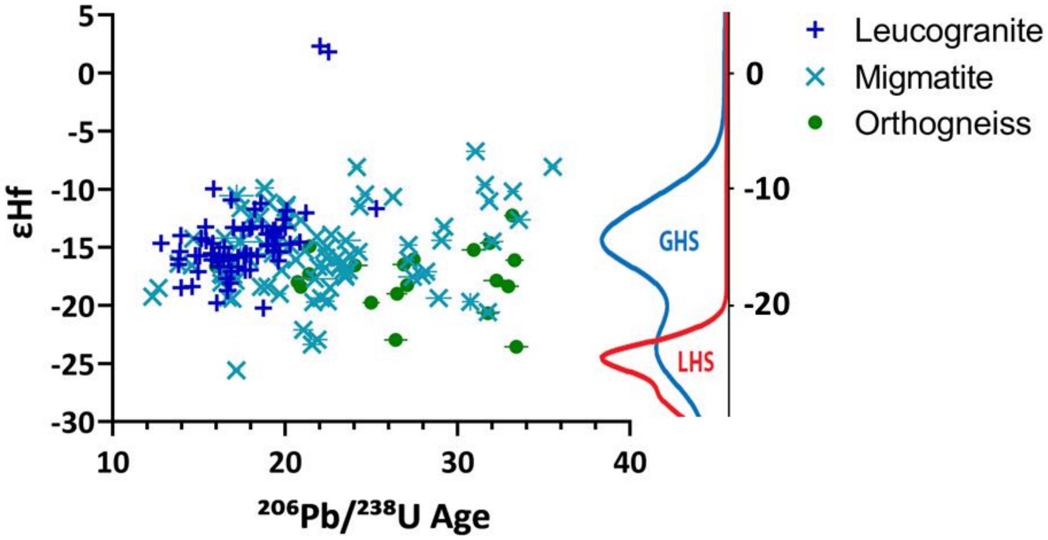

Figure 4.46 – Compiled zircon rim εHf values compared to coinciding $^{206}Pb/^{238}U$ ages. Error bars are 2σ for both εHf and age, however, they are mostly smaller than the symbols. KDEs of GHS and LHS zircon εHf values after Hopkinson et al. (2020) (CC BY 3.0), based on the compilation of Spencer et al. (2018).

Combined Hf-O isotopes, where Hf and O isotopes are measured from the same U-Th-Pb dated zircon growth domain, can be used to characterise melt source(s) (Roberts and Spencer, 2015). Hf-O signatures from Himalayan-aged zircon rims presented in this study plots in the same Hf-O space as GHS leucogranites in Bhutan (Figure 4.47); εHf of -8.5 to -25.5, and $\delta^{18}O$ of 7.8 to 11.8 ‰ (Hopkinson et al., 2017). This highlights the isotopic uniformity present across the GHS, with two sets of Himalayan-aged zircon ~1000 km apart yielding the same range of Hf and O isotopes. As with the study in Bhutan, it can also be inferred that rocks that underwent partial melting in the Garhwal region received no input from a mantle source, as analyses do not lie along a mixing line between the mantle (εHf of 15-17, $\delta^{18}O$ of 5.3 ‰) (Bouvier et al., 2008; Valley, 2003) and a metasedimentary end-member (εHf of -12, $\delta^{18}O$ of 11 ‰) (Hopkinson et al., 2017). As such, migmatite and leucogranite samples from the Garhwal Himalaya represent pure crustal recycling of sedimentary material.

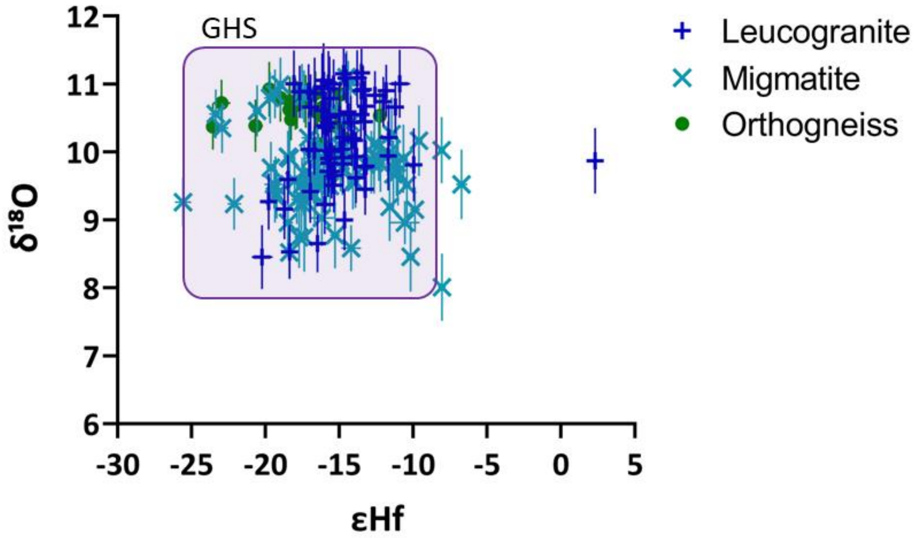

Figure 4.47 – Compiled zircon rim εHf values compared to coinciding $\delta^{18}O$ values. Error bars are 2σ for both εHf and $\delta^{18}O$, however, for εHf they are mostly smaller than the symbols. GHS zone of εHf and $\delta^{18}O$ values (purple) based on leucogranites from Bhutan, after Hopkinson et al. (2017).

4.5 Summary

The metamorphic history of the region can be examined through the timing of zircon and monazite rim growth. Scattered ages between 35 and 25 Ma suggest only minor episodes or volumes of melting during peak metamorphic conditions (Kawabata et al., 2021; Catlos et al., 2007), followed by a considerable increase in zircon and monazite growth at 25 Ma in migmatites and 19.5 Ma in leucogranites. These data suggest that widespread anatexis started 2-3 Ma before the modelled age of rapid exhumation at 22 Ma (Maiti and Mandal, 2021), which in turn was likely triggered by the weakening of the mid-crust. The peak of leucogranite zircon crystallisation then occurred later during decompression. The tectonic importance of muscovite-dehydration melting in the mid-crust is demonstrated through the onset of regional decompression and rapid exhumation between 22 and 17 Ma (Maiti and Mandal, 2021). Monazite age peaks are commonly 1.5-2.0 Ma older than zircon in the same sample, suggesting melt became saturated with respect to LREE significantly before Zr, which agrees with modelled dissolution rates in anatectic melt (Yakymchuk and Brown, 2014).

Groupings of major and trace element zoning patterns in zircon and monazite align with the fluid-present and fluid-absent melt reaction groups suggested by petrographic and major phase geochemistry presented in Chapters 2 & 3. Zircon from samples with fluid-present melting signatures have high-contrast rim domains in CL images, with low U concentrations, relatively weak negative Eu anomalies and low HREE concentrations. Monazite in these samples has low Th concentrations and patchy internal zoning patterns. Zircon from samples with fluid-absent melting signatures display oscillatory zoning in CL images with high U concentrations, and strongly negative Eu anomalies with high HREE abundance. Monazite grains show either simple or oscillatory zoning in Ce-Th-Y maps. Low U and Th concentrations in zircon and monazite from fluid-present melt samples suggest limited availability during crystallisation compared to fluid-absent melt samples, potentially due to low melt volume or interconnectivity (Rubatto, 2017), or in-source authigenic growth (Catlos, 2013; Čopjaková et al., 2011; Cabella et al., 2001). Differences in Eu anomalies between the two groups implies increased competition for Eu in fluid-absent melt samples, due to coexistence with peritectic K-feldspar (Rubatto, 2002; Hinton and Upton, 1991; Murali et al., 1983).

Hf isotopes indicate that migmatite and leucogranite melts in the Garhwal Himalaya are entirely sourced from within the GHS (Hopkinson et al., 2020; Spencer et al., 2018), while combined Hf-O isotopes display the similarity in isotopic systematics between the GHS of the Garhwal Himalaya and Bhutan. Hf-O isotopes also exclude any potential input from the mantle during anatexis; only crustal recycling of sedimentary material was involved (Hopkinson et al., 2017).

5 Synthesis

This thesis set out to characterise the petrographic and chemical signatures of different melt reaction, and to answer questions around the sources, conditions, and timing of melt formation in the Greater Himalayan Sequence (GHS) of the Garhwal Himalaya. The work presented in previous chapters details the textural and geochemical signatures for both fluid-present incongruent melting and fluid-absent dehydration melting of muscovite and biotite. Accessory phases provide insight into the relative timing of these melt reactions and source rock contributions to leucogranitic melt. The key findings of this thesis include:

- Leucogranite, migmatite, and orthogneiss samples from the Garhwal GHS can be placed into three groups based on the presence and textures of peritectic phases formed as a result of differing melt reactions.
    - Fluid-present – peritectic sillimanite, with little (or no) K-feldspar present.
    - Muscovite-dehydration – peritectic K-feldspar and sillimanite, with systematic coarsening of K-feldspar with increasing melt volumes (Dyck et al., 2020).
    - Biotite-dehydration – as with muscovite-dehydration melting, with the addition of peritectic garnet cores with randomly oriented micro-inclusions (Dorais and Campbell, 2022; Dorais and Spencer, 2014; Taylor and Stevens, 2010).
- Melt volumes are lower (<8%) for migmatite samples near the base of the Badrinath Formation and roof of the Joshimath Formation, compared to higher-up stratigraphy in the Badrinath Formation (see Figure 1.2 in Chapter 1).
- Melt reactions are linked to elemental signatures in major phases, attributed to the ratio of mica and plagioclase consumed during melting (Harris et al., 1993, 1995; Gao et al., 2017).
- Ti-in-biotite thermometry indicates lower temperatures for migmatites with fluid-present melting signatures (<750°C) and higher temperatures for those with muscovite-dehydration melting signatures (>750°C). Questions still remain about the Ti activity in a reaction volume during melting and, therefore, when Ti-in-biotite temperatures are recorded along the P-T path.
- Elevated Ti concentrations in garnets from leucogranite sample 06, with acicular rutile exsolution along the core-rim boundary, suggests peritectic garnet core formation at >800°C (Proyer et al., 2013) followed by continued growth within a melt. The tectonic significance of this melting event remains unclear.
- Major and trace element zoning in zircon and monazite for each sample correlate with fluid-present and fluid-absent melting signatures.

  - Fluid-present – zircon grains are rounded, with low-U overgrowths and relatively weak negative Eu anomalies, while monazite grains have low Th concentrations and irregular zoning patterns.
  - Fluid-absent – zircon grains are euhedral, with high-U rims and strongly negative Eu anomalies, while monazite has simple or oscillatory zoning patterns.
- Zircon rim ages spread between 35-25 Ma, from samples with fluid-present melt signatures, suggests brief, low volume melting episodes during peak metamorphic conditions (Kawabata et al., 2021).
- A sharp increase in the volume of zircon and monazite crystallisation in migmatites with fluid-absent melt signatures around 25 Ma, followed by a sharp increase in leucogranite samples at ~19.5 Ma, suggests widespread anatexis started in migmatites 2-3 Ma before the modelled age of rapid exhumation and further widespread melting (Maiti and Mandal, 2021).
  - The spike of zircon crystallisation in fluid-absent melting samples at these times highlights the importance of the muscovite-dehydration reaction to orogenic tectonics.
- Hf isotopes in zircon rims indicate melt was entirely sourced from within the GHS, with T_{DM} ages between ~1550 and ~ 2600 Ma.
- Combined Hf-O data display similar isotopic systematics between the GHS in the Garhwal and Bhutan, while excluding any input from the mantle during anatexis (Hopkinson et al., 2017).

5.1 Petrographic and chemical distinctions of fluid-present and fluid-absent melting

The formation of melt greatly weakens the mechanical strength of the local crust (Rosenberg and Handy, 2005; Vigneresse et al., 1996), while facilitating the exchange and concentration of elements from source to magma (Brown, 2007; Watt et al., 1996; Harris et al., 1995). However, insight into the metamorphic history of a region can be gained through the identification of the prominent melt reactions that have occurred, linked to the timing of their occurrence. As such, the characterisation of textural and geochemical signatures of melt reactions could provide easier identification and interpretation of melting reactions in future research.

Melt reaction signatures in leucogranites and metapelitic migmatites of the Garhwal GHS are recorded in petrographic textures, major phase geochemistry, and accessory phase zoning and trace element abundances. These are summarised in Table 5.1.

Table 5.1 – Summarised signatures of fluid-present and fluid-absent melting for various features and phases.

Feature/ Phase	**Fluid-present incongruent melting**	**Fluid-absent melting**	
		Muscovite-dehydration	**Biotite-dehydration**
Leucosomes	Discrete boundaries with mesosomes	Diffuse boundaries with mesosomes	
K-feldspar	Minor component Primarily in the leucosome Inclusion-poor ↑ Ba, Eu, ↓ Rb/Sr	Major component Leucosome and mesosome Perthitic + inclusion-rich ↓ Ba, Eu, ↑ Rb/Sr	Major component Perthitic + inclusion-rich ↓↓ Ba, Eu, ↑↑ Rb/Sr
Garnet	Partially resorbed Major elements largely homogenised Rim Mn-enrichment	Major elements homogenised Rim Mn-enrichment	Euhedral with micro-inclusions in core Major element zoning Mn-rich core
Mica	↑ Ba, ↓ Sn, Rb/Sr	↓ Ba, ↑ Sn, Rb/Sr	↓↓ Ba, ↑↑ Sn, Rb/Sr
Zircon	Rounded grains + zones Low-U overgrowth Weakly negative Eu/Eu* ↓ HREE	Euhedral grains High-U oscillatory zoning Strongly negative Eu/Eu* ↑ HREE	
Monazite	Irregular zoning ↓ Th	Simple or oscillatory zoning	

In samples that have undergone fluid-present melting, leucosomes and mesosomes form discrete domains with sharp boundaries. K-feldspar has few inclusions, low modal abundance (≤1%), and is primarily present in leucosomes. K-feldspar grains have elevated concentrations of Ba (>3000 ppm), and Eu (up to 4 ppm), with low Rb/Sr values of 0.5-2.0. Micas have elevated concentrations of Ba

(>800 ppm), relatively low Sn, and Rb/Sr values <20 for muscovite and <1000 for biotite. Garnets often show resorption textures, with largely homogenised major elements, and rim enrichment of Mn. Zircon rims are recrystallised, low-U overgrowths, with round internal boundaries and grain morphology. Zircon chondrite-normalised REE profiles show weakly negative Eu anomalies, and relatively low HREE concentrations. Monazite shows irregular patchwork zoning, especially evident in Y maps, and relatively low Th concentrations.

In samples that have undergone fluid-absent muscovite-dehydration melting, leucosomes and mesosomes typically have diffuse boundaries. K-feldspar is present as a major component, forming either clusters of grains replacing plagioclase, or as inclusion-rich porphyroblasts, with perthitic textures common in both. K-feldspar grains have low concentrations of Ba (<3000 ppm), and Eu (<2.5 ppm), with high Rb/Sr values of 2-10. Micas have low concentrations of Ba (<700 ppm), relatively high Sn, and high Rb/Sr values of >40 for muscovite and >1000 for biotite. Major element concentrations in metamorphic garnets are homogenised, with minor (retrogressive) rim enrichment of Mn. Zircon grains are euhedral, with high-U oscillatory zoned rims, and strongly negative Eu anomalies with relatively high HREE concentrations. Monazite shows simple or oscillatory zoning with respect to Ce, Th, and Y.

Signatures of fluid-absent biotite-dehydration melting are only recorded in one leucogranite sample, and as such, are likely to provide an incomplete picture. However, this sample is texturally the same as those recording muscovite-dehydration signatures, with the addition of euhedral garnet with micro-inclusion-rich cores. Garnet major element concentrations are strongly zoned, with high Mn concentrations in the core which decrease steadily towards the rim. K-feldspar has very low concentrations of Ba (<100 ppm), and Eu (<0.5 ppm), with high Rb/Sr values >20. Muscovite has very low concentrations of Ba (<30 ppm), high Sn, and very high Rb/Sr values >400. Zircon textures and trace elements are indistinguishable from samples with muscovite-dehydration signatures, as is the zoning recorded in monazite.

5.2 Implications for tectonics

The P-T-t paths that migmatites in the Garhwal GHS experienced can be pieced together through the combined use of temperature and pressure indicators, melt reaction identification and geochronological data. These paths allow the tectonic evolution across this critical time period to be inferred.

5.2.1 Constraining P-T-t pathways

Temperatures reached by the Garhwal GHS are indicated by Ti-in-biotite thermometry (Chapter 3). For samples recording fluid-present melting signatures, maximum temperatures were between 670-730°C, similar to proposed maximum temperatures of the Lower Badrinath Formation and Badrinath Shear Zone (BSZ) by Benetti et al. (2021). Samples recording fluid-absent melting signatures experienced higher maximum temperatures between 760-780°C, in line with the Upper Badrinath Formation temperatures proposed by Iaccarino et al. (2017) of ≥750°C.

Mineral assemblages can provide a lower bound for pressure, as kyanite and sillimanite observed in sample 10 (Chapter 2), as well as kyanite replacement by sillimanite in mylonitic migmatites from Malari (Iaccarino et al., 2017), indicate pressures >0.7 GPa at temperatures of ~700°C (Hodges and Spear, 1982). Gt-Pl-Ms-Bt and Gt-Pl-Al_2SiO_5-Qtz barometry by Spencer et al. (2012), indicates pressures between 0.85-1.05 GPa.

From zircon and monazite crystallisation ages (Chapter 4), fluid-present melting can be constrained to occur largely along the prograde path, between 35-25 Ma, followed by fluid-absent muscovite-dehydration melting just prior to, and during decompression and exhumation.

These parameters informed phase equilibrium modelling using Perple_X version 6.9.1, in the MnNCKFMASHT (MnO-Na_2O-CaO-K_2O-FeO-MgO-Al_2O_3-SiO_2-H_2O-TiO_2) system. Modelling used the thermodynamic database of Holland and Powell (2011) (hp633ver.dat), and the solid solution models Bio(TCC) for biotite, Mica(W) for muscovite, Gt(W) for garnet, Pl(h) for plagioclase, and melt(W) for magmatic melt. Modelling is based on the mesosome bulk chemistry (derived from EDS maps) of sample 08, presented in Table 5.2 alongside the composition of the average pelite (Forshaw and Pattison, 2021). The concentration of K_2O in sample 08 (6.6 wt%) is notably higher than the average pelite (3.8 wt%), this is likely the effect of using migmatite bulk compositions which would have been changed during partial melting. As such, a modified K_2O concentration of 4 wt%, pre-normalisations with variable H_2O, has been used in the modelling.

Both “wet” and “dry” pelitic compositions were used for modelling, defined as assemblages with and without a subsolidus free aqueous phase along the prograde path. The H_2O wt% values for these two assemblages were determined by phase equilibrium modelling in T-XH_2O space at a fixed pressure of 0.95 GPa (Figure 5.1). The "dry" value of 1.5 wt% H_2O was selected as the lowest concentration of H_2O allowing for a typical prograde pelitic assemblage of muscovite + plagioclase + biotite + garnet + kyanite + rutile. The "wet" value of 2.0 wt% H_2O allows for typical prograde assemblages and a free aqueous phase, with higher concentrations resulting in little change to the assemblage or positions of melt-forming reaction lines.

Table 5.2 – Concentrations (wt%) of relevant oxide phases in the average pelite (Forshaw & Pattison, 2021) and dry and wet pelite compositions, based on sample 08, used for modelling.

	SiO_2	TiO_2	Al_2O_3	Fe_2O_3	FeO	MnO	MgO	CaO	Na_2O	K_2O	H_2O
Average pelite (Forshaw & Pattison, 2021)	60.77	0.97	18.43	1.91	5.11	0.12	2.58	1.29	1.79	3.8	-
Wet modelled composition	64.28	1.00	18.94	-	6.57	0.17	1.43	0.54	1.11	3.96	2.00
Dry modelled composition	64.61	1.01	19.04	-	6.60	0.17	1.44	0.54	1.12	3.98	1.50

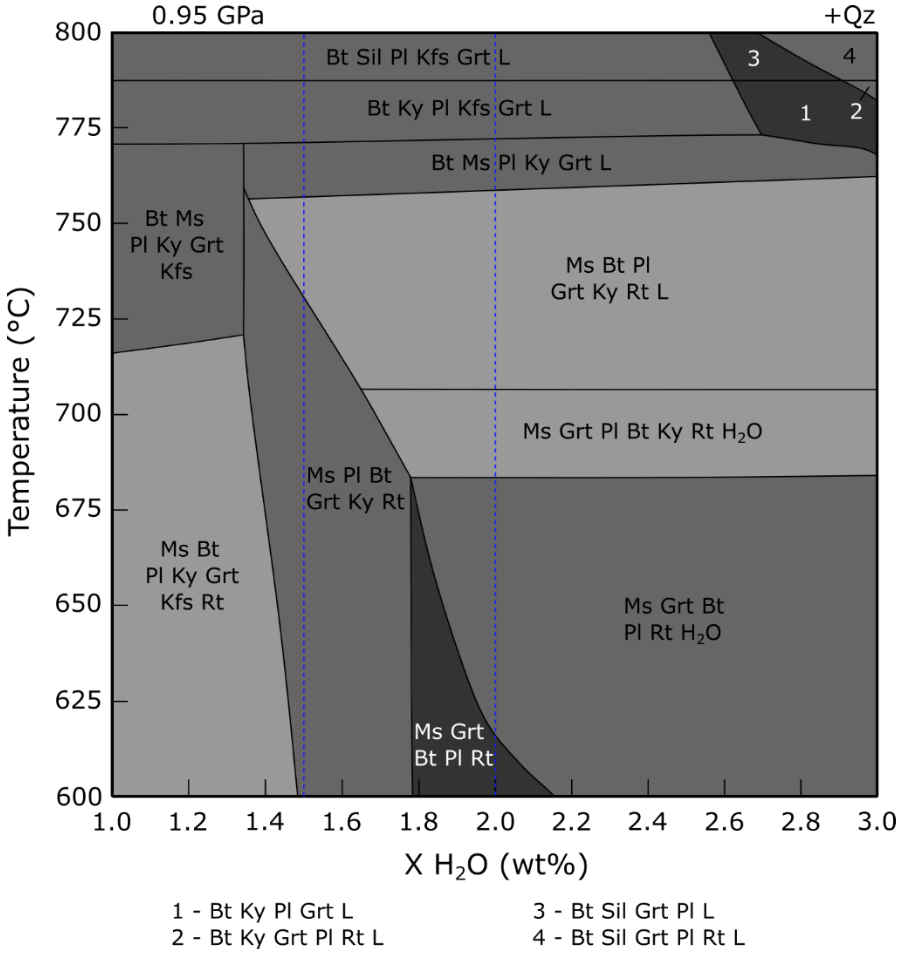

Figure 5.1 – T-XH_2O diagram at a fixed pressure of 0.95 GPa, calculated in Perple_X. Dotted blue lines mark the chosen "dry" (1.5 wt%) and "wet" (2.0 wt%) concentrations of H_2O.

Modelling does not take Fe^{3+} into account as the primary concern of the model is muscovite stability and there is also no correlation across P-T space of muscovite modal abundance and the number of Fe^{3+} cations in muscovite (Forshaw and Pattison, 2021). Fe^{3+} cation values would also be estimates only, that are currently poorly constrained by existing solution models (Forshaw and Pattison, 2021). Also excluded from the model is CO_2, as it is the activity of H_2O that controls the position of the wet solidus in pelites, while partial CO_2 activity marginally suppresses H_2O activity, resulting in little change to the solidus until a_{CO_2} reaches ~40% of total H_2O and CO_2 activity (Weinberg and Hasalová, 2015; Johannes and Holtz, 1996).

P-T pseudosections are presented in Figure 5.2, with (a) 2.0 wt% H_2O and (b) 1.5 wt% H_2O. Potential pathways are shown for the Lower and Middle-Upper Badrinath Formation, which largely agree with those proposed for the BSZ and Pandukeshwar Formation by Benetti et al. (2021) and Iaccarino et al. (2020), and towards the stratigraphic top of the Badrinath Formation by Iaccarino et al. (2017), respectively. The system is oversaturated at 2.0 wt% H_2O, with a free fluid phase present below the solidus, which occurs between 675-710°C. This agrees with the Ti-in-biotite temperatures for fluid-present melt samples. At 1.5 wt% H_2O, the system is saturated, with hydrous phases dominating subsolidus assemblages, while a free fluid phase is only present at temperatures of 600-700°C and pressures less than 0.85 GPa. The solidus intercepts the prograde path between 700-750°C, with a wedge-shaped domain of fluid-present melting encountered shortly before the muscovite-out reaction, i.e. muscovite-dehydration melting, at temperatures of ≥760°C for pressures of ≥0.9 GPa.

Calculated assemblage modal abundances suggests that a system with 2.0 wt% H_2O can generate a melt volume of >8% before reaching the muscovite-out reaction line, while a system with 1.5 wt% H_2O will only generate 2-4% melt before intercepting the muscovite-out line and generating a larger volume of melt (up to ~12% more). As such, under “dry” conditions, muscovite-dehydration is the dominant melt-forming reaction.

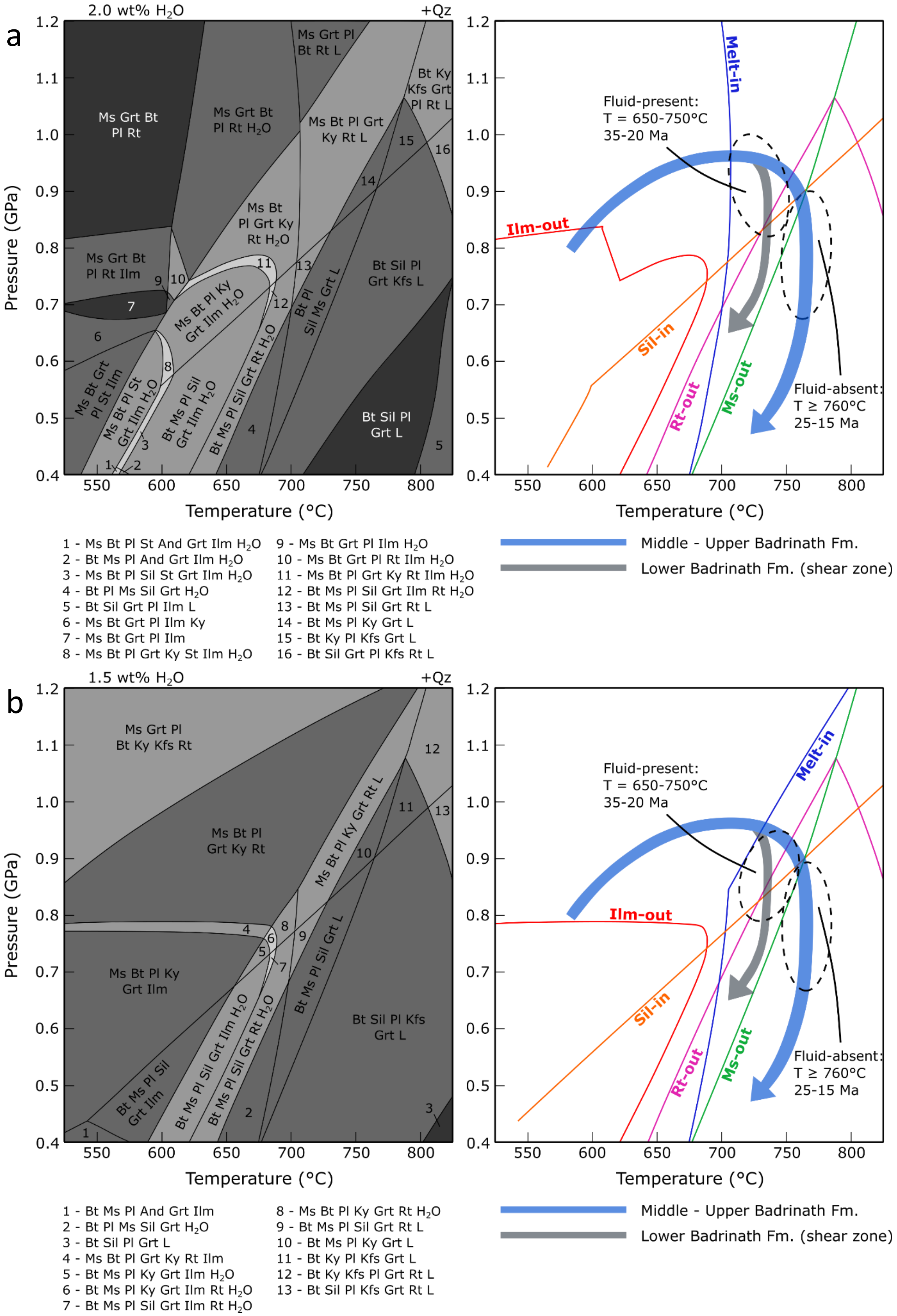

Figure 5.2 – Phase equilibrium diagrams in the MnNCKFMASHT system of pelite compositions in Table 5.2, and charts of main phase stability curves for (a) 2.0 wt% H_2O and (b) 1.5 wt% H_2O, calculated in Perple_X. Also shown are P-T-t paths for the lower and middle-upper portions of the Badrinath Fm, with relative ages of fluid-present and fluid-absent melting.

5.2.2 Evolution of Garhwal crustal architecture

The zircon and monazite crystallisation ages of fluid-present and fluid-absent melt samples suggest there was a transition at around 25 Ma from a system of discrete fluid-present melting events, to one of widespread, fluid-absent melting lasting ~13 Ma (Chapter 4). The BSZ also became active at approximately 23 Ma (Benetti et al., 2021). From this the tectonic evolution of the Garhwal Himalaya can be inferred during this period of anatexis and exhumation.

Melt formation in the Garhwal GHS and the development of the major tectono-stratigraphic discontinuities are summarised in Figure 5.3. Between 35-25 Ma, the upper GHS is under peak P-T conditions, with isolated fluid-present partial melting. Between 25-15 Ma, fluid-absent muscovite-dehydration melting weakens the upper GHS, movement along the BSZ begins, and the Main Central Thrust (MCT) and South Tibetan Detachment System (STDS) are also active from ~20 Ma (Iaccarino et al., 2020, 2017). Isolated fluid-present melting also occurs in the upper Joshimath Formation at 22 Ma (sample 11a – Chapter 4). In its modern configuration, the Badrinath Formation is stratified, with migmatites formed through fluid-present melting found towards the base, as well as (less commonly) further up section, while migmatites in the middle and upper portions formed through dominantly fluid-absent muscovite-dehydration melting.

a) 35 - 25 Ma: Prograde metamorphism and fluid present melting

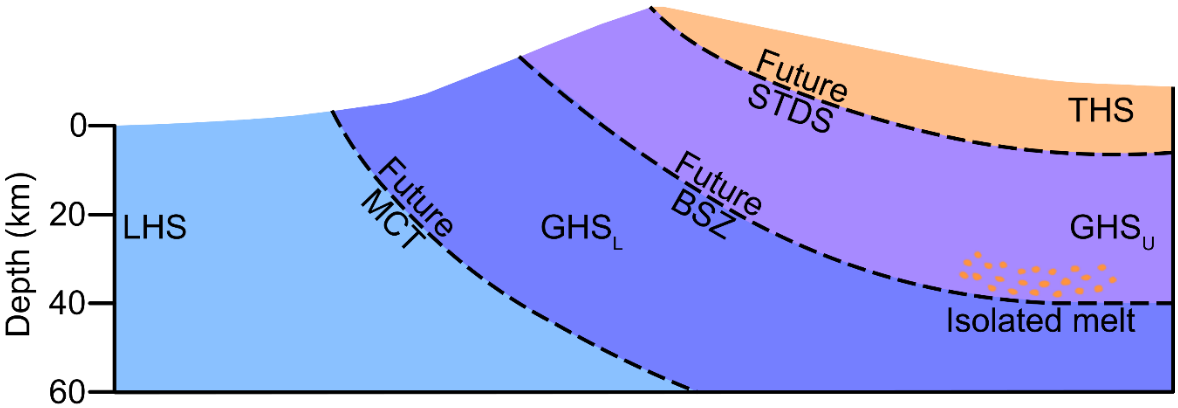

b) 25 - 15 Ma: fluid-absent Ms-dehydration melting and decompression

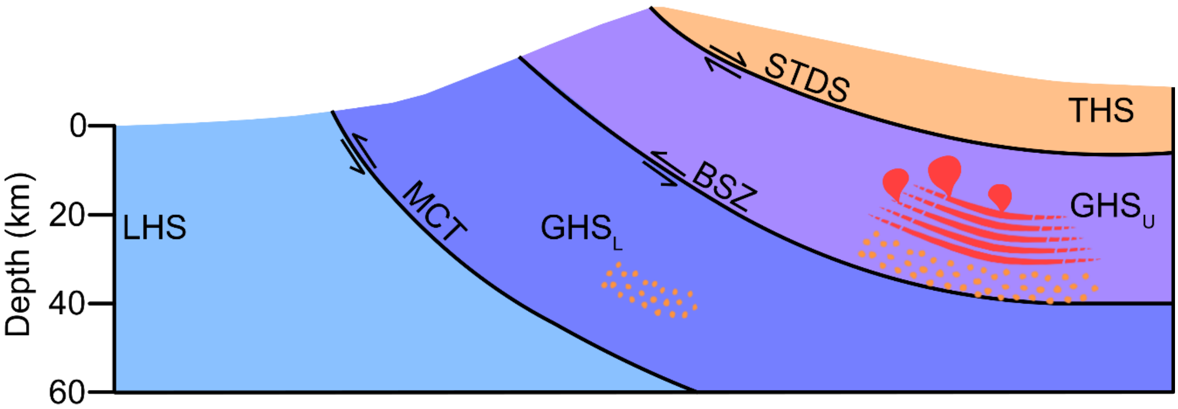

c) Modern

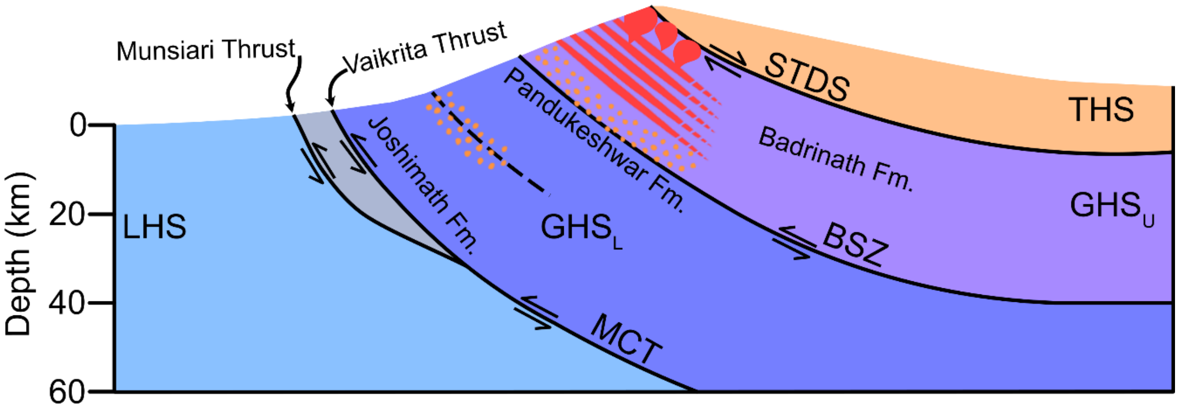

Figure 5.3 – Schematic diagram of the tectonic evolution in the Garhwal GHS. a) Prograde metamorphism with isolated fluid-present melting (orange) in the Badrinath Fm between 35-25 Ma. b) Widespread fluid-absent melting in the Badrinath Fm (red), and isolated fluid-present melting in the Joshimath Fm. Major stratigraphic boundary systems also activate: the Badrinath Shear Zone (BSZ), Main Central Thrust (MCT), and South Tibetan Detachment System (STDS). c) In its modern configuration, migmatites with fluid-present melt signatures are found at the top of the Joshimath Fm, and the Badrinath Fm is stratified between fluid-present melting signatures dominant towards the base, and fluid-absent melting signatures dominant in the middle and upper portions.

5.3 Future work

5.3.1 Identification of peritectic products and melt volumes

Further petrographic characterisation, using CL imaging, is required for plagioclase and K-feldspar in migmatite samples to establish a more straightforward workflow for identification of metamorphic and peritectic grains compared to those crystallised from a melt. The chemical mapping of peritectic garnet cores to observe the distribution and phase-type of micro-inclusions may also provide insight into the mechanics of peritectic garnet nucleation and growth.

The work of Dyck et al. (2020), establishing the stoichiometric relationship between the volume of melt and peritectic K-feldspar and sillimanite during muscovite-dehydration melting, is useful for primary observations in migmatites with K-feldspar. However, there is currently no equivalent empirical stoichiometry for fluid-present melting, and the relationship between melt and sillimanite volume is assumed. A similar study, with migmatites of various melt volumes formed through fluid-present melting, could confirm this relationship.

5.3.2 What temperatures do migmatites recorded?

The application of Ti-in-biotite thermometry to migmatites is discussed in Chapter 3. The a_{TiO_2} in a metapelite or rhyolitic magma is fairly well understood; however, for mixed systems such as migmatites, there are few data available. Further modelling of a_{TiO_2} in an actively melting system, or experimental petrography is therefore needed to establish the impacts of melting on calculating Ti-in-biotite temperatures.

The application of additional thermometers on my sample set would further constrain the P-T-t path. Ti-in-zircon thermometry is well calibrated and would relate directly to the zircon crystallisation ages. This would require further LA-ICP-MS analysis to measure Ti concentrations in zircon rim domains with higher precision. The application of two-feldspar thermometry on peritectic K-feldspar and exsolved perthitic albite would also potentially provide a temperature constraint at the point of muscovite-dehydration melting. Monazite-xenotime thermometry could also be applied to samples where xenotime has been identified as an accessory phase, using calibrations of the temperature-sensitive substitution of Y and HREE into monazite (Pyle et al., 2001; Gratz and Heinrich, 1997, 1998).

5.3.3 Determining melt chemistry

Trace elements concentration measurements from dated monazite grains would provide insight into melt chemistry prior to Zr-saturation and zircon growth, such as the resorption of garnet with Y and HREE concentrations and crystallisation alongside K-feldspar with Eu anomalies. This could also, therefore, provide another chemical indicator for distinguishing between fluid-present or fluid-absent melting.

5.3.4 Sensitivity of melt reactions and of melting conditions to source lithology

Phase equilibrium modelling of semipelite and greywacke protolith compositions within the Garhwal GHS would refine the P-T-t pathways inferred from pelitic assemblages and other constraints. It would also be beneficial to model the separate melt and restitic components, together with melt volumes and periodic melt extraction. As discussed in 5.2.1, the presence of K-feldspar before the muscovite-out stability curve also needs to be addressed so that modelled assemblages more closely resemble petrographic observations. A reduction in K_2O wt% would also likely reduce the fluid-saturation point, as the relative proportions of micas to anhydrous phases would decrease.

6 References

Andersen, T., Elburg, M. A. and Magwaza, B. N. (2019) ‘Sources of bias in detrital zircon geochronology: Discordance, concealed lead loss and common lead correction’, *Earth-Science Reviews*, vol. 197, p. 102899 [Online]. DOI: 10.1016/j.earscirev.2019.102899.

Ashley, K. T. and Law, R. D. (2015) ‘Modeling prograde TiO2 activity and its significance for Ti-in-quartz thermobarometry of pelitic metamorphic rocks’, *Contributions to Mineralogy and Petrology*, vol. 169, no. 2, p. 23 [Online]. DOI: 10.1007/s00410-015-1118-7.

Axler, J. A. and Ague, J. J. (2015) ‘Oriented multiphase needles in garnet from ultrahigh-temperature granulites, Connecticut, U.S.A.’, *American Mineralogist*, vol. 100, no. 10, pp. 2254–2271 [Online]. DOI: 10.2138/am-2015-5018.

Baertschi, P. (1976) ‘Absolute18O content of standard mean ocean water’, *Earth and Planetary Science Letters*, vol. 31, no. 3, pp. 341–344 [Online]. DOI: 10.1016/0012-821X(76)90115-1.

Banno, S. and Chii, S. (1978) ‘A model to explain the Mn enrichment in the rim of zoned garnet.’, *GEOCHEMICAL JOURNAL*, vol. 12, no. 4, pp. 253–257 [Online]. DOI: 10.2343/geochemj.12.253.

Bea, F. (1996) ‘Controls on the trace element composition of crustal melts’, *Earth and Environmental Science Transactions of The Royal Society of Edinburgh*, Royal Society of Edinburgh Scotland Foundation, vol. 87, no. 1–2, pp. 33–41 [Online]. DOI: 10.1017/S0263593300006453.

Beaumont, C., Jamieson, R. A., Nguyen, M. H. and Lee, B. (2001) ‘Himalayan tectonics explained by extrusion of a low-viscosity crustal channel coupled to focused surface denudation’, *Nature*, Nature Publishing Group, vol. 414, no. 6865, pp. 738–742 [Online]. DOI: 10.1038/414738a.

Benetti, B., Montomoli, C., Iaccarino, S., Langone, A. and Carosi, R. (2021) ‘Mapping tectono-metamorphic discontinuities in orogenic belts: implications for mid-crust exhumation in NW Himalaya’, *Lithos*, vol. 392–393, p. 106129 [Online]. DOI: 10.1016/j.lithos.2021.106129.

Blichert-Toft, J. and Albarède, F. (1997) ‘The Lu-Hf isotope geochemistry of chondrites and the evolution of the mantle-crust system’, *Earth and Planetary Science Letters*, vol. 148, no. 1, pp. 243–258 [Online]. DOI: 10.1016/S0012-821X(97)00040-X.

Boehnke, P., Watson, E. B., Trail, D., Harrison, T. M. and Schmitt, A. K. (2013) ‘Zircon saturation re-revisited’, *Chemical Geology*, vol. 351, pp. 324–334 [Online]. DOI: 10.1016/j.chemgeo.2013.05.028.

Borisov, A. and Aranovich, L. (2020) ‘Rutile solubility and TiO2 activity in silicate melts: An experimental study’, *Chemical Geology*, vol. 556, p. 119817 [Online]. DOI: 10.1016/j.chemgeo.2020.119817.

Bouvier, A., Vervoort, J. D. and Patchett, P. J. (2008) ‘The Lu–Hf and Sm–Nd isotopic composition of CHUR: Constraints from unequilibrated chondrites and implications for the bulk composition of terrestrial planets’, *Earth and Planetary Science Letters*, vol. 273, no. 1, pp. 48–57 [Online]. DOI: 10.1016/j.epsl.2008.06.010.

Breton, N. L. and Thompson, A. B. (1988) ‘Fluid-absent (dehydration) melting of biotite in metapelites in the early stages of crustal anatexis’, *Contributions to Mineralogy and Petrology*, vol. 99, no. 2, pp. 226–237 [Online]. DOI: 10.1007/BF00371463.

Brown, M. (2007) ‘Crustal melting and melt extraction, ascent and emplacement in orogens: mechanisms and consequences’, *Journal of the Geological Society*, vol. 164, no. 4, pp. 709–730 [Online]. DOI: 10.1144/0016-76492006-171.

Brown, M. (2013) ‘Granite: From genesis to emplacement’, *GSA Bulletin*, vol. 125, no. 7–8, pp. 1079–1113 [Online]. DOI: 10.1130/B30877.1.

Cabella, R., Lucchetti, G. and Marescotti, P. (2001) ‘Authigenic monazite and xenotime from pelitic metacherts in pumpellyite–actinolite-facies conditions, Sestri–Voltaggio zone, central Liguria, Italy’, *The Canadian Mineralogist*, vol. 39, no. 3, pp. 717–727 [Online]. DOI: 10.2113/gscanmin.39.3.717.

Caddick, M. J., Konopásek, J. and Thompson, A. B. (2010) ‘Preservation of Garnet Growth Zoning and the Duration of Prograde Metamorphism’, *Journal of Petrology*, vol. 51, no. 11, pp. 2327–2347 [Online]. DOI: 10.1093/petrology/egq059.

Carosi, R., Montomoli, C. and Iaccarino, S. (2018) ‘20 years of geological mapping of the metamorphic core across Central and Eastern Himalayas’, *Earth-Science Reviews*, vol. 177, pp. 124–138 [Online]. DOI: 10.1016/j.earscirev.2017.11.006.

Carosi, R., Montomoli, C., Langone, A., Turina, A., Cesare, B., Iaccarino, S., Fascioli, L., Visonà, D., Ronchi, A. and Rai, S. M. (2015) ‘Eocene partial melting recorded in peritectic garnets from kyanite-gneiss, Greater Himalayan Sequence, central Nepal’, *Geological Society, London, Special Publications*, The Geological Society of London, vol. 412, no. 1, pp. 111–129 [Online]. DOI: 10.1144/SP412.1.

Catlos, E. (2013) ‘Generalizations about monazite: Implications for geochronologic studies’, *American Mineralogist*, vol. 98, pp. 819–832 [Online]. DOI: 10.2138/am.2013.4336.

Catlos, E. J., Shekhar Dubey, C., Marston, R. A. and Harrison, T. M. (2007) ‘Geochronologic constraints across the Main Central Thrust shear zone, Bhagirathi River (NW India): Implications for Himalayan tectonics’, in Cloos, M., Carlson, W. D., Gilbert, M. C., Liou, J. G., and Sorensen, S. S. (eds), *Convergent Margin Terranes and Associated Regions: A Tribute to W.G. Ernst*, Geological Society of America, vol. 419, p. 0 [Online]. DOI: 10.1130/2006.2419(07) (Accessed 13 January 2023).

Cawood, P. A., Johnson, M. R. W. and Nemchin, A. A. (2007) ‘Early Palaeozoic orogenesis along the Indian margin of Gondwana: Tectonic response to Gondwana assembly’, *Earth and Planetary Science Letters*, vol. 255, no. 1, pp. 70–84 [Online]. DOI: 10.1016/j.epsl.2006.12.006.

Chambers, J. A. and Kohn, M. J. (2012) ‘Titanium in muscovite, biotite, and hornblende: Modeling, thermometry, and rutile activities of metapelites and amphibolites’, *American Mineralogist*, vol. 97, no. 4, pp. 543–555 [Online]. DOI: 10.2138/am.2012.3890.

Chinner, G. A. (1961) ‘The Origin of Sillimanite in Glen Clova, Angus’, *Journal of Petrology*, vol. 2, no. 3, pp. 312–323 [Online]. DOI: 10.1093/petrology/2.3.312.

Claiborne, L. L., Miller, C. F. and Wooden, J. L. (2010) ‘Trace element composition of igneous zircon: a thermal and compositional record of the accumulation and evolution of a large silicic batholith, Spirit Mountain, Nevada’, *Contributions to Mineralogy and Petrology*, vol. 160, no. 4, pp. 511–531 [Online]. DOI: 10.1007/s00410-010-0491-5.

Čopjaková, R., Novák, M. and Franců, E. (2011) ‘Formation of authigenic monazite-(Ce) to monazite-(Nd) from Upper Carboniferous graywackes of the Drahany Upland: Roles of the chemical composition of host rock and burial temperature’, *Lithos*, vol. 127, no. 1, pp. 373–385 [Online]. DOI: 10.1016/j.lithos.2011.08.001.

Copley, A., Avouac, J.-P. and Royer, J.-Y. (2010) 'India-Asia collision and the Cenozoic slowdown of the Indian plate: Implications for the forces driving plate motions', *Journal of Geophysical Research: Solid Earth*, vol. 115, no. B3 [Online]. DOI: 10.1029/2009JB006634 (Accessed 13 January 2023).

Cottle, J. M., Kylander-Clark, A. R. and Vrijmoed, J. C. (2012) 'U–Th/Pb geochronology of detrital zircon and monazite by single shot laser ablation inductively coupled plasma mass spectrometry (SS-LA-ICPMS)', *Chemical Geology*, vol. 332–333, pp. 136–147 [Online]. DOI: 10.1016/j.chemgeo.2012.09.035.

Cottle, J. M., Larson, K. P. and Kellett, D. A. (2015) 'How does the mid-crust accommodate deformation in large, hot collisional orogens? A review of recent research in the Himalayan orogen', *Journal of Structural Geology*, vol. 78, pp. 119–133 [Online]. DOI: 10.1016/j.jsg.2015.06.008.

Dahlen, F. A. (1990) 'Critical taper model of fold-and-thrust belts and accretionary wedges', *Annual Review of Earth and Planetary Sciences*, vol. 18, no. 1, pp. 55–99 [Online]. DOI: 10.1146/annurev.ea.18.050190.000415.

Deer, W. A., Howie, R. A. and Zussman, J. (2013) 'An Introduction to the Rock-Forming Minerals', [Online]. DOI: 10.1180/DHZ (Accessed 26 October 2022).

Dorais, M. J. and Campbell, S. (2022) 'Peritectic and phenocrystic garnet accumulation and the origin of strongly peraluminous granitic rocks: The Flagstaff Lake Igneous Complex, Maine', *Lithos*, vol. 418–419, p. 106680 [Online]. DOI: 10.1016/j.lithos.2022.106680.

Dorais, M. J. and Spencer, C. J. (2014) 'Revisiting the importance of residual source material (restite) in granite petrogenesis: The Cardigan Pluton, New Hampshire', *Lithos*, vol. 202–203, pp. 237–249 [Online]. DOI: 10.1016/j.lithos.2014.05.007.

Dyck, B., St-Onge, M., Searle, M. P., Rayner, N., Waters, D. and Weller, O. M. (2019) 'Protolith lithostratigraphy of the Greater Himalayan Series in Langtang, Nepal: implications for the architecture of the northern Indian margin', *Geological Society, London, Special Publications*, The Geological Society of London, vol. 483, no. 1, pp. 281–304 [Online]. DOI: 10.1144/SP483.9.

Dyck, B., Waters, D. J., St-Onge, M. R. and Searle, M. P. (2020) 'Muscovite dehydration melting: Reaction mechanisms, microstructures, and implications for anatexis', *Journal of Metamorphic Geology*, vol. 38, no. 1, pp. 29–52 [Online]. DOI: 10.1111/jmg.12511.

Erdmann, S., Scaillet, B. and Kellett, D. A. (2012) 'Textures of Peritectic Crystals as Guides to Reactive Minerals in Magmatic Systems: New Insights from Melting Experiments', *Journal of Petrology*, vol. 53, no. 11, pp. 2231–2258 [Online]. DOI: 10.1093/petrology/egs048.

Ferry, J. M. and Watson, E. B. (2007) 'New thermodynamic models and revised calibrations for the Ti-in-zircon and Zr-in-rutile thermometers', *Contributions to Mineralogy and Petrology*, vol. 154, no. 4, pp. 429–437 [Online]. DOI: 10.1007/s00410-007-0201-0.

Fisher, C. M., Vervoort, J. D. and DuFrane, S. A. (2014) 'Accurate Hf isotope determinations of complex zircons using the "laser ablation split stream" method', *Geochemistry, Geophysics, Geosystems*, vol. 15, no. 1, pp. 121–139 [Online]. DOI: 10.1002/2013GC004962.

Forshaw, J. B. and Pattison, D. R. M. (2021) 'Ferrous/ferric (Fe2+/Fe3+) partitioning among silicates in metapelites', *Contributions to Mineralogy and Petrology*, vol. 176, no. 9, p. 63 [Online]. DOI: 10.1007/s00410-021-01814-4.

Frost, B. R. and Chacko, T. (1989) ‘The Granulite Uncertainty Principle: Limitations on Thermobarometry in Granulites’, *The Journal of Geology*, The University of Chicago Press, vol. 97, no. 4, pp. 435–450.

Gao, L.-E., Zeng, L. and Asimow, P. D. (2017) ‘Contrasting geochemical signatures of fluid-absent versus fluid-fluxed melting of muscovite in metasedimentary sources: The Himalayan leucogranites’, *Geology*, vol. 45, no. 1, pp. 39–42 [Online]. DOI: 10.1130/G38336.1.

Gao, S., Liu, X., Yuan, H., Hattendorf, B., Günther, D., Chen, L. and Hu, S. (2002) ‘Determination of Forty Two Major and Trace Elements in USGS and NIST SRM Glasses by Laser Ablation-Inductively Coupled Plasma-Mass Spectrometry’, *Geostandards Newsletter*, vol. 26, no. 2, pp. 181–196 [Online]. DOI: 10.1111/j.1751-908X.2002.tb00886.x.

Gardien, V., Thompson, A., Grujic, D. and Ulmer, P. (1995) ‘Experimental melting of biotite + plagioclase + quartz ± muscovite assemblages and implications for crustal melting’, *Journal of Geophysical Research*, vol. 100, p. 15581 [Online]. DOI: 10.1029/95JB00916.

Gee, D. G., Fossen, H., Henriksen, N. and Higgins, A. K. (2008) ‘From the Early Paleozoic Platforms of Baltica and Laurentia to the Caledonide Orogen of Scandinavia and Greenland’, *Episodes Journal of International Geoscience*, International Union of Geological Sciences, vol. 31, no. 1, pp. 44–51 [Online]. DOI: 10.18814/epiiugs/2008/v31i1/007.

Gehrels, G., Decelles, P., Martin, A., Ojha, T., Pinhassi, G. and Upreti, B. (2003) ‘Initiation of the Himalayan Orogen as an Early Paleozoic Thin-skinned Thrust Belt’, *Gsa Today*, vol. 13 [Online]. DOI: 10.1130/1052-5173(2003)13<4:IOTHOA>2.0.CO;2.

Goldstein, J. I., Newbury, D. E., Michael, J. R., Ritchie, N. W. M., Scott, J. H. J. and Joy, D. C. (2017) *Scanning Electron Microscopy and X-Ray Microanalysis*, Springer.

Gratz, R. and Heinrich, W. (1997) ‘Monazite-xenotime thermobarometry: Experimental calibration of the miscibility gap in the binary system CePO4-YPO4’, *American Mineralogist*, vol. 82, pp. 772–780 [Online]. DOI: 10.2138/am-1997-7-816.

Gratz, R. and Heinrich, W. (1998) ‘Monazite-xenotime thermometry; III, Experimental calibration of the partitioning of gadolinium between monazite and xenotime’, *European Journal of Mineralogy*, vol. 10, no. 3, pp. 579–588.

Griffin, W. L., Belousova, E. A., Shee, S. R., Pearson, N. J. and O’Reilly, S. Y. (2004) ‘Archean crustal evolution in the northern Yilgarn Craton: U–Pb and Hf-isotope evidence from detrital zircons’, *Precambrian Research*, Archaean Tectonics, Volume 2, vol. 131, no. 3, pp. 231–282 [Online]. DOI: 10.1016/j.precamres.2003.12.011.

Grujic, D., Casey, M., Davidson, C., Hollister, L. S., Kündig, R., Pavlis, T. and Schmid, S. (1996) ‘Ductile extrusion of the Higher Himalayan Crystalline in Bhutan: evidence from quartz microfabrics’, *Tectonophysics*, vol. 260, no. 1, pp. 21–43 [Online]. DOI: 10.1016/0040-1951(96)00074-1.

Harris, N., Ayres, M. and Massey, J. (1995) ‘Geochemistry of granitic melts produced during the incongruent melting of muscovite: Implications for the extraction of Himalayan leucogranite magmas’, *Journal of Geophysical Research: Solid Earth*, vol. 100, no. B8, pp. 15767–15777 [Online]. DOI: 10.1029/94JB02623.

Harris, N., Massey, J. and Inger, S. (1993) ‘The role of fluids in the formation of High Himalayan leucogranites’, *Geological Society, London, Special Publications*, The Geological Society of London, vol. 74, no. 1, pp. 391–400 [Online]. DOI: 10.1144/GSL.SP.1993.074.01.26.

Hatch, F. H., Well, A. K. and Wells, M. K. (1961) 'Petrology of the igneous rocks', in 12th edition., London, Thomas Murby and Co., vol. 1, p. 515.

Henry, D. and Guidotti, C. (2002) 'Titanium in biotite from metapelitic rocks: Temperature effects, crystal-chemical controls, and petrologic applications', *American Mineralogist*, vol. 87, pp. 375–382 [Online]. DOI: 10.2138/am-2002-0401.

Hibbard, M. J. (1979) 'Myrmekite as a marker between preaqueous and postaqueous phase saturation in granitic systems', *GSA Bulletin*, vol. 90, no. 11, pp. 1047–1062 [Online]. DOI: 10.1130/0016-7606(1979)90<1047:MAAMBP>2.0.CO;2.

Hinton, R. W. and Upton, B. G. J. (1991) 'The chemistry of zircon: Variations within and between large crystals from syenite and alkali basalt xenoliths', *Geochimica et Cosmochimica Acta*, The Macalpine Hills Lunar Meteorite Consortium, vol. 55, no. 11, pp. 3287–3302 [Online]. DOI: 10.1016/0016-7037(91)90489-R.

Hirschmiller, J., Grujic, D., Bookhagen, B., Coutand, I., Huyghe, P., Mugnier, J.-L. and Ojha, T. (2014) 'What controls the growth of the Himalayan fold-and-thrust belt?', *Geology*, vol. 42, pp. 247–250 [Online]. DOI: 10.1130/G35057.1.

Hodges, K. V. (2000) 'Tectonics of the Himalaya and southern Tibet from two perspectives', *GSA Bulletin*, vol. 112, no. 3, pp. 324–350 [Online]. DOI: 10.1130/0016-7606(2000)112<324:TOTHAS>2.0.CO;2.

Hodges, K. V. and Spear, F. S. (1982) 'Geothermometry, geobarometry and the Al2SiO5 triple point at Mt. Moosilauke, New Hampshire', *American Mineralogist*, vol. 67, no. 11–12, pp. 1118–1134.

Holland, T. J. B. and Powell, R. (2011) 'An improved and extended internally consistent thermodynamic dataset for phases of petrological interest, involving a new equation of state for solids', *Journal of Metamorphic Geology*, vol. 29, no. 3, pp. 333–383 [Online]. DOI: 10.1111/j.1525-1314.2010.00923.x.

Hopkinson, T., Harris, N., Roberts, N. M. W., Warren, C. J., Hammond, S., Spencer, C. J. and Parrish, R. R. (2020) 'Evolution of the melt source during protracted crustal anatexis: An example from the Bhutan Himalaya', *Geology*, vol. 48, no. 1, pp. 87–91 [Online]. DOI: 10.1130/G47078.1.

Hopkinson, T. N., Harris, N. B. W., Warren, C. J., Spencer, C. J., Roberts, N. M. W., Horstwood, M. S. A., Parrish, R. R., and Eimf (2017) 'The identification and significance of pure sediment-derived granites', *Earth and Planetary Science Letters*, vol. 467, pp. 57–63 [Online]. DOI: 10.1016/j.epsl.2017.03.018.

Hoskin, P. W. O. (2000) 'Patterns of chaos: fractal statistics and the oscillatory chemistry of zircon', *Geochimica et Cosmochimica Acta*, vol. 64, no. 11, pp. 1905–1923 [Online]. DOI: 10.1016/S0016-7037(00)00330-6.

Hoskin, P. W. O. and Schaltegger, U. (2003) 'The Composition of Zircon and Igneous and Metamorphic Petrogenesis', *Reviews in Mineralogy and Geochemistry*, vol. 53, no. 1, pp. 27–62 [Online]. DOI: 10.2113/0530027.

Hwang, S. L., Yui, T. F., Chu, H. T., Shen, P., Schertl, H. P., Zhang, R. Y. and Liou, J. G. (2007) 'On the origin of oriented rutile needles in garnet from UHP eclogites', *Journal of Metamorphic Geology*, vol. 25, no. 3, pp. 349–362 [Online]. DOI: 10.1111/j.1525-1314.2007.00699.x.

Hwang, S.-L., Shen, P., Chu, H.-T. and Yui, T.-F. (2016) ‘On the forbidden and the optimum crystallographic variant of rutile in garnet’, *Journal of Applied Crystallography*, International Union of Crystallography, vol. 49, no. 6, pp. 1922–1940 [Online]. DOI: 10.1107/S1600576716014151.

Iaccarino, S., Montomoli, C., Carosi, R., Massonne, H.-J., Langone, A. and Visonà, D. (2015) ‘Pressure–temperature–time–deformation path of kyanite-bearing migmatitic paragneiss in the Kali Gandaki valley (Central Nepal): Investigation of Late Eocene–Early Oligocene melting processes’, *Lithos*, vol. 231, pp. 103–121 [Online]. DOI: 10.1016/j.lithos.2015.06.005.

Iaccarino, S., Montomoli, C., Carosi, R., Montemagni, C., Massonne, H.-J., Langone, A., Jain, A. K. and Visonà, D. (2017) ‘Pressure-Temperature-Deformation-Time Constraints on the South Tibetan Detachment System in the Garhwal Himalaya (NW India)’, *Tectonics*, vol. 36, no. 11, pp. 2281–2304 [Online]. DOI: 10.1002/2017TC004566.

Iaccarino, S., Montomoli, C., Montemagni, C., Massonne, H.-J., Langone, A., Jain, A. K., Visonà, D. and Carosi, R. (2020) ‘The Main Central Thrust zone along the Alaknanda and Dhauli Ganga valleys (Garhwal Himalaya, NW India): Insights into an inverted metamorphic sequence’, *Lithos*, vol. 372–373, p. 105669 [Online]. DOI: 10.1016/j.lithos.2020.105669.

Inger, S. and Harris, N. (1993) ‘Geochemical Constraints on Leucogranite Magmatism in the Langtang Valley, Nepal Himalaya’, *Journal of Petrology*, vol. 34, no. 2, pp. 345–368 [Online]. DOI: 10.1093/petrology/34.2.345.

Inger, S. and Harris, N. B. W. (1992) ‘Tectonothermal evolution of the High Himalayan Crystalline Sequence, Langtang Valley, northern Nepal’, *Journal of Metamorphic Geology*, vol. 10, no. 3, pp. 439–452 [Online]. DOI: 10.1111/j.1525-1314.1992.tb00095.x.

Jackson, S. E., Pearson, N. J., Griffin, W. L. and Belousova, E. A. (2004) ‘The application of laser ablation-inductively coupled plasma-mass spectrometry to in situ U–Pb zircon geochronology’, *Chemical Geology*, vol. 211, no. 1, pp. 47–69 [Online]. DOI: 10.1016/j.chemgeo.2004.06.017.

Jain, A., M., S., Seth, P., Kanyan, L., Carosi, R., Montomoli, C., Iaccarino, S. and Mukherjee, P. k (2014) ‘The Higher Himalayan Crystallines, Alaknanda – Dhauli Gan-ga Valleys, Garhwal Himalaya, India’, *Journal of the Virtual Explorer*, vol. 47, p. 35.

Jenner, F. E. and O’Neill, H. S. C. (2012) ‘Major and trace analysis of basaltic glasses by laser-ablation ICP-MS’, *Geochemistry Geophysics Geosystems*, vol. 13, no. 3 [Online]. Available at https://oro.open.ac.uk/38166/ (Accessed 18 October 2022).

Jessup, M. J. (2013) ‘Mid-crustal processes in the Himalaya’, *Speaking of Geoscience* [Online]. Available at https://speakingofgeoscience.org/2013/08/28/mid-crustal-processes-in-the-himalaya/ (Accessed 23 January 2023).

Johannes, W. and Holtz, F. (1996) *Petrogenesis and Experimental Petrology of Granitic Rocks*, Springer Science & Business Media.

Jung, S., Pfänder, J. A., Mezger, K., Hellebrand, E. and Brandt, S. (2022) ‘Polyphase growth history of peritectic garnet from a granite: Trace-element zonation, Lu-Hf ages and their significance for the duration of granite-forming processes’, *Lithos*, vol. 418–419, p. 106675 [Online]. DOI: 10.1016/j.lithos.2022.106675.

Kawabata, R., Imayama, T., Bose, N., Yi, K. and Kouketsu, Y. (2021) ‘Tectonic discontinuity, partial melting and exhumation in the Garhwal Himalaya (Northwest India): Constrains from spatial and temporal pressure-temperature conditions along the Bhagirathi valley', *Lithos*, vol. 404–405, p. 106488 [Online]. DOI: 10.1016/j.lithos.2021.106488.

Kemp, A. I. S., Hawkesworth, C. J., Foster, G. L., Paterson, B. A., Woodhead, J. D., Hergt, J. M., Gray, C. M. and Whitehouse, M. J. (2007) 'Magmatic and Crustal Differentiation History of Granitic Rocks from Hf-O Isotopes in Zircon', *Science*, American Association for the Advancement of Science, vol. 315, no. 5814, pp. 980–983.

Kemp, A. I. S., Hawkesworth, C. J., Paterson, B. A., Foster, G. L., Kinny, P. D., Whitehouse, M. J., Maas, R. and EIMF (2006) 'Exploring the plutonic-volcanic link: a zircon U-Pb, Lu-Hf and O isotope study of paired volcanic and granitic units from southeastern Australia', *Earth and Environmental Science Transactions of The Royal Society of Edinburgh*, Royal Society of Edinburgh Scotland Foundation, vol. 97, no. 4, pp. 337–355 [Online]. DOI: 10.1017/S0263593300001498.

Kessel, R., Schmidt, M. W., Ulmer, P. and Pettke, T. (2005) 'Trace element signature of subduction-zone fluids, melts and supercritical liquids at 120–180 km depth', *Nature*, Nature Publishing Group, vol. 437, no. 7059, pp. 724–727 [Online]. DOI: 10.1038/nature03971.

King, E. M., Valley, J. W., Davis, D. W. and Edwards, G. R. (1998) 'Oxygen isotope ratios of Archean plutonic zircons from granite–greenstone belts of the Superior Province: indicator of magmatic source', *Precambrian Research*, vol. 92, no. 4, pp. 365–387 [Online]. DOI: 10.1016/S0301-9268(98)00082-5.

Koblinger, B. M. and Pattison, D. R. M. (2017) 'Crystallization of Heterogeneous Pelitic Migmatites: Insights from Thermodynamic Modelling', *Journal of Petrology*, vol. 58, no. 2, pp. 297–326 [Online]. DOI: 10.1093/petrology/egx017.

Kohn, M. (2014) 'Himalayan Metamorphism and Its Tectonic Implications', *Annual Review of Earth and Planetary Sciences*, vol. 42, pp. 381–419 [Online]. DOI: 10.1146/annurev-earth-060313-055005.

Kohn, M. J. (2008) 'P-T-t data from central Nepal support critical taper and repudiate large-scale channel flow of the Greater Himalayan Sequence', *GSA Bulletin*, vol. 120, no. 3–4, pp. 259–273 [Online]. DOI: 10.1130/B26252.1.

Kohn, M. J. and Spear, F. (2000) 'Retrograde net transfer reaction insurance for pressure-temperature estimates', *Geology*, vol. 28, no. 12, pp. 1127–1130 [Online]. DOI: 10.1130/0091-7613(2000)28<1127:RNTRIF>2.0.CO;2.

Kylander-Clark, A. R. C., Hacker, B. R. and Cottle, J. M. (2013) 'Laser-ablation split-stream ICP petrochronology', *Chemical Geology*, vol. 345, pp. 99–112 [Online]. DOI: 10.1016/j.chemgeo.2013.02.019.

Lederer, G. W., Cottle, J. M., Jessup, M. J., Langille, J. M. and Ahmad, T. (2013) 'Timescales of partial melting in the Himalayan middle crust: insight from the Leo Pargil dome, northwest India', *Contributions to Mineralogy and Petrology*, vol. 166, no. 5, pp. 1415–1441 [Online]. DOI: 10.1007/s00410-013-0935-9.

Lee, J. K. W., Williams, I. S. and Ellis, D. J. (1997) 'Pb, U and Th diffusion in natural zircon', *Nature*, Nature Publishing Group, vol. 390, no. 6656, pp. 159–162 [Online]. DOI: 10.1038/36554.

Li, X., Tang, G., Gong, B., Yang, Y., Hou, K., Hu, Z., Li, Q., Liu, Y. and Li, W. (2013) 'Qinghu zircon: A working reference for microbeam analysis of U-Pb age and Hf and O isotopes', *Chinese Science Bulletin*, vol. 58, no. 36, pp. 4647–4654 [Online]. DOI: 10.1007/s11434-013-5932-x.

Li, X.-H., Long, W.-G., Li, Q.-L., Liu, Y., Zheng, Y.-F., Yang, Y.-H., Chamberlain, K. R., Wan, D.-F., Guo, C.-H., Wang, X.-C. and Tao, H. (2010) 'Penglai Zircon Megacrysts: A Potential New Working Reference Material for Microbeam Determination of Hf–O Isotopes and U–Pb Age', *Geostandards and Geoanalytical Research*, vol. 34, no. 2, pp. 117–134 [Online]. DOI: 10.1111/j.1751-908X.2010.00036.x.

Luo, T., Zhao, H., Li, Q., Li, Y., Zhang, W., Guo, J., Liu, Y., Zhang, J. and Hu, Z. (2020) 'Non-Matrix-Matched Determination of Th-Pb Ages in Zircon, Monazite and Xenotime by Laser Ablation-Inductively Coupled Plasma-Mass Spectrometry', *Geostandards and Geoanalytical Research*, vol. 44, no. 4, pp. 653–668 [Online]. DOI: 10.1111/ggr.12356.

Maiti, G. and Mandal, N. (2021) 'Early Miocene Exhumation of High-Pressure Rocks in the Himalaya: A Response to Reduced India-Asia Convergence Velocity', *Frontiers in Earth Science*, vol. 9 [Online]. Available at https://www.frontiersin.org/articles/10.3389/feart.2021.632806 (Accessed 6 December 2022).

Meinhold, G. (2010) 'Rutile and its applications in earth sciences', *Earth-Science Reviews*, vol. 102, no. 1, pp. 1–28 [Online]. DOI: 10.1016/j.earscirev.2010.06.001.

Mezger, K. and Krogstad, E. J. (2004) 'Interpretation of discordant U-Pb zircon ages: An evaluation', *Journal of Metamorphic Geology*, vol. 15, pp. 127–140 [Online]. DOI: 10.1111/j.1525-1314.1997.00008.x.

Miller, C., Thöni, M., Frank, W., Grasemann, B., Klötzli, U., Guntli, P. and Draganits, E. (2001) 'The early Palaeozoic magmatic event in the Northwest Himalaya, India: source, tectonic setting and age of emplacement', *Geological Magazine*, Cambridge University Press, vol. 138, no. 3, pp. 237–251 [Online]. DOI: 10.1017/S0016756801005283.

Montel, J.-M., Foret, S., Veschambre, M., Nicollet, C. and Provost, A. (1996) 'Electron microprobe dating of monazite', *Chemical Geology*, vol. 131, no. 1, pp. 37–53 [Online]. DOI: 10.1016/0009-2541(96)00024-1.

Montomoli, C., Carosi, R. and Iaccarino, S. (2015) 'Tectonometamorphic discontinuities in the Greater Himalayan Sequence: a local or a regional feature?', *Geological Society, London, Special Publications*, The Geological Society of London, vol. 412, no. 1, pp. 25–41 [Online]. DOI: 10.1144/SP412.3.

Morel, M. L. A., Nebel, O., Nebel-Jacobsen, Y. J., Miller, J. S. and Vroon, P. Z. (2008) 'Hafnium isotope characterization of the GJ-1 zircon reference material by solution and laser-ablation MC-ICPMS', *Chemical Geology*, vol. 255, no. 1, pp. 231–235 [Online]. DOI: 10.1016/j.chemgeo.2008.06.040.

Murali, A. V., Parthasarathy, R., Mahadevan, T. M. and Das, M. S. (1983) 'Trace element characteristics, REE patterns and partition coefficients of zircons from different geological environments—A case study on Indian zircons', *Geochimica et Cosmochimica Acta*, vol. 47, no. 11, pp. 2047–2052 [Online]. DOI: 10.1016/0016-7037(83)90220-X.

Nábělek, J., Hetényi, G., Vergne, J., Sapkota, S., Kafle, B., Jiang, M., Su, H., Chen, J., Huang, B.-S. and Team, the H.-C. (2009) 'Underplating in the Himalaya-Tibet Collision Zone Revealed by the Hi-CLIMB Experiment', *Science*, American Association for the Advancement of Science, vol. 325, no. 5946, pp. 1371–1374 [Online]. DOI: 10.1126/science.1167719.

Nabelek, P. I. (2019) 'Petrogenesis of leucogranites in collisional orogens', *Geological Society, London, Special Publications*, The Geological Society of London, vol. 491, no. 1, pp. 179–207 [Online]. DOI: 10.1144/SP491-2018-181.

O’Neil, J. R. and Taylor Jr., H. P. (1969) ‘Oxygen isotope equilibrium between muscovite and water’, *Journal of Geophysical Research (1896-1977)*, vol. 74, no. 25, pp. 6012–6022 [Online]. DOI: 10.1029/JB074i025p06012.

Palme, H. and O’Neill, H. St. C. (2014) ‘Cosmochemical Estimates of Mantle Composition’, in *Treatise on Geochemistry*, Elsevier, pp. 1–39 [Online]. DOI: 10.1016/B978-0-08-095975-7.00201-1 (Accessed 22 November 2022).

Parneix, J. C., Beaufort, D., Dudoignon, P. and Meunier, A. (1985) ‘Biotite chloritization process in hydrothermally altered granites’, *Chemical Geology*, vol. 51, no. 1, pp. 89–101 [Online]. DOI: 10.1016/0009-2541(85)90089-0.

Patchett, P. J. and Tatsumoto, M. (1981) ‘A routine high-precision method for Lu-Hf isotope geochemistry and chronology’, *Contributions to Mineralogy and Petrology*, vol. 75, no. 3, pp. 263–267 [Online]. DOI: 10.1007/BF01166766.

Patiño Douce, A. E. and Harris, N. (1998) ‘Experimental Constraints on Himalayan Anatexis’, *Journal of Petrology*, vol. 39, no. 4, pp. 689–710 [Online]. DOI: 10.1093/petroj/39.4.689.

Paton, C., Hellstrom, J., Paul, B., Woodhead, J. and Hergt, J. (2011) ‘Iolite: Freeware for the visualisation and processing of mass spectrometric data’, *Journal of Analytical Atomic Spectrometry*, The Royal Society of Chemistry, vol. 26, no. 12, pp. 2508–2518 [Online]. DOI: 10.1039/C1JA10172B.

Paton, C., Woodhead, J. D., Hellstrom, J. C., Hergt, J. M., Greig, A. and Maas, R. (2010) ‘Improved laser ablation U-Pb zircon geochronology through robust downhole fractionation correction’, *Geochemistry, Geophysics, Geosystems*, vol. 11, no. 3 [Online]. DOI: 10.1029/2009GC002618 (Accessed 20 June 2023).

Paul, S. K. (1998) ‘Geology and tectonics of the Central Crystallines of northeastern Kumaun Himalaya, India’, *Journal of Nepal Geological Society*, vol. 18, pp. 151–167 [Online]. DOI: 10.3126/jngs.v18i0.32249.

Piccolo, A., Faccenda, M., Carosi, R., Montomoli, C. and Visonà, D. (2018) ‘Crustal strength control on structures and metamorphism in collisional orogens’, *Tectonophysics*, Understanding geological processes through modelling - A Memorial Volume honouring Evgenii Burov, vol. 746, pp. 470–492 [Online]. DOI: 10.1016/j.tecto.2017.09.018.

Pickering, J. M. and Johnston, D. A. (1998) ‘Fluid-Absent Melting Behavior of a Two-Mica Metapelite: Experimental Constraints on the Origin of Black Hills Granite’, *Journal of Petrology*, vol. 39, no. 10, pp. 1787–1804 [Online]. DOI: 10.1093/petroj/39.10.1787.

Prince, C. I., Harris, N. and Vance, D. (2001) ‘Fluid-enhanced melting during prograde metamorphism’, *Journal of the Geological Society*, vol. 158, no. 2, pp. 233–241 [Online]. DOI: 10.1144/jgs.158.2.233.

Proyer, A., Habler, G., Abart, R., Wirth, R., Krenn, K. and Hoinkes, G. (2013) ‘TiO2 exsolution from garnet by open-system precipitation: evidence from crystallographic and shape preferred orientation of rutile inclusions’, *Contributions to Mineralogy and Petrology*, vol. 166, no. 1, pp. 211–234 [Online]. DOI: 10.1007/s00410-013-0872-7.

Pyle, J. M., Spear, F. S., Rudnick, R. L. and McDonough, W. F. (2001) ‘Monazite–Xenotime–Garnet Equilibrium in Metapelites and a New Monazite–Garnet Thermometer’, *Journal of Petrology*, vol. 42, no. 11, pp. 2083–2107 [Online]. DOI: 10.1093/petrology/42.11.2083.

Pyle, J. and Spear, F. (1999) 'Yttrium zoning in garnet: Coupling of major and accessory phases during metamorphic reactions', *Geological Materials Research*, vol. 1.

Que, M. and Allen, A. R. (1996) 'Sericitization of plagioclase in the Rosses Granite Complex, Co. Donegal, Ireland', *Mineralogical Magazine*, Cambridge University Press, vol. 60, no. 403, pp. 927–936 [Online]. DOI: 10.1180/minmag.1996.060.403.07.

Rapp, R. P. and Watson, E. B. (1986) 'Monazite solubility and dissolution kinetics: implications for the thorium and light rare earth chemistry of felsic magmas', *Contributions to Mineralogy and Petrology*, vol. 94, no. 3, pp. 304–316 [Online]. DOI: 10.1007/BF00371439.

Rivers, T. (2012) *Tectonic styles in Canada: the Lithoprobe perspective*, Percival, J. A., Clowes, R., and Cook, F. A. (eds), Geological Association of Canada special paper, St. John's, Newfoundland, Canada, Geological Association of Canada.

Roberts, N. M. W. and Spencer, C. J. (2015) 'The zircon archive of continent formation through time', *Geological Society, London, Special Publications*, The Geological Society of London, vol. 389, no. 1, pp. 197–225 [Online]. DOI: 10.1144/SP389.14.

Rosenberg, C. L. and Handy, M. R. (2005) 'Experimental deformation of partially melted granite revisited: implications for the continental crust', *Journal of Metamorphic Geology*, vol. 23, no. 1, pp. 19–28 [Online]. DOI: 10.1111/j.1525-1314.2005.00555.x.

Rubatto, D. (2002) 'Zircon trace element geochemistry: partitioning with garnet and the link between U–Pb ages and metamorphism', *Chemical Geology*, vol. 184, no. 1, pp. 123–138 [Online]. DOI: 10.1016/S0009-2541(01)00355-2.

Rubatto, D. (2017) 'Zircon: The Metamorphic Mineral', *Reviews in Mineralogy and Geochemistry*, vol. 83, no. 1, pp. 261–295 [Online]. DOI: 10.2138/rmg.2017.83.9.

Rubatto, D. and Gebauer, D. (2000) 'Use of Cathodoluminescence for U-Pb Zircon Dating by Ion Microprobe: Some Examples from the Western Alps', in Pagel, M., Barbin, V., Blanc, P., and Ohnenstetter, D. (eds), *Cathodoluminescence in Geosciences*, Berlin, Heidelberg, Springer, pp. 373–400 [Online]. DOI: 10.1007/978-3-662-04086-7_15 (Accessed 13 January 2023).

Rubatto, D., Williams, I. S. and Buick, I. S. (2001) 'Zircon and monazite response to prograde metamorphism in the Reynolds Range, central Australia', *Contributions to Mineralogy and Petrology*, vol. 140, no. 4, pp. 458–468 [Online]. DOI: 10.1007/PL00007673.

Sachan, H. K., Kohn, M. J., Saxena, A. and Corrie, S. L. (2010) 'The Malari leucogranite, Garhwal Himalaya, northern India: Chemistry, age, and tectonic implications', *GSA Bulletin*, vol. 122, no. 11–12, pp. 1865–1876 [Online]. DOI: 10.1130/B30153.1.

Scaillet, B., France-Lanord, C. and Le Fort, P. (1990) 'Badrinath-Gangotri plutons (Garhwal, India): petrological and geochemical evidence for fractionation processes in a high Himalayan leucogranite', *Journal of Volcanology and Geothermal Research*, vol. 44, no. 1, pp. 163–188 [Online]. DOI: 10.1016/0377-0273(90)90017-A.

Scherer, E. E., Whitehouse, M. J. and Münker, C. (2007) 'Zircon as a Monitor of Crustal Growth', *Elements*, vol. 3, no. 1, pp. 19–24 [Online]. DOI: 10.2113/gselements.3.1.19.

Schiller, D. and Finger, F. (2019) 'Application of Ti-in-zircon thermometry to granite studies: problems and possible solutions', *Contributions to Mineralogy and Petrology*, vol. 174, no. 6, p. 51 [Online]. DOI: 10.1007/s00410-019-1585-3.

Searle, M. P. (1999) ‘Emplacement of Himalayan leucogranites by magma injection along giant sill complexes: examples from the Cho Oyu, Gyachung Kang and Everest leucogranites (Nepal Himalaya)’, *Journal of Asian Earth Sciences*, vol. 17, no. 5, pp. 773–783 [Online]. DOI: 10.1016/S1367-9120(99)00020-6.

Searle, M. P., Cottle, J. M., Streule, M. J. and Waters, D. J. (2009) ‘Crustal melt granites and migmatites along the Himalaya: melt source, segregation, transport and granite emplacement mechanisms’, *Earth and Environmental Science Transactions of The Royal Society of Edinburgh*, Royal Society of Edinburgh Scotland Foundation, vol. 100, no. 1–2, pp. 219–233 [Online]. DOI: 10.1017/S175569100901617X.

Sen, A., Dey, A. and Sen, K. (2022) ‘Age, petrogenesis, and metamorphic modelling of high-pressure garnet-amphibolite from the Tethyan Himalayan Sequence of Bhagirathi Valley, Western Garhwal Himalaya’, *Geological Journal*, vol. n/a, no. n/a, pp. 1–17 [Online]. DOI: 10.1002/gj.4638.

Shau, Y.-H., Yang, H.-Y. and Peacor, D. R. (1991) ‘On oriented titanite and rutile inclusions in sagenitic biotite’, *American Mineralogist*, vol. 76, no. 7–8, pp. 1205–1217.

Singh, S. (2019) ‘Protracted zircon growth in migmatites and in situ melt of Higher Himalayan Crystallines: U–Pb ages from Bhagirathi valley, NW Himalaya, India’, *Geoscience Frontiers*, Special Issue: Advances in Himalayan Tectonics, vol. 10, no. 3, pp. 793–809 [Online]. DOI: 10.1016/j.gsf.2017.12.014.

Sláma, J., Košler, J., Condon, D. J., Crowley, J. L., Gerdes, A., Hanchar, J. M., Horstwood, M. S. A., Morris, G. A., Nasdala, L., Norberg, N., Schaltegger, U., Schoene, B., Tubrett, M. N. and Whitehouse, M. J. (2008) ‘Plešovice zircon — A new natural reference material for U–Pb and Hf isotopic microanalysis’, *Chemical Geology*, vol. 249, no. 1, pp. 1–35 [Online]. DOI: 10.1016/j.chemgeo.2007.11.005.

Spear, F. S. (2014) ‘The duration of near-peak metamorphism from diffusion modelling of garnet zoning’, *Journal of Metamorphic Geology*, vol. 32, no. 8, pp. 903–914 [Online]. DOI: 10.1111/jmg.12099.

Spencer, C. J., Dyck, B., Mottram, C. M., Roberts, N. M. W., Yao, W.-H. and Martin, E. L. (2018) ‘Deconvolving the pre-Himalayan Indian margin – Tales of crustal growth and destruction’, *Geoscience Frontiers*, Special Issue: Advances in Himalayan Tectonics, vol. 10, no. 3, pp. 863–872 [Online]. DOI: 10.1016/j.gsf.2018.02.007.

Spencer, C. J., Harris, R. A. and Dorais, M. J. (2012a) ‘The metamorphism and exhumation of the Himalayan metamorphic core, eastern Garhwal region, India’, *Tectonics*, vol. 31, no. 1 [Online]. DOI: 10.1029/2010TC002853 (Accessed 12 July 2022).

Spencer, C. J., Harris, R. A. and Dorais, M. J. (2012b) ‘Depositional provenance of the Himalayan metamorphic core of Garhwal region, India: Constrained by U–Pb and Hf isotopes in zircons’, *Gondwana Research*, vol. 22, no. 1, pp. 26–35 [Online]. DOI: 10.1016/j.gr.2011.10.004.

Spencer, C. J., Kirkland, C. L., Roberts, N. M. W., Evans, N. J. and Liebmann, J. (2020) ‘Strategies towards robust interpretations of in situ zircon Lu–Hf isotope analyses’, *Geoscience Frontiers*, vol. 11, no. 3, pp. 843–853 [Online]. DOI: 10.1016/j.gsf.2019.09.004.

Stacey, J. S. and Kramers, J. D. (1975) ‘Approximation of terrestrial lead isotope evolution by a two-stage model’, *Earth and Planetary Science Letters*, vol. 26, no. 2, pp. 207–221 [Online]. DOI: 10.1016/0012-821X(75)90088-6.

Stern, C. R., Kligfield, R., Schelling, D., Virdi, N. S., Futa, K., Peterman, Z. E. and Amini, H. (1989) 'The Bhagirathi leucogranite of the High Himalaya (Garhwal, India); Age, petrogenesis, and tectonic implications', in Malinconico, L. L., Jr. and Lillie, R. J. (eds), *Tectonics of the western Himalayas*, Geological Society of America, vol. 232, p. 0 [Online]. DOI: 10.1130/SPE232-p33 (Accessed 13 October 2022).

Stern, R. A., Bodorkos, S., Kamo, S. L., Hickman, A. H. and Corfu, F. (2009) 'Measurement of SIMS Instrumental Mass Fractionation of Pb Isotopes During Zircon Dating', *Geostandards and Geoanalytical Research*, vol. 33, no. 2, pp. 145–168 [Online]. DOI: 10.1111/j.1751-908X.2009.00023.x.

Taylor, J. and Stevens, G. (2010) 'Selective entrainment of peritectic garnet into S-type granitic magmas: Evidence from Archaean mid-crustal anatectites', *Lithos*, vol. 120, no. 3, pp. 277–292 [Online]. DOI: 10.1016/j.lithos.2010.08.015.

Thöni, M., Miller, C., Hager, C., Grasemann, B. and Horschinegg, M. (2012) 'New geochronological constraints on the thermal and exhumation history of the Lesser and Higher Himalayan Crystalline Units in the Kullu–Kinnaur area of Himachal Pradesh (India)', *Journal of Asian Earth Sciences*, vol. 52, pp. 98–116 [Online]. DOI: 10.1016/j.jseaes.2012.02.015.

Tischendorf, G., Rieder, M., Förster, H.-J., Gottesmann, B. and Guidotti, Ch. V. (2004) 'A new graphical presentation and subdivision of potassium micas', *Mineralogical Magazine*, vol. 68, no. 4, pp. 649–667 [Online]. DOI: 10.1180/0026461046840210.

Trail, D., Bruce Watson, E. and Tailby, N. D. (2012) 'Ce and Eu anomalies in zircon as proxies for the oxidation state of magmas', *Geochimica et Cosmochimica Acta*, vol. 97, pp. 70–87 [Online]. DOI: 10.1016/j.gca.2012.08.032.

Valdiya, K. S. (1979) 'An Outline of the Structural Set-Up of the Kumaun Himalaya', *Geological Society of India*, vol. 20, no. 4, pp. 145–157.

Valley, J. (2003) 'Oxygen Isotopes in Zircon', *Reviews in Mineralogy & Geochemistry*, vol. 53 [Online]. DOI: 10.2113/0530343.

Valley, J. W., Lackey, J. S., Cavosie, A. J., Clechenko, C. C., Spicuzza, M. J., Basei, M. A. S., Bindeman, I. N., Ferreira, V. P., Sial, A. N., King, E. M., Peck, W. H., Sinha, A. K. and Wei, C. S. (2005) '4.4 billion years of crustal maturation: oxygen isotope ratios of magmatic zircon', *Contributions to Mineralogy and Petrology*, vol. 150, no. 6, pp. 561–580 [Online]. DOI: 10.1007/s00410-005-0025-8.

Vermeesch, P. (2012) 'On the visualisation of detrital age distributions', *Chemical Geology*, vol. 312–313, pp. 190–194 [Online]. DOI: 10.1016/j.chemgeo.2012.04.021.

Vermeesch, P. (2021) 'On the treatment of discordant detrital zircon U–Pb data', *Geochronology*, Copernicus GmbH, vol. 3, no. 1, pp. 247–257 [Online]. DOI: 10.5194/gchron-3-247-2021.

Vervoort, J. D. and Kemp, A. I. S. (2016) 'Clarifying the zircon Hf isotope record of crust–mantle evolution', *Chemical Geology*, vol. 425, pp. 65–75 [Online]. DOI: 10.1016/j.chemgeo.2016.01.023.

Vigneresse, J. L., Barbey, P. and Cuney, M. (1996) 'Rheological Transitions During Partial Melting and Crystallization with Application to Felsic Magma Segregation and Transfer', *Journal of Petrology*, vol. 37, no. 6, pp. 1579–1600 [Online]. DOI: 10.1093/petrology/37.6.1579.

Waters, D. J. (2019) 'Metamorphic constraints on the tectonic evolution of the High Himalaya in Nepal: the art of the possible', *Geological Society, London, Special Publications*, The Geological Society of London, vol. 483, no. 1, pp. 325–375 [Online]. DOI: 10.1144/SP483-2018-187.

Watson, E. B., Chemiak, D. J., Hanchar, J. M., Harrison, T. M. and Wark, D. A. (1997) 'The incorporation of Pb into zircon', *Chemical Geology*, vol. 141, no. 1, pp. 19–31 [Online]. DOI: 10.1016/S0009-2541(97)00054-5.

Watson, E. B. and Cherniak, D. J. (1997) 'Oxygen diffusion in zircon', *Earth and Planetary Science Letters*, vol. 148, no. 3, pp. 527–544 [Online]. DOI: 10.1016/S0012-821X(97)00057-5.

Watson, E. B. and Harrison, T. M. (1983) 'Zircon saturation revisited: temperature and composition effects in a variety of crustal magma types', *Earth and Planetary Science Letters*, vol. 64, no. 2, pp. 295–304 [Online]. DOI: 10.1016/0012-821X(83)90211-X.

Watt, G. R., Burns, I. M. and Graham, G. A. (1996) 'Chemical characteristics of migmatites: accessory phase distribution and evidence for fast melt segregation rates', *Contributions to Mineralogy and Petrology*, vol. 125, no. 1, pp. 100–111 [Online]. DOI: 10.1007/s004100050209.

Weinberg, R. F. (2016) 'Himalayan leucogranites and migmatites: nature, timing and duration of anatexis', *Journal of Metamorphic Geology*, vol. 34, no. 8, pp. 821–843 [Online]. DOI: 10.1111/jmg.12204.

Weinberg, R. F. and Hasalová, P. (2015) 'Water-fluxed melting of the continental crust: A review', *Lithos*, vol. 212–215, pp. 158–188 [Online]. DOI: 10.1016/j.lithos.2014.08.021.

Weller, O. M., Mottram, C. M., St-Onge, M. R., Möller, C., Strachan, R., Rivers, T. and Copley, A. (2021) 'The metamorphic and magmatic record of collisional orogens', *Nature Reviews Earth & Environment*, Nature Publishing Group, vol. 2, no. 11, pp. 781–799 [Online]. DOI: 10.1038/s43017-021-00218-z.

Whittington, A. G. and Treloar, P. J. (2002) 'Crustal anatexis and its relation to the exhumation of collisional orogenic belts, with particular reference to the Himalaya', *Mineralogical Magazine*, vol. 66, no. 1, pp. 53–91 [Online]. DOI: 10.1180/0026461026610015.

Wiedenbeck, M., Allé, P., Corfu, F., Griffin, W. l., Meier, M., Oberli, F., Quadt, A. V., Roddick, J. c. and Spiegel, W. (1995) 'Three Natural Zircon Standards for U-Th-Pb, Lu-Hf, Trace Element and Ree Analyses', *Geostandards Newsletter*, vol. 19, no. 1, pp. 1–23 [Online]. DOI: 10.1111/j.1751-908X.1995.tb00147.x.

Williams, M. A., Kelsey, D. E. and Rubatto, D. (2022) 'Thorium zoning in monazite: A case study from the Ivrea–Verbano zone, NW Italy', *Journal of Metamorphic Geology*, vol. 40, no. 6, pp. 1015–1042 [Online]. DOI: 10.1111/jmg.12656.

Woodhead, J. D. and Hergt, J. M. (2005) 'A Preliminary Appraisal of Seven Natural Zircon Reference Materials for In Situ Hf Isotope Determination', *Geostandards and Geoanalytical Research*, vol. 29, no. 2, pp. 183–195 [Online]. DOI: 10.1111/j.1751-908X.2005.tb00891.x.

Worden, R. H., Walker, F. D. L., Parsons, I. and Brown, W. L. (1990) 'Development of microporosity, diffusion channels and deuteric coarsening in perthitic alkali feldspars', *Contributions to Mineralogy and Petrology*, vol. 104, no. 5, pp. 507–515 [Online]. DOI: 10.1007/BF00306660.

Wu, C.-M. and Chen, H. (2015) 'Revised Ti-in-biotite geothermometer for ilmenite- or rutile-bearing crustal metapelites', *Science Bulletin*, vol. 60 [Online]. DOI: 10.1007/s11434-014-0674-y.

Yakymchuk, C. and Brown, M. (2014) ‘Behaviour of zircon and monazite during crustal melting’, *Journal of the Geological Society*, vol. 171, no. 4, pp. 465–479 [Online]. DOI: 10.1144/jgs2013-115.

Yang, Q., Xia, X., Zhang, W., Zhang, Y., Xiong, B., Xu, Y., Wang, Q. and Wei, G. (2018) ‘An evaluation of precision and accuracy of SIMS oxygen isotope analysis’, *Solid Earth Sciences*, vol. 3, no. 3, pp. 81–86 [Online]. DOI: 10.1016/j.sesci.2018.05.001.

7 Appendices

7.1 Appendix A

The accompanying Excel worksheets for Appendix A can be found at: https://doi.org/10.21954/ou.rd.23608428

7.1.1 EDS data collection and reduction methods

The EDS was calibrated using the cobalt in the Geo MkII standard block (P&H Developments: https://pandhdevelopments.com/geological.html) for ~200,000 counts (10-15 seconds). EDS acquisition settings were as follows:

- Number of Channels – 2048
- Process time – 4
- Acquisition Time (s) – 30.00

Results were not normalized to allow for unquantifiable chemical species (e.g. Li, Be, OH, F, Cl). Two measurements of the almandine standard from the Geo MkII block were taken periodically to monitor the EDS sensitivity, as well as after each calibration with the cobalt. Here is an example order of analysis:

- Site 1 –
    - Beam Measurement 1 – cobalt calibration
    - Electron Image 1 – Low-res. image of standard (i.e. Almandine)
    - Spectrum 1 – standard
    - Spectrum 2 – standard
- Site 2 –
    - Electron Image 2 – High-res. image of sample analysis site
    - Spectrum 3 – sample
    - Spectrum 4 – sample
    - Spectrum 5 – sample
- Site 3 & 4 – as with Site 2
- Site 5 –
    - Electron Image 5 – Low-res. image of standard
    - Spectrum 12 – standard
    - Spectrum 13 – standard

Almandine standard total oxide wt% measurements were monitored, and totals below ~99.5% resulted in EDS recalibration to cobalt.

In order to account for EDS detector sensitivity loss, a time value was allocated to each analysis; 0.5 for each spectrum and 1.0 for each move to another analysis site, with the time allocation reset before each recalibration.

Total oxide wt% values for standard measurements were then plotted against time, with the trendline equation used to correct relative sensitivity loss for each sample’s oxide measurements with its given time allocation. For R^2 values <0.85, individual corrections were applied, or uncorrected measurements were used.

7.1.2 EDS standard evaluation and error

See the accompanying Excel file ‘Appendix A’ sheets labelled 7.1.2 Standards and 7.1.2 Error.

7.1.3 Major element concentration results

See the accompanying Excel file ‘Appendix A’ sheets labelled 7.1.3 Oxide wt% results and 7.1.3 **Mineral** apfu.

7.1.4 Garnet profile endmember compositions

See the accompanying Excel file ‘Appendix A’ sheets labelled 7.1.4 **Sample number**.

7.2 Appendix B

The accompanying Excel worksheets for Appendix B can be found at:

https://doi.org/10.21954/ou.rd.23608716

7.2.1 LA-ICP-MS standard analyses

See the accompanying Excel file ‘Appendix B’ sheets labelled 7.2.1 BCR **Sample numbers**, where BCR standard analyses are evaluated for each analytical batch.

7.2.2 Trace element concentration results

See the accompanying Excel file ‘Appendix B’ sheets labelled 7.2.2 Trace element results and 7.2.2 06 garnet grain mount.

7.3 Appendix C

The accompanying Excel worksheets for Appendix C can be found at:

https://doi.org/10.21954/ou.rd.23608734

7.3.1 Ti-in-biotite thermometry calculation and results

See the accompanying Excel file 'Appendix C' sheets labelled 7.3.1 EDS data and 7.3.1 LA-ICP-MS data.

7.4 Appendix D

The accompanying Excel worksheets for Appendix D can be found at:
https://doi.org/10.21954/ou.rd.23608749

7.4.1 Zircon U-Th-Pb, O, and Hf isotope and trace element standard measurements

See the accompanying Excel file 'Appendix D' sheets labelled 7.4.1 U-Th-Pb stnds, 7.4.1 d18O stnds, 7.4.1 Hf stnds, and 7.4.1 Trace 612 stnds.

7.4.2 Zircon spot analysis locations

Presented here are the CL images of zircon grains from each sample analysed with U-Th-Pb ages relevant to the Himalayan orogen. Red dashed circles mark the Hf isotopes and trace element concentration laser ablation pit (33 µm) on top of the previous $\delta^{18}O$ and U-Th-Pb analytical sites. Where present, blue dashed circles mark $\delta^{18}O$ and U-Th-Pb analytical sites in cases where Hf isotopes and trace elements were measured at a separate site or not at all.

Sample 01d

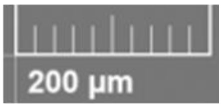

003

001

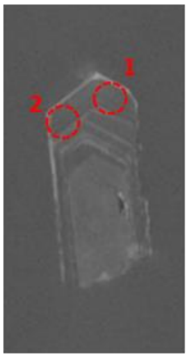

002

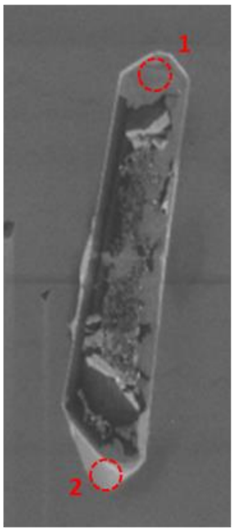

004

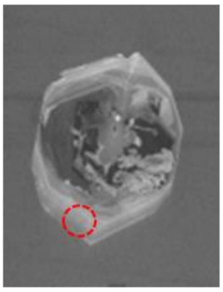

005

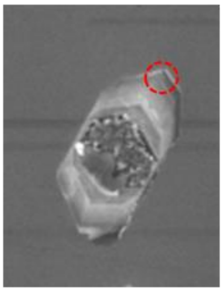

007

006

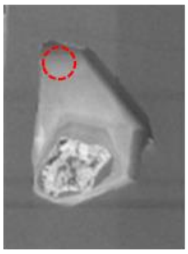

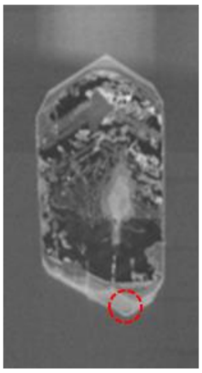

008

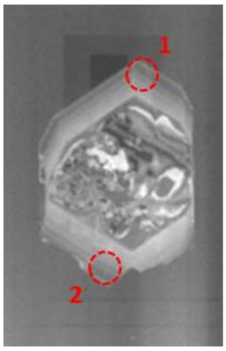

009

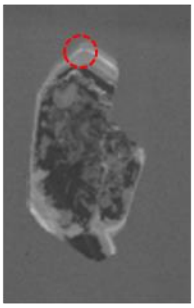

013

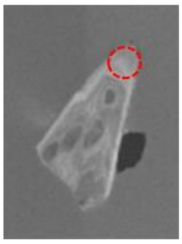

014

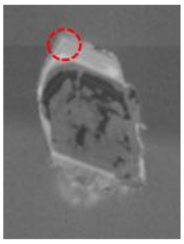

015

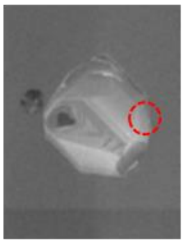

016

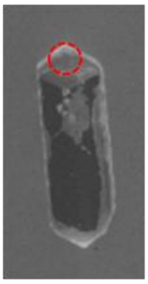

020

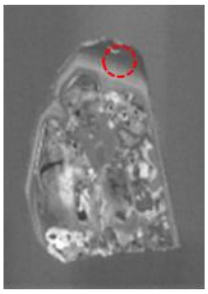

021

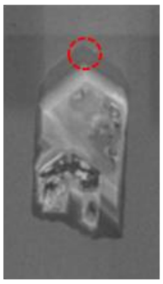

022

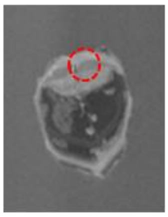

023

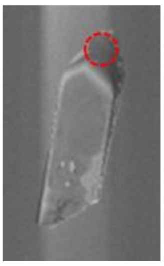

024

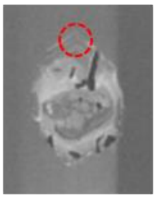

Sample 02a

001

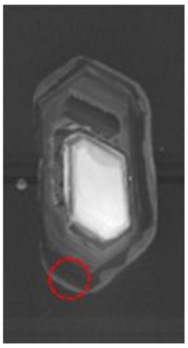

003

004

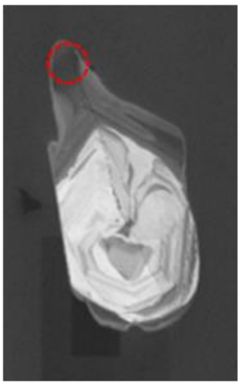

006

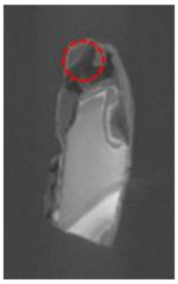

007

018

020

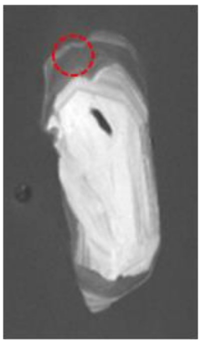

028

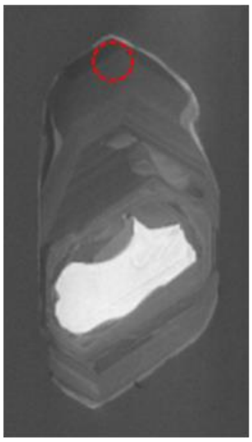

030

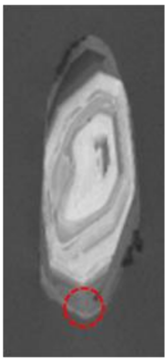

035

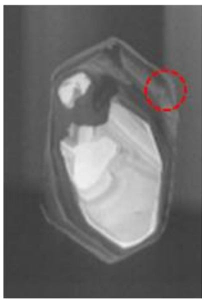

038

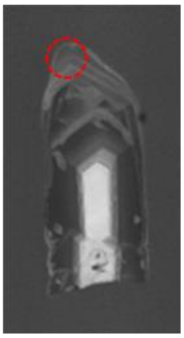

Sample 02b

001

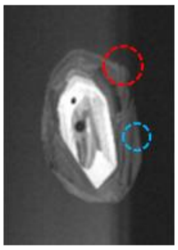

004

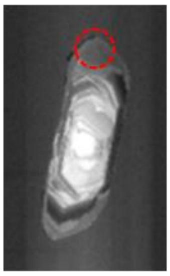

006

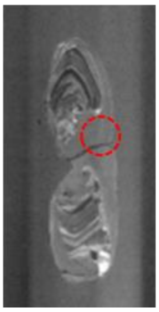

016

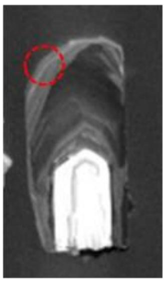

022

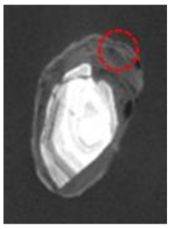

Sample 03

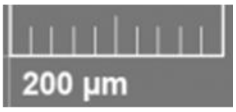

001

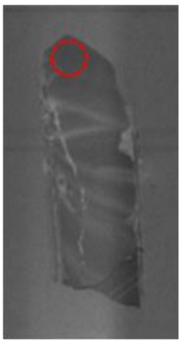

004

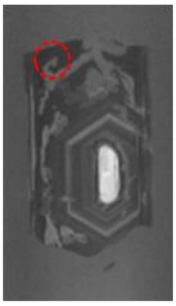

005

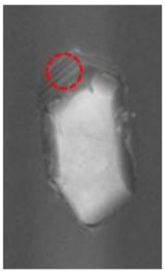

006

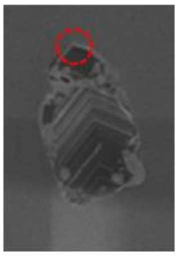

007

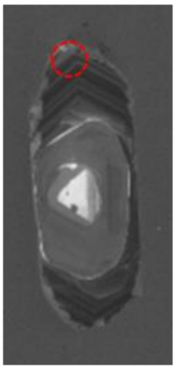

008

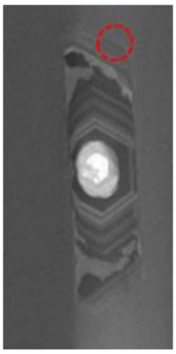

009

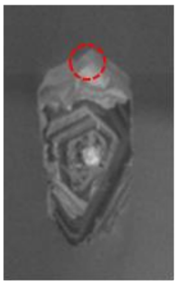

010

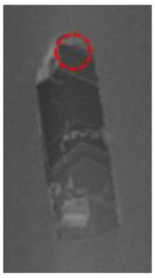

011

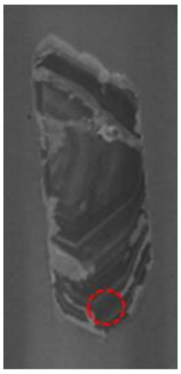

012

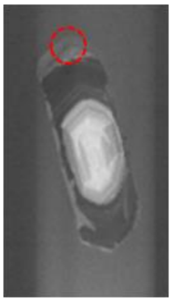

013

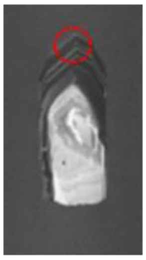

015

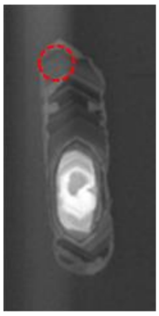

016

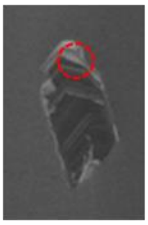

017

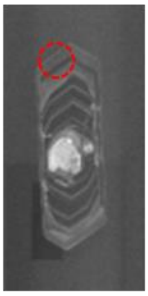

018

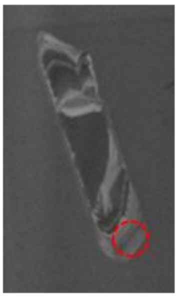

019

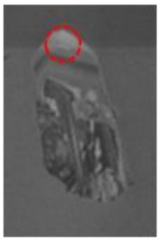

020

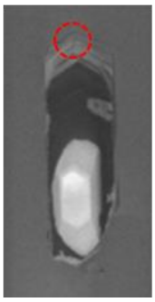

021

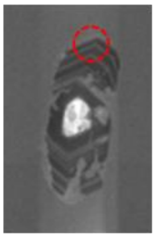

022

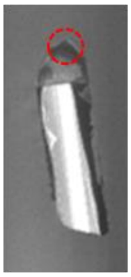

Sample 04a

001

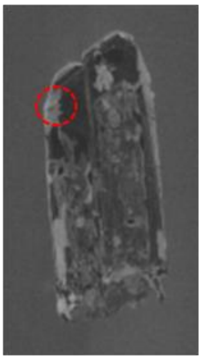

005

010

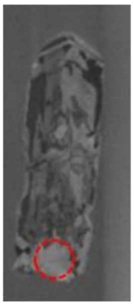

013

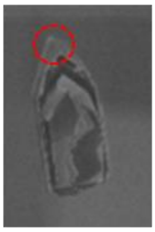

014

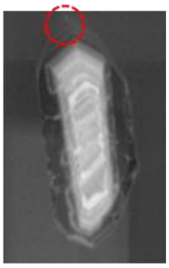

025

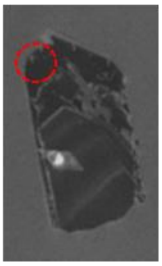

Sample 04b

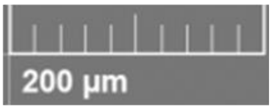

013

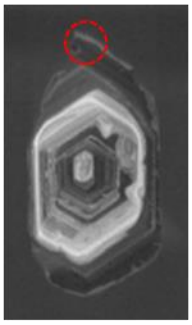

015

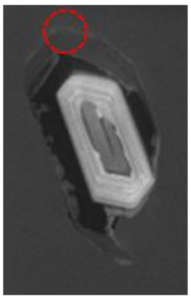

027

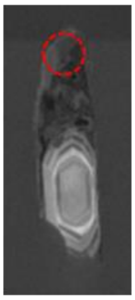

029

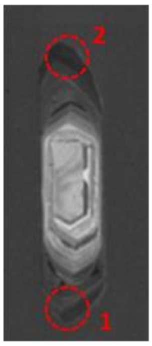

Sample 06

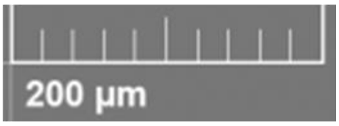

005

006

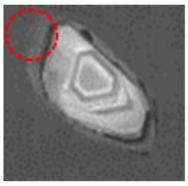

007

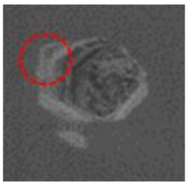

Sample 07a

002

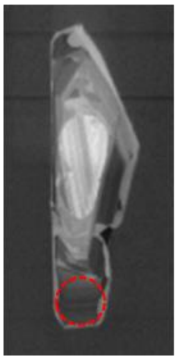

019

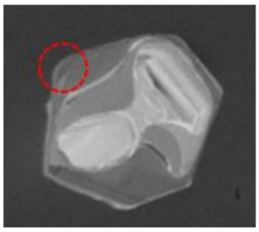

Sample 07b

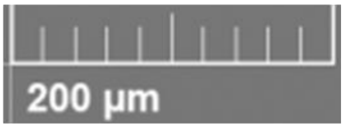

012

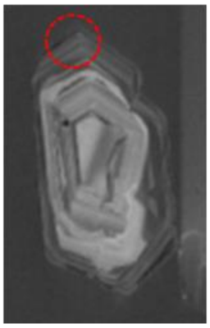

018

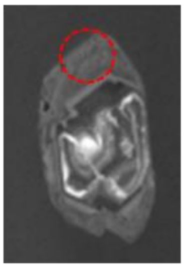

026

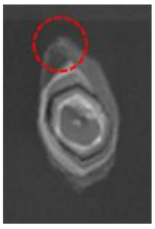

028

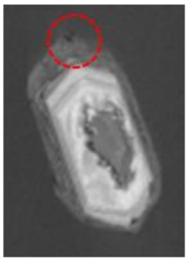

029

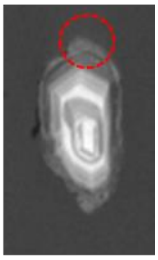

Sample 07c

003

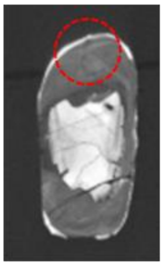

007

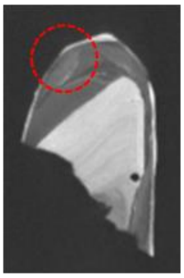

008

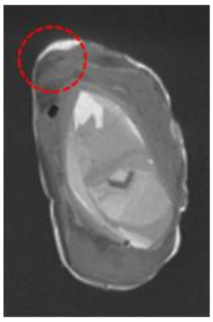

010

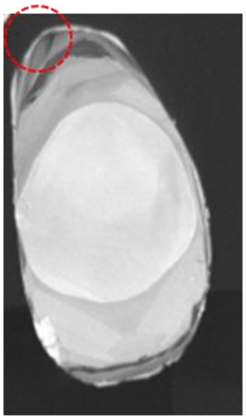

013

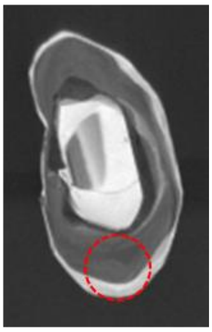

014

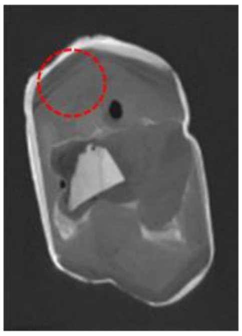

015

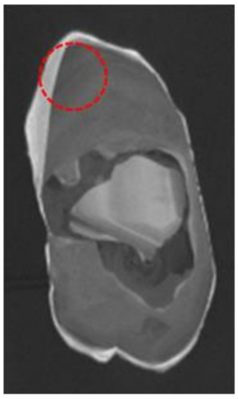

024

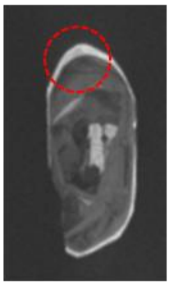

025

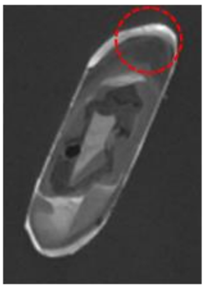

027

028

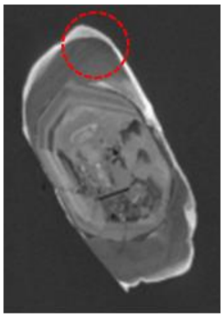

029

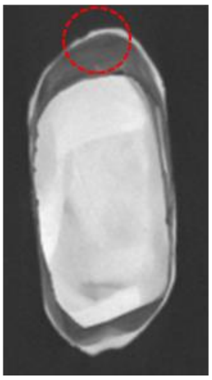

030

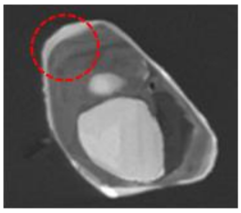

032

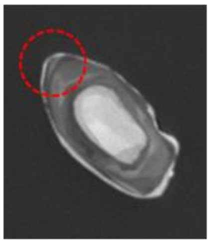

Sample 09b

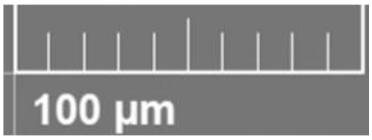

001

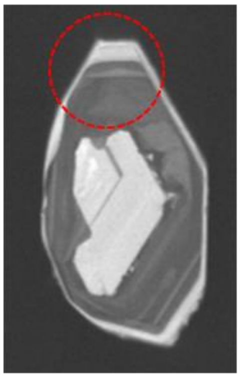

003

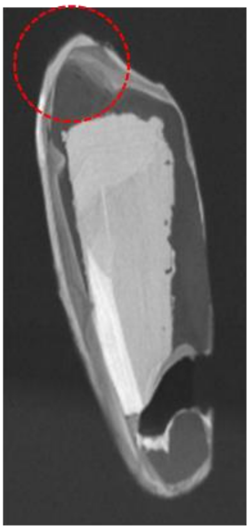

005

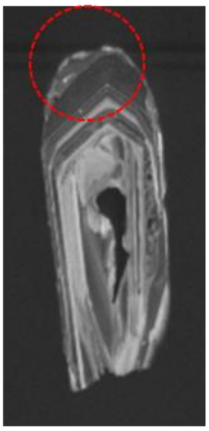

008

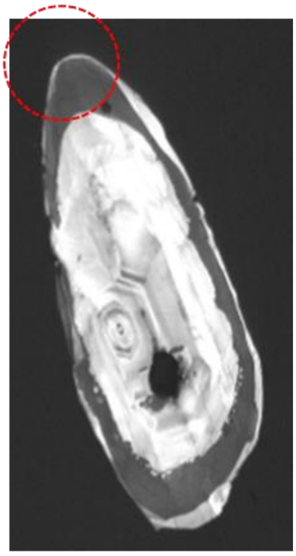

009

010

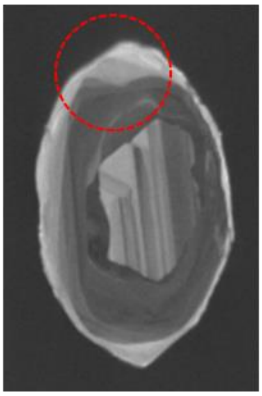

Sample 10

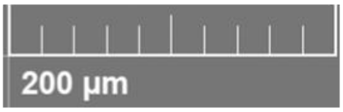

001

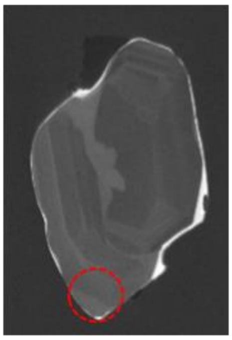

002

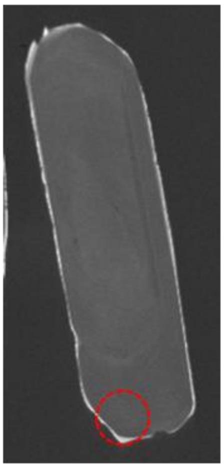

003

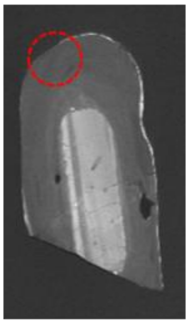

005

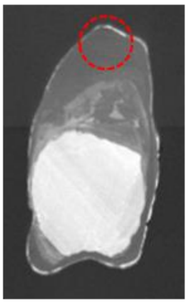

006

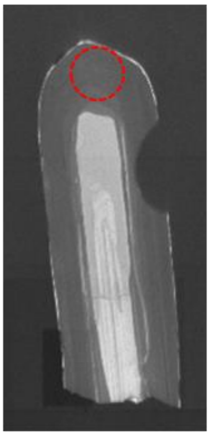

008

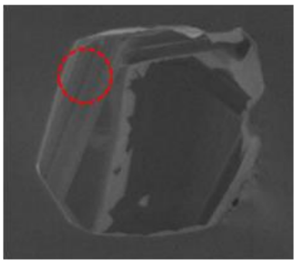

010

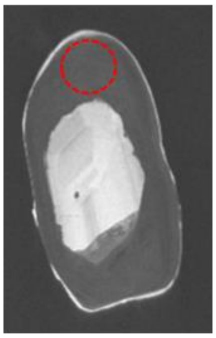

011

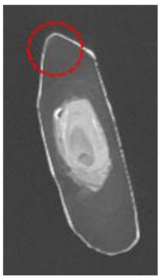

013

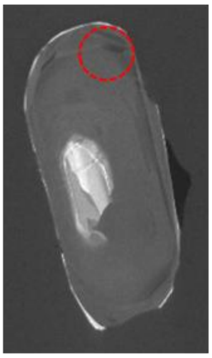

015

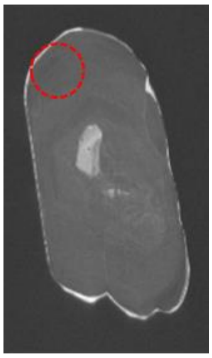

016

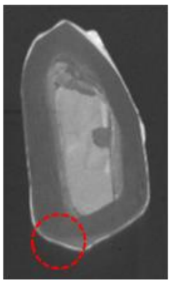

018

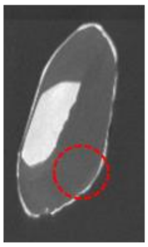

020

021

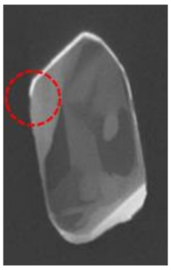

023

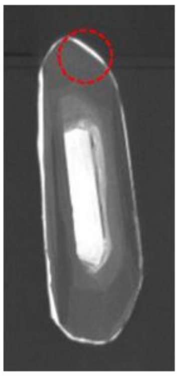

024

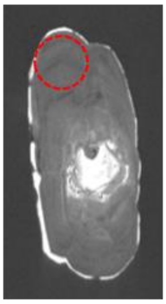

028

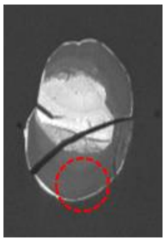

029

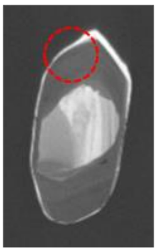

030

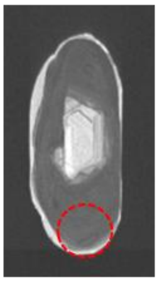

033

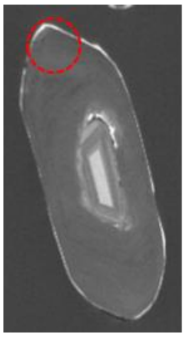

Sample 11a

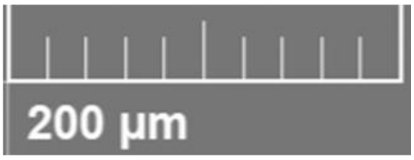

005

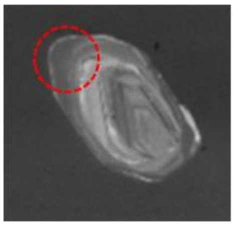

006

Sample f03

023

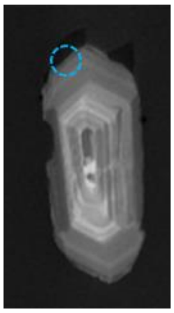

Sample f02

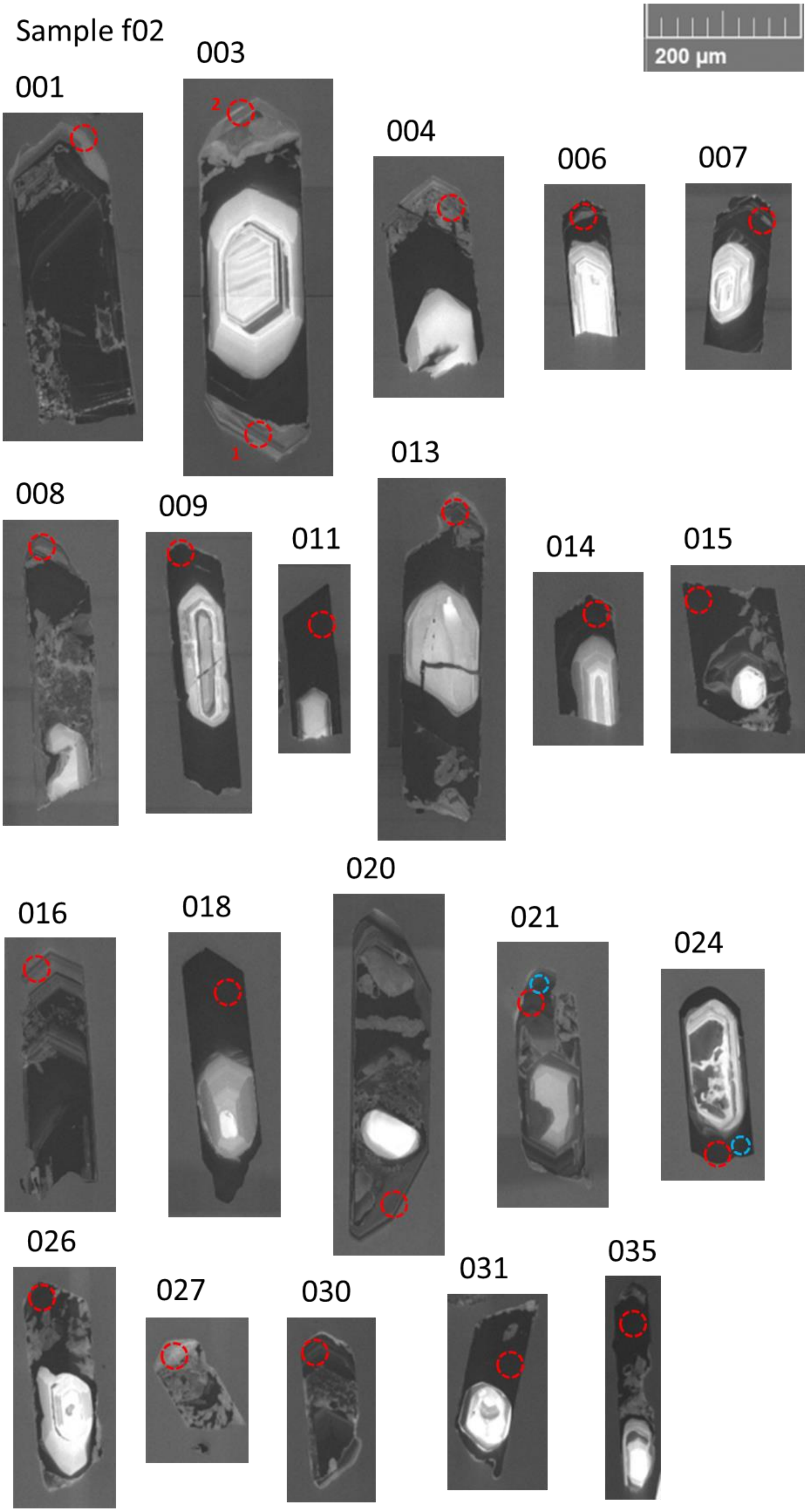
200 µm
001
003
2
1
004
006
007
008
009
011
013
014
015
016
018
020
021
024
026
027
030
031
035

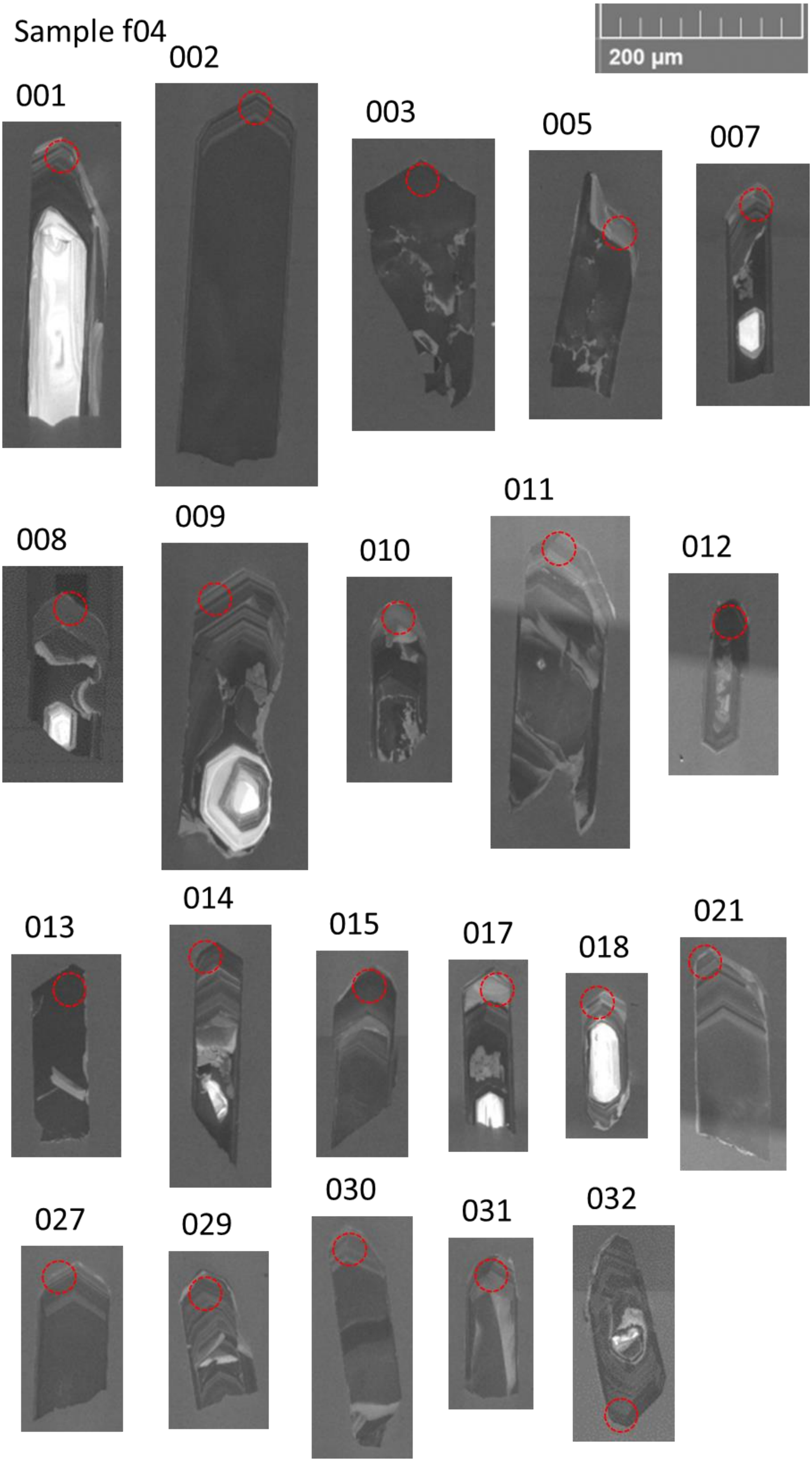
Sample f04
200 μm
001
002
003
005
007
008
009
010
011
012
013
014
015
017
018
021
027
029
030
031
032

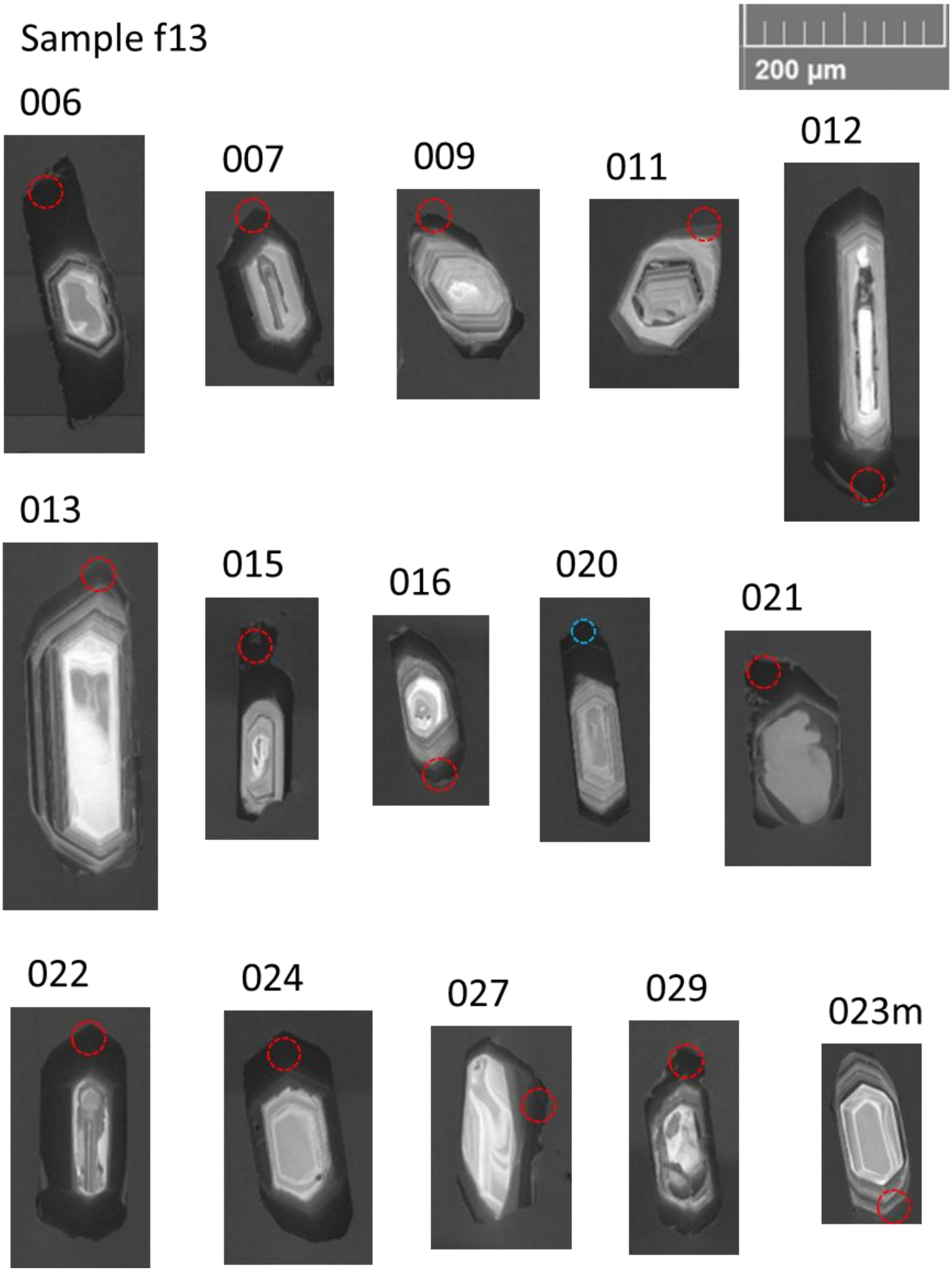
Sample f13
200 μm
006
007
009
011
012
013
015
016
020
021
022
024
027
029
023m

7.4.3 Compiled zircon isotope and trace element results

See the accompanying Excel file 'Appendix D' sheet labelled 7.4.3 Compiled zircon data.

7.4.4 Zircon REE profiles

See the accompanying Excel file 'Appendix D' sheet labelled 7.4.4 CI-normalised zircon REEs for full REE normalisation calculations and data points.

Present here are the chondrite-normalised REE profiles for zircon analyses in each sample:

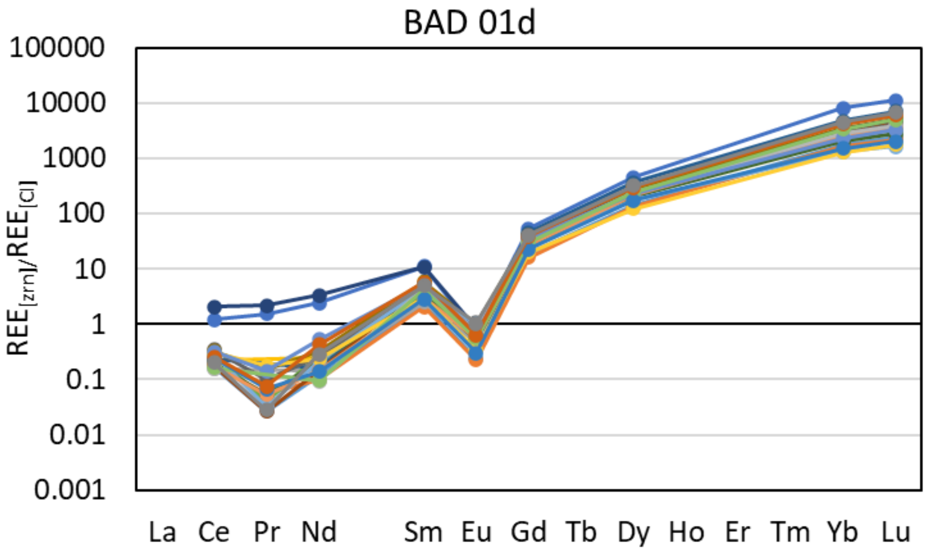

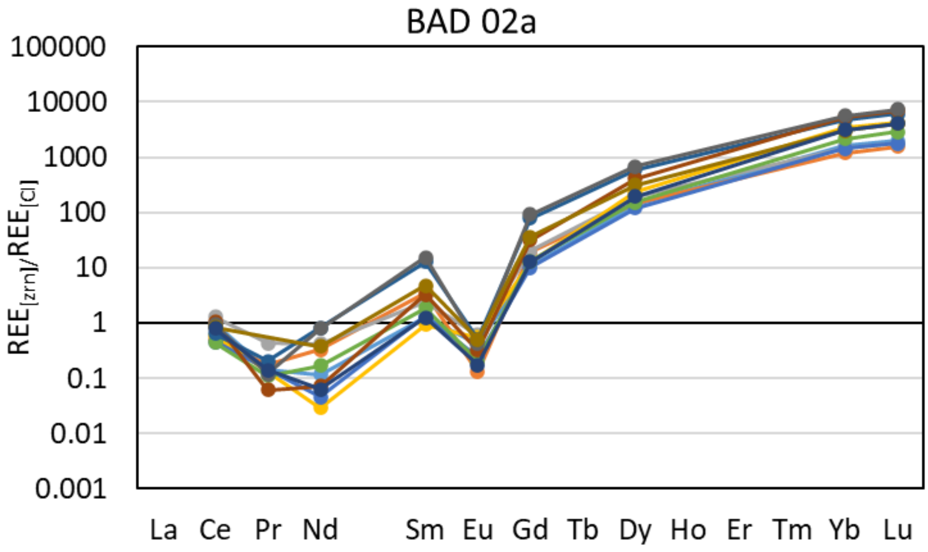

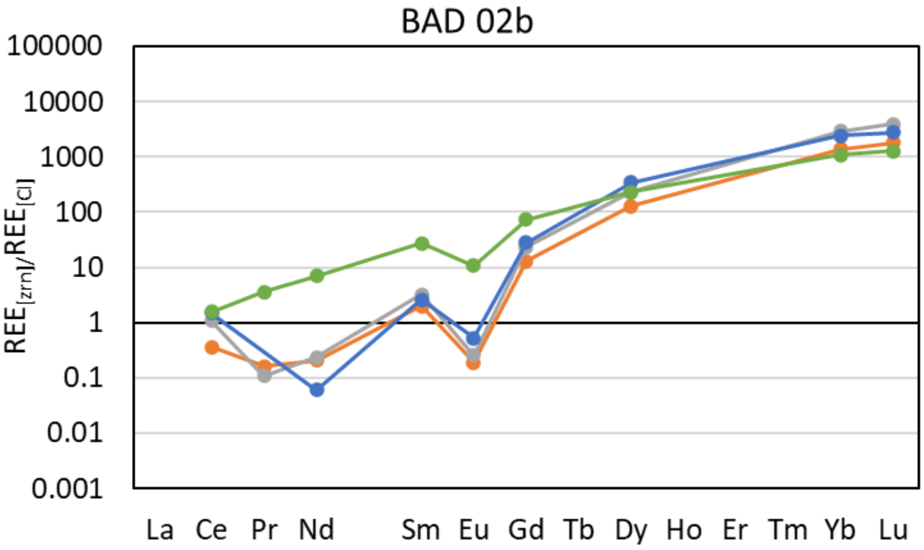
BAD 02b
100000
10000
1000
100
10
1
0.1
0.01
0.001
$REE_{[zrn]}/REE_{[CI]}$
La
Ce
Pr
Nd
Sm
Eu
Gd
Tb
Dy
Ho
Er
Tm
Yb
Lu

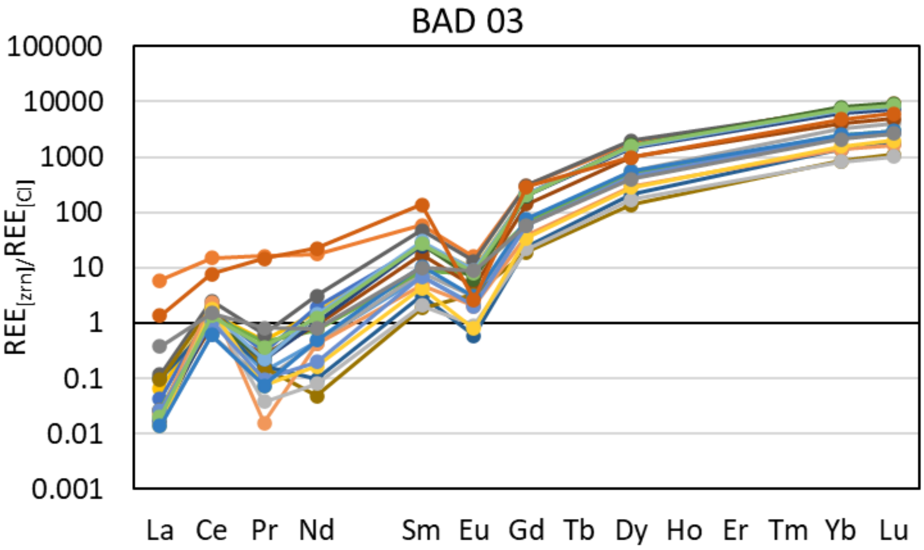
BAD 03
100000
10000
1000
100
10
1
0.1
0.01
0.001
$REE_{[zrn]}/REE_{[CI]}$
La
Ce
Pr
Nd
Sm
Eu
Gd
Tb
Dy
Ho
Er
Tm
Yb
Lu

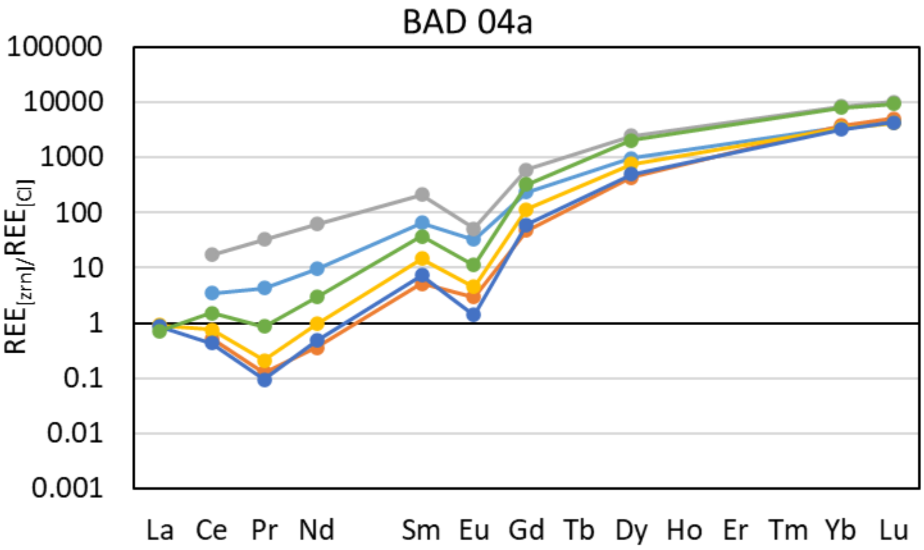
BAD 04a
100000
10000
1000
100
10
1
0.1
0.01
0.001
$REE_{[zrn]}/REE_{[CI]}$
La
Ce
Pr
Nd
Sm
Eu
Gd
Tb
Dy
Ho
Er
Tm
Yb
Lu

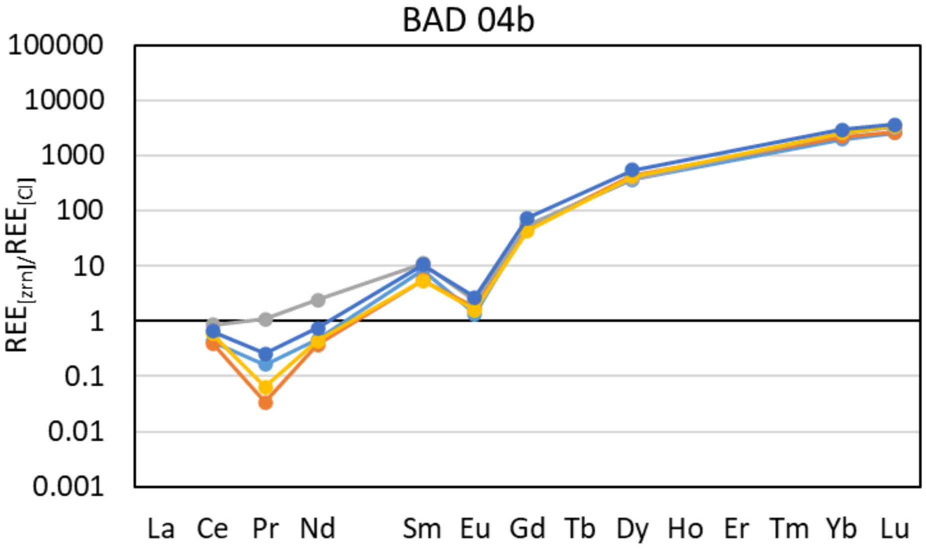
BAD 04b
100000
10000
1000
100
10
1
0.1
0.01
0.001
REE[zrn]/REE[CI]
La
Ce
Pr
Nd
Sm
Eu
Gd
Tb
Dy
Ho
Er
Tm
Yb
Lu

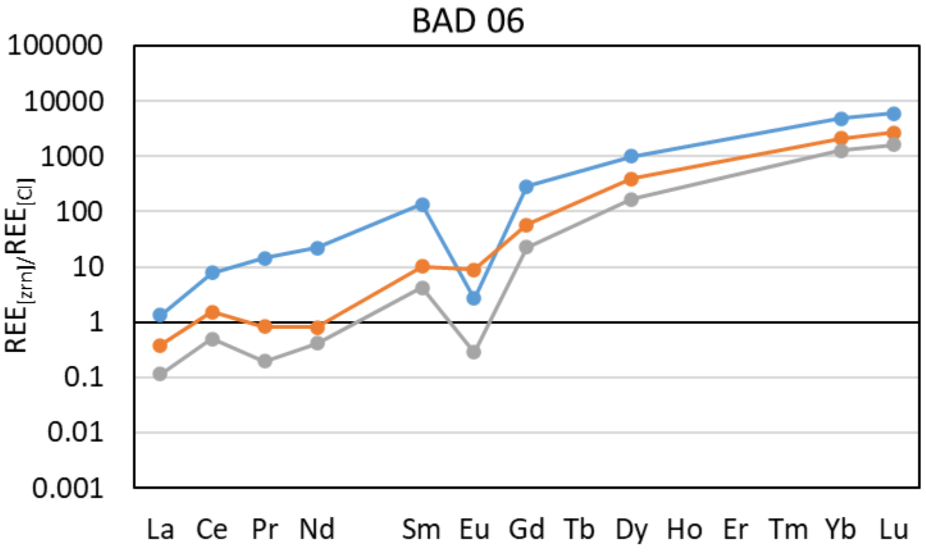
BAD 06
100000
10000
1000
100
10
1
0.1
0.01
0.001
REE[zrn]/REE[CI]
La
Ce
Pr
Nd
Sm
Eu
Gd
Tb
Dy
Ho
Er
Tm
Yb
Lu

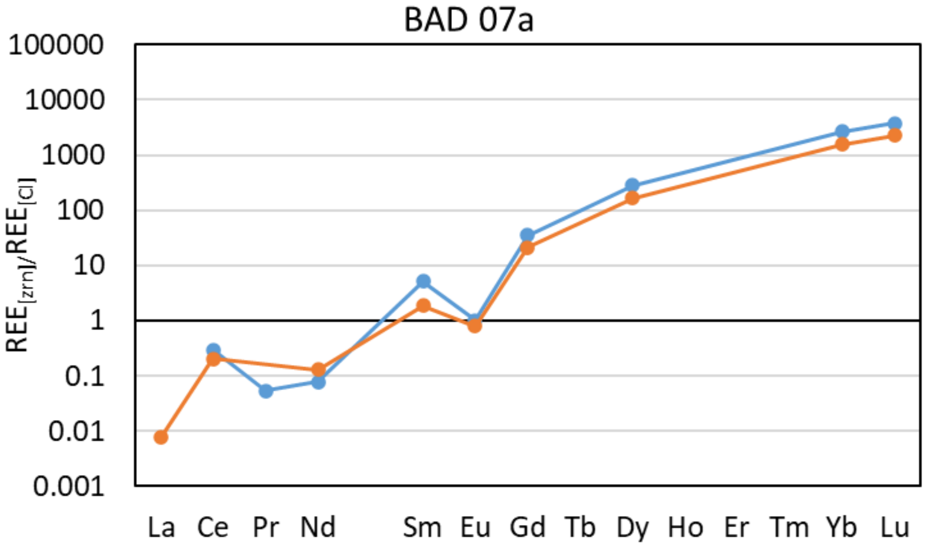
BAD 07a
100000
10000
1000
100
10
1
0.1
0.01
0.001
REE[zrn]/REE[CI]
La
Ce
Pr
Nd
Sm
Eu
Gd
Tb
Dy
Ho
Er
Tm
Yb
Lu

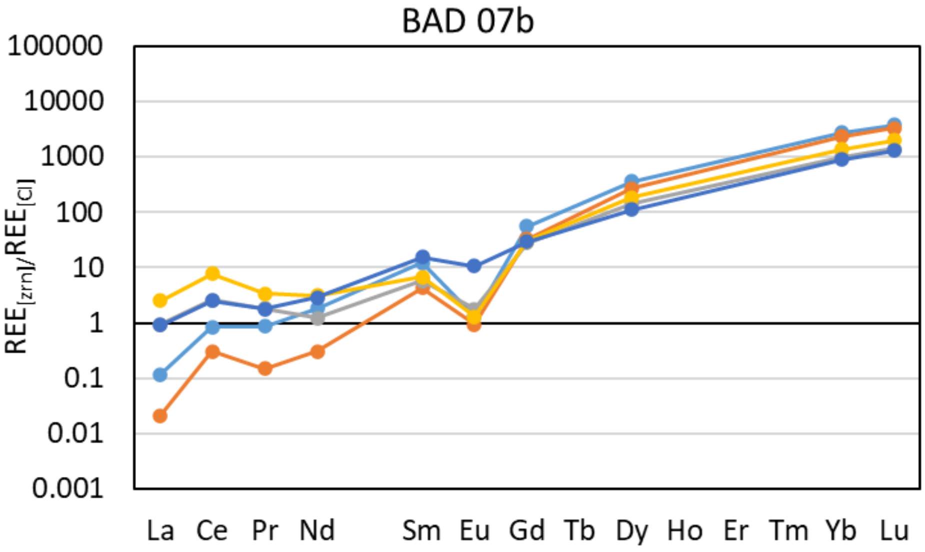
BAD 07b
100000
10000
1000
100
10
1
0.1
0.01
0.001
REE[zrn]/REE[CI]
La
Ce
Pr
Nd
Sm
Eu
Gd
Tb
Dy
Ho
Er
Tm
Yb
Lu

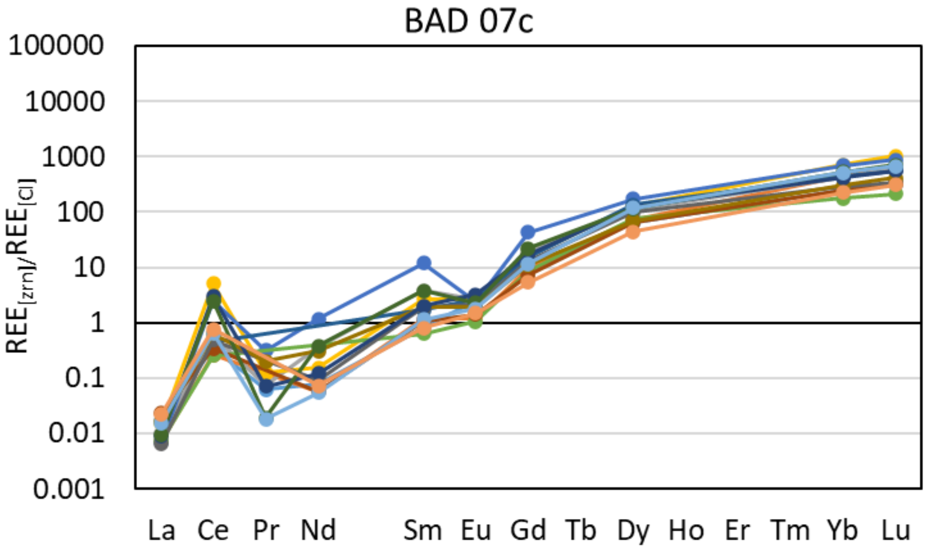
BAD 07c
100000
10000
1000
100
10
1
0.1
0.01
0.001
REE[zrn]/REE[CI]
La
Ce
Pr
Nd
Sm
Eu
Gd
Tb
Dy
Ho
Er
Tm
Yb
Lu

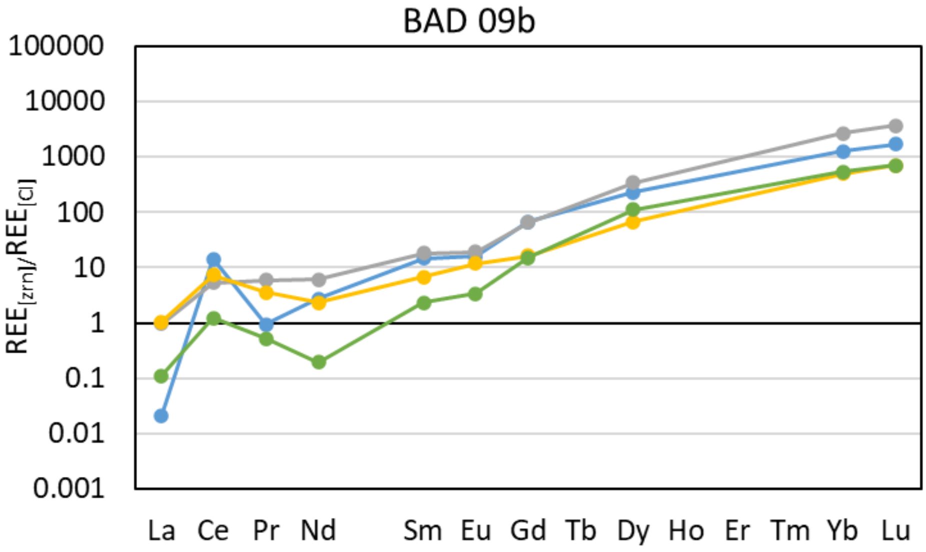
BAD 09b
100000
10000
1000
100
10
1
0.1
0.01
0.001
REE[zrn]/REE[CI]
La
Ce
Pr
Nd
Sm
Eu
Gd
Tb
Dy
Ho
Er
Tm
Yb
Lu

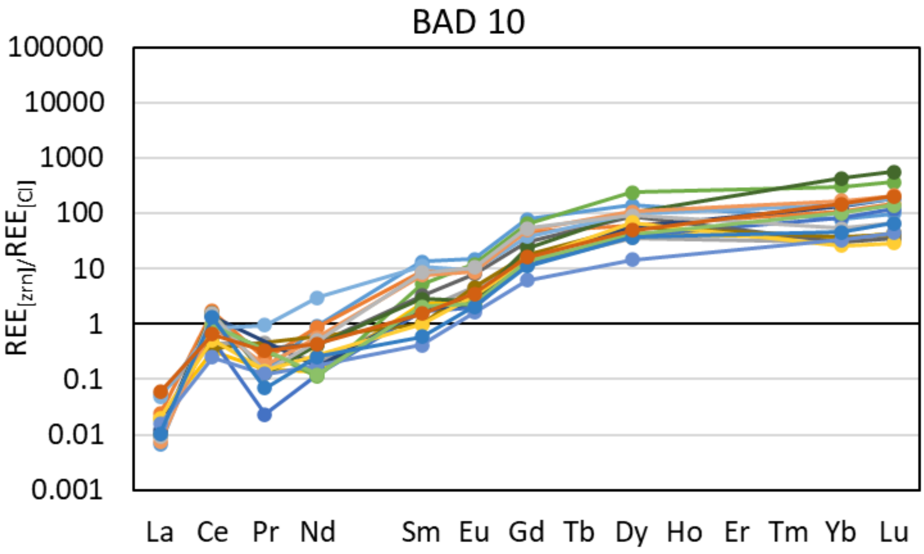
BAD 10
100000
10000
1000
100
10
1
0.1
0.01
0.001
$REE_{[zrn]}/REE_{[CI]}$
La
Ce
Pr
Nd
Sm
Eu
Gd
Tb
Dy
Ho
Er
Tm
Yb
Lu

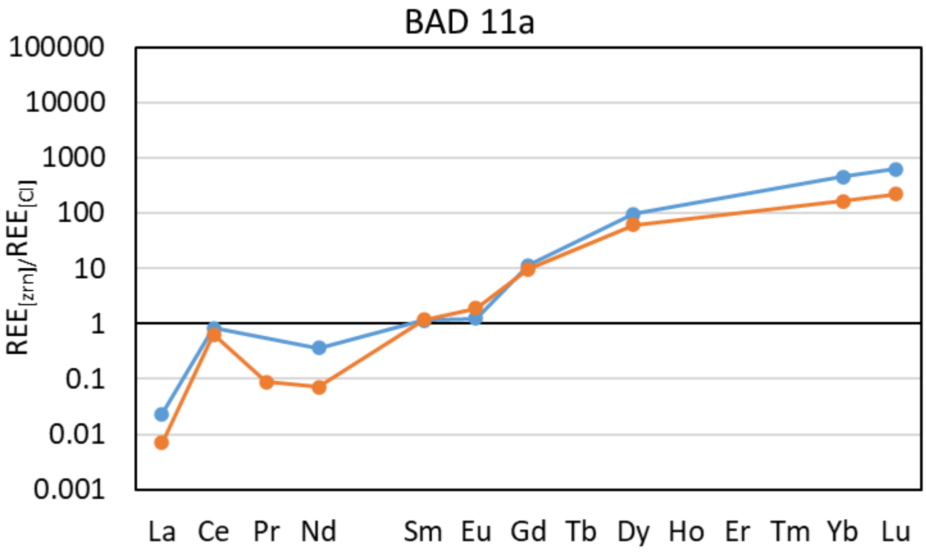
BAD 11a
100000
10000
1000
100
10
1
0.1
0.01
0.001
$REE_{[zrn]}/REE_{[CI]}$
La
Ce
Pr
Nd
Sm
Eu
Gd
Tb
Dy
Ho
Er
Tm
Yb
Lu

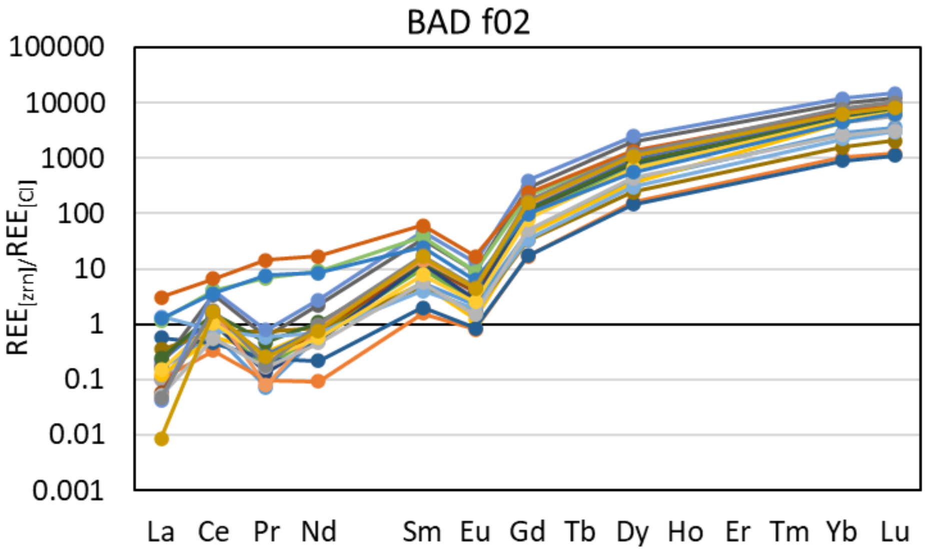
BAD f02
100000
10000
1000
100
10
1
0.1
0.01
0.001
$REE_{[zrn]}/REE_{[CI]}$
La
Ce
Pr
Nd
Sm
Eu
Gd
Tb
Dy
Ho
Er
Tm
Yb
Lu

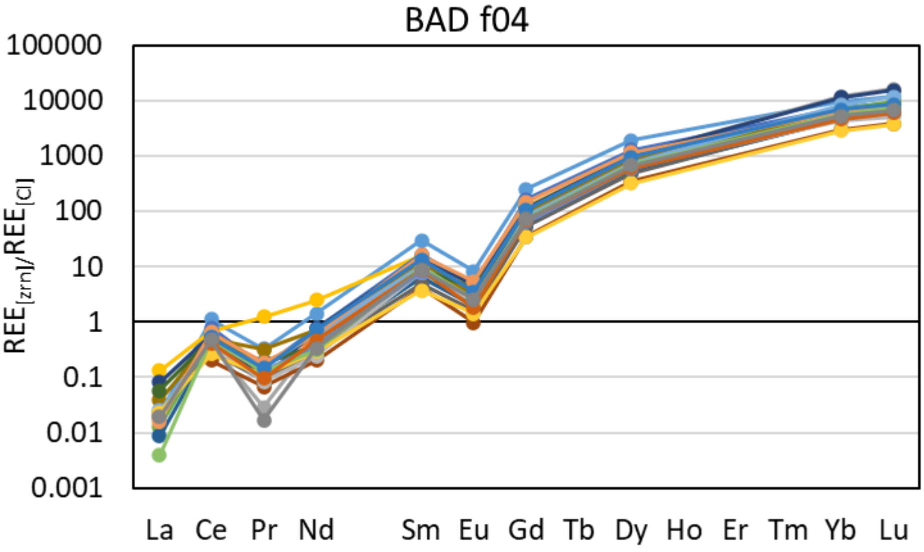
BAD f04
100000
10000
1000
100
10
1
0.1
0.01
0.001
REE[zrn]/REE[CI]
La Ce Pr Nd Sm Eu Gd Tb Dy Ho Er Tm Yb Lu

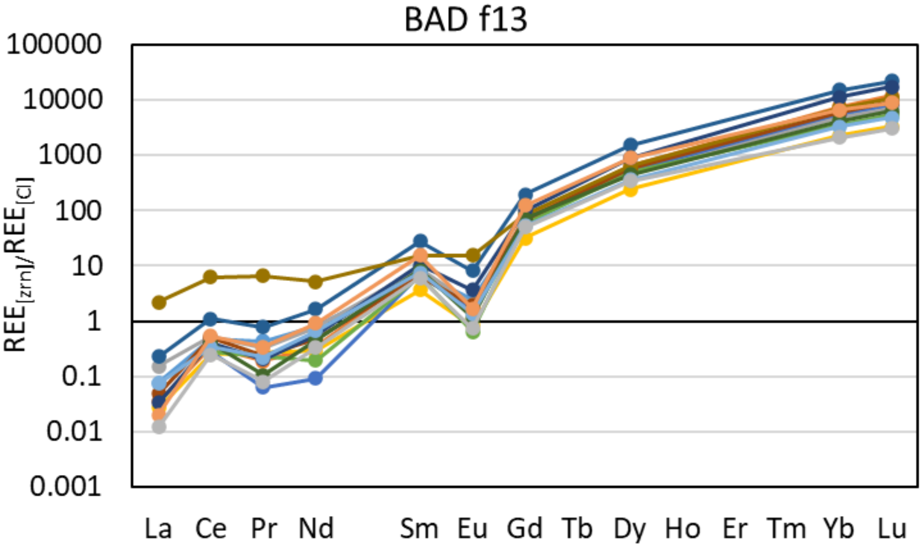
BAD f13
100000
10000
1000
100
10
1
0.1
0.01
0.001
REE[zrn]/REE[CI]
La Ce Pr Nd Sm Eu Gd Tb Dy Ho Er Tm Yb Lu

7.5 Appendix E

The accompanying Excel worksheets for Appendix E can be found at:

https://doi.org/10.21954/ou.rd.23608794

7.5.1 Monazite U-Th-Pb isotope standard measurements

See the accompanying Excel file 'Appendix E' sheet labelled 7.5.1 U-Th-Pb stnds.

7.5.2 Monazite spot analysis locations

Presented here are Ce, Th, and Y EDS maps for monazite grains from each sample analysed with U-Th-Pb ages relevant to the Himalayan orogen. Red dashed circles mark the U-Th-Pb analysis laser ablation pit (~11 µm). The colour scale is in counts per second (cps) at the following scale:

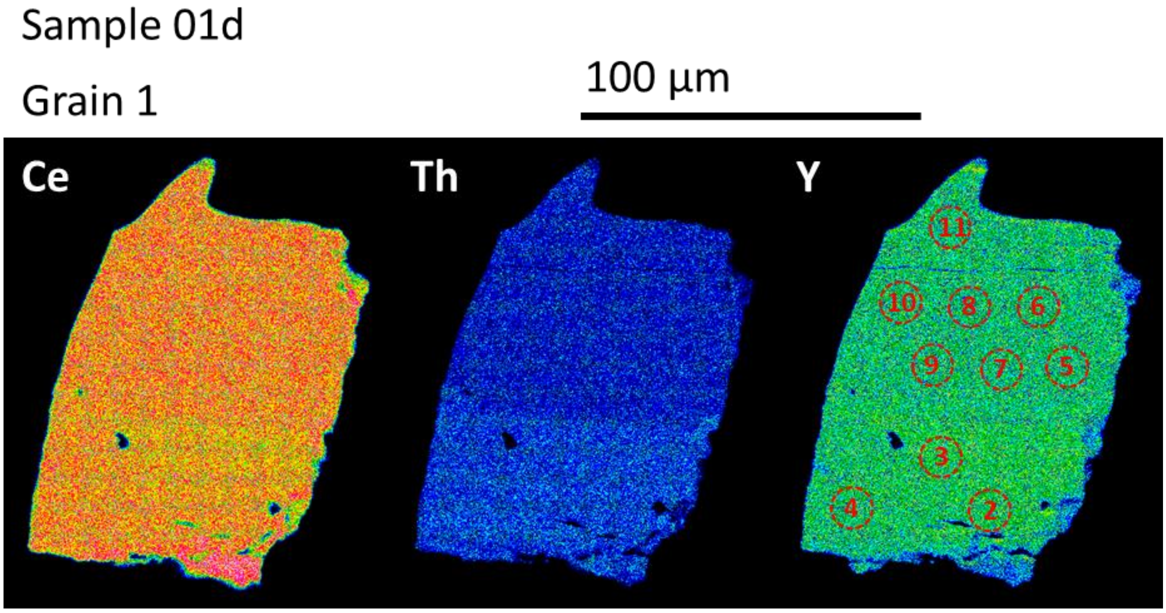

Sample 02a

Grain 1

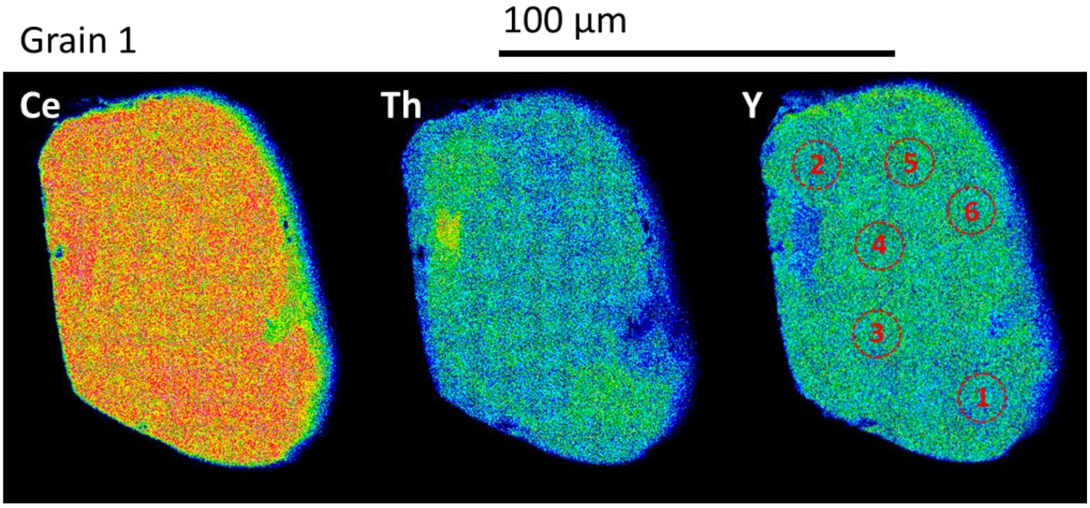

Grain 2

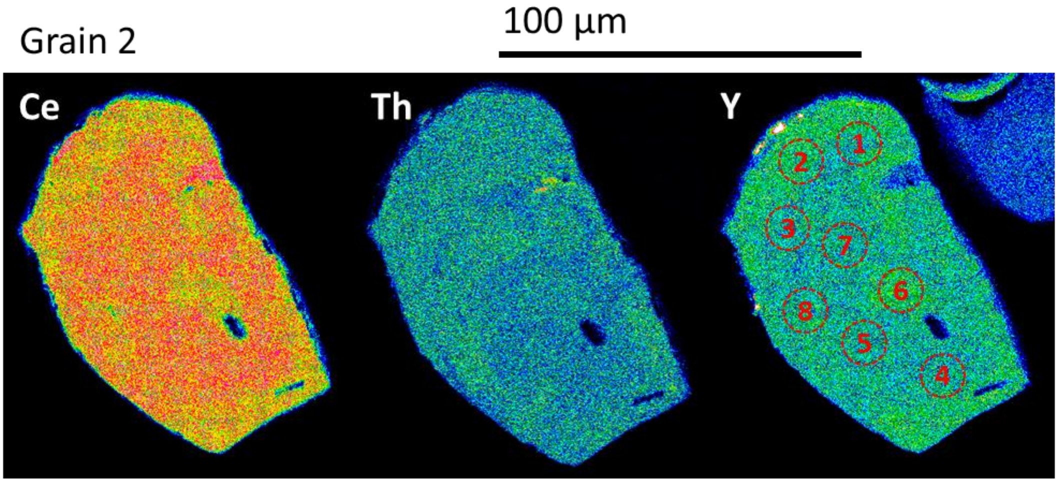

Sample 02b

Grain 1

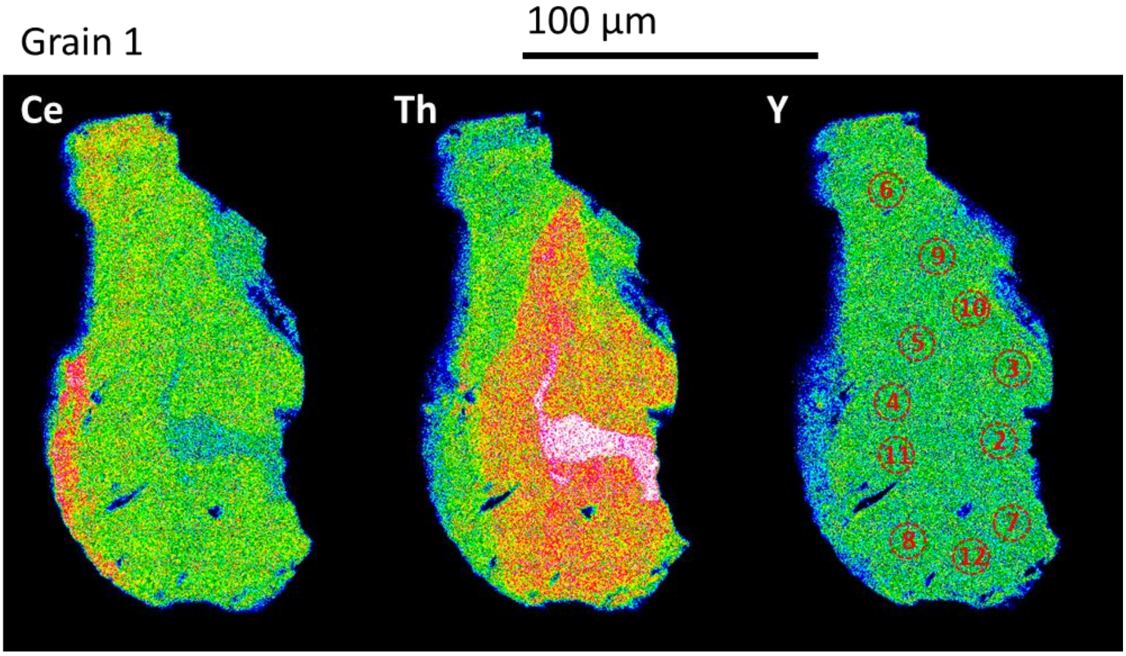

Sample 04a

Grain 1

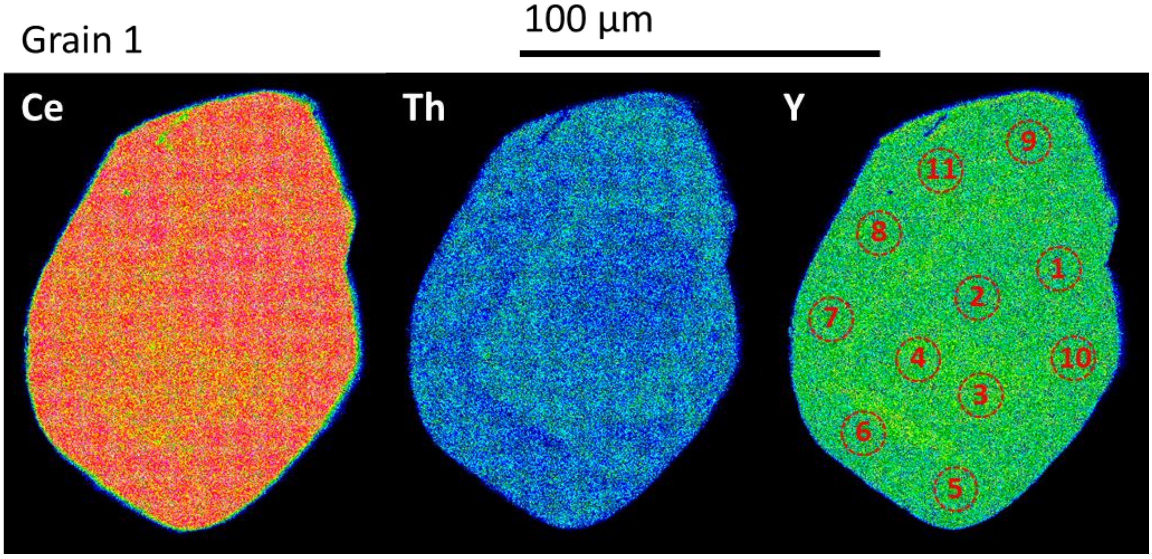

Sample 04b

Grain 1

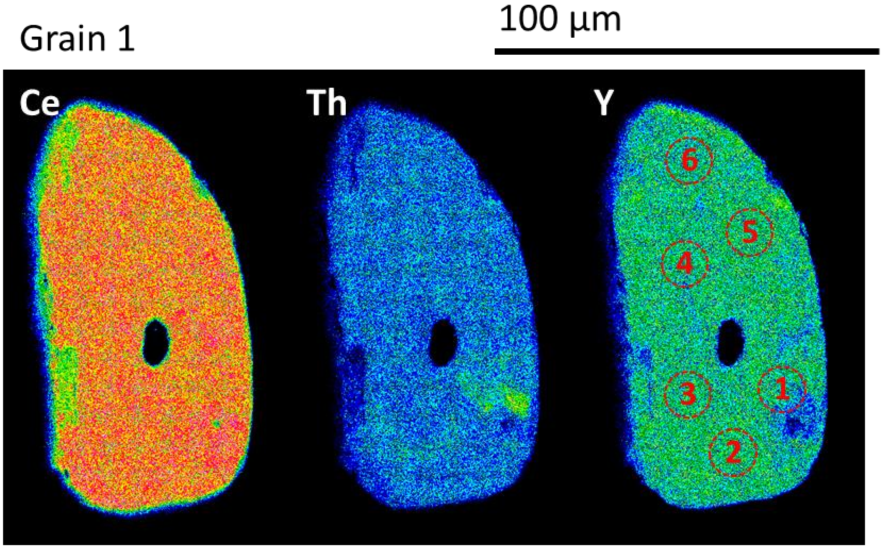

Grain 2

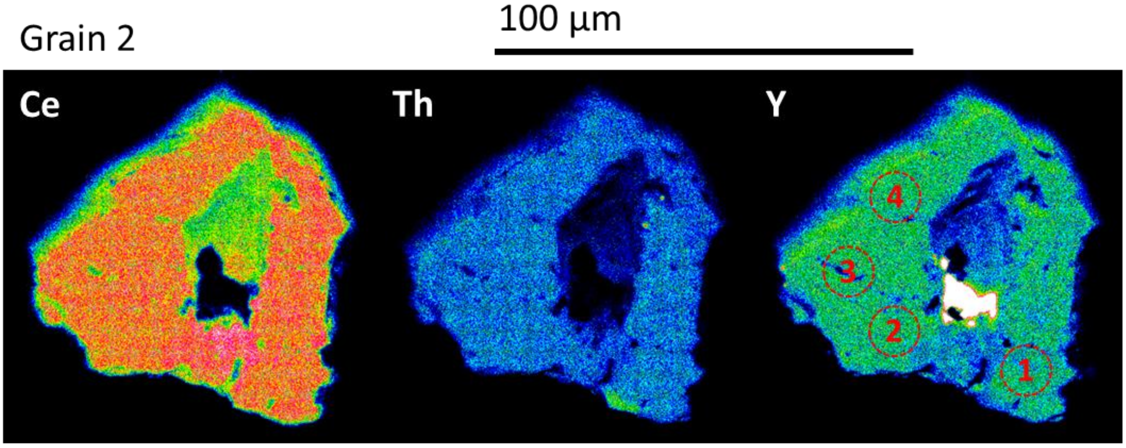

Grain 3

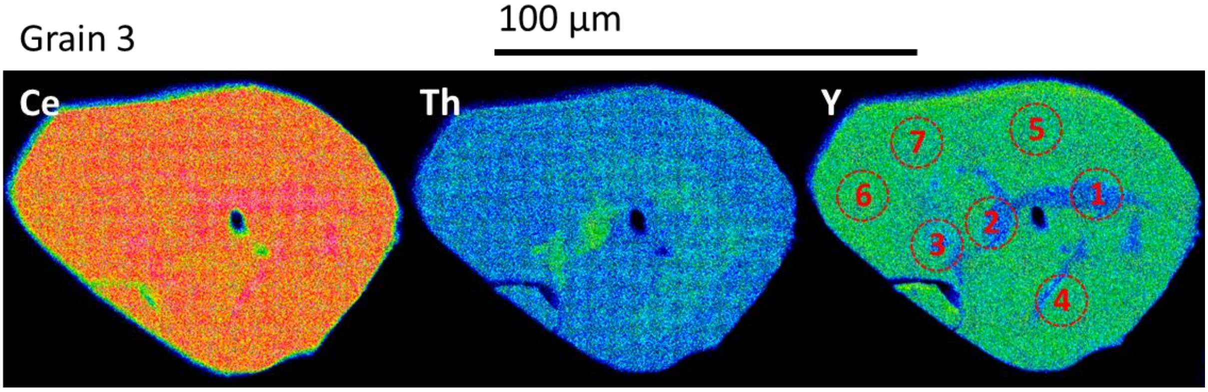

Sample 05b

Grain 1

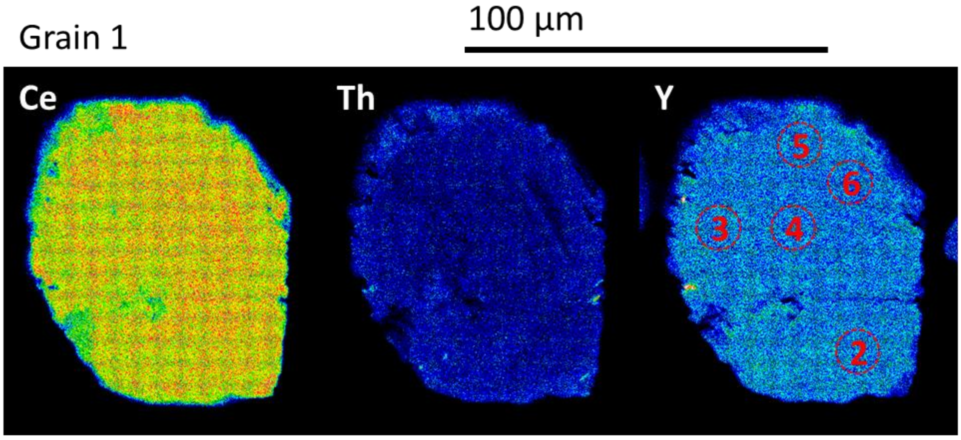

Grain 2

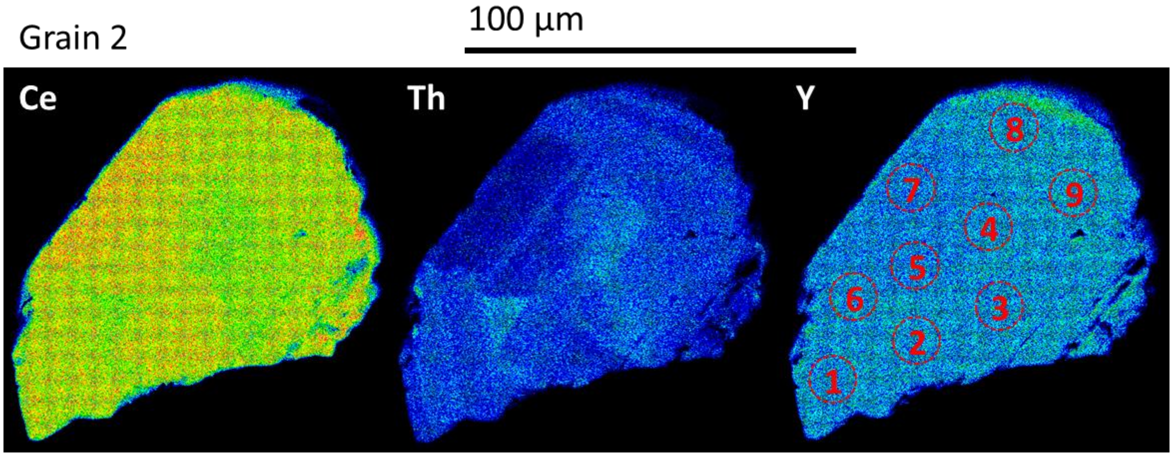

Grain 3

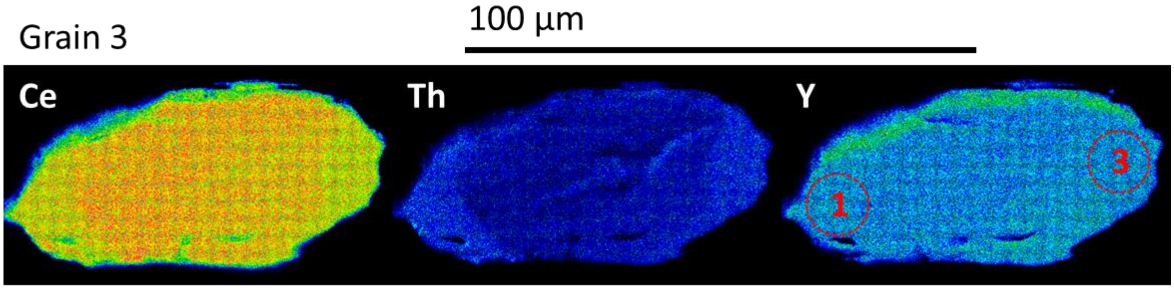

Grain 3

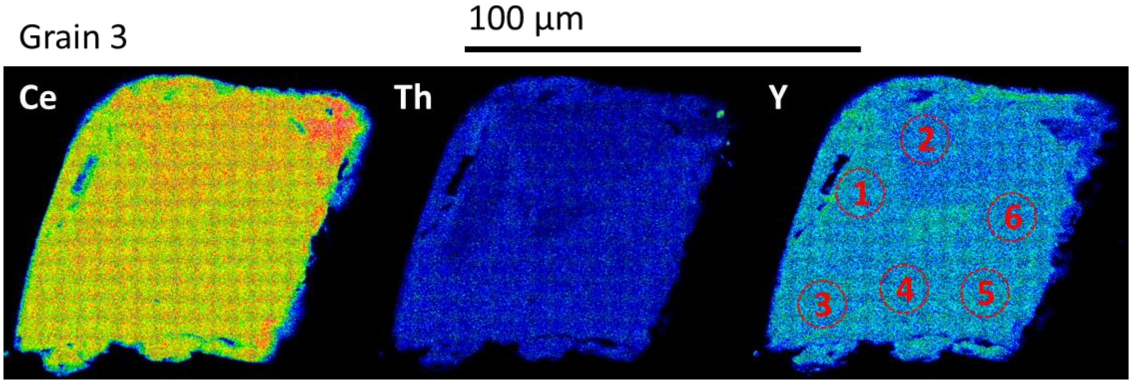

Sample 05b cont.

Grain 5

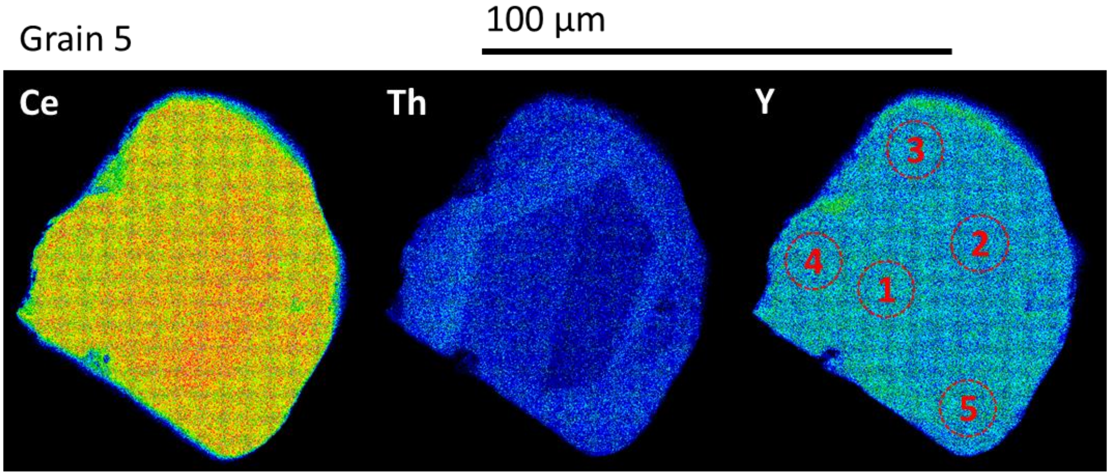

Grain 6

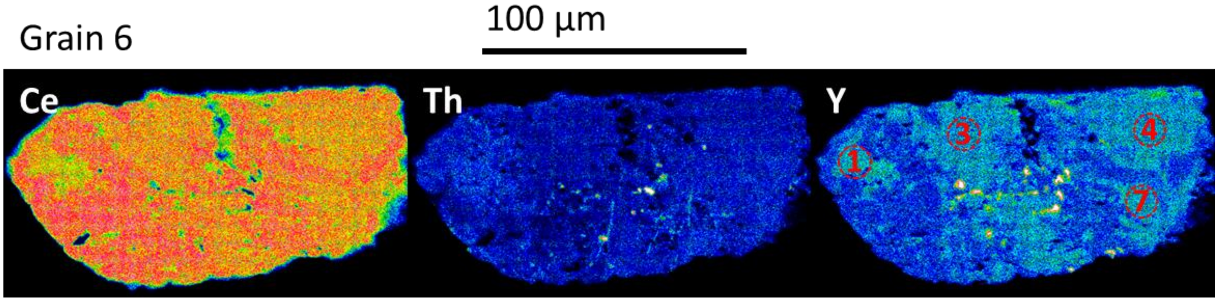

Sample 06

Grain 1

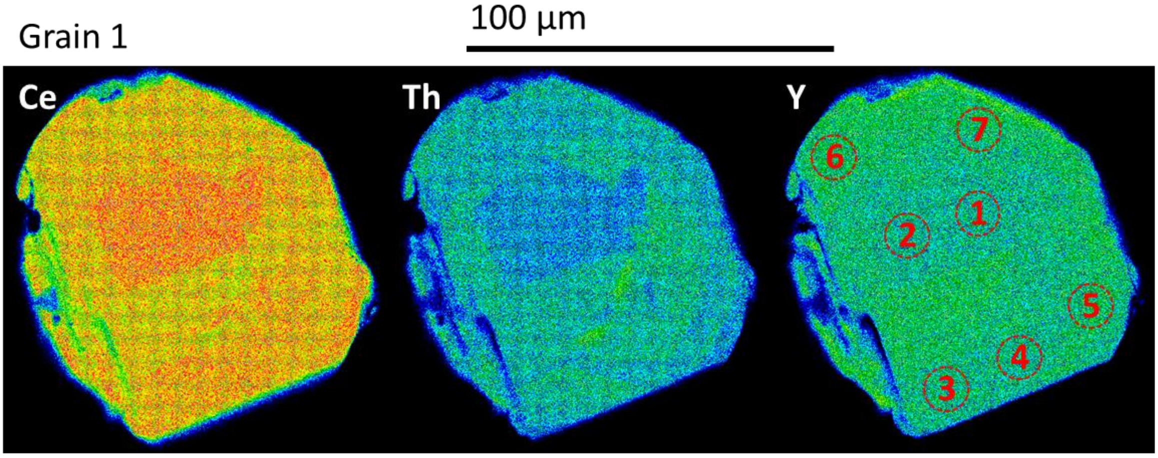

Grain 2

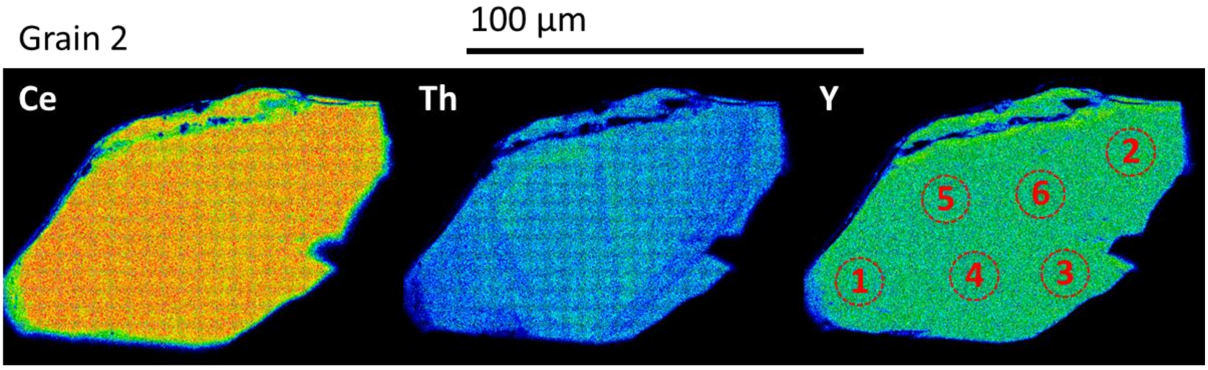

Grain 3

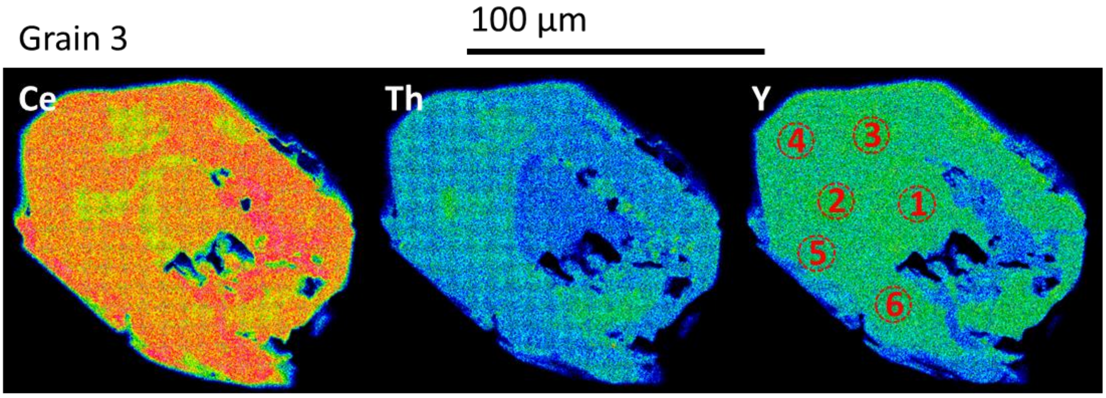

Grain 4

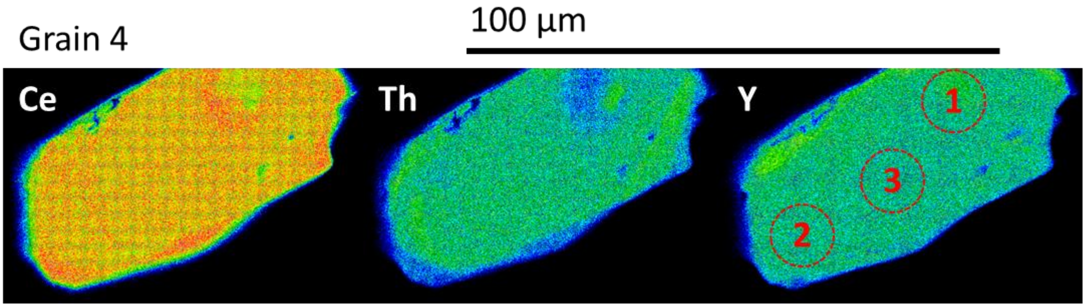

Sample 06 cont.

Grain 5

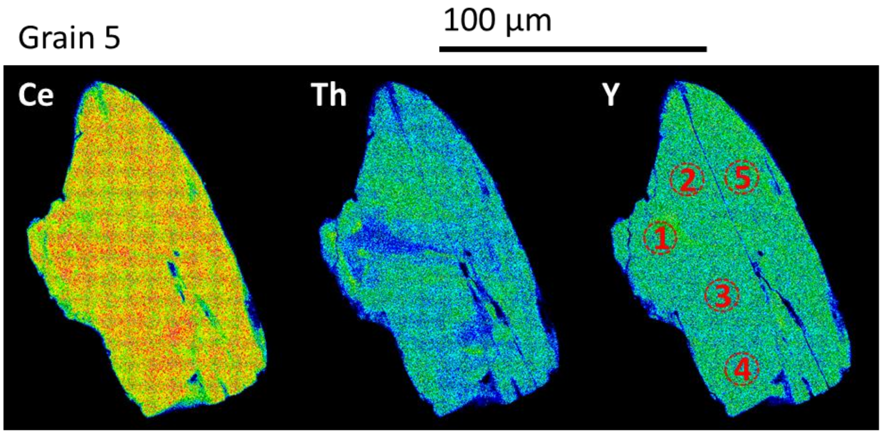

Grain 6

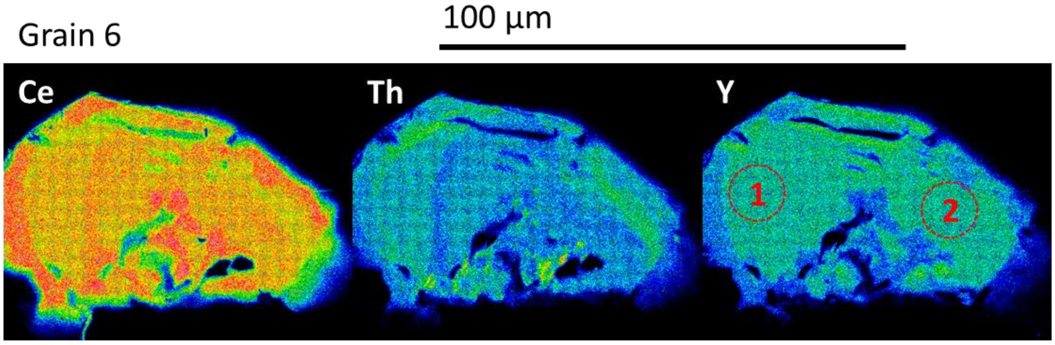

Grain 7

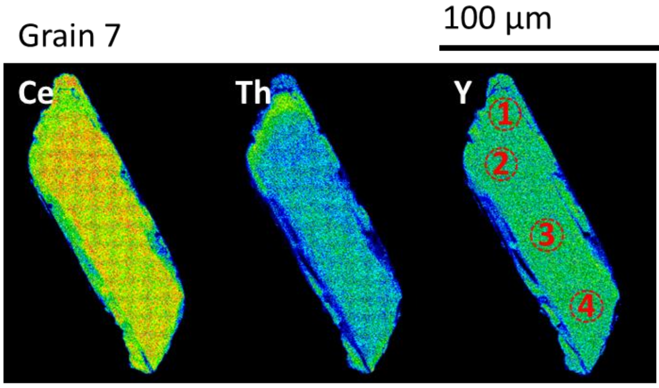

Grain 8

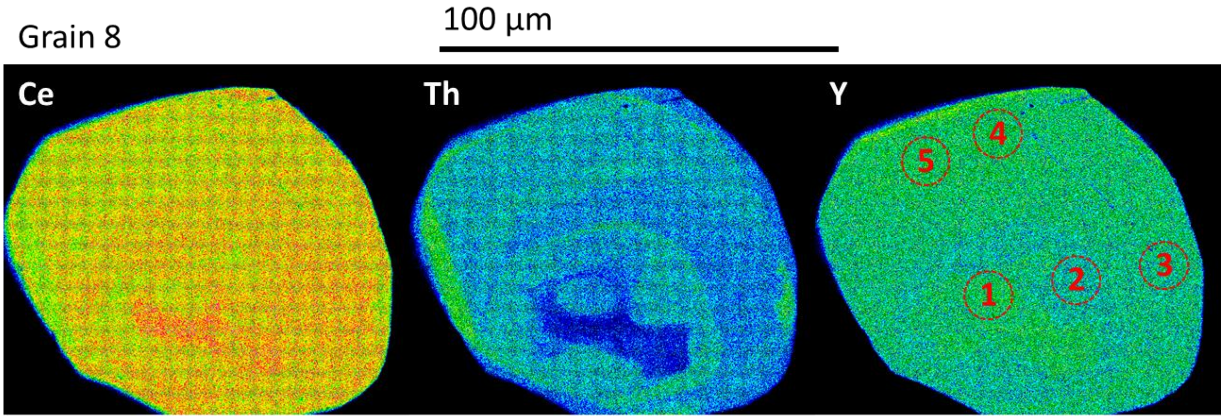

Sample 06 cont.

Grain 9

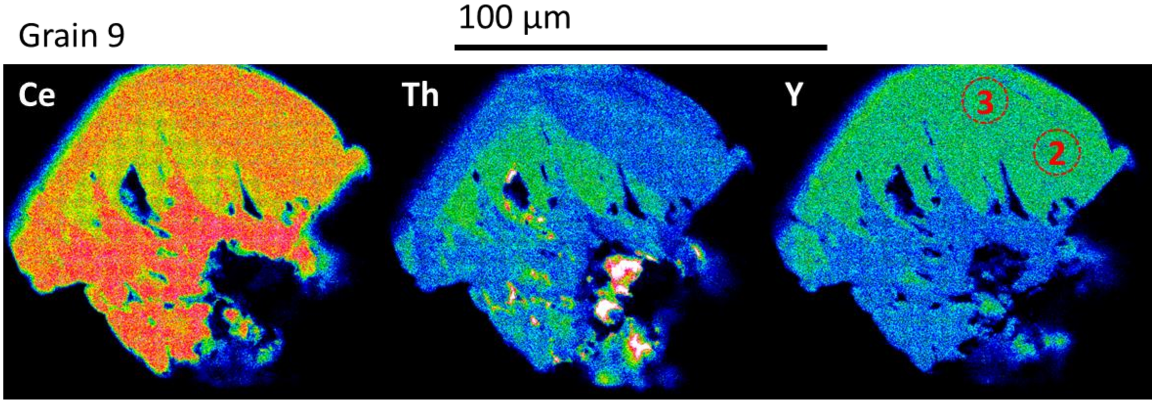

Sample 07c

Grain 1

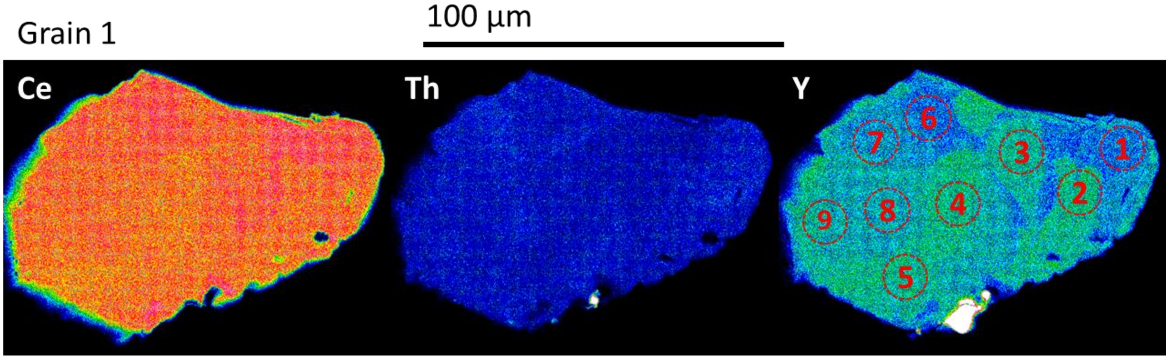

Sample 09b

Grain 1

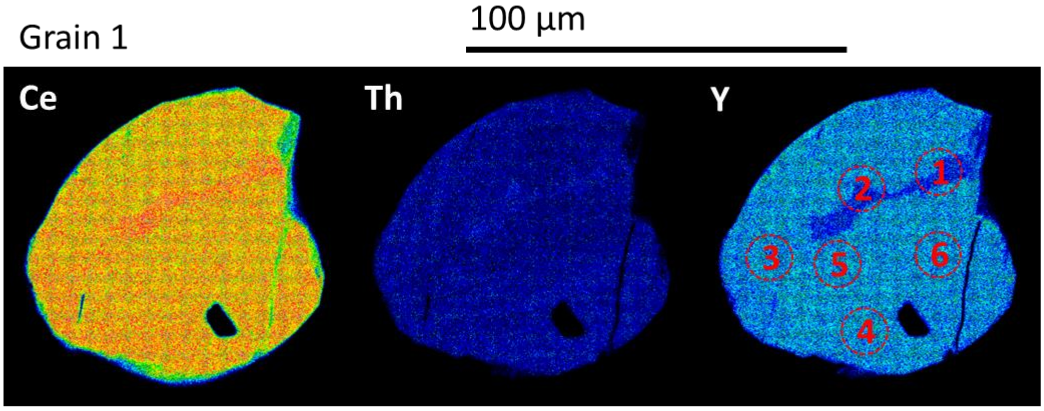

Grain 2

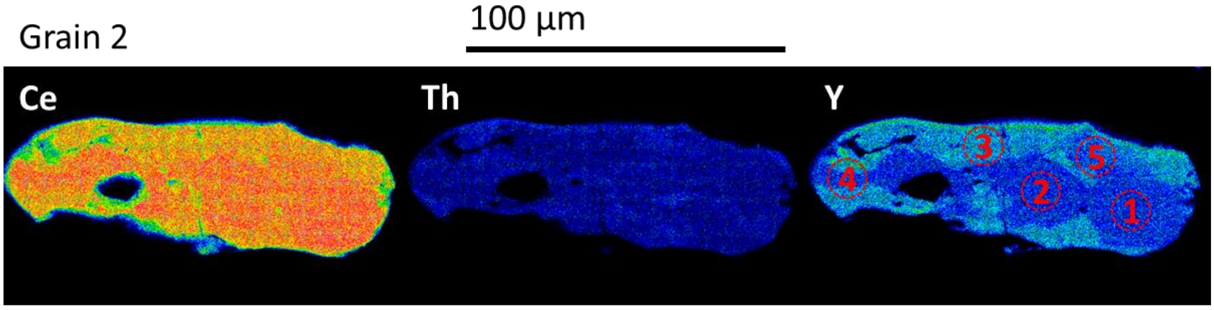

Grain 3

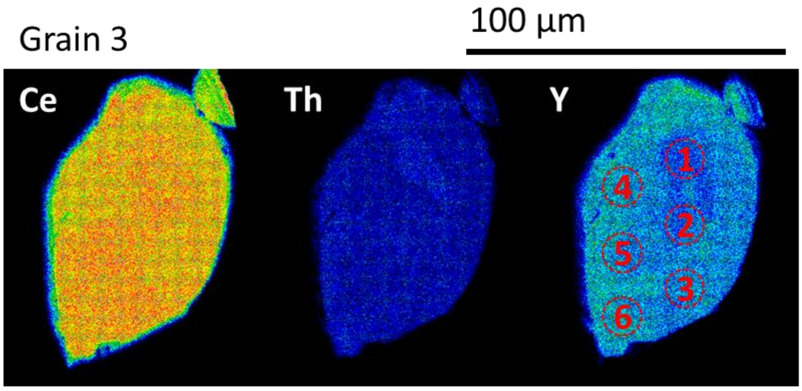

Grain 4

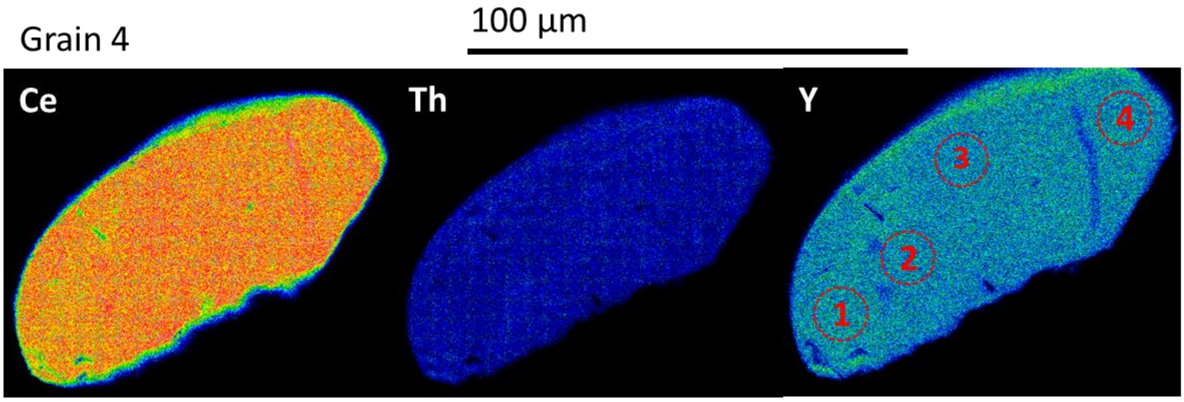

Sample 09b cont.

Grain 5

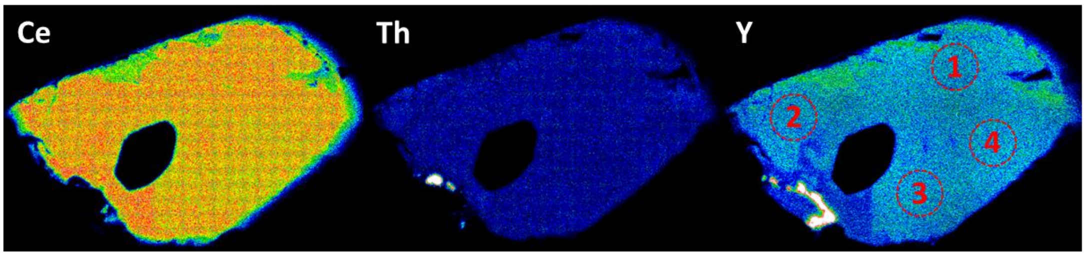

Grains 6 (left) & 7 (right)

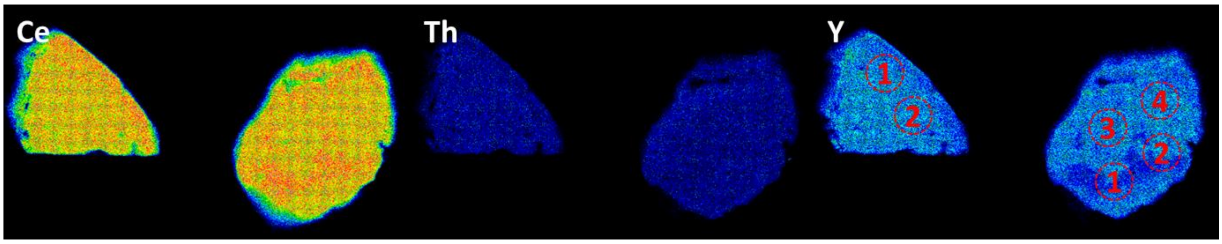

Grain 8

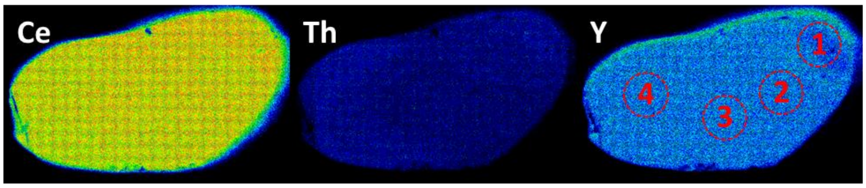

Grain 9

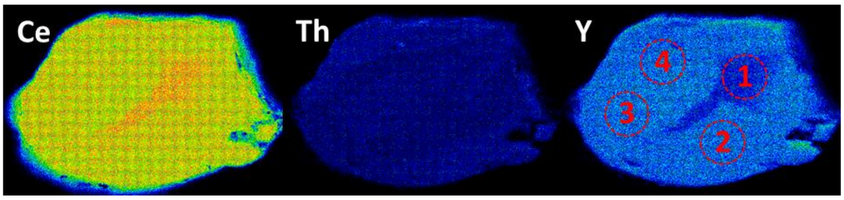

Grain 10

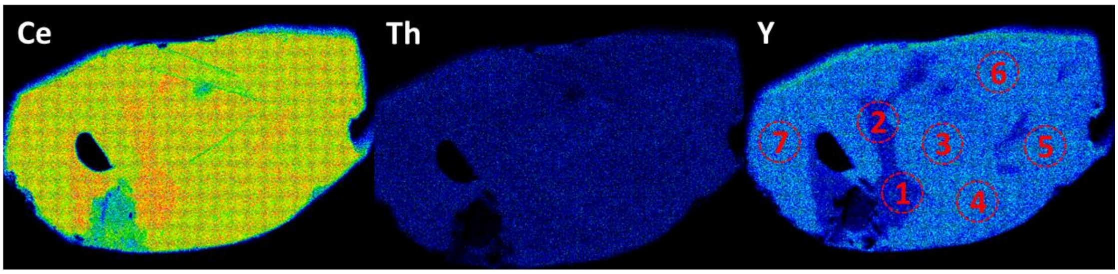

Sample 10

Grain 1

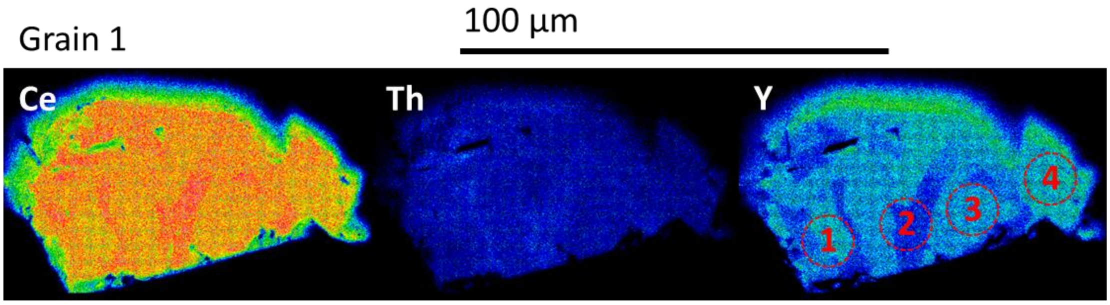

Grain 2

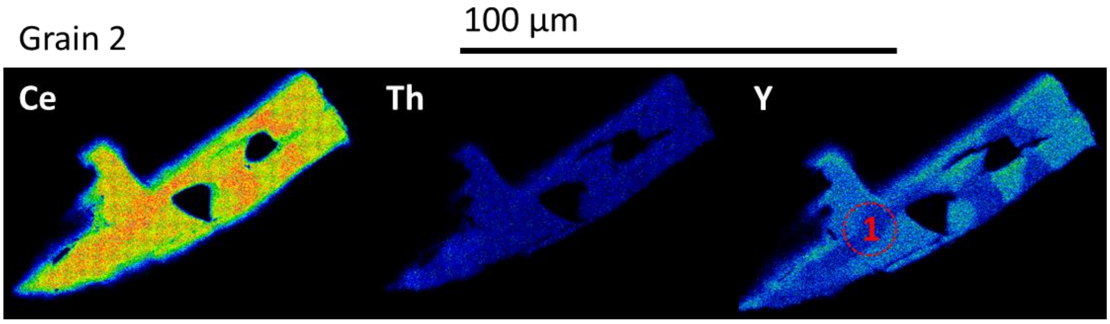

Grain 3

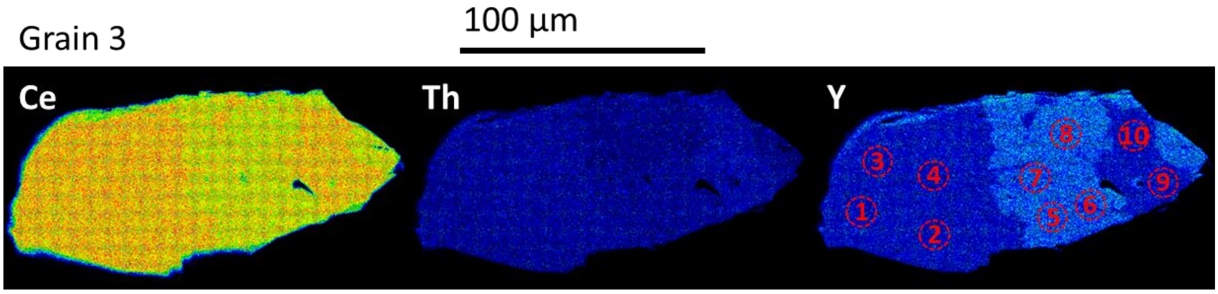

Sample f02

Grain 1

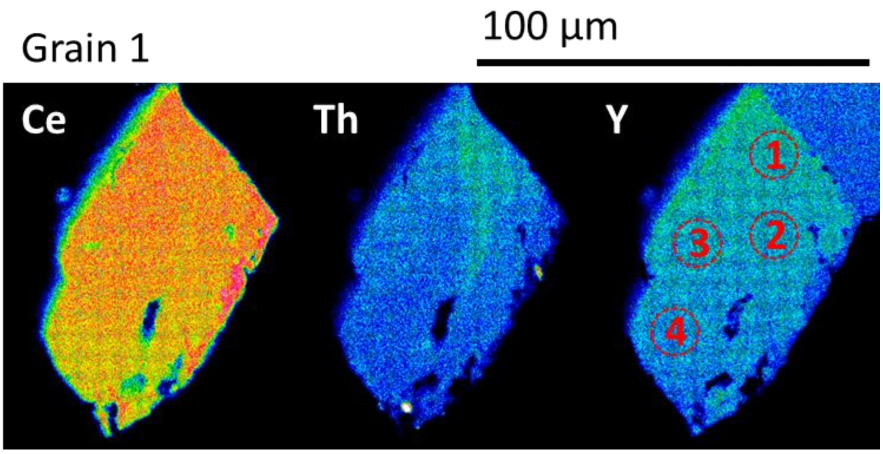

Sample f04

Grain 1

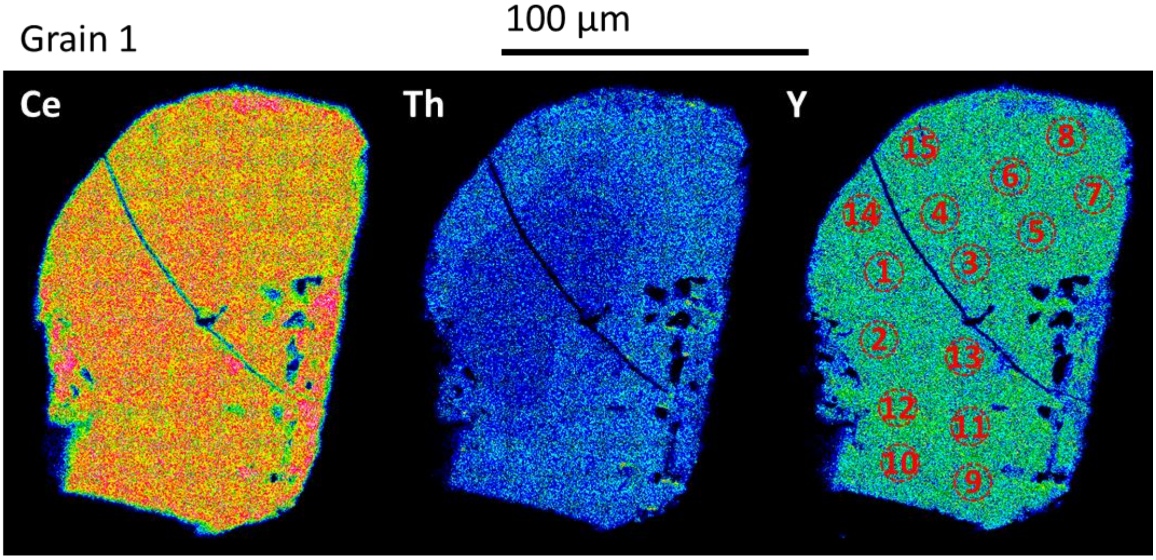

Sample f13

Grain 1

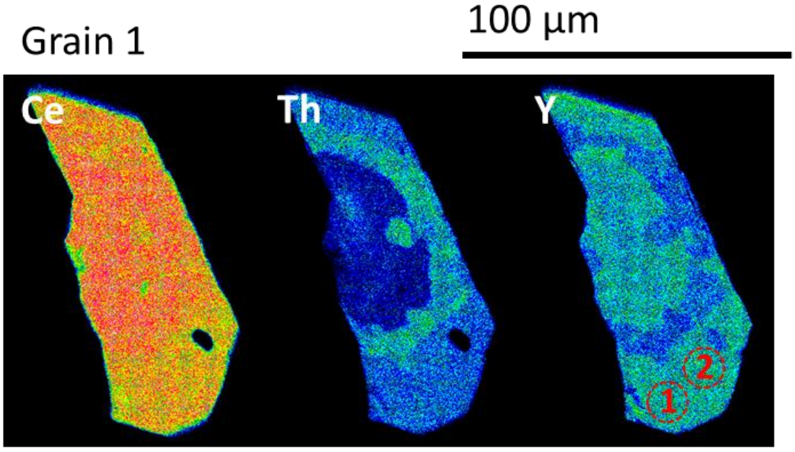

Grain 2

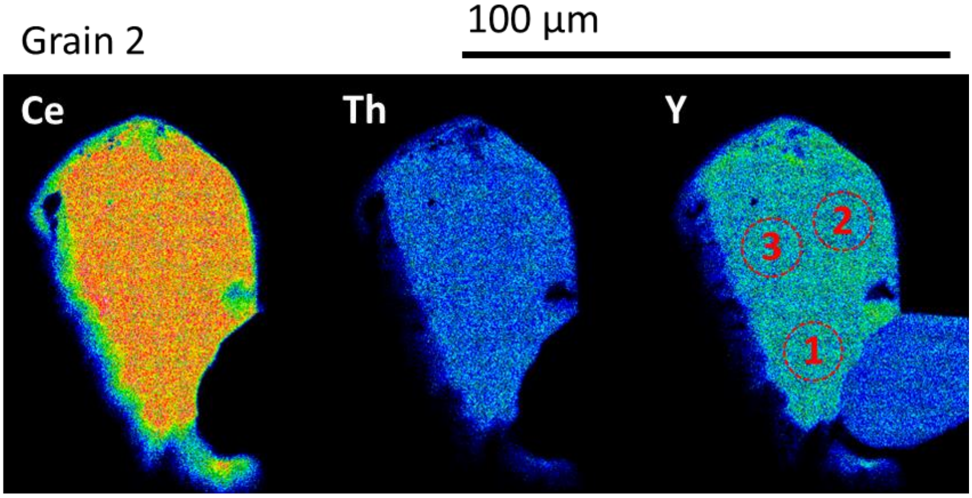

7.5.3 Monazite U-Th-Pb results

See the accompanying Excel file ‘Appendix E’ sheet labelled 7.5.3 Monazite age data.